BRIDGMAN GROWTH OF $CuInSe_2$ MONOCRYSTALS FOR PHOTOVOLTAIC CELL RESEARCH

Ziad Aziz Shukri, (B.Eng, M.Eng., McGill),

Department of Electrical Engineering,
McGill University, Montreal
July, 1996.

A thesis submitted to the Faculty of Graduate Studies and Research
in partial fulfilment of the requirements of the degree of
Doctor of Philosophy.

National Library of Canada

Acquisitions and Bibliographic Services Branch

395 Wellington Street
Ottawa, Ontario
K1A 0N4

Bibliothèque nationale du Canada

Direction des acquisitions et des services bibliographiques

395, rue Wellington
Ottawa (Ontario)
K1A 0N4

Your file Votre référence

Our file Notre référence

ISBN 0-612-19773-5

Canada

ABSTRACT

Ingots of the semiconducting compound $CuInSe_2$ have been grown by the Bridgman method using a single sealed quartz ampoule for both the compound synthesis, from starting elements of copper, indium and selenium, and the subsequent crystal growth. The resulting ingots, containing monocrystals of up to 2 centimetres in one dimension, were free of microcracks, voids and free of adhesion to the inner wall of the quartz ampoule. This was made possible by the unique use of a coating of boron nitride deposited on the inner wall of the ampoule prior to charging with the elements. The boron nitride acted as an effective getter in reducing the oxygen content in the starting copper, thus eliminating the adhesion between the ingot and the quartz. Reduction of the oxygen in the copper, by prior heat-treatment under high vacuum pumping, was found to be less effective than the boron nitride. The one-ampoule method used, resulted always in ingots having a uniform composition and conductivity type, which was p-type for stoichiometric starting proportions of the elements. In ingots with non-stoichiometric starting compositions, the resulting conductivity type, in the main part of the ingot, was also uniform, either p-type or n-type, with a composition close to stoichiometry. However, for non-stoichiometric melts, the last region to freeze contained binary compound phases of the elements with an excess over stoichiometry. In the main single phase chalcopyrite region, it was found that, generally speaking, n-type conductivity prevailed when the indium content was greater than about 25 % and p-type when it was less than this proportion, as determined by EPMA. This was apparently irrespective of the copper or selenium content. The ingots were found to cleave, up to 1 cm^2 in area, in one of two principal cleavage planes, which are the {112} and {101}.

A third *macroscopic* cleavage plane, the {110}, was also observed in the ingots, although less frequently but was found to be made up of {112} microcleavages. Twinning was present in the grown crystals and was found to occur only in the {112} plane. Preliminary photovoltaic cells of the structure $CuInSe_2$(p)/CdO(n) were fabricated using monocrystalline cleaved $CuInSe_2$ substrates. In a cell where the substrate was annealed at atmospheric pressure, prior to the CdO deposition, a solar conversion efficiency of over 6 % was obtained, despite a 23 % lattice mismatch between the $CuInSe_2$ and the CdO. Minority carrier diffusion lengths were estimated in the $CuInSe_2$ substrates by the photocurrent-capacitance method to be about 3 micrometers, which was about twice the value obtained for a high efficiency polycrystalline commercial thin film $CuInSe_2$ cell, using the same method.

RÉSUMÉ

Des lingots du composé semi-conducteur $CuInSe_2$ on été produits selon la méthode de Bridgman dans une seule ampoule de quartz scellée, où se sont déroulées tant la synthèse du composé à partir des éléments de base (cuivre, indium et sélénium) que la croissance du cristal. Les lingots contenaient des monocristaux atteignant 2 centimètres dans une dimension; ils étaient exempts de microfractures et de cavités et n'adhéraient pas à la paroi intérieure de l'ampoule, grâce à une solution unique qui a consisté à déposer du nitrure de bore sur cette paroi avant d'introduire les éléments dans l'ampoule. Employé comme dégazeur, le nitrure de bore s'est révélé efficace pour réduire la concentration d'oxygène que produit dans le lingot le cuivre utilisé au départ et supprimer l'adhérence du lingot à l'ampoule de quartz. À cet égard, la réduction de la teneur en cuivre par préchauffage sous vide poussé s'est révélée moins efficace que l'ajout de nitrure de bore. La méthode à une seule ampoule utilisée produits toujours des lingots uniformes quant à la composition et à la conductivité, qui est de type p lorsque les éléments de base sont en proportions stoechiométriques. Dans les lingots de composition initiale non stoechiométriques, la conductivité de la partie principale du lingot était uniformément de type p ou n. Dans la partie principale du lingot, la composition déviait à peine de la stoechiométrie, même dans les lingots produits à partir d'éléments en proportions non stoechiométriques. Dans ces lingots, la dernière région à se solidifier contenait toutefois des composés binaires formés à partir des éléments excédant les proportions stoechiométriques. Dans la principale région uniphasée de chalcopyrite, on a constaté que la conductivité était généralement de type n lorsque la teneur en indium dépassait 25 % et de type p lorsqu'elle était inférieure à cette proportion, déterminée par micro-analyse à sonde électronique. Ce phénomène ne semblait pas tributaire de la teneur en cuivre ou en sélénium. Les lingots se clivaient en des surfaces atteignant 1 cm^2 , selon un des deux plans de clivage principaux, soit les plans {112} et {101}. Un troisième clivage *macroscopique*, le plan {110}, moins fréquent , était constitué de microclivages {112}. Il y a eu formation de macles dans les cristaux obtenus par croissance mais seulement sur le plan {112}. Des cellules photovoltaïques préliminaires de structure $CuInSe_2$(p)/CdO(n) ont été fabriquées à l'aide de substrats clivés de $CuInSe_2$ monocristallin. Dans une cellule dont le substrat avait été recuit à la pression atmosphérique avant déposition du CdO, on a obtenu un rendement de conversion solaire supérieur à 6 % malgré une erreur d'adaptation cristalline de 23 % entre le $CuInSe_2$ et le CdO. À l'aide de la méthode *photocourant-capacité*, on a estimé que les longueurs de diffusion des porteurs minoritaires étaient d'environ 3 micromètres dans les substrats de $CuInSe_2$, cette valeur étant environ deux fois plus élevée que celle mesurée par la même méthode dans une cellule commerciale à haut rendement faite de $CuInSe_2$ polycristallin à couche mince.

ACKNOWLEDGEMENTS

The author wishes to express his sincere gratitude to his supervisor professor C.H. Champness for his continued guidance, constructive discussions and patient advice throughout this work, without which this work would not have been possible.

The author would also like to thank further, the following people for their valuable assistance: Mr. Joseph Mui for his kindly help and professional advice with photographic work, Mr. Glenn Poirier for his assistance with the electron probe measurements and data analyses, professor Robert Harris for supplying the oxygen-free copper and for his discussion on gettering, Mr. Peter Noutsios for his assistance with the laser-goniometer setup for angle measurements, Mr.Salah Shata for his help with the automated X-ray diffractometry work, Dr. Isabella. Bassignana (*Bell Northern Research*) for carrying out the rocking curve measurements, Dr. Ishiang Shih and Mrs. Helen Campbell for their help with SEM work, the *National Renewable Energy Laboratory* (Golden, Co.) for testing and calibration of the $CdO/CuInSe_2$ photovoltaic devices, the *Noranda Technology Center* for supplying the high purity selenium, Mr. Galaly Ahmed for carrying out the Hall measurements, Mr. Kezia Cheng for his maintenance of laboratory equipment and finally Mr. Don Pavlasek, for his help in machining the various mechanical components.

The author would also like to acknowledge the financial support of this work by a strategic grant from the Natural Sciences and Engineering Research Council of Canada (NSERC). The author is in debt to his mother for her continued moral support, encouragement and unconditional love throughout his life, to whom he dedicates this thesis.

TABLE OF CONTENTS

CHAPTER 1

INTRODUCTION

The object of the work of this thesis is the growth of single crystals of the chalcopyrite semiconductor $CuInSe_2$ in order to facilitate the use of this material in photovoltaic solar cells. The provision of such crystals will enable this and other laboratories to obtain information on fundamental properties of this material, which are difficult, or in some cases impossible, to obtain on polycrystalline thin films. It will also enable technologies to be developed and understood in using single crystals in laboratory cell structures. This being so, the first question to be answered is why prepare $CuInSe_2$ and not other solar cell materials and the second question is why work on single crystals, rather than on the more economic polycrystalline thin films of this semiconductor.

In respect of thin films, it is necessary to point out that photovoltaic cells should ultimately be cheaper to make in thin film form than using single crystals, since less material is used in the process. In present day single- and poly-crystalline silicon cells, a thickness of some 50 to 100 micrometers is needed for the absorber layer. This is because the absorption coefficient, α, is not very large in crystalline silicon (x-Si) as compared with amorphous silicon (a-Si), as indicated in Fig.1.1, and thus a larger absorber layer, with a thickness of the order of $1/\alpha$, is needed to convert most of the incident photons into electron-hole pairs, provided the minority carrier diffusion length is large enough. In the economics of solar cell fabrication, the cost of the semiconductor absorber material is important because of the essential lateral simplicity of the device. This is in contrast to an integrated circuit, where the main cost is in the design and fabrication of the many junctions and special areas on the chip, so that the silicon material cost by comparison is negligible. Thus, in a solar cell, if the absorber layer can be made thinner, there is a cost saving. The material $CuInSe_2$ has one of the highest values of α among all semiconductors over the main part of the solar spectrum. For instance, Fig.1.1, shows that at a wavelength of about 550 nm, corresponding to the sun's maximum terrestrial energy, α would be well over 10^5 cm^{-1} for $CuInSe_2$. This corresponds to a penetration depth for light of the order of 10^{-5} cm (or 0.1 micrometer) which, in practice, means that a film of 1 micrometer would capture most of the sun's incident photon energy. Thus, $CuInSe_2$ is a very suitable material for the absorber layer of a thin film solar cell. Other candidate materials, which have a high optical absorption coefficient are cadmium telluride and hydrogenated amorphous silicon. However, these materials have given somewhat lower conversion efficiencies, in laboratory cells, as compared with $CuInSe_2$ and , furthermore, amorphous silicon solar cells suffer from a light-induced degradation in performance, known as the Staebler-Wronski effect. For these reasons it was decided to work on the material $CuInSe_2$. This material has also attracted the interest of the Noranda Technology Centre, a research division of an important Canadian company, for its potential use of selenium.

At the present time, much work is under way in laboratories in Europe and the USA on developing an efficient photovoltaic cell using thin film polycrystalline $CuInSe_2$. At the National Renewable Energy Laboratory (NREL), in Golden Colorado, a thin film cell has been recently developed, using the basic structure $Cu(In,Ga)Se_2(p)/CdS(n)/ZnO(n+)$, having a conversion efficiency of 17.7%, which at the present time is a world record for thin film cells. However, compared to other semiconductors, such as silicon and gallium arsenide, $CuInSe_2$ is relatively a new-comer, and many of its fundamental physical properties have not been determined. This is also true for the technology of its processing for devices, involving heat treatment, doping, etching, etc. The effect of crystal orientation in thin film polycrystalline structures on the cell performance is also not known. There is consequently a demand, in a number of world laboratories, for single crystals of the chalcopyrite $CuInSe_2$ and indeed, monocrystals have been sent from our laboratory to the National Renewable Energy Laboratory in the USA, the University of Stuttgart, in Germany and also to France. One of the important and interesting aspects of $CuInSe_2$ is its defect chemistry, since in this ternary material, there are many possibilities for defect centers to occur. There have been numerous studies on single crystals of $CuInSe_2$ to investigate properties such as intrinsic defects [1.1], photoluminescence [1.2],[1.3], extrinsic doping [1.4], ion implantation, surface oxidation [1.5] chemical etching, transport measurements, DLTS [1.6] and energy band offset determination. There has also been much interest to grow and study homoepitaxial thin film layers of $CuInSe_2$ [1.7] as well as heteroexpitaxial films [1.8],[1.9]. For these studies, there is a need for high quality single crystal $CuInSe_2$ substrates large enough to be cleaved or polished in specific predetermined orientations.

Up until recently, single crystals of $CuInSe_2$ of good quality have not been available. Some frequent problems have been the presence of microcracks in the crystals and the non-uniformity in conductivity type, whereby some parts of the ingot were n-type and other parts p-type. Single crystals prepared in this laboratory, by contrast, have been microcrack-free and the conductivity type has always been uniform. In the measurement of many fundamental parameters, single crystals are preferred not only because they are more handleable, but also because they have precise crystallographic orientation, so that any anisotropic effects can be determined. In particular, it is not clear at the moment, if partial orientation of grains in a polycrystalline film parallel to a [221] direction is optimal or not. Furthermore, studies of laboratory cells fabricated with a monocrystalline absorber substrate are likely to shed more light on the photovoltaic action in the cell and possibly lead to higher performance. It is therefore clear that there is a need for high quality single crystals of $CuInSe_2$ and the present thesis is an effort to begin supplying this need.

In this work, crystals of $CuInSe_2$ were grown from the melt, since this is more convenient than from the vapour. Starting from the elements copper, indium and selenium, the compound was first synthesized and then single crystals were grown in an ingot by slowly freezing liquid material from one end using a vertical Bridgman process. Of the three elements involved, selenium, by far, has the largest vapour pressure, so that if an open crucible was used, most of this element would be lost. The synthesis and growth of the compound must therefore be done under pressure. If the pressure is not externally applied, say using argon, the process must be done in a closed vessel capable of withstanding the selenium saturated vapour pressure at the highest operating temperature. Accordingly, in the present work, the synthesis and growth were carried out in a single thick-walled sealed quartz ampoule. In previous work, in other laboratories, the synthesis and growth were carried out in separate sealed ampoules but this led to non-uniformity in conductivity type due to partial loss of selenium. The author believes that the single ampoule method, using his boron nitride procedure, as will be explained later, is a preferred process.

The crystal structure of $CuInSe_2$, at room temperature, is the chalcopyrite structure, shown in Fig.1.2. This structure is similar to zincblende in having two interpenetrating face-centered cubic sublattices (f.c.c.). Here, the selenium atoms are located on one f.c.c. sublattice and the metal atoms on the other. However, the copper and indium atoms are symmetrically arranged on this sublattice, as shown in the figure. The unit cell for $CuInSe_2$, like many other I-III-VI_2 compounds, has a **c/a** ratio of almost 2. In the case of $CuInSe_2$, the ratio is 2.006 with $\mathbf{a} = 5.789$ Å and $\mathbf{c} = 11.612$ Å [1.10] and it belongs to the space group $I\bar{4}2d$ (D_{2d}^{12} Schoenflies notation). Above a temperature of 810 °C, the compound is reported to have a sphalerite structure with the copper and indium atoms randomly arranged on the f.c.c. sublattice so that this material has cubic symmetry. As a semiconductor, $CuInSe_2$ has a direct energy gap of $E_G = 1.02$ eV and it can be made either n-type or p-type. Like many other semiconductors, the electron mobility in $CuInSe_2$ is much higher than the mobility of the holes.

This thesis concentrates on the growth of the compound by the Bridgman method using a two-section resistively-heated furnace, which is described in detail. The main problem in the melt growth, which has been perhaps somewhat greater with the one-ampoule method, is the adherence of the grown ingot to the inner wall of the quartz ampoule. This problem, however, was completely solved in the present work and how this was done is a major part of the present thesis. Besides work on stoichiometric material, efforts were made to grow and study material from non-stoichiometric starting proportions of the elements. A study was also made of the cleavage and twinning properties of $CuInSe_2$ crystals, representing the first comprehensive investigation of this topic for this material. Since a principal objective of the growth of the crystals was to further the understanding of photovoltaic cells using $CuInSe_2$, a preliminary study was initiated to fabricate cells with monocrystalline substrates. This work was carried out with photovoltaic cells having the structure $CuInSe_2$ (p)/CdO(n), where the CdO was the window layer. The CdO material, while not the best choice for a solar cell, is one where the techniques of deposition were well established in the author's laboratory and this experience was extensively made use of in the present work. As will be seen, the cells in fact gave better performance than expected and demonstrated that the $CuInSe_2$ was of device quality and thus capable of yielding even higher efficiency in a cell with a suitable lattice-matched window layer.

The structure of the thesis is as follows. A historical survey of the growth of $CuInSe_2$ by melt processes is first given in chapter 2. This is followed, in chapter 3, by a description of the vertical Bridgman method used, the steps taken to avoid ingot-ampoule sticking and the results of the growth runs. In chapter 4, the investigation of the cause of ingot sticking is described and the identification of the agent involved. Chapter 5, reports the results of growth runs with non-stoichiometric proportions in the melt and chapter 6 presents the results of the determination of all the principal cleavage planes in the $CuInSe_2$ crystals, along with the identification of its twinning plane. Work on preliminary $CuInSe_2$ /CdO photovoltaic cells is described in chapter 7, together with estimates of the minority carrier diffusion length in the substrates. Finally, in chapter 8, the results of the thesis as a whole are discussed and the main conclusions stated.

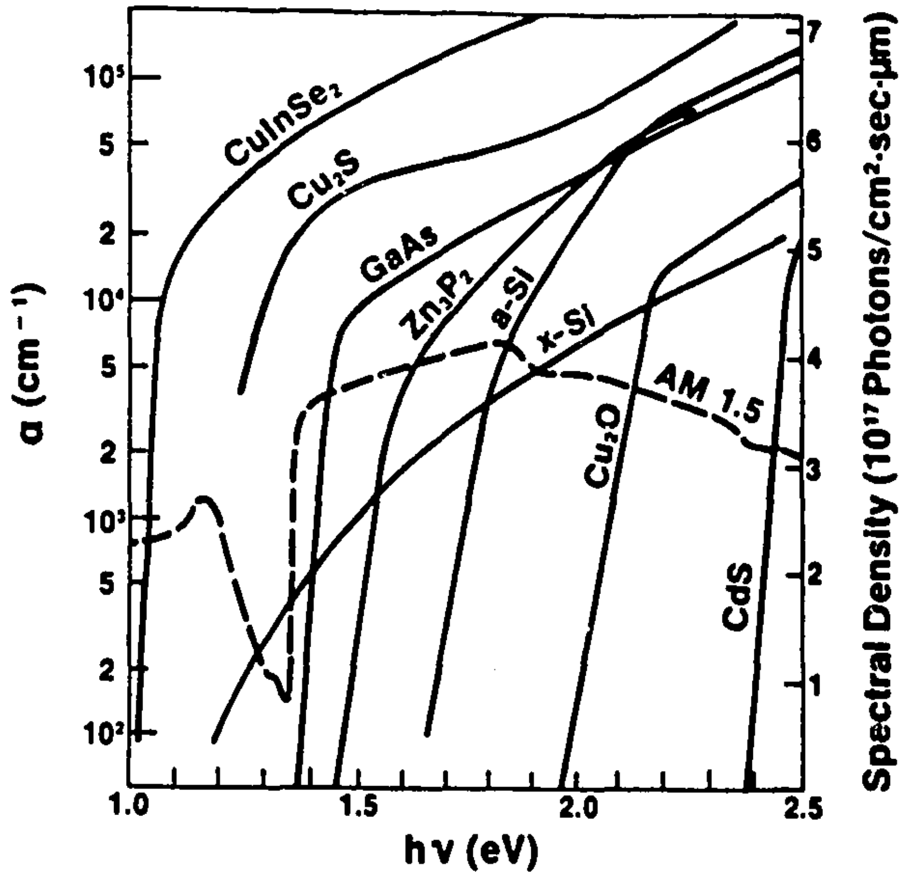

Fig.1.1 Plot of optical absorption coefficient against incident photon energy for selected semiconductor materials (After K. Mitchell and S. Wagner, Tutorial Notebook, *20th IEEE Photovoltaics Specialists Conf*, 1988).

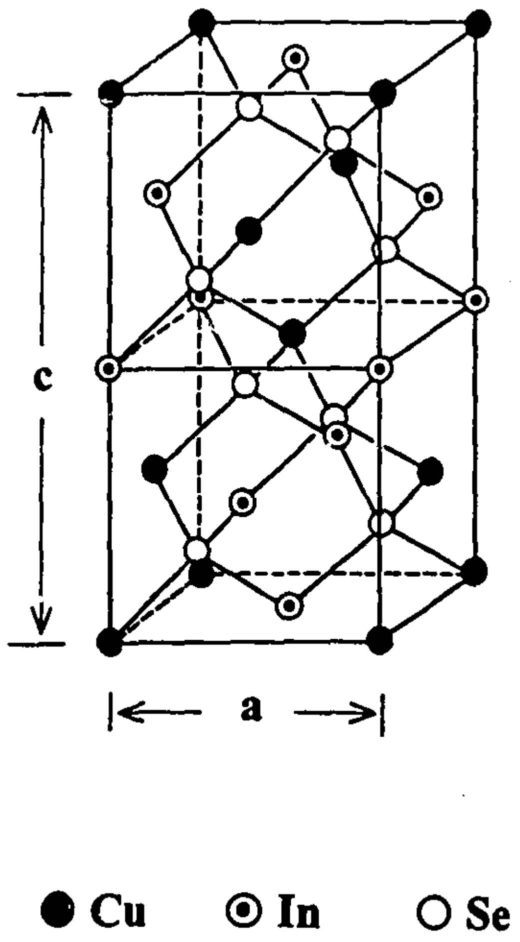

Fig.1.2 Schematic diagram of the chalcopyrite unit cell of $CuInSe_2$,where the values of the lattice parameters a and c are 5.789 and 11.612 Å respectively.

CHAPTER 2

HISTORICAL SURVEY OF MELT-GROWTH OF CuInSe$_2$

2.1 INTRODUCTION

Copper indium diselenide has been prepared in single crystal form, or in multicrystalline form with large grains, in many ways. However, since the present thesis is concerned with its preparation by the Bridgman method, it is of interest, for a historical survey, to concentrate on melt grown CuInSe$_2$. Accordingly, this chapter attempts to describe the main contributions to bulk crystal growth of the compound from the melt and hence work on thin films and other techniques, such as iodine transport growth, are not surveyed. The effect of dopants in CuInSe$_2$ is also not covered in this chapter.

2.2 1953 - 1970

An early reference to the synthesis of CuInSe$_2$ was in 1953 by Hahn, Frank, Klinger, Meyer and Störger [2.1], who prepared a number of I-III-VI$_2$ compounds. Starting with a mixture of the elements copper, indium and selenium in an evacuated sealed quartz ampoule, they heated the contents at 900°C for 12 hours. The result for CuInSe$_2$ was a fine-grained crystalline material, which like the other I-III-VI$_2$ compounds (where I was Cu or Ag, III was

Aℓ, Ga, In or Tℓ and VI was S, Se or Te), gave a chalcopyrite lattice from X-ray diffraction studies.

In 1956, $CuInSe_2$, along with some other chalcopyrites, were prepared by Austin, Goodman and Pengelly [2.2] by heating the starting elements in an evacuated sealed silica tube, followed by zone melting. The resulting ingots were all polycrystalline with numerous cracks, attributed by the authors to the differential thermal expansion between the **a** and **c** directions of 3×10^{-6} per °C for $CuInSe_2$.

Palatnik and Rogacheva [2.3], in 1967, determined the phase diagram for the pseudo binary system Cu_2Se-In_2Se_3, reproduced for the approximate range of 20 to 70 % mole In_2Se_3, in Fig.2.1. This shows a maximum in the liquidus curve at 50 mole % of In_2Se_3, corresponding to the compound $CuInSe_2$ with a melting point of about 986 °C. Between 1000 and 810 °C, there exsists a δ phase, which is a sphalerite structure, where the Cu and In atoms are randomly disposed on their face-centered sublattice, so that the material has a cubic symmetry. Below 810 °C, there is the chalcopyrite structure (γ-phase), which near room temperature, extends from 50 to about 54 % indium. Thus, this phase diagram indicates multi-phase material would be obtained for compositions with less than 50 % or more than 54 % indium.In other words, the chalcopyrite phase can tolerate a 4 % excess of indium but apparently no excess at all of copper.

2.3 1970-1978

Because of perceived applications for non-linear optical components and fiber optic infrared detectors, interest grew in preparing I-III-VI$_2$ compounds and in 1973, improved melt-grown CuInSe$_2$ was reported by Shay, Tell, Kasper and Schiavone [2.4] of the Bell Telephone Laboratories and by Parkes, Tomlinson and Hampshire [2.5] of the University of Salford. Using stoichiometric proportions of the starting elements in an evacuated sealed silica ampoule, Shay *et al* [2.4] slowly raised the temperature to 1050 °C. Using gradient freezing, the temperature was lowered at a rate of 2 °C/ hr with crystallization taking place at the end of the silica boat within the ampoule. Electroreflection measurements made on this material indicated CuInSe$_2$ to have a direct energy gap of E_G = 1.01 eV at 77K. The preparations of Parkes *et al* [2.5], were done in a two stage process. The compound CuInSe$_2$ was first synthesized by pre-reacting the high purity starting elements in an evacuated sealed quartz ampoule, where the temperature was raised to 1050 °C. In the first stage, the heating rate was 4-6 °C/min until a temperature of 200 °C was reached and was maintained at this temperature for 4 hours, so that the exothermic heat could dissipate from the reaction between the Se and the In. The heating was then continued at a rate of 2-3 °C/min up to 1050 °C. After cooling down to room temperature, the ingot was removed from the ampoule and found to have extensive micro-cracking and voids. The second stage was then begun, whereby the ingot was powdered and introduced into a long evacuated quartz tube and sealed off. The tube was then made to traverse forwards and backwards through a horizontal three-zone furnace, where the central zone was maintained at 1050 °C. After 10 zone passes at a rate of 1.8 cm/hr, and a final traverse at the slower rate of 0.18 cm/hr, the ampoule was allowed to cool slowly over a period of two days. The resulting zone-grown ingots from stoichiometric starting proportions were invariably n-type and yielded void-free crystals with a typical size of 0.5 × 0.5 × 0.2 cm^3 but with some microcracks. The [221] direction was found to be within a few degrees of the growth direction. Both Parkes *et al* [2.5] and Tell, Shay and Kasper [2.6] found that p-type material could be obtained by heating these n-type crystals under excess selenium pressure.

In 1974, Wagner, Shay, Migliorato and Kasper [2.7] reported the first $CuInSe_2$(p)/CdS(n) photovoltaic cell with a 5 % solar conversion efficiency, where they used, as the substrate, their gradient-freeze material converted from n to p-type by annealing at 600°C for 24 hrs in a selenium atmosphere. About a year later, Shay, Wagner and Kasper [2.8] reported their, now famous 12% efficiency $CuInSe_2$/CdS cell with an antireflection coating for a small active area of about 0.8 mm^2. Without the antireflection coating, the efficiency was about 10.6 %.

Around this time, in 1974, Rau [2.9] published more accurate values of the saturated vapour pressure of selenium as a function of temperature and his data is reproduced in Fig.2.2. It is noted that at 1100 °C, the vapour pressure of selenium is more than 40 atmospheres and this is the reason for synthesis of $CuInSe_2$ in thick sealed ampoules. Since the boiling point of selenium is 685 °C, preparation of selenium compounds at temperatures above this value in open crucibles will result in a considerable loss of this element. It should be noted here that, since the boiling points of the copper and indium are respectively 2567 °C and 2080 °C, their saturated vapour pressures at 1100 °C would be very low.

Crack-free single crystals of $CuInSe_2$ were reported by Tell, Wagner and Bridenbaugh [2.10] in 1976, using a zone melting technique from stoichiometric starting proportions. The procedure consisted of three passes at 1 mm/hr through a zone with a maximum temperature of about 1015 °C and a temperature gradient of about 60 °C/cm. The crystals were p-type with a room temperature hole concentration of 3×10^{17} cm^{-3} and a mobility of about 20 cm^2/ (volt.sec). Tell and Bridenbaugh [2.11] also used 2 % (by weight) extra of Se, as well as stoichiometric mixtures, to obtain p-type material and made pn-junctions with Cd- and Zn-plated p-type substrates.

Haupt and Hess [2.12] in 1977 grew $CuInSe_2$ ingots of 1 cm in diameter and up to 5 cm in length using vertical Bridgman and Stockbarger methods; they also grew crystal platelets by an iodine transport technique. In their melt-growth work, they used the two stage process of pre-reaction of the high purity starting elements in one evacuated sealed silica ampoule, followed by removal and transfer of the polycrystalline compound into another ampoule with a pointed end. After sealing this ampoule, it was heated to 1080 °C, maintained at this temperature for 24 hours and then either lowered through a temperature gradient of 5 -10 °C/cm at a rate of 0.5 - 2.5 mm/hr (Bridgman method) or alternatively kept in a fixed position (Stockbarger method) in a temperature gradient and the temperature was slowly decreased at 2 °C/hr from 1020 to 750 °C and at a faster rate of 10° C/hr below 750° C. Haupt and Hess [2.12] in this work claimed that the use of already-reacted polycrystalline compound as the starting material for the crystal growth stage was advantageous because it avoided crystal cracking and voids. While they reported that their crystals were crack-free, they found it was necessary to have a slight excess of selenium to obtain low resistivity p-type crystals. implying that n-type material resulted from their stoichiometric starting proportions.

In the same year of 1977. Hörig, Neumann. Höbler and Kühn [2.13] prepared melt-grown $CuInSe_2$ ingots by slowly heating the starting elements in an evacuated sealed quartz ampoule to 1100 °C, holding at this temperature for 15 hours and then cooling at the relatively fast rate of 100 °C/hr. Their resulting material was invariably n-type with a relatively low electron mobility of 100 cm^2/(volt.sec) or less.

2.4 1979-1989

In 1979, Irie, Endo and Kimura [2.14] prepared $CuInSe_2$ ingots by heating the starting elements in an evacuated sealed quartz tube to about 1100 °C, maintaining this temperature for 10 hours and then. with normal freezing, cooling to room temperature at a rate of 10 °C/hr. With excess selenium over stoichiometry, they obtained p-type material and with excess indium, n-type. Their hole mobilities in p-type material at room temperature were in the range 10 to 20 cm^2/(volt.sec). Gonzalez, Rincon, Redondo and Negrete [2.15] in 1980. used a vertical Bridgman method to obtain p-type crystals with a hole concentration of 6×10^{16} cm^{-3} and a mobility of about 20 cm^2 /(volt.sec). The temperature of the top hot region of the furnace was 1040 °C and that of the cooler region 750° C with a 30° C/cm temperature gradient; the lowering rate was 2 mm/hr with rotation of the ampoule. Prior to descent. the ampoule was cooled from a temperature or 1100 °C, at which the compound synthesis had been carried out.

Using a monocrystalline substrate, Arya, Warminsky, Beaulieu, Kwietniak and Loferski in 1983 [2.16] fabricated a $CuInSe_2/CdS$ cell yielding a solar conversion efficiency of 10.6 % with an effective cell area of about 0.8 mm^2, thus matching the results of Shay *et al* [2.8]. The small area was due to avoiding microcracks in the substrate, which was obtained from an ingot prepared by the two-stage Bridgman method. Here, the furnace temperature was stated to be 1000 °C, which is only just at the melting point of $CuInSe_2$.

Prior to 1984, where experimental details were given, melt-growth of $CuInSe_2$ was done using the two-stage process. In this, compound synthesis was done in one ampoule, the pre-reacted material transfered to another ampoule and the crystal growth by a Bridgman or Stockbarger method was carried out. To some extent, this avoided the problem of ingot sticking to the inner wall of the ampoule and, with good mixing, minimized voids in the ingot. However, if stoichiometric starting proportions were used, the final ingot was either n-type or n-type in one region and p-type in another. For instance, Tomlinson [2.17] reported an ingot to be n-type in the first 3 cm from the end first-to-freeze and p-type in the last 1.5 cm. The first clearly stated use of a one-ampoule method, for both synthesis and crystal growth was by Shih, Shahidi and Champness [2.18] in 1984. They used either a Bridgman or a Stockbarger horizontal growth procedure and found that, for stoichiometric starting proportions, the ingots were always uniformly p-type. The one-ampoule method prevented the loss of selenium, which otherwise led to n-type behaviour, and thus resulted in obtaining uniform p-type behaviour, which was a significant improvement. However, Shih *et al* [2.18], found that ingot sticking to the ampoule often occurred and while grinding the inner surface of the quartz ampoule or depositing a thin carbon film helped somewhat, it was not always successful.

In 1984, Bachmann, Fearheiley, Shing and Tran [2.19] reported further phase relation work for the Cu, In, Se system and found (in addition to $CuInSe_2$) a compound of composition Cu_5InSe_4, with a high melting point of 943 °C. However, this compound , which can be regarded as 5 Cu_2Se + In_2Se_3 ,is unstable at room temperature. Bachmann *et al* [2.19] also prepared $CuInSe_2$ crystals by directional freezing but since the Se vapour pressure was kept below 0.5 atmosphere during the growth, it is likely that their ingots were deficient in Se because, at the melting point of $CuInSe_2$, the saturated vapour pressure of this element is more than 18 atmospheres. It is interesting to note that they found a pyrolitic boron nitride crucible to be a most suitable material which did not adhere to the $CuInSe_2$.

An important contribution to the melt-growth of $CuInSe_2$ was made in 1985 by Ciszek [2.20]. He grew crystals in an open crucible of quartz or boron nitride using boric oxide (B_2O_3) as a liquid encapsulent under an argon pressure of 50 to 70 atmospheres. Using a Bridgman / Stockbarger method, the crucible was either lowered through an r.f. coil or kept stationary with slow reduction of the r.f. power. Using a Czochralski method, a "seed" consisting of a quartz rod with a graphite core, was lowered through the liquid B_2O_3 to reach the $CuInSe_2$ surface and an ingot was pulled from the $CuInSe_2$ melt. It was found , in the case of the directionally frozen ingots that, cracks occurred if the cool-down rate was too fast. Stoichiometric starting proportions yielded n-type material but p-type ingots were obtained with excess initial selenium. A photograph of a Czochralski-grown ingot suggested the presence of many crystals but the method would seem promising, with further development.

In the view of Tomlison, expressed in a paper in 1986 [2.21], the vertical Bridgman method is superior to the zone growth procedure for obtaining larger $CuInSe_2$ crystals. In his Bridgman setup, at the University of Salford, *the furnace was moved over the ampoule* at a speed of 1 mm/hr. This may have advantages over the usual arrangement of keeping the furnace fixed and moving the ampoule.

A revised phase diagram for the pseudo binary system Cu_2Se-In_2Se_3 was determined by Fearheiley [2.22] in 1986 and is reproduced in Fig.2.3. This indicates that the highest liquidus maximum is at a temperature of 1005 °C with a composition of $CuIn_{1.22}Se_{2.33}$ (corresponding to $CuInSe_2$ + 11.1 % In_2Se_3) and not $CuInSe_2$. This would apparently mean that from a stoichiometric liquid, the first material to freeze would be $CuInSe_2$ with dissolved excess In_2Se_3. Indeed, excess indium was found by Vahid Shahidi *et al* [1.10] along the main part of their ingots and Tomlinson [2.17] reported a significant build-up of copper close to the last end-to-freeze in his ingots. In addition, the phase diagram of Fearheiley in Fig.2.3, also shows a liquidus maximum at the composition $CuIn_3Se_5$, as well as that previously reported at Cu_5InSe_4. Becker and Wagner [2.23], from differential thermal analysis, reported a phase transformation, not only at 810 °C, but also at 665 °C for $CuInSe_2$. However, the latter temperature has not been confirmed in later work and is not evident in Fig.2.3.

2.5 1989 - 1992

In a review in 1989, Tomlinson [2.24] stated that the adhesion between $CuInSe_2$ and the wall of the silica ampoule was promoted by the presence of water vapour, which accelerated the devitrification of the quartz. He recommended as a remedy out-gassing of the charged ampoule at 100 °C just prior to seal-off. However, use of this procedure in the present author's laboratory was not found to eliminate the sticking problem. Tomlinson [2.24], also stated that the presence of any undissolved Cu_2Se (melting point above 1100 °C) in the melt could lead to cracking and voids in the ingot.

In the same year of 1989, using r.f. heating and a graphite susceptor, Weng, Yip, Shih and Champness [2.25], with a vertical Bridgman method, grew ingots from stoichiometric melts. They employed an accelerated crucible rotation technique to obtain better mixing but the use of r.f. heating was found to be no better than resistance heating and more difficult to control. In their one-ampoule procedure, with stoichiometric starting proportions, only p-type material was obtained.

In 1990, Yip, Weng, Shih and Champness [2.26] reported on the preparation of ingots from non-stoichiometric initial proportions. Despite strong deviations from initial stoichiometry, they found the first part of every ingot to be single phase chalcopyrite, with multi-phases only in the end part of the ingot - the last region to freeze. In this region, Cu_4In was identified [2.27] in material with excess copper and Cu_7In_4 in material with excess indium, along with an apparently undocumented compound of composition In_3Se_2. It is interesting to note that the binary compounds Cu_2Se and In_2Se_3 were never observed in the multi-phase regions in these studies. In the single phase region of the ingots, the relation between conductivity type, n or p, and composition was not simple [2.28] and did not correlate well with the results of Neumann and Tomlinson [2.29] . However, there was a clear relation between *starting* composition and conductivity type.

After about 1991, $CuInSe_2$ ingots were prepared by Bridgman methods in the laboratory of the author and in that of L.S. Yip, using resistance-heated furnaces rather than an r.f. heated furnace. The problem of the adherence between the ingot and the quartz wall of the ampoule remained. Then, in 1992, a breakthrough occurred and procedures for obtaining completely adhesion-free ingots were obtained [2.30][2.31] by the inclusion of sufficient graphite [2.32] or flamed-in boron nitride coating [2.33] into the ampoule, prior to charging. The BN procedure is an essential part of this thesis and will be fully discussed in the following chapters. Following this successful development, ingots free of microcracks and voids and of uniform conductivity type became available for other studies.

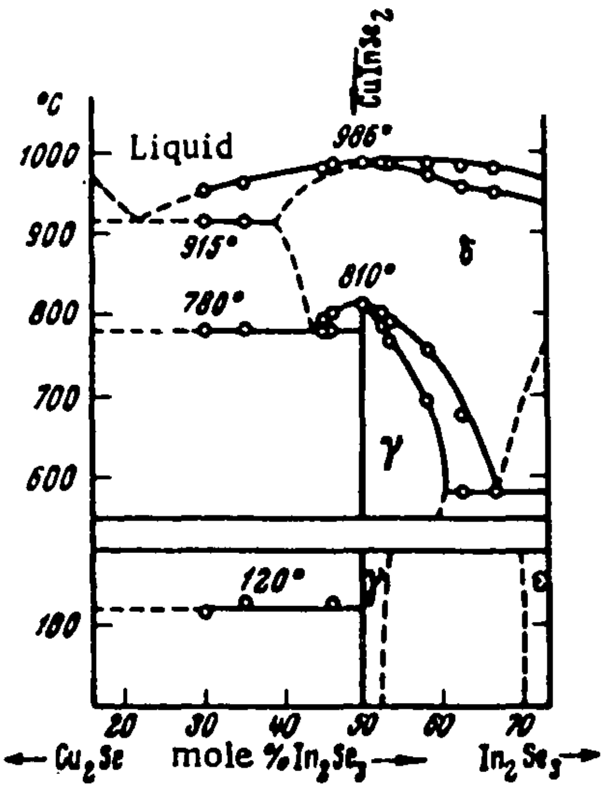

Fig.2.1 Pseudo binary phase diagram of the Cu_2Se-In_2Se_3 system in the concentration range of 20 to 70 mole % In_2Se_3, after Palatnik and Rogacheva [2.3].

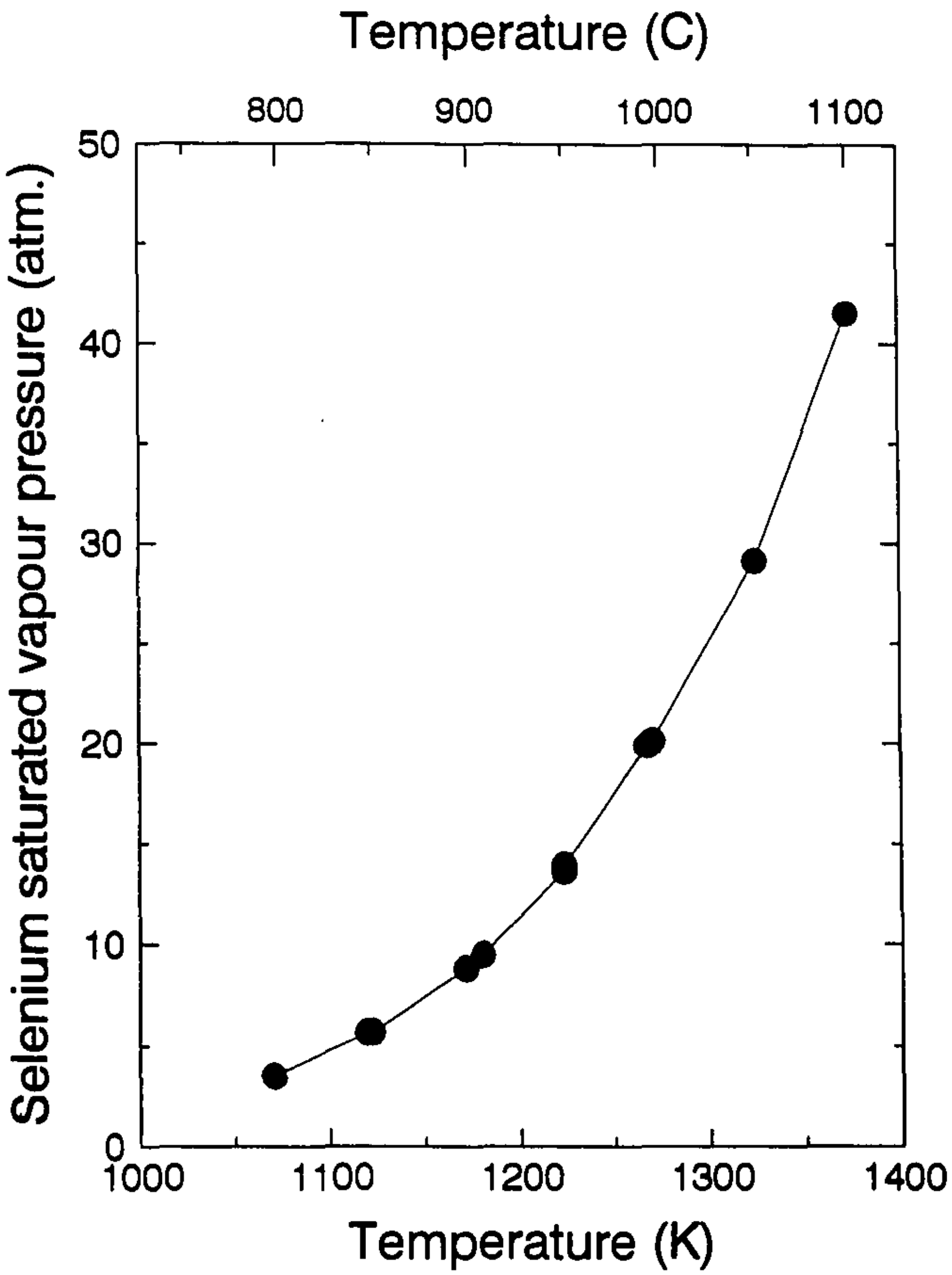

Fig.2.2 Plot of experimentally-determined selenium saturated vapour pressure against temperature, in the range of 1000 to 1400 K, after H. Rau [2.9].

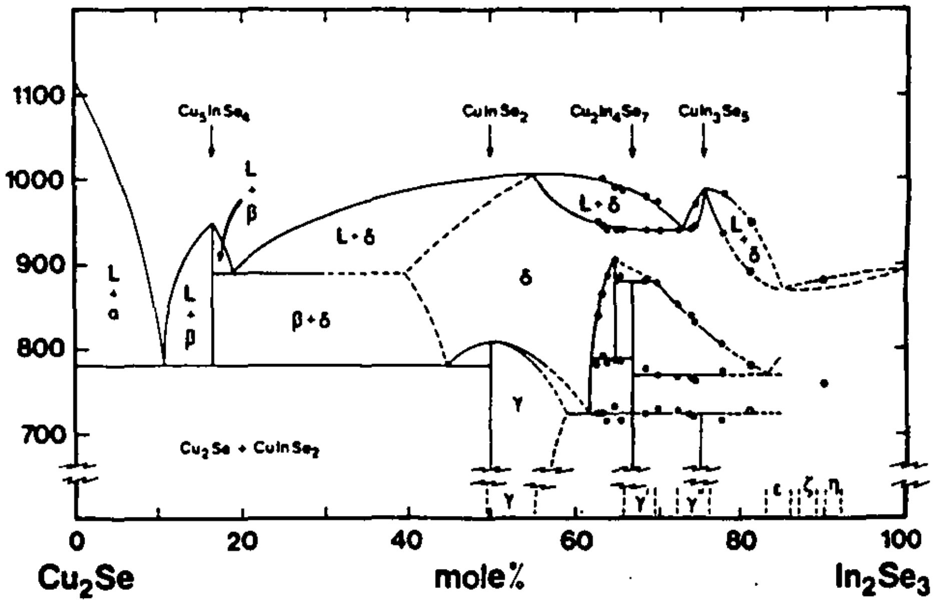

Fig.2.3 Pseudo binary phase diagram of the Cu_2Se-In_2Se_3 system, after Fearheiley *et al* [2.22].

CHAPTER 3

VERTICAL BRIDGMAN GROWTH OF $CuInSe_2$ MONOCRYSTALS

3.1 INTRODUCTION

The use of the one-ampoule method, pioneered mostly in this laboratory, and used in the present work, has the advantage of minimizing the loss of selenium. This loss takes place in the two-ampoule process, often used by previous workers and leads to inhomogeneity of conductivity type. The one-ampoule method, by contrast, results in uniformly p-type material if stoichiometric starting proportions of the elements are used. However, the adhesion problem between the quartz and the $CuInSe_2$ charge seems to be somewhat worse with the one-ampoule method, since the original charge is not broken-up in any way. As will be seen in this chapter, this adhesion problem was completely solved in the author's work by the introduction of boron nitride into the ampoule, in the form of a powder coating on the ampoule wall, prior to charging with the elements. Hence, with this solution, the one-ampoule Bridgman method would seem to be a preferred process and this is the one adopted by the author. Thus, in this chapter, the growth procedure is described in detail together with the results of growth runs with variation of some of the parameters. As will be seen, the use of the one-ampoule Bridgman procedure with boron nitride has resulted in obtaining single crystals of the chalcopyrite $CuInSe_2$ on a routine basis, which are large enough for many studies.

3.2 CRYSTAL GROWTH

In this section, the details of the crystal growth procedure, including the preparation of the ampoule using the boron nitride coating technique is presented. First, the growth apparatus is described.

3.2 (a) Crystal Growth Apparatus

The crystal growth of $CuInSe_2$ in this work was carried out by a vertical Bridgman method, using a resistively heated, 4600 watt, two-zone furnace (Thermcraft Inc. model 23/238-24-2ZV-ST). The temperature of the two zones of the furnace was controlled with a Honeywell programmable digital controller (model UDC 5000) with an accuracy of about ± 0.1 degree. A schematic diagram of the setup is shown in Fig.3.1, along with an actual measured temperature profile of the two zones. In order to obtain a high temperature gradient for the crystal growth, a ceramic baffle was placed between the top and bottom zones, which yielded a gradient of about 70 °C/cm. From the temperature profile, the solidification position of the compound was estimated to be at a depth of some 43 to 45 cm below the top surface of the furnace.

3.2 (b) Ampoule Cleaning

In this work, the $CuInSe_2$ charge synthesis and crystal growth were carried out in the same ampoule. The ampoule was made from a quartz tube, having an inner diameter of 12 mm and an outer diameter of 16 mm. It was shaped, using an oxygen-hydrogen flame, from one end to obtain a pointed tip resembling the letter V, in order to facilitate nucleation during early stages of the growth. The quartz tube, with only one end open, was cleaned with a mixture of HNO_3 and HCl (1:1 by volume) for a period of about 24 hours and then rinsed thoroughly in de-ionized (DI) water. The ampoule was then soaked in acetone for a similar period of time to remove any organic contaminants. Finally, the ampoule was rinsed again in DI water and dried, gently with the flame. The ampoule was now ready for the BN coating.

3.2 (c) Boron Nitride Coating

The boron nitride coating process of the ampoule was found to be an important step in the fabrication of adhesion- and void-free ingots of $CuInSe_2$. It makes possible employment of the same ampoule for both the synthesis and growth of the compound, resulting in ingots which are uniform in conductivity type. Furthermore, it does not require a supporting crucible within the ampoule. The boron nitride (BN) coating employed in this work was deposited as follows [2.33]. Boron nitride was obtained either in the form of a powder, of nominal purity 99.5%, from Johnson Matthey Ltd., or in the form of BN slurry, from Carborundum Company. The BN slurry was obtained in two types: V-BN, consisting of BN mixed with silica, and S-BN, where the boron nitride was mixed with an alumina phase. A small quantity (less than 5 gram) of the BN source was thoroughly mixed with about 10 to 20 ml of acetone to create a suspension with a thick consistency. The mixture was then transferred to the ampoule and given a manual agitation for some 2 to 3 minutes. This action allowed the ampoule wall to be coated with BN particles. The excess quantity of the suspension was poured out of the ampoule. After introducing the BN, the coating was made more uniform by spreading it out with a special brush until the desired thickness was obtained on the wall. The coated area was localized at the bottom end of the ampoule by rinsing away the excess coating elsewhere using DI water. After this, the ampoule, coated with the appropriate amount of BN, was gently heated between 80 to 100 °C in a small oven to drive out any residual acetone remaining behind. Fig.3.2(a) shows a photograph of an ampoule indicating the appearance of the BN. At this stage, the BN particles were loosely bound to the quartz and were easily removed with rinsing. In order to harden the coating, it was necessary to heat intensely, using a flame, both the quartz and the coating until the quartz was almost white hot. In the case of the 99.5% purity BN, the coating became fully transparent inside the ingot, as shown in Fig.3.2(b). In using the BN slurry as the source of BN, the coating was not completely transparent after the flame treatment; however, it was of superior hardness compared with powdered BN of equal thickness. In order to remove any residual BN particles, the ampoule was given a final rinse with DI water and dried gently with the flame. The intense flaming of the BN is an important step in the deposition of the coating whereby, if it is not done, the BN particles would be washed away by the molten charge and may cause contamination of the ingot.

3.2 (d) Preparation of Charge

In most of the growth runs carried out in this study, a stoichiometric charge of the elements was used for the synthesis of the compound. The starting materials of copper, indium and selenium were acquired in pellet form, each pellet with a diameter of about 3 to 5 mm, having a nominal purity of about 99.999%. The suppliers for these materials were

CERAC Coating Materials Inc. for the copper, Metal Specialties Inc. for the indium and Noranda Technology Center for the selenium. Stoichiometric proportions of the Cu, In and Se were calculated from their respective atomic weights, and the elements were weighed separately from a pre-etched supply of material. The pellets were etched prior to the weighing of the charge to avoid unwanted changes in the starting composition due to the etching action. The chemical etching of the Cu was carried out in dilute HNO_3 (1:10 in DI water by volume), while the etching of the In and Se was done in dilute HCl (1:10 in DI water by volume). The pellets were rinsed thoroughly in DI water and then dried in a flow of nitrogen. Fig.3.3(a) shows a photograph of the etched and cleaned elemental pellets, prior to introduction into the ampoule. After the etching, the charge was transferred to the BN-coated quartz ampoule which was attached, in a vertical position, to a vacuum pumping system (by Edwards Ltd.) equipped with a stainless steel manifold, having a 16 mm diameter ampoule inlet port. The system, with the ampoule in place, was then evacuated down to a pressure of about 4×10^{-7} Torr in some 2 to 3 hours. Using an oxygen-hydrogen flame, the ampoule was then sealed under vacuum from a position some 10 cm above the elemental charge pellets to avoid unwanted heating and possibly loss of selenium at this stage. As a precaution, the tip of the ampoule was kept cool in a water-soaked cloth. Prior to loading the ampoule for pumping, the position of sealing was marked and the quartz was thinned down to facilitate its melting. Using the flame, the thinned wall of the ampoule was gently melted, while the ampoule was rotated until the quartz wall had collapsed under the influence of vacuum, forming a sealed neck. Extra care is needed in the sealing-off process, especially in separating the ampoule from the remainder of the quartz tube, where the quartz may crack if too much force is used. After the sealing was complete, the ready ampoule, some 15 to 20 cm in length was allowed to cool down prior to the beginning of the next step.

3.2 (e) Reaction of Charge

The ampoule, with the charge inside, was placed in a horizontal position in a brick furnace, where the initial reaction between the elements was carried out. Here, the temperature was first raised slowly from room temperature to about 300°C, at about 2°C/min to allow the exothermic reaction between the indium and the selenium, near the temperature of 220°C, to take place. If the rise in temperature is too fast, an explosion would occur. To ensure a complete reaction, the temperature was maintained at 300°C for some 24 hours. At this stage, the only reactants were the In and the Se, while the Cu remained in pellet form. This can be seen in Fig.3.3(b), where the contents of a run, interrupted at a temperature of about 300°C, are shown, clearly indicating the presence of un-reacted elemental Cu. Next, the same ampoule was transferred to the top zone of the vertical crystal growth furnace, where the remainder of the reaction was carried out. To do this, the ampoule was attached, from its top end, to a quartz rod some 60 cm in length. The rod was connected to the mechanical lowering mechanism of the assembly and, with the furnace turned off, the ampoule was positioned in the center of the top zone of the furnace, at a depth of about 35 cm. Next, the temperature was set to 300°C and the furnace was allowed to stabilize for about 1 hour. The temperature was then raised at a rate of about 5°C/min up to 1100°C, that is some 100° C above the melting point of $CuInSe_2$. The reaction with the copper was complete however, before the melting point of this element (of around 1080°C) was reached. This is demonstrated in Fig3.3(c), where the contents of a run, interrupted at around 700°C, were powdered and are shown to reveal the absence of any Cu pellets. In order to ensure homogenization of the melt, the ampoule was maintained at 1100°C typically for 24 to 48 hours and given a thorough manual agitation several times during this soaking period.

3.2 (f) Crystal Growth Procedure

After the reaction and soaking of the charge was complete in the top furnace zone, the temperature of the lower zone was set to about 700 °C and the bottom furnace was allowed to stabilize for about 1 to 2 hours. This resulted in a temperature gradient of about 70°C/cm between the top and bottom zones. The directional freezing of the melt was then begun. The ampoule, in the top zone, was slowly manually displaced downwards to a depth of about 40 cm, nearer to the solidification position, where the temperature was still well above the melting point of the compound. The motorized lowering mechanism was then activated and the control was set to a lowering rate of 2 to 10 mm/hr. The growth was continued for 24 to 48 hours until the ingot was completely solidified, well into the cooler zone. The temperature of the top zone was then reduced to that of the bottom zone and the entire furnace cooled at a rate of about 20 to 30°C/hr. The resulting ingot is shown in Fig.3.4(a), where it is clearly seen to be loose inside the ampoule, due to the effect of the BN coating and was thus easily extracted from the quartz ampoule. In contrast, an ingot exhibiting severe adhesion and residue is shown in Fig.3.4(b) of this figure, for comparison, where no BN was used. Here. the ingot contained voids and cracks, as will be later discussed in this chapter. Table 3.1 summarizes all of the crystal growth runs reported in this thesis with a few additional runs of special interest.

3.3 RESULTS ON CRYSTAL GROWTH

In this section, the results of applying the procedure to grow Bridgman ingots of $CuInSe_2$, described in the previous section, are presented. Included here, are the effects of the BN, ingot characteristics, monophase confirmation and the effects of growth rate variation and of interrupted growth.

3.3 (a) Effect of Boron Nitride

The boron nitride coating was clearly found to eliminate the adhesion of the $CuInSe_2$ ingot to the quartz ampoule. This was a major breakthrough in this work, where for the first time in this laboratory, ampoules were routinely grown without any difficulties with cracking or adhesion. It was also found to reduce significantly the amount of voids in the interior of the ingot. Because of this, the growth of larger monocrystals was made possible and crystals with significant cleavage areas were obtained. This is demonstrated in Fig.3.5(a), where a run using BN (run 64, Table 3.1) is shown to yield an ingot with a complete cleaved surface of greater than 40 mm^2 in area. This is compared with run 21 (Table 3.1), where no BN coating was used, and where the resulting ingot exhibited a large density of voids (Fig.3.5(b)). Another beneficial aspect of the BN coating was that it allowed the ingot to develop facets on the exterior wall, particularly when thicker BN coatings were used. In some cases, this yielded information about the orientation of monocrystalline regions inside the ingot. While this was useful from the point of view of crystal growth, it was found that the BN did not have to be in physical contact with the melt to work. An experiment was carried out whereby the BN was in the form of a block located inside the ampoule but well above the melt. The result was again an adhesion-free ingot. Thus, this showed clearly that the BN did not act as a physical barrier.

3.3 (b) Ingot characteristics

The grown ingot was removed from the ampoule and observed under a light source which revealed its exterior facetting. This facetting was often an indication of regions of monocrystalline habit which manifested itself externally by a singular reflection of light. It was found that these facets corresponded almost always to the low index plane {112}. It was also possible to use this information to cleave the ingot appropriately, so that an internal {112} plane was obtained. This is indicated in Fig.3.6(a), where an ingot is shown, with its exterior exhibiting a region some 3 cm in length having one common reflection. The ingot was cleaved whereby, the cleavage plane, while not very large, had a reflection which coincided with that seen from the rough exterior surface of the ingot, as shown in Fig.3.6(b) and (c).

Table 3.2 lists all of the cleavage planes obtained on the ingots, including their dimensions. Here, it is seen that the largest cleavage areas, and thus the largest confirmed monocrystals, were those in ingots 86 and 91, with an area of about 2 cm^2. The general location of the cleavage in the ingot is also indicated in the table, showing that the majority of the larger monocrystals were located near the bottom end, which was the first region to freeze. Fig.3.7 shows two such ingots, 119 and 125, exhibiting cleavages, where the largest dimension was around 1.9 and 1.5 cm respectively, which were essentially parallel to the direction of the growth. This is different from earlier work [2.5], where the growth axis was said to be essentially along the [221] direction, perpendicular to the {112} plane.

In order to verify that these mirror-like planes did indeed correspond to one crystal, multiple-exposure Laue photographs were taken at three different locations on the cleaved plane of ingot 119 . Fig.3.8 shows a schematic diagram of the usual X-ray back-reflection Laue setup used. The exposure time was about 45 minutes per location and the X-ray generator current and voltage were 30 mA and 22 kV respectively. The three exposures were obtained by moving the sample linearly, in the plane perpendicular to the incident beam, into the three different positions, which are indicated in Fig.3.9(a). Fig.3.9(b) gives the resulting polaroid picture showing the spot pattern indicative of a three fold symmetry. More importantly, the three exposures reveal clear single circular spots of the three superimposed images, which do not exhibit streaking or splitting, that otherwise is an indication of a misorientation between adjacent grains.

Another measure of the crystalline quality of these cleaved ingots is shown in Fig.3.10. Here, a rocking curve was obtained on 5×5 mm^2 cleaved surface of ingot 125, shown in Fig.3.10. The measurement was carried out by Dr. Isabella Bassignana at the Advanced Technology Laboratory of Bell Northern Research Ltd. In this measurement, the cleaved sample was placed in an X-ray diffractometer with its cleavage parallel to the surface of the mounting stage, making an equal angle with the incident and reflected beams. The angle of incidence was then fixed at the Bragg angle corresponding to this plane and the diffracted X-ray intensity was measured with small deviation from the Bragg angle. The rocking curve indicates a full width half maximum (FWHM) value of about 200 arc seconds for this crystal. This is much smaller than the value of about 680 arc seconds, reported by Tiwari *et al* [3.1] for their heteroepitaxially-grown thin film $CuInSe_2$ structures but larger than the figure of some 70 arc seconds reported by Cheuvart *et al* for CdTe [3.2], and of course larger than those observed for present-day high quality Si and GaAs single crystal wafers.

3.3 (c) Crystal Structure

The crystal structure of $CuInSe_2$ ingots having a nominal stoichiometric starting composition, has been determined by powder X-ray diffraction using a Rigaku diffractometer (model D/Max -2400), a schematic of which is shown in Fig.3.11. Pieces were extracted from the ingot and crushed to a fine powder. The $CuInSe_2$ powder was transferred on to a special glass slide which fits into the sample holder of the diffractometer. X-ray scans were then taken from 10 to 100 degrees of 2θ, at a rate of 6 degrees per minute. The incident X-ray wavelength was 1.5405Å obtained from a Cu target. The actual measured diffraction peaks for a specimen from a typical ingot growth run are given in Fig.3.12. The diffraction pattern is consistent with the JCPDS data for the reflections of the chalcopyrite structure for this compound, given in Appendix A.1. Unlike the standard specimen, the intensity of the 220 peak measured here, was slightly greater than that for the 112 peak. The presence of reflections from $\{hk\ell\}$ planes where the value of the index ℓ is odd, such as 101, 103 and 105, is consistent with the presence of the chalcopyrite phase [3.3].

3.3 (d) Effect of Growth Rate

As indicated in Table 3.1, the crystal growth of most of the ingots was carried out using a lowering rate of less than 10 mm/hr. In this range, the size of the grains in the ingots did not seem to vary significantly. In quenched samples, however, very fine grains were observed. Therefore, in order to establish an upper limit for the growth rate, an experiment was carried out, whereby several ingots were grown mostly under similar conditions with the lowering rate varied well over two orders of magnitude from about 700 mm/hr down to 2 mm/hr. Pieces were then extracted from the ingots and polished first with sand paper and then with 0.3 μm alumina powder, to obtain flat surfaces. The grains of the ingot were then revealed by etching the sample in a 5% brome-methanol solution and an estimate for the size of the grains was obtained.

The results of the etching are shown in Fig.3.13. A total of five stoichiometric ingots were prepared, runs 101, 151, 43, 63 and 137, with solidification rates of 700, 277, 18, 10 and 2 mm/hr respectively (Table 3.1). Fig.3.13(a) shows a sample from ingot 101 grown at 700 mm/hr. Here, the grain structure is seen to be very fine, where the grain size is estimated to be around 0.3 mm. These grains appeared to grow radially, possibly due to the lateral heat loss during the quenching action. In Fig.3.13(b), where the growth rate was 277 mm/hr, the grains were slightly larger, but still relatively small in comparison with the ingot dimensions, with an average grain size of some 2 mm. At the slower growth rate of 18 mm/hr, shown in Fig.3.13(c), the grains exhibited a greater size, where the average dimension was about 5 mm. The size of the grains, however, was largest at growth rates of 10 mm/hr or below. This is seen in Figs.3.13(d) and (e), where samples from the ingots grown at 10 and 2 mm/hr respectively, are shown. In both figures, the grain size was comparable to the diameter of the ampoule and in the case of the 2 mm/hr sample, the entire piece was one grain, as evidenced by the presence of only one facet, revealed by the etching. The straight dark lines seen in Figs.3.13(d) and (e) indicate twin boundaries in these samples. The results of this experiment are summarized in Table 3.3. The average grain size of these samples is plotted in Fig.3.14 against ampoule lowering rate on double logarithmic scales. Here, the trend of the points appears to be a general decrease in grain size with increasing lowering rate, as would be expected. The error bars in this figure were obtained for each sample by taking the minimum and maximum estimates for the size of the grains.

3.3 (e) Interrupted Growth Runs

An important parameter in the growth of crystals from the melt, is the solid-liquid interface shape. Several techniques have been used in the past to visualize this interface during or after the growth [3.4], [3.5], [3.6], [3.7]. Arising from the result of section 3.3(c), where most of the grown ingots exhibited cleavage near the tip of the ampoule, a preliminary attempt was made, in this study, to look at the solid-liquid interface shape at different positions along the ingot as the solidification progressed. To delineate the solid-liquid interface, about 3 extra grams of copper were added to a typical stoichiometric elemental charge mixture of 20 grams. A set of three ampoules was then prepared, runs 155, 156, and 157, which were grown under nominally similar conditions but which were interrupted at different stages of the lowering of the ingot. The soaking of the melt at 1100 °C was carried out for 48 hours or more, for all three runs and the growth rate was about 6 mm/hr. The growth of the ingot was then interrupted at a given position during the solidification and the entire ampoule quenched to room temperature. The ingot was then extracted from the quartz ampoule and cut, using a diamond saw, along its axis. The cut surface was then polished using 0.3 μm alumina powder to obtain a fine finish. It was found that the rapidly quenched material contained precipitated copper (or a copper compound) but with none visible in the slowly grown portion. Thus, an interface was apparent between the copper-containing quenched material and the slowly grown portion of the ingot. Table 3.1 gives the fabrication conditions of these runs.

Fig.3.15 shows the result of the three runs, interrupted at successively higher positions along the growth direction. The segregated copper is seen as the greyish area in the upper portion of the ingots. A schematic is also given to highlight the interface shape. As is clearly seen here, in all cases, the shape of the interface was concave in respect of the monocrystalline material. The degree of concavity, however, appeared to increase with growth distance from the tip. Near the tip, the concavity was small, while near the top end the concavity was very large and also severely distorted, which if it is a true indication of the interface shape, would suggest excessive nucleation from the ampoule walls. In these ingots, it is also seen that, in the grown lower region, a significant density of macro-cracks was apparent. This is due to the quenching action, since such cracks were not observed in regular unquenched ingots. This is clear from Fig.3.16, which shows a comparison between a quenched run 157 and another run 138, also using excess copper, but one which was fully grown at a rate of 3 mm/hr. As opposed to the quenched run, ingot 138 was cooled after solidification at the much slower rate of about 28°C/hr. Here, the interface shape of ingot 138, while still concave, was nearer to a flat interface than that of the quenched run 157, even though the interface was at a higher position in the ingot. This suggests that the method used to "freeze-in" the solid-liquid interface may affect its shape if carried out under thermal non-equilibrium conditions. Table 3.4 summarizes the results of this experiment. The lines seen on the section of ingot 138 arose from the cutting action of the diamond saw.

3.3 (f) Surface Treatments

Two types of surface treatment, carried out on mechanically polished surfaces, were chemical etching and thermal etching. Fig3.17(a) shows a photograph of a sample surface etched in a 5% brome-methanol solution, which, as shown earlier, revealed grain boundaries and as shown here, twinning lines. Twinning was also revealed by thermal etching in vacuum, as indicated in Fig.3.17(b), showing a sample with multiple twin bands, where a sample was annealed at a temperature of 300 °C for about 2 hours. Thermal etching also revealed etch pits, as shown in Fig.3.18. In Fig.3.18(a), near triangular pits on a polished {112} surface, annealed in vacuum at 300°C, are shown. In Fig.3.18(b), the annealing was carried out at 600°C for a period of some 4 hours, showing better, the triangular shape of the etch pits.

3.3 (g) Electrical Measurements

Little work was done on the electrical evaluation of the grown ingots but some Hall effect and conductivity measurements at room temperature were carried out with the help of G. Ahmed on filamentary samples cut from stoichiometric ingots. The measurements were done using a magnetic field of about 10kG and values obtained for Hall mobility, resistivity and carrier concentration were of the order of 30 $cm^2/(volt.sec)$, 5 ohm.cm and

10^{17} cm^{-3} respectively. The Hall coefficient indicated p-type conductivity, which was consistent with thermoelectric hot point probe determinations on these samples. The conductivity type of all stoichiometric runs, as determined by hot probing, was uniformly p-type throughout the ingot, without exception, including the last region to freeze. In non-stoichiometric growth runs, however, n-type conductivity was obtained in ingots with controlled deviations from stoichiometry, which will be reported on, in more detail, in chapter 5.

3.3 (h) Miscellaneous Experiments

Several preliminary attempts were made in this work, other than those already discussed earlier, to improve the size of monocrystals in the ingot. However, while no immediate success was obtained in these particular runs, a review of them is helpful since the techniques employed yielded improved crystal quality in other materials. For example, an attempt was made to incorporate a seed inside the tip of the ampoule. With seeding, the yield of single crystals could be increased. Heterogeneous seeding of $CuGaSe_2$ was reported by Miyake *et al* [3.8], using a travelling heater method, while homogeneous seeding of Bridgman-grown $AgGaSe_2$ was reported by Feigelson and Route [3.9]. In the present work, on $CuInSe_2$, three growth runs were carried out using a sapphire, Al_2O_3 single crystal seed, a SiO_2 single crystal seed and a seed taken from a commercial silicon single crystal wafer. In each case, the seed was locked-into the quartz ampoule tip, by gentle flaming under vacuum. The growth of $CuInSe_2$ was carried out under the usual conditions. However, the seeding experiments did not yield a significant increase in monocrystallinity, perhaps due to the fact that the growth parameters were not yet fully optimized . In the case of the silicon seed, it was completely dissolved by the molten $CuInSe_2$, during the soaking, at the temperature of 1100°C.

Attempts were also made to study the effect of ampoule taper angle on the monocrystallinity within the ingot, which was also reported to have an effect on the structural integrity of ingots of $AgGaSe_2$ [3.9]. However, due to the small diameter of the ampoules used in this work, of about 12 mm, the length of a grown ingot with a large taper angle would have been too short to reveal long range order and therefore, a larger diameter quartz ampoule was needed. This, however, necessitated a scale-up of the ampoule fabrication process, which was beyond the resources available.

Finally, two runs were attempted, whereby an inverted Bridgman growth was carried out. Here, the ingot was pulled upwards from the bottom zone, set at its maximum temperature of 1000°C to the upper zone set at 800 C. Unlike the conventional vertical Bridgman used, where the tip promoted the nucleation, in the inverted method, the free surface of the melt solidified first. Here, it was hoped that such surfaces might promote self-seeding of the ingot. This is because these free surfaces were observed to grow only along {112} planes. However, difficulties were encountered when the upper part of the ampoule cooled first, as it entered the top zone, leading to condensation of vapour from the melt. The results of these runs indicated that more work was needed to establish the appropriate growth conditions for such a technique. An inverted Bridgman technique was used by Grasza and Jedrzejczak to study heat convection in the material PbSnTe [3.10].

3.4 DISCUSSION

The main obstacle in the growth of $CuInSe_2$ *by* the Bridgman method, in this work, has been the adhesion problem. To a considerable extent, this prevented large monocrystals from being obtained and used for other studies. The boron nitride coating method, developed in this study, was successful in eliminating the adhesion completely and enabling adhesion-free and void-free ingots to be obtained routinely. This also allowed, for the first time, the cleavage of surfaces of area greater than 1 cm^2 to be obtained on $CuInSe_2$. The inclusion of graphite in the ampoule, in the work of L.S. Yip [3.11], was found to be equally effective in eliminating the adhesion problem. However, he reported that the graphite, when deposited as a film on the inside of the ampoule wall, flaked-off and was invariably incorporated into the melt. This did not occur with the boron nitride coating used in this work, since the intense flaming step carried out, caused a hardening of the BN layer. Thus, no BN was observed to be incorporated, macroscopically, into the melt. The BN coating method does not require the BN to be in the form of a crucible, which alone, without a containing quartz ampoule, would be more difficult to seal off. Since the BN coating can be deposited to a controlled thickness onto the ampoule wall, it eliminates the need for a crucible. In the work of Bachmann *et al* [2.19] on $CuInSe_2$, Yasuda *et al* [3.12] on CdTe and Omino and Suzuki [3.13] on ZnSe, using a *pre-reacted* charge, a BN crucible was employed inside a quartz ampoule. In the one ampoule method adopted in this work, where an elemental charge was used, a BN crucible can sometimes crack inside the quartz ampoule due to accumulation of reaction products between the crucible and ampoule walls. Thus, the coating method offers a less troublesome alternative for using the BN for the crystal growth, if the one ampoule technique is used. As far as adhesion goes, the BN does not have to be in contact with the melt in order to prevent the sticking. It has been shown that the use of a block of BN inside the ampoule, away from the charge, has a similar action. This is consistent with the results of L.S.Yip [3.11] with the use of graphite inside the quartz ampoule. It is thus, speculated that the boron nitride (or graphite) acts as a getter of some gaseous agent. It will be shown in chapter 4, that this was indeed the case.

While the advantage of having BN in the quartz ampoule is clear, it posed, never-the-less, a possible risk of *microscopic* contamination of the $CuInSe_2$ charge. No analysis, in this work however, was done to see if significant traces of boron were present in the $CuInSe_2$ ingot after the growth. In the work of Yasuda *et al* on CdTe [3.12] and Omino and Suzuki [3.13] on ZnSe, where BN crucibles were used, no measurable amount of boron was found in the ingots. In the work of Ciszek [3.14], on solid solution growth of $CuIn_xGa_{1-x}Se_2$ crystals, where a B_2O_3 encapsulent was used, the boron trace was below the detection limit of 30 ppm (by weight). However, boron contamination was reported by Yoshida *et al* [3.15] for ZnSe if unpurified BN crucibles were used. In any case, such analysis for $CuInSe_2$ would be required, especially if boron is shown to have a doping role in $CuInSe_2$.

The BN method made possible the growth of ingots with large monocrystals having dimensions comparable to the size of the containing quartz ampoule. However, the vertical Bridgman crystal growth procedure, in this laboratory, was by no means fully optimized and many parameters still need to be carefully studied in order to understand their effect on the ingot solidification. These include: the soaking temperature above the melting point of $CuInSe_2$, the temperature of the bottom zone and also the temperature gradient at the freezing mark. In this work, the gradient of temperature was fixed at about 70°C/cm, which was believed to be high enough to avoid constitutional supercooling. However, this needs to be verified by experiment. The absence of ampoule rotation during the soaking and the growth did not seem to hinder severely the growth of large monocrystals; however, it would appear to be beneficial from the point of view of thermal homogenization of the ingot, particularly during the solidification stage. In the work of Weng *et al* [2.25], an accelerated crucible rotation technique (ACRT) was employed for the vertical Bridgman growth of $CuInSe_2$.

The upper furnace zone temperature, in this work, was kept at 1100 °C in almost all the runs. While this parameter may not seem to be critical , it was reported [3.16] that, such an elevated temperature, above the melting point of the compound during the growth, may cause the solid-liquid interface shape to become concave, as viewed from the solid, which is undesirable. The interrupted growth experiments showed that the apparent solid-liquid interface shape in these ingot was concave with respect to the solid. However, it is possible that the quenching action itself influences the concavity and thus, the surface indicated misrepresents the actual shape of the interface. This is because heat is lost more rapidly from the walls than from the interior of the ingot, which in turn causes the copper to segregate in the central part of the ingot as the walls solidify first. Be this as it may, the relative degree of concavity could indeed increase with growth, as evidenced by the presence of larger monocrystals near the bottom of the ingot compared with those in the last region to freeze.

The results of the experiment on the variation of growth rate are not surprising. Here, it would appear that a growth rate of some 10 mm/hr or less is sufficient for obtaining ingot-sized monocrystals, at least using the present growth conditions of temperature gradient and ampoule size. For example, using a larger diameter ampoule may require a much slower growth rate in order to maintain the thermal equilibrium needed. The quartz ampoule used, had a wall thickness of about 2 mm, which seemed to be strong enough to withstand the very high saturated vapour pressure of the selenium of more that 40 atmospheres at the soaking temperature of 1100 °C. This soaking temperature was also apparently high enough to synthesize completely the $CuInSe_2$ compound, since no other elemental or binary phases were observed in the ingots, after the growth. While the X-ray diffraction pattern on a powdered sample indicated only the presence of the chalcopyrite phase, the presence of the sphalerite phase of $CuInSe_2$ cannot be completely ruled out [2.20], particularly since the second zone temperature of the furnace was set to about 600 to 700°C, in order to obtain a high gradient at the freezing mark, which was less than the 810°C sphalerite-to-chalcopyrite transition temperature. This could have hindered the phase transformation, rendering it incomplete. A more careful study is therefore needed to verify if the sphalerite phase was indeed present in these ingots. While no microscopic cracks were observed in any of the ingots, very limited *macroscopic* cracking was observed in some runs where the cooling rate was too fast and particularly evidenced in the quenched ingots. Thus, slower cooling rates below those used in this study, of around 25 to 30 °C/hr, may be recommended to reduce the possible incidence of cracks in these crystals [2.20].

Table 3.1

Summary of Bridgman Growth Conditions for Ingots Reported in this Work

Run No.	Starting charge[1]	BN coating[2]	Soak time[3] (hr)	T_C[4] (°C)	Lowering rate (mm/hr)	Cooling rate (°C/hr)	Comments
21	Stoich	None	72	650	2	27	Sticking and voids present
36	Stoich	Pwdr	48	600	2	25	
41	Stoich	Pwdr	48	600	1	25	
43	Stoich	Pwdr	24	650	18	25	Intermediate growth rate
55	Stoich	Pwdr	48	700	3	19	
63	Stoich	Pwdr	24	650	10	27	
64	Stoich	S-BN	24	560	3	23	Large {101} cleavage
76	Stoich	Pwdr	48	550	2	22	
83	Stoich	Pwdr	96	520	7	22	Large {112} cleavage
86	Stoich	Pwdr	20	520	2	22	
91	Stoich	V-BN	10	850	4	18	Large {110} cleavage
95	Stoich	V-BN	22	850	4	11	
101	Stoich	V-BN	48	RT	700	Quench	Fast growth rate
105	Stoich	V-BN	68	850	6	20	
107	Stoich	Pwdr	2	600	-	-	Si seed dissolved during soaking
110	Stoich	S-BN	24	620	6	26	
111	Stoich	Pwdr	48	660	5	25	Al_2O_3 single crystal seed used
112	Stoich	S-BN	24	650	7	25	SiO_2 single crystal seed used
113	Stoich	Pwdr	26	660	6	31	Quartz ampoule diameter was 2.5 cm

---

1. Elemental charge used at the start of the growth (Stoich = stoichiometric).
2. Type of boron nitride used for the ampoule coating, Pwdr= powdered boron nitride of 99.5% purity obtained from Johnson Matthey Ltd., V-BN = slurry of boron nitride and silica obtained from Carborundum, S-BN slurry of boron nitride and alumina obtained from the Carborundum Company and Block = Block of pyrolytic boron nitride.
3. Time allowed for homogenization of the molten charge at a soaking temperature of 1100°C.
4. Temperature of the second cooler zone of the furnace.

Table 3.1 (cont'd)

Summary of Bridgman Growth Conditions for Ingots Reported in this Work

Run No.	Starting charge[1]	BN coating[2]	Soak time[3] (hr)	T_C[4] (°C)	Lowering rate (mm/hr)	Cooling rate (°C/hr)	Comments
115	Stoich	V-BN	12	800	7	27	Inverted growth[5]
116	Stioch	V-BN	12	900	8	30	Inverted growth[5]
119	Stoich	V-BN	48	680	2	28	Large monocrystal
125	Stoich	S-BN	68	670	2	27	
137	Stoich	Block	48	600	2	25	Slow growth rate
138	Cu excess	V-BN	47	670	3	28	EPMA growth runs
140	Se deficient	Pwdr	24	670	3	28	
141	In excess	Pwdr	20	670	3	28	
142	Se excess	Pwdr	24	640	3	53	
143	Cu excess	Pwdr	21	670	3	50	
144	Stoich	Pwdr	28	900	3	37	
145	In deficient	Pwdr	48	900	6	30	
146	In excess	Block	43	800	3	33	
149	Stoich	Pwdr	24	700	6	30	
151	Stoich	S-BN	24	700	277	50	
155	Cu excess	S-BN	72	700	6	Quench	Interrupted growth runs
156	Cu excess	S-BN	48	700	7	Quench	
157	Cu excess	S-BN	48	700	7	Quench	

---

1. Elemental charge used at the start of the growth (Stoich = stoichiometric).
2. Type of boron nitride used for the ampoule coating, Pwdr= powdered boron nitride of 99.5% purity obtained from Johnson Matthey Ltd., V-BN = slurry of boron nitride and silica obtained from Carborundum, S-BN slurry of boron nitride and alumina obtained from the Carborundum Company and Block = Block of pyrolytic boron nitride.
3. Time allowed for homogenization of the molten charge at a soaking temperature of 1100°C.
4. Temperature of the second cooler zone of the furnace.
5. Soaking temperature was 1000°C

Table 3.2
Summary of Cleavage in Bridgman-Grown $CuInSe_2$ Ingots[1]

Run No.	Location in ingot[2]	{hkl} plane	Area[3] (cm^2)	Max. dim.[4] (cm)	Comments
36	L	112	0.3	0.6	
41	C	101	0.4	0.8	
55	C	112	0.6	1.2	
63	C	112	0.8	1.5	
64	L	101	0.5	1.2	Largest {101} cleavage.
76	U	112	0.1	0.4	
83	L	112	1.0	1.3	
86	L	112	1.9	2.2	Largest {112} cleavage.
91	L	110	2.0	2.0	Only ingot with {110} Cleavage plane.
95	L	101	0.8	1.0	
105	L	112	0.8	1.1	
110	L	101	0.1	0.6	
119	L	112	1.3	1.9	
125	L	112	0.7	1.5	
149	L	101	0.7	1.0	

1. Summary of cleavage planes observed in all the ingots prepared in this work.
2. Location of the cleavage in the ingot: L=lower region, C= central region and U=upper region. Total length of a typical ingot was 4 cm.
3. Estimate of the area of the cleavage plane.
4. Length of maximum dimension of cleaved region.

Table 3.3 Effect of Variation of Ampoule Lowering Rate

Run No.	Lowering rate (cm/hr)	Average grain size[1] (mm)	Comments
101	70	≈ 0.3	Ingot quenched from 1100 to 900 °C.
151	28	≈ 2.0	Ingot contained some voids.
43	1.8	≈ 5.0	
63	1.0	≥ 9.0	Large cleavage.
137	0.2	≥ 11.0	Ingot-wide grains.

1. Average width of grains revealed by polishing and etching the $CuInSe_2$ substrate with 5% brome in methanol solution.

Table 3.4 Interrupted Growth Runs[1]

Run No.	Lowering rate (mm/hr)	Interface position [2]	Cooling rate	Degree of concavity[3]	Polished grown region after cooling
155	6	0.25	Quench[4]	0.2	Some cracking
156	6	0.50	Quench	0.5	Significant cracking
157	7	0.65	Quench	0.9	Significant cracking
138	3	0.90	25°C/hr	0.2	Little or no cracks

1. Ingots of $CuInSe_2$ with excess copper grown partially, at the given growth rate and quenched at a given stage of the growth to "freeze-in" the solid liquid interface, except for the last run which was grown completely.

2. Interface position along the ingot axis given as a fraction of the total ingot length as measured from the tip.

3. Ratio of the amount of central depression in the solid-liquid interface, below its level at the ingot edge, to the diameter of the ingot.

4. Quenching was carried out by manually lowering the ampoule from near the solidification temperature of $CuInSe_2$ of about 980 °C to a position outside the furnace.

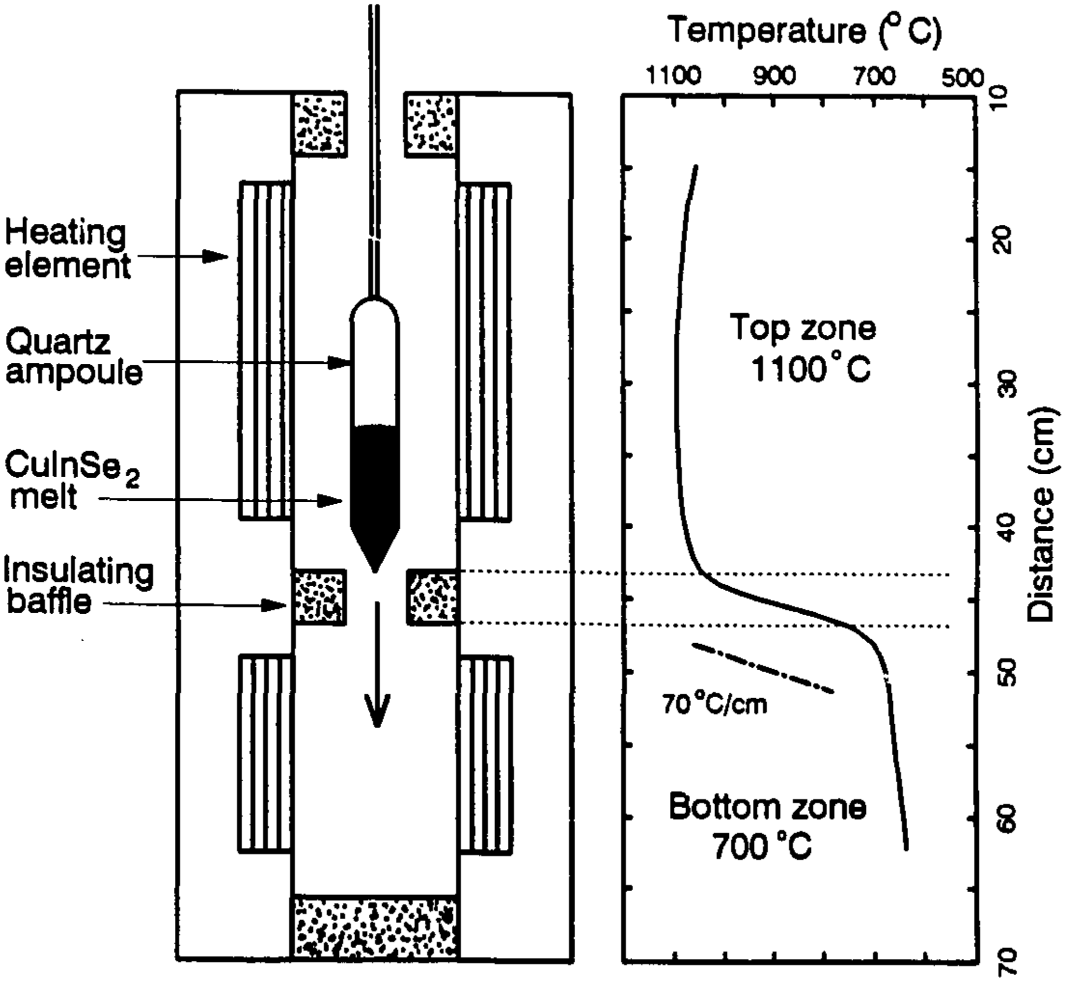

Fig.3.1 Schematic diagram of the vertical Bridgman growth setup , showing also the temperature profile of the furnace.

BN powder coating

Ampoule transparent after flaming-in of BN

Fig.3.2 Photographs of the quartz ampoule used for the crystal growth, showing (a) the powdered boron nitride coating as deposited on its wall and (b) the ampoule transparent after the intense flaming treatment.

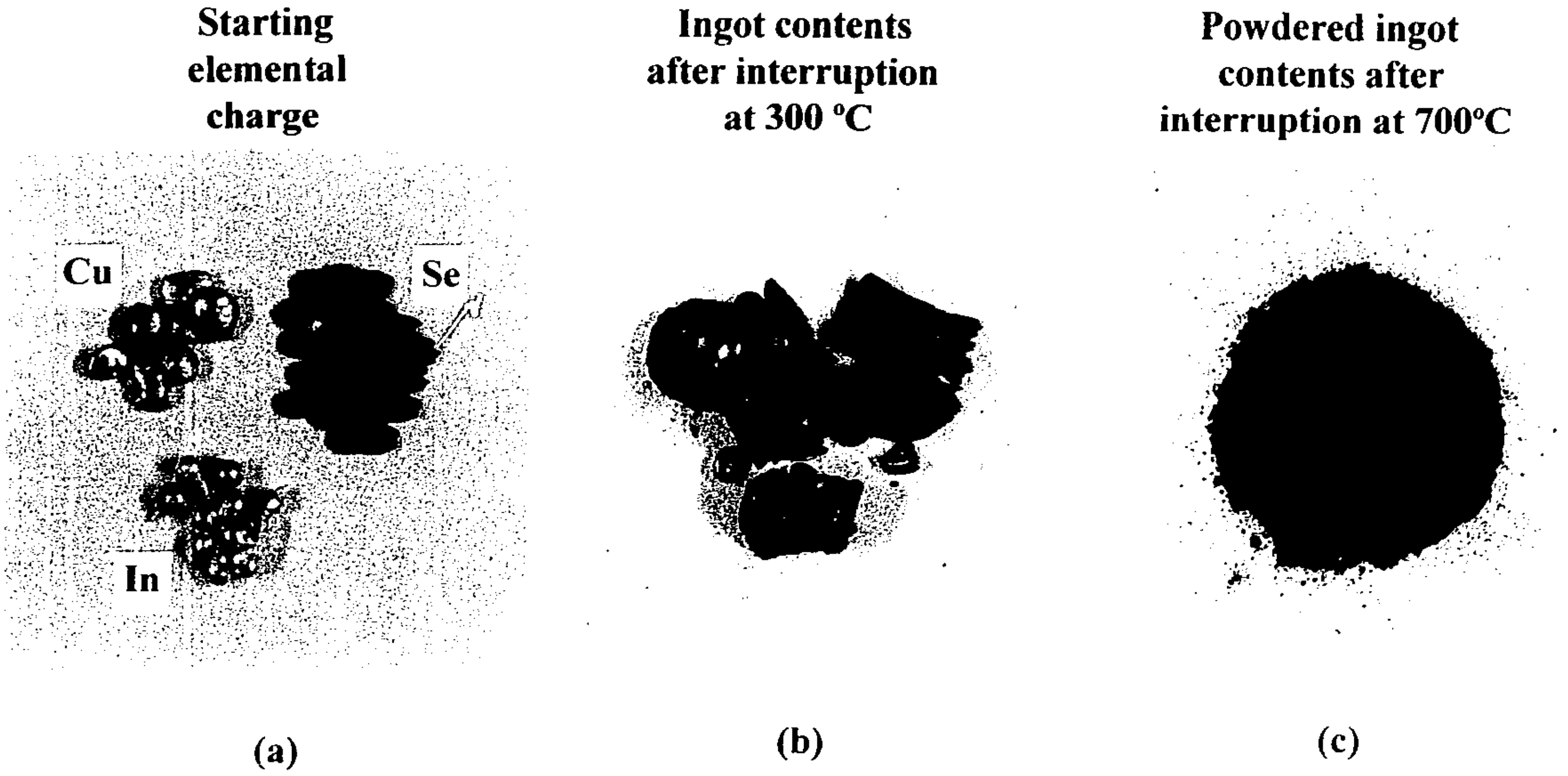

Starting elemental charge

Ingot contents after interruption at 300 °C

Powdered ingot contents after interruption at 700°C

(a)

(b)

(c)

Fig.3.3 Photographs showing (a) the elemental charge before loading into the ampoule , (b) the charge after treatment at about 300°C, showing residual copper pellets and (c) the charge reacted at a temperature near 700 °C, after powdering.

With BN

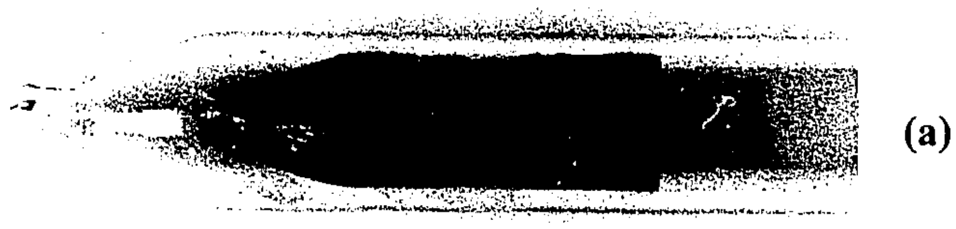

$CuInSe_2$ ingot completely loose after growth

Without BN

$CuInSe_2$ ingot stuck inside quartz ampoule after growth

Fig3.4 Photographs showing (a) ampoule pre-treated with BN, yielding an ingot completely loose inside and (b) ampoule without BN, where the ingot exhibited adhesion, cracks and residue on the quartz wall.

With BN

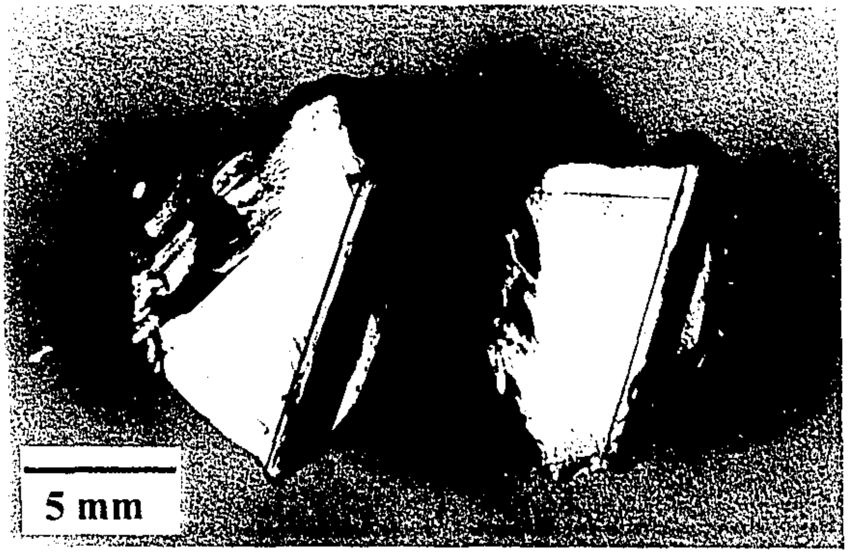

Without BN

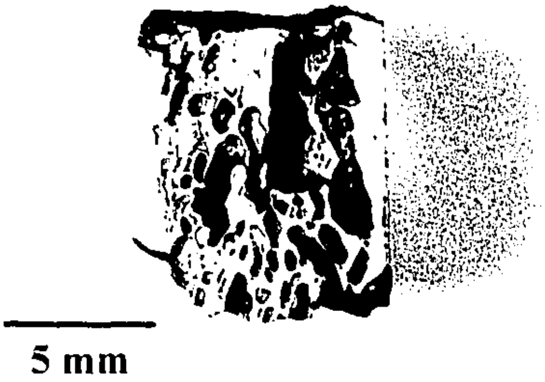

Fig.3.5 Photographs showing the interior of ingots (a) a run where boron nitride was used in the growth revealing the two halves of a cleaved single crystal and (b) a run where BN was not used , showing high void density.

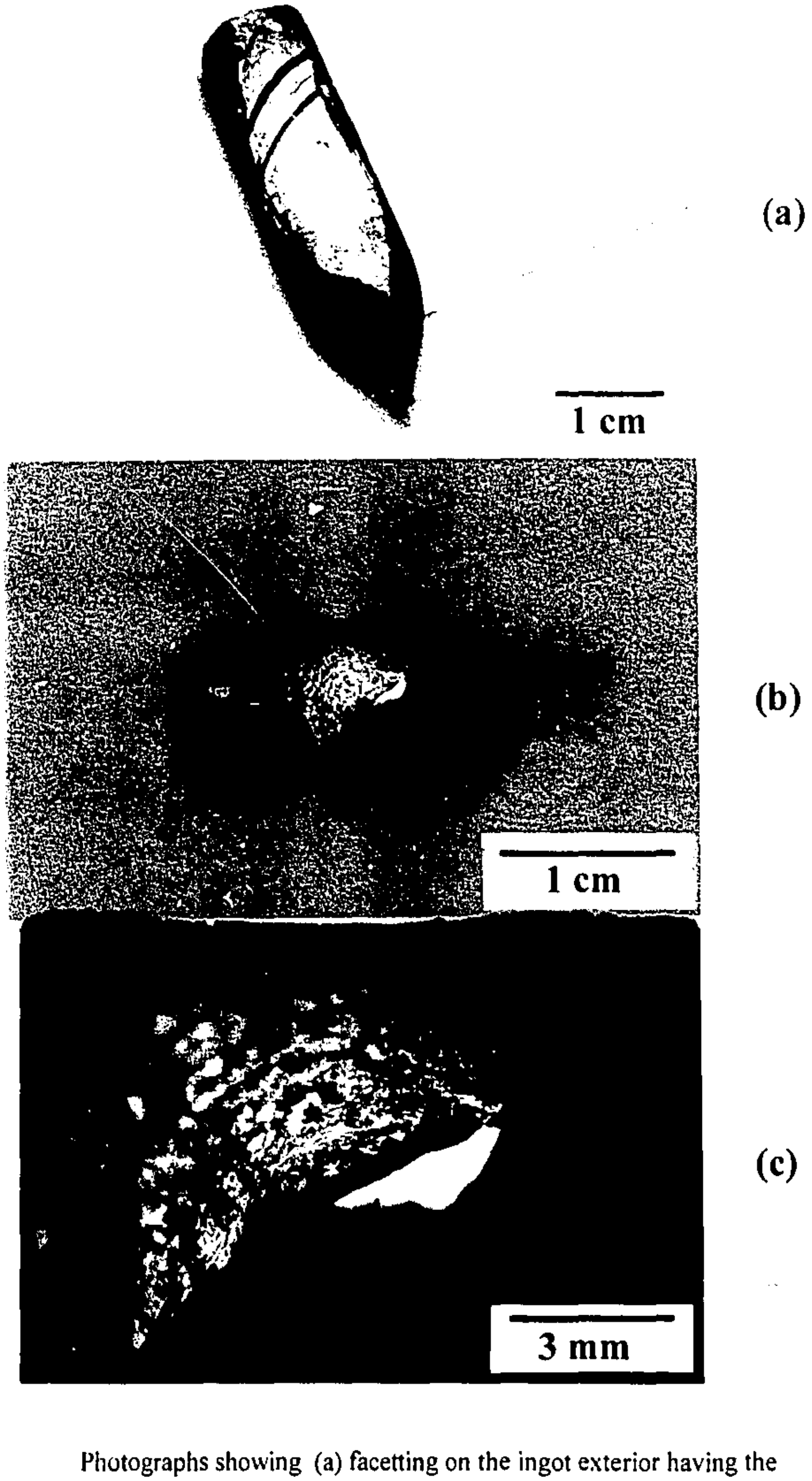

Fig.3.6 Photographs showing (a) facetting on the ingot exterior having the same orientation as (b) an internal cleavage plane, shown in a close-up view in (c).

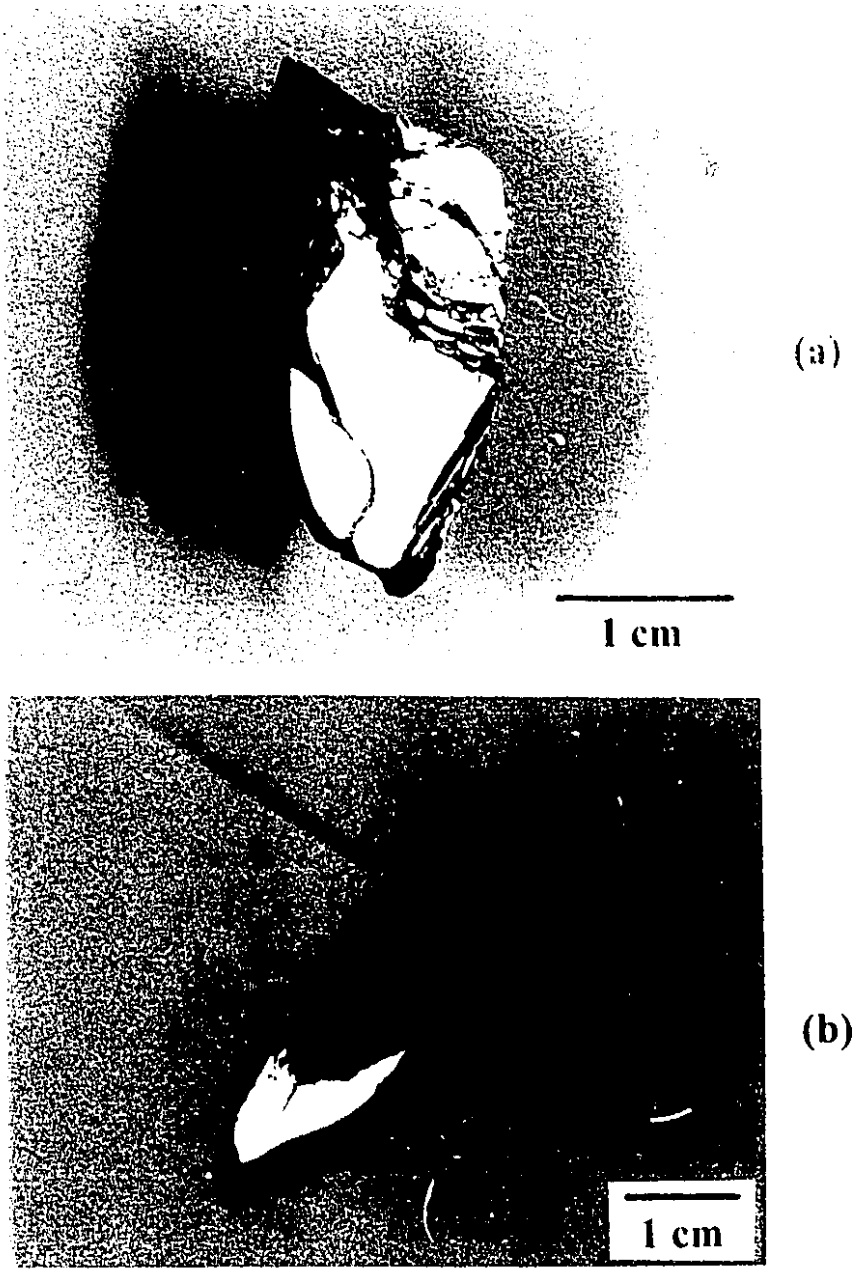

Fig.3.7 Representative samples showing (a) the bottom half of ingot 119, exhibiting a {112} cleavage plane of over 1 cm^2 in area and (b) ingot 125, where the {112} cleavage at the bottom was some 70 mm^2 in area.

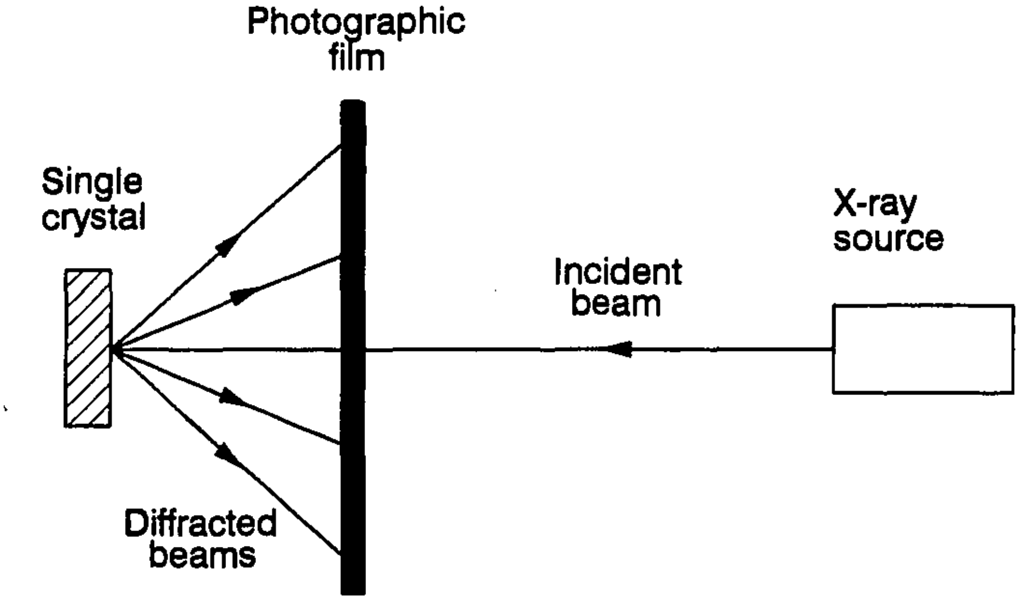

Fig.3.8 Schematic diagram showing the Laue X-ray back-reflection method used in this study.

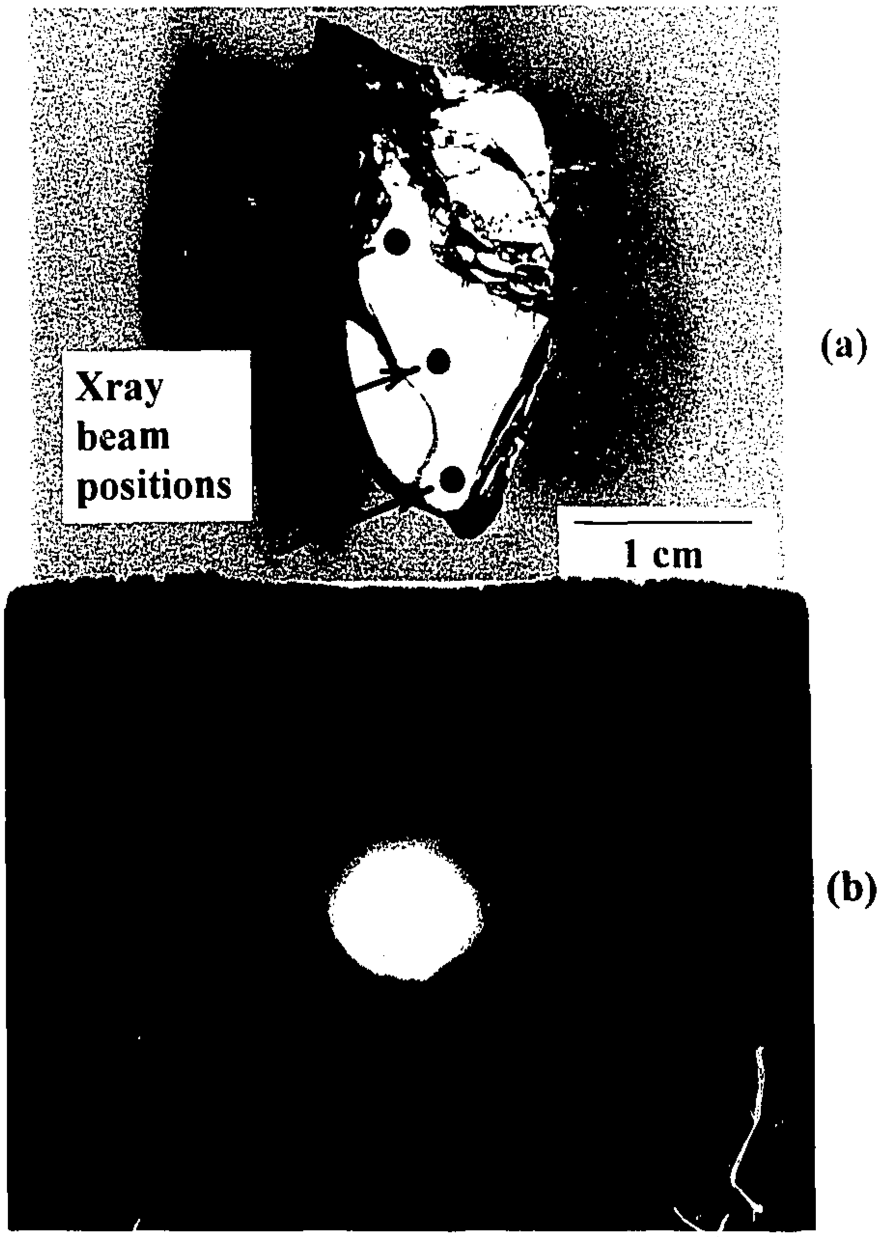

Fig.3.9 (a) Photograph showing the positions of three Laue X-ray exposures on the cleaved $\{112\}$ plane of ingot 119 and (b) the resulting superimposed image indicating the region to be one crystal.

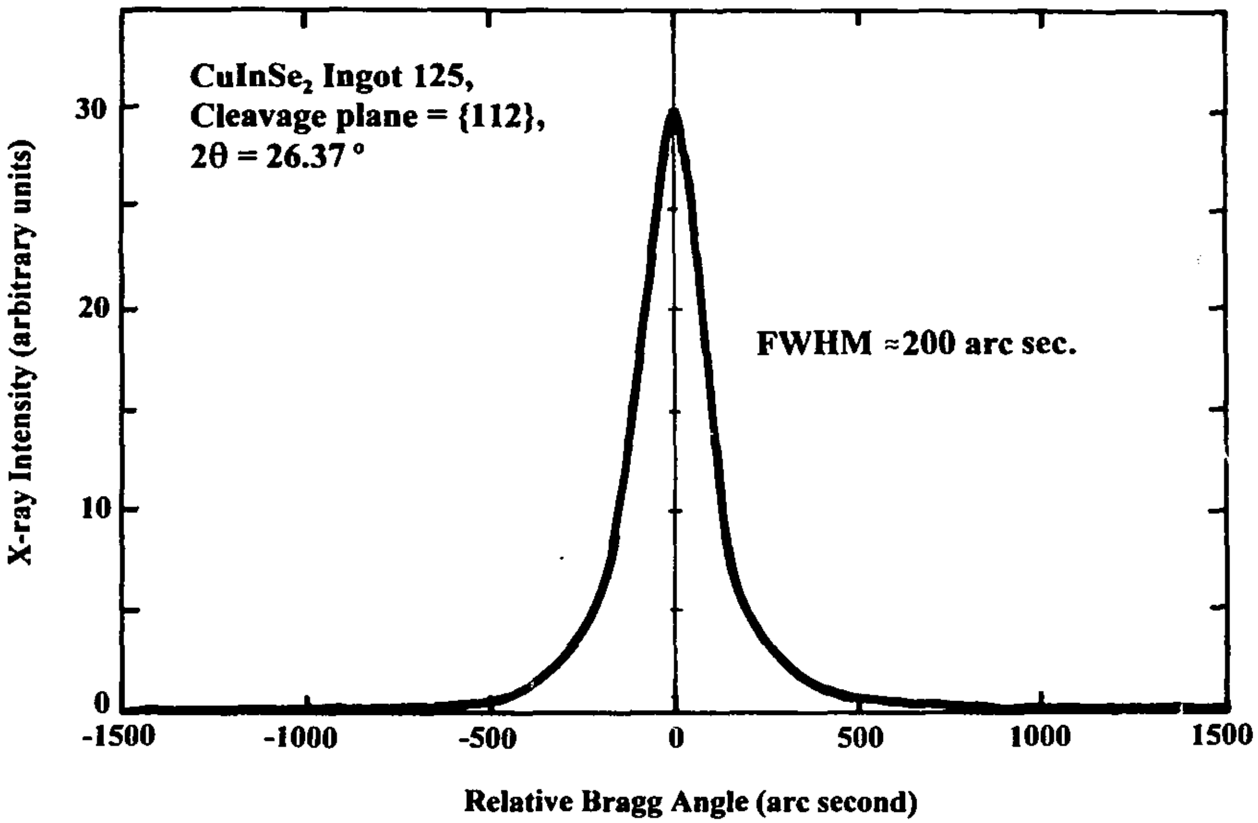

Fig.3.10 Rocking curve on a {112} cleaved sample of ingot 125, indicating a full width half maximum of about 200 arc seconds (taken at Bell Northern Research Ltd.).

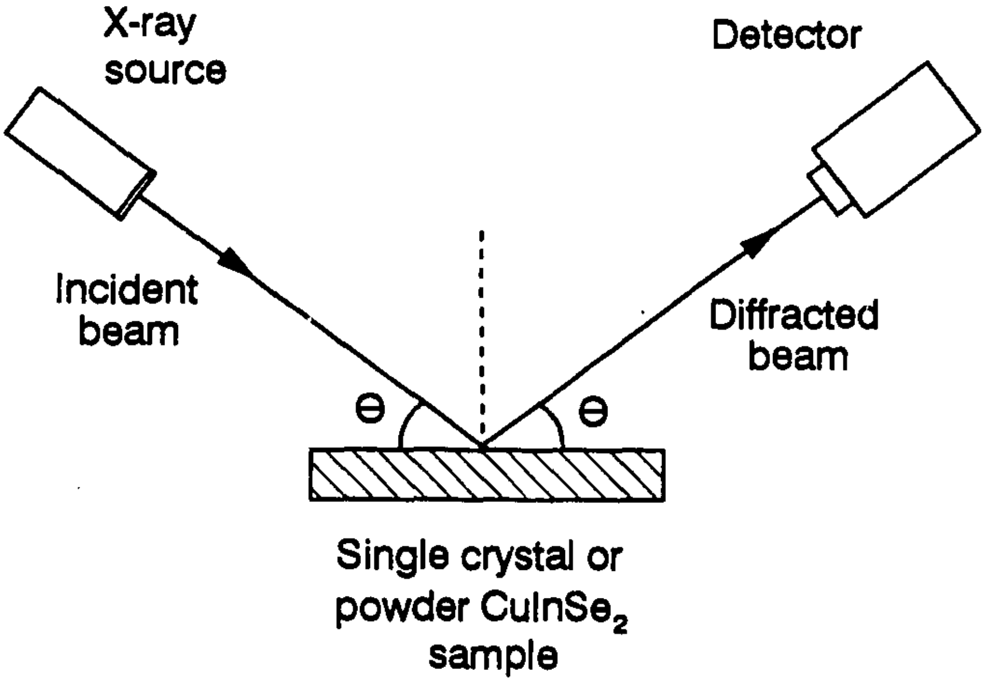

Fig.3.11 Schematic diagram of the X-ray diffraction setup.

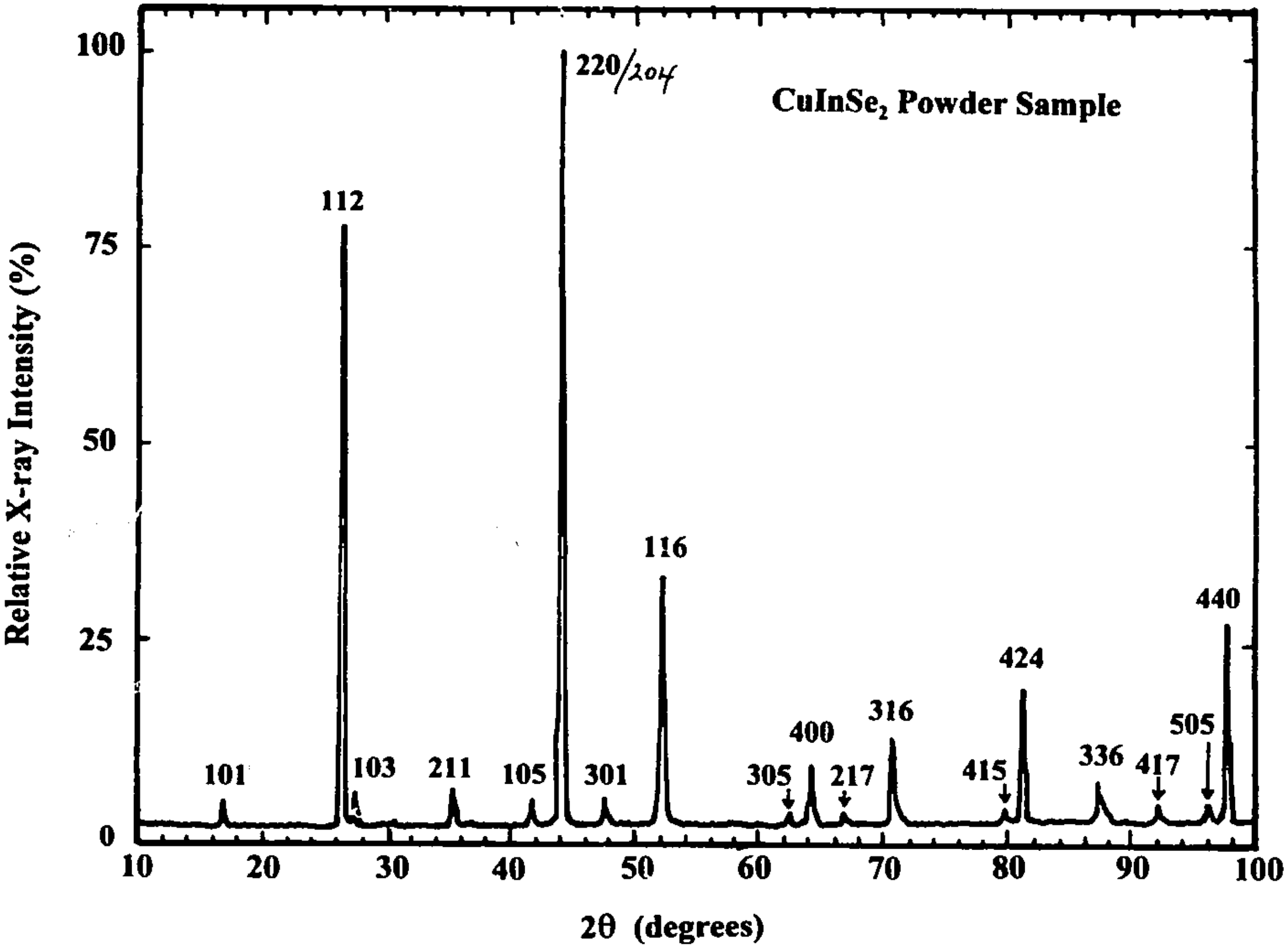

Fig.3.12 X-ray diffraction peaks of a powder sample of CuInSe$_2$ obtained from a stoichiometric growth run, showing the presence of all of the chalcopyrite structure peaks as listed in Appendix A.1.

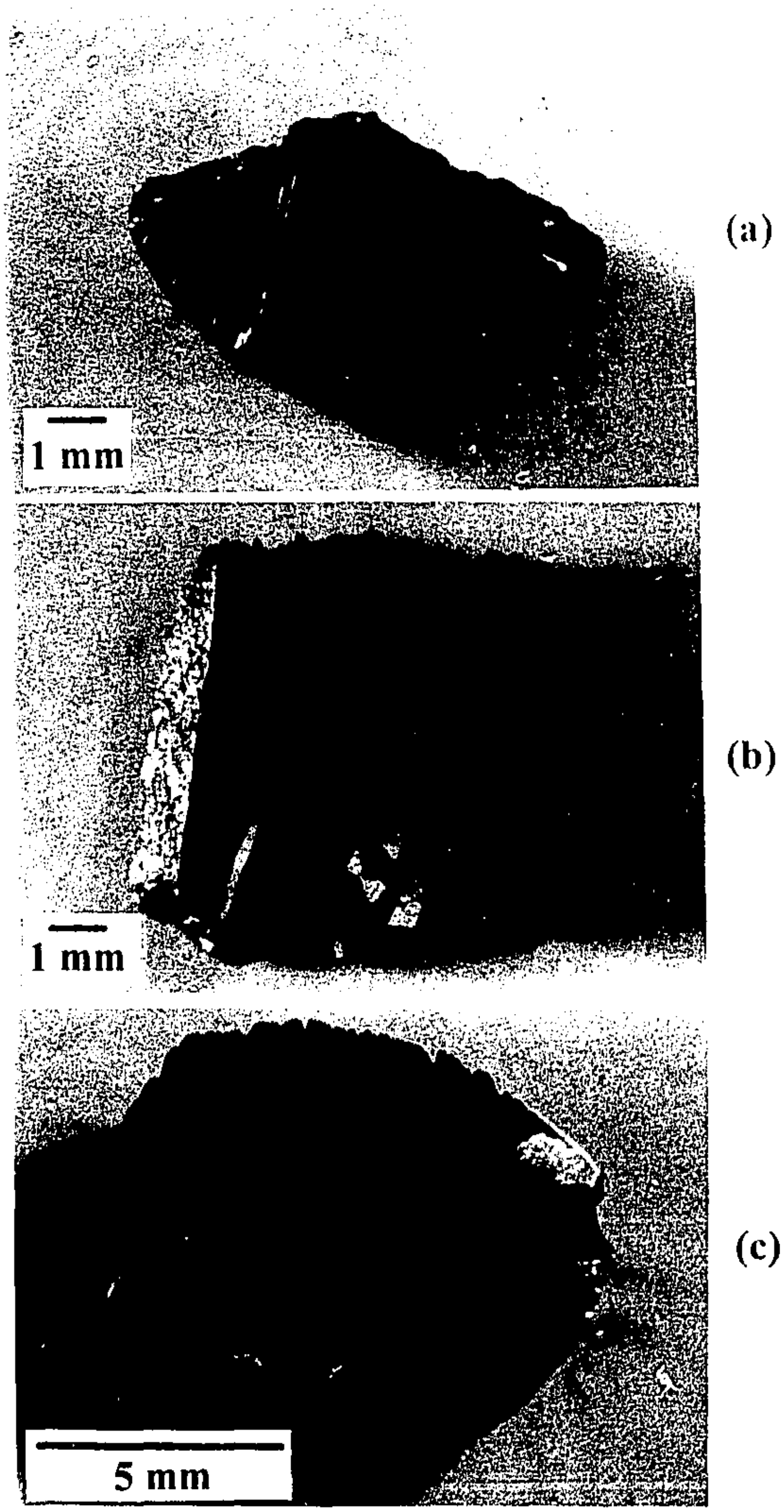

Fig.3.13 Photographs of samples with variation of growth rate at (a) 700 mm/hr, (b) 280 mm/hr, (c) 18 mm/hr, where, the samples were polished and etched to reveal grain boundaries.

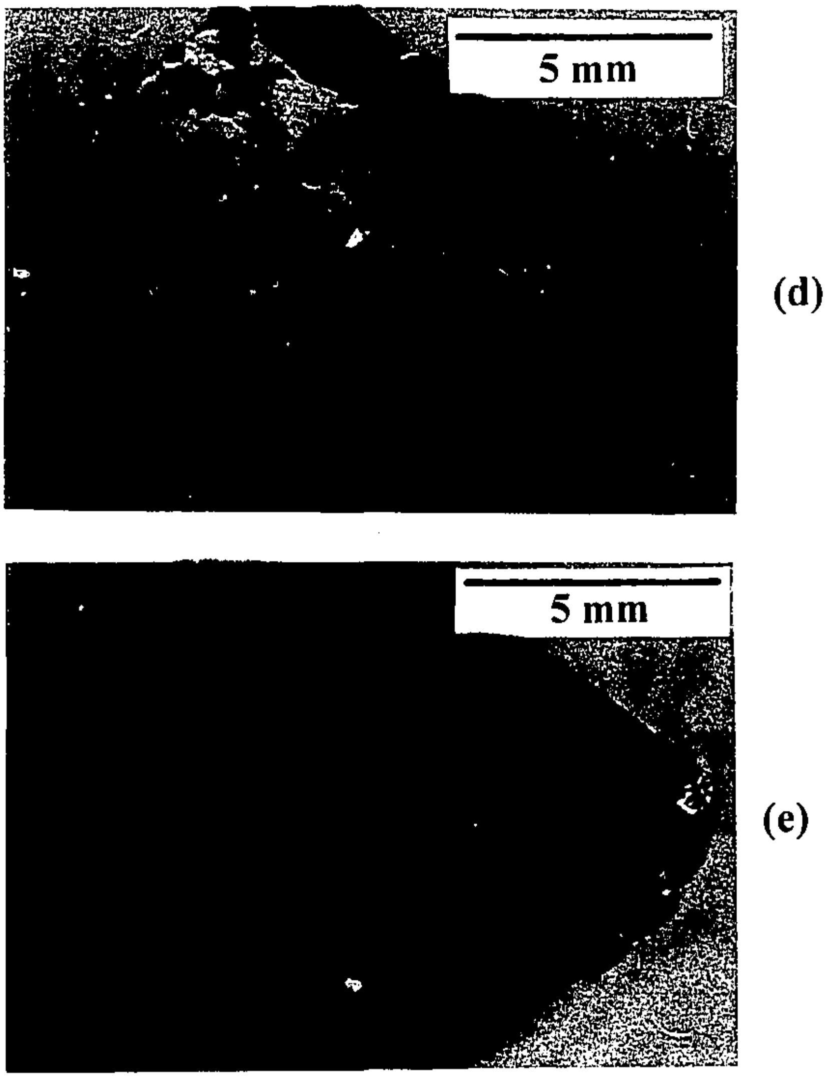

Fig.3.13 (cont'd) Photographs of samples with variation of growth rate at (d) 10 mm/hr and (e) 2 mm/hr.

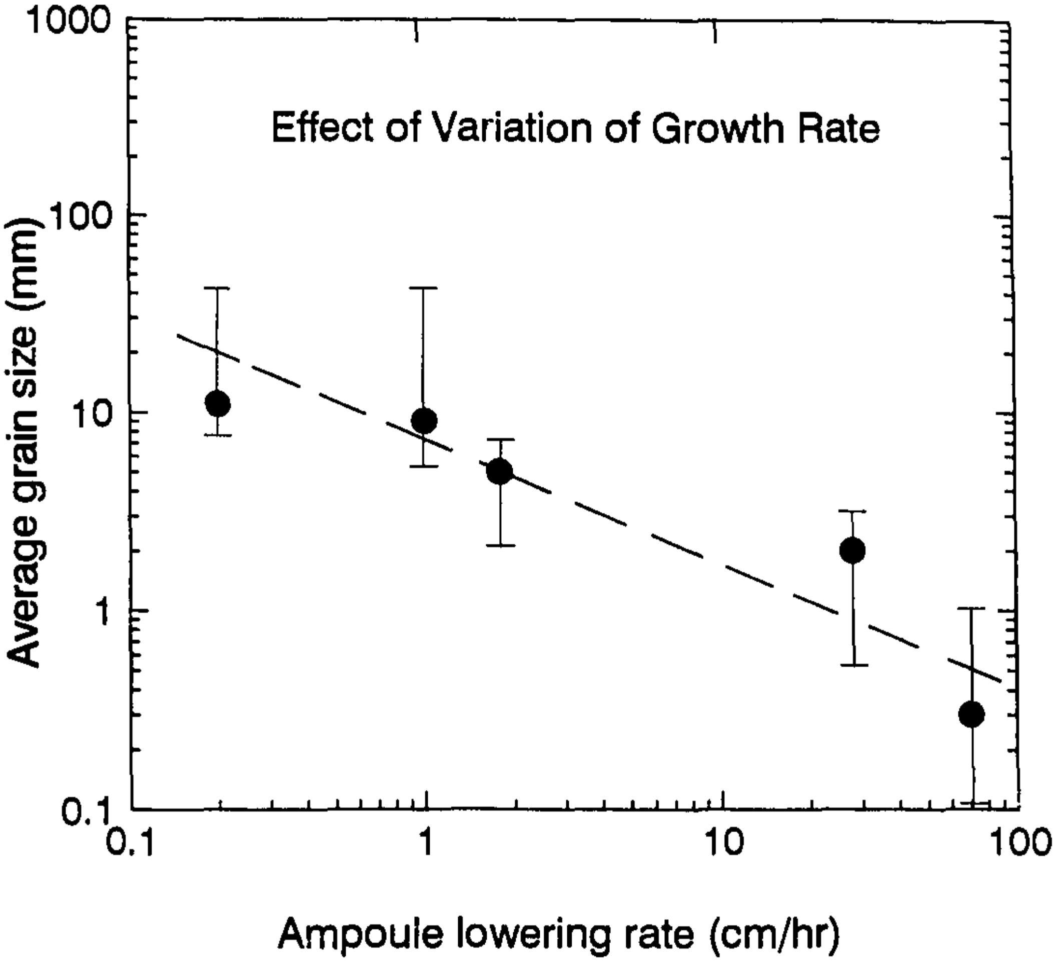

Fig.3.14 Double logarithmic plot of average grain size against ampoule lowering rate for the samples of Fig.3.13. The error bars represent the minimum and maximum grain size estimates obtained for each sample.

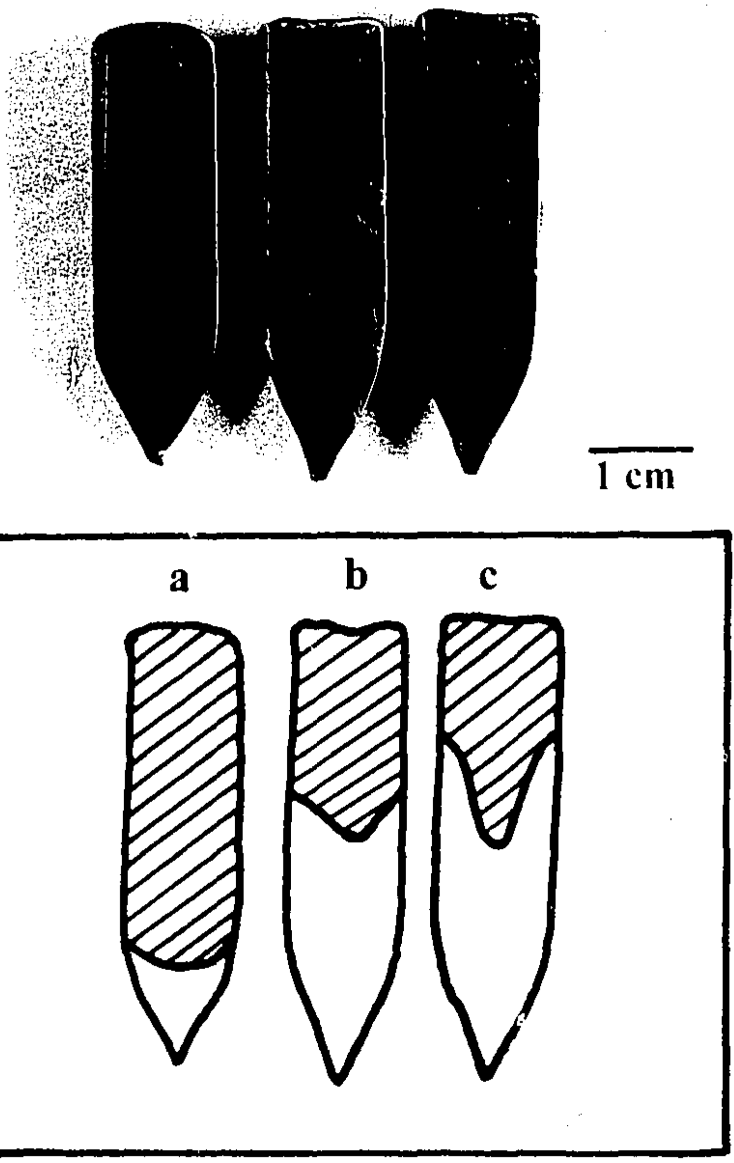

Fig.3.15 Photograph of the three interrupted growth runs (a) 155, (b) 156 and (c) 157, all prepared with excess Cu. The shaded areas on the schematic represent the directly quenched regions in the ingots, while the plane areas indicate the directionally grown portions.

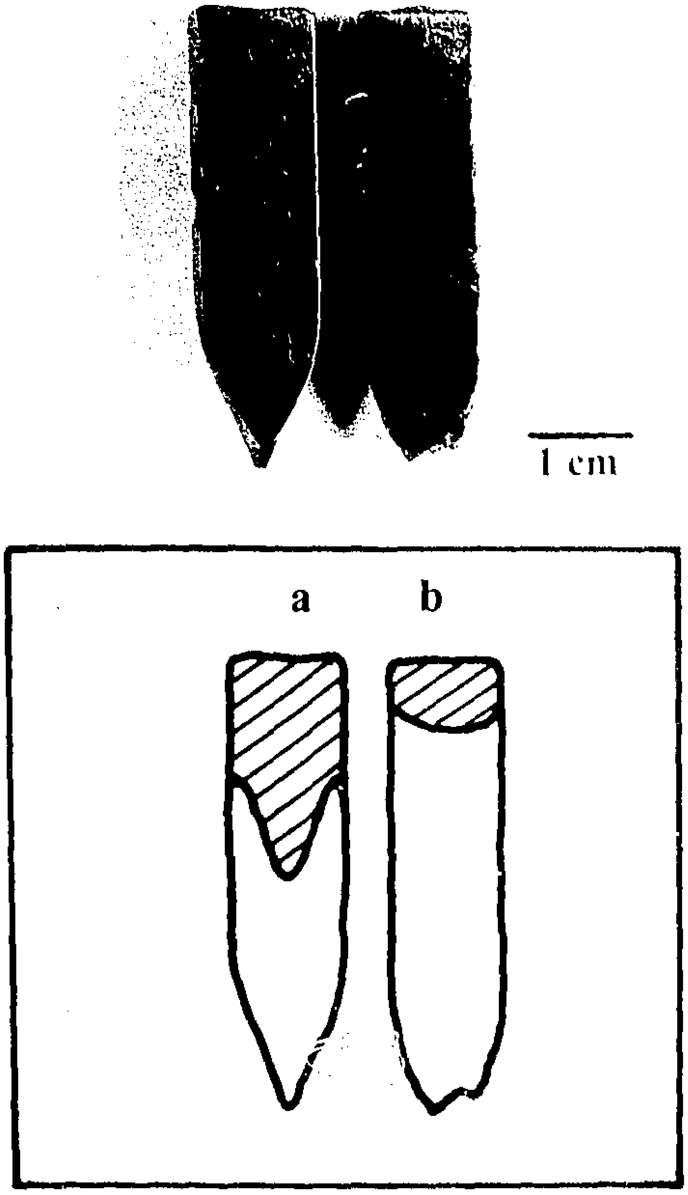

Fig.3.16 Photograph showing a comparison between two ingots (a) interrupted and quenched growth run 157, showing a severely concave demarcation line and (b) a fully grown ingot, run 138, exhibiting a less concave interface, both with prepared with excess Cu.

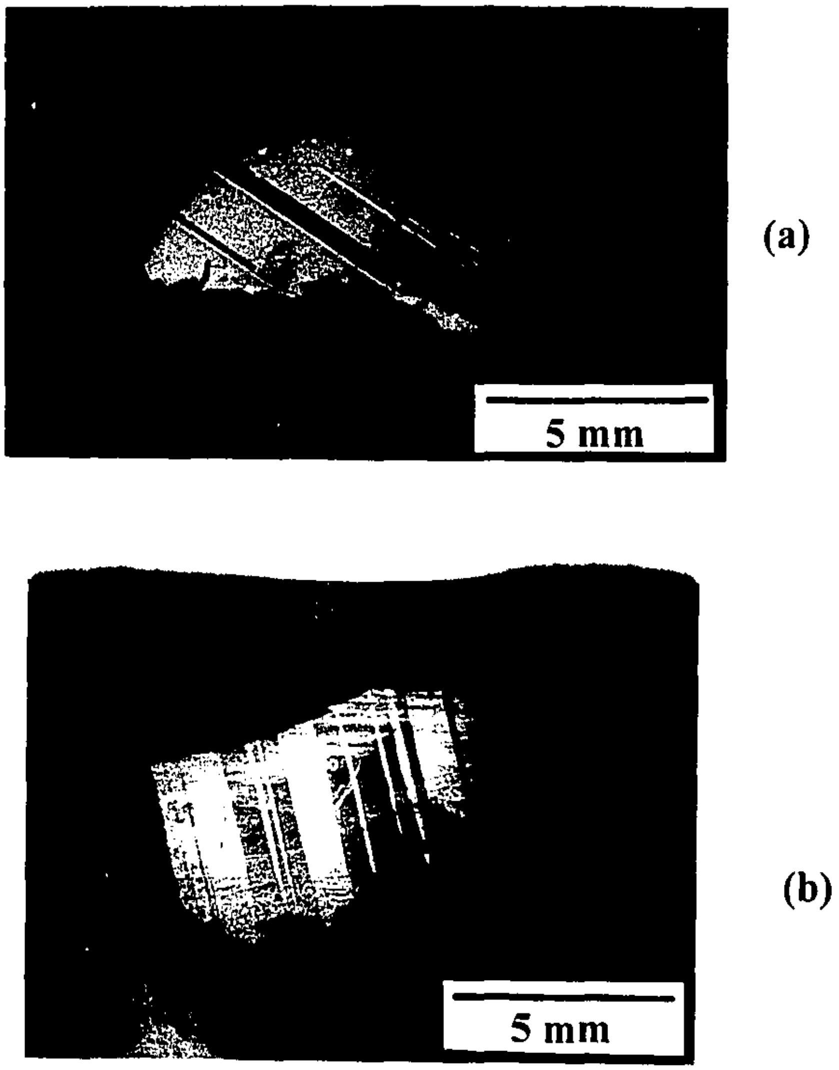

Fig.3.17 Twin bands seen in polished samples as revealed by (a) chemical etching in 5% brome - methanol solution and (b) thermal etching under vacuum at a temperature of about 300°C for 2 hours.

Thermal Etch Pits

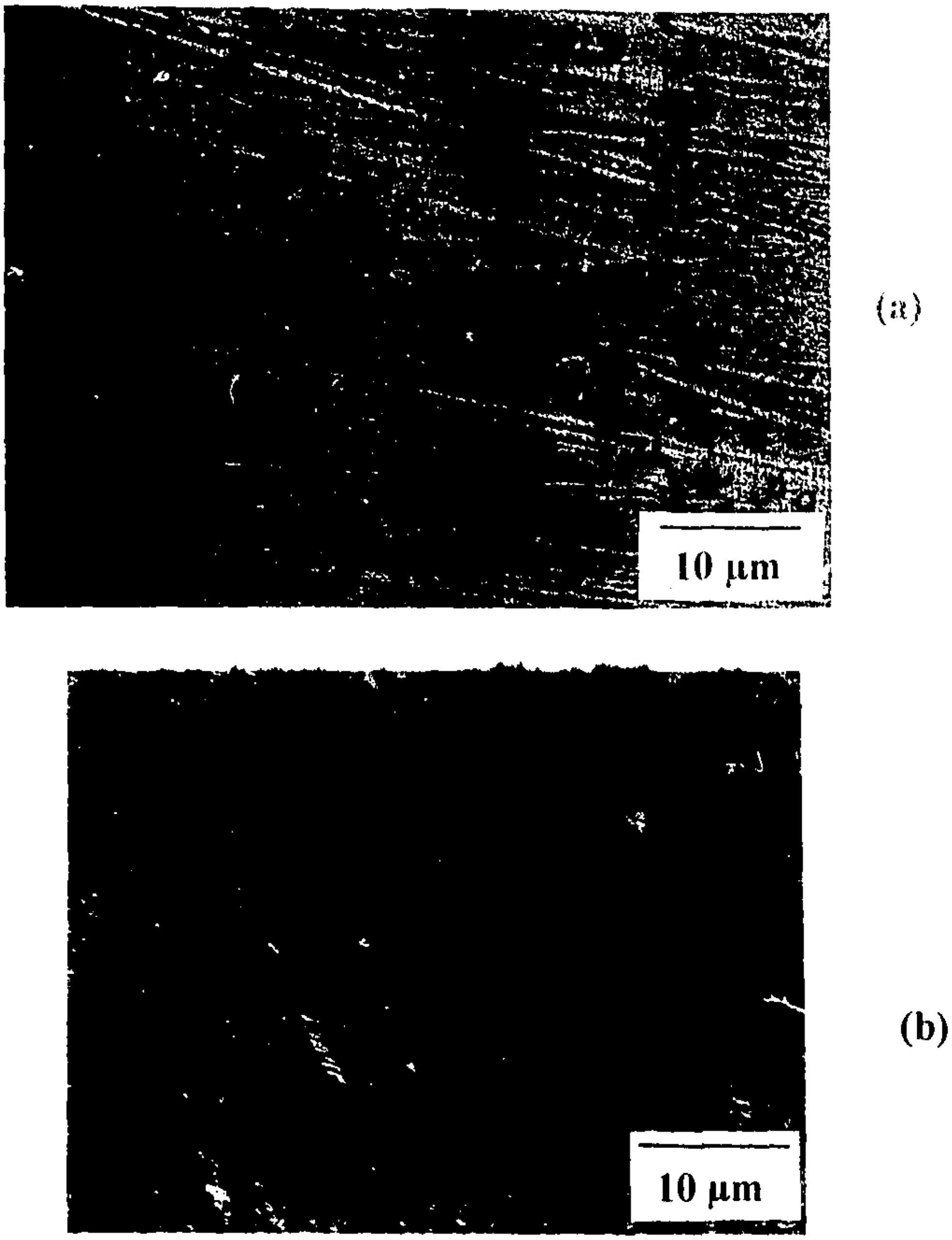

Fig.3.18 Thermal etch pits obtained on polished {112} surfaces, treated under vacuum, showing triangular features. (a) Sample heated at 300°C for 2 hours and (b) sample annealed at 600°C for 4 hours.

CHAPTER 4

IDENTIFICATION OF THE SOURCE OF ADHESION IN BRIDGMAN-GROWN $CuInSe_2$ INGOTS

4.1 INTRODUCTION

As discussed in chapter 3, in the early stages of the growth of $CuInSe_2$ from its starting elements in a quartz ampoule, the resulting ingot adhered strongly to the inner wall of the quartz tube. This was detrimental to the mechanical properties of the grown crystal and also prevented the extraction of the ingot from the ampoule. The problem was avoided by using a getter, such as boron nitride, in the ampoule as was shown earlier in chapter 3. It was also found, in earlier studies [2.31], that the agent causing the adhesion originated from the starting elements and not from the quartz ampoule. The starting element selenium, was also exonorated as the source of adhesion of the ingot[2.31]. Thus, the source of the problem was either the starting, so-called high purity, copper or the high purity indium. Furthermore, the identity of the gaseous agent involved was not known. Accordingly, in the present chapter, work is reported first on the isolation of the elemental source metal causing the sticking, and then on the identification of the gaseous agent itself.

4.2 TREATMENT OF THE COPPER AND INDIUM

Since the quartz and the selenium were already exonerated as the possible sources of the sticking agent gas , efforts were directed at pre-treatment of the indium and copper starting elements, which were supplied as nominally of five nines purity. Table 4.1 summarizes the experiments that were carried out. In these experiments, the Cu and In metals were individually treated prior to the synthesis of the compound. First, the indium was heated at 1100 °C in an evacuated sealed quartz ampoule with boron nitride for 48 hours. The indium was then reacted for a period of about 48 hours with the untreated high purity copper and selenium to form the $CuInSe_2$ compound. This time period was long enough for the sticking to occur, so that the Bridgman-growth step was not carried out. Using this indium, the resulting ingot showed the undesired properties of ampoule sticking, quartz cracking, film deposition and residual material, as indicated in the first row of Table 4.1 and also as shown earlier in Fig.3.4(b). Next, the high purity copper was similarly heated with boron nitride for 24 hours but this time, upon combining with the indium and selenium, the resulting ingot showed no sticking or quartz cracking, no residue and only a slight film deposit on the ampoule wall. A repeat of this run, carried out with the longer treatment of 45 hours for the copper, produced essentially the same result. Arising from this, the copper was heated at 1100 °C in a vacuum of about 2×10^{-7} torr *without* the boron nitride but with continuous pumping for a period of 24 hours. This produced a $CuInSe_2$ ingot with some sticking, cracking, deposit and residue but on a reduced scale. A repeat of this (row 5, Table 4.1) for a longer heat-treatment time of 44 hours, however, resulted in an ingot without any sticking or cracking but with some wall deposit and residue. These experiments thus pointed to a gaseous agent in the starting copper as the cause of ingot sticking.

4.3 IDENTIFICATION OF THE AGENT CAUSING STICKING

In order to determine more precisely the gaseous agent present in the five nines copper pellets, a quadrupole gas analyzer (Spectramass Inc., model SM100) was attached to the pumping system in which the Cu treatment was carried out, as shown schematically in Fig.4.1., so as to record the gaseous emissions from the Cu pellets during heating. In order to do this, is was necessary at first to measure the residual vapour content of the vacuum system without the Cu pellets. Therefore, the system was first pumped down with the quartz ampoule containing an empty quartz boat. The ampoule was heated at a temperature of about 1000 °C for a period of about 2 hours and a scan was then taken between about 2 and 50 atomic mass units (AMU). Fig.4.2(a) shows gas analyzer partial pressure peaks as a function of mass number where, it is seen that, the largest peaks consisted of water vapour peaks at 17 and 18 AMUs, as well as a peak at about 28 AMUs correspoding to both nitrogen and carbon monoxide. After this, the experiment was repeated but this time with the addition of about 10 grams of the 5 nines Cu pellets heated under the same conditions. The result of this analysis is given in Fig.4.2(b). It is quite clear here, that at a temperature of about 1000 °C, there was significant enhancement of the two oxygen peaks at 16 and 32 AMUs (corresponding to its ionization states of -2 and -1 respectively) . In this run , it was also found that the oxygen peaks were at a maximum at the thermocouple reading of 1030 °C corresponding (with a room-temperature correction of the cold junction) to the melting point of copper at 1083 °C , and diminished quickly with further increase of temperature. This is exhibited in Fig.4.3 which shows three scans shortly after the initial detection of the oxygen, taken at successively higher temperatures. It is evident here that the oxygen level was at its peak near the melting point of the Cu and was almost undetectable at the higher temperature of about 1200 °C. However, this process was found to be reversible and the oxygen peaks re-appeared upon decreasing the temperature from 1200°C back to about the melting point of Cu.

The oxygen content in the Cu, however, was found to decrease irreversibly with continued pumping and heating. This was evident when the Cu was maintained at a temperature near 1080°C and scans were taken at regular intervals over an extended period of about 4 days. Fig.4.4 shows scans taken at three times during this period, where it is evident that the two oxygen peaks progressively decreased with pumping and heating time and after some 72 hours of treatment, the oxygen levels were reduced to the background level of the vacuum system.

In order to verify the effect of the "de-oxygenation" of the Cu on the ingot adhesion, copper treated in this way was reacted in the form of a lump with the untreated indium and selenium pellets, as shown in Fig.4.5(a). After the compound synthesis, the ingot was heat-soaked at 1100°C for a longer than usual period of some 72 hours. The resulting ingot is shown in Fig.4.5(b), yielding a clean $CuInSe_2$ ingot with no sticking or residue what-so-ever. Finally, instead of the five nines copper, some commercial vertically cast, oxygen-free copper (from Otokumpo Ltd) was reacted, without any heat-treatment, with the indium and selenium, yielding a synthesized compound ingot with essentially no sticking or cracking.

4.4 DISCUSSION

The experiments carried out in this study clearly demonstrate that oxygen in the copper is the source of the sticking problem of $CuInSe_2$ ingots to the quartz ampoule. The earlier report by Tomlinson [2.24] that water vapour from the ampoule was the culprit was not confirmed in the present results. An ideal solution would appear to be the use oxygen-free copper as a starting material. However, using a gettering agent , such as BN, along with the five nines Cu has essentially the same outcome and might even be the preferred process if the presence of BN was in the form of a coating. This is because this coating was shown to have a beneficial effect on the crystal growth. As far as removing the oxygen from the copper is concerned, the gettering action of the BN is apparently far more efficient in extracting the oxygen than simply pumping and heating the copper under a vacuum of some 10^{-6} Torr [4.1]. While it was understandable for the oxygen levels to decrease with continued pumping and heating, it was not clear why this element was essentially undetectable at the elevated temperature near about 1200 °C, above the melting point of the Cu. One explanation could be that, at these higher temperatures, where copper vapour becomes more pronounced, the oxygen removed from the copper reacts with the Cu vapour to form CuO, which condenses onto the cooler portion of the quartz tube wall before reaching the detector. Fig.4.6 shows photographs of two segments of the portion of the tube outside the furnace (well away from the Cu pellets), where condensation of Cu vapour occurred. In Fig.4.6(a) the segment closest to the furnace shows a reddish deposit, which is likely to be an oxide of copper, while in Fig.4.6(b), which shows the cooler tube part nearer to the mass detector, the deposit appears to be mostly elemental copper. If this was indeed the case, it would suggest that at the higher temperatures, the oxygen is in fact removed and possibly at a higher rate but it is not detected due to its reaction with the Cu vapour.

Table 4.1 Effect of Pre-treatment of Copper and Indium

Pre-treatment of Cu and In Starting Metals[1].						Synthesis of CuInSe$_2$ Ingot.[6]				
Metal[2]	Purity[3]	Treat.[4]	Temp. (°C)	Soak time (hr)	Result	Adhesion ingot to ampoule	Cracks in ampoule	Deposit on ampoule	Residue above ingot	Comments
In	5N	BN	1100	48	In lightly attaches to quartz ampoule wall.	yes	yes	yes	yes	BN does not affect the In.
Cu	5N	BN	1100	24	Cu sticks to the quartz. Ampoule wall cracks.	no	no	very little	no	BN affects the Cu markedly. Ingot sticking eliminated.
Cu	5N	BN	1100	45	Cu becomes less adherent. Quartz does not crack.	no	no	very little	no	Ingot sticking eliminated. Some voids present in ingot.
Cu	5N	Vac	about 1100	24	Cu shatters quartz boat. Reddish deposit occurs	yes	yes	yes	yes	24 hr pumping is insufficient to eliminate sticking.
Cu	5N	Vac	about 1100	44	same as above	no	no	yes	yes	Pumping does reduce sticking but slower than BN.
Cu	5N	Vac	about 1080	98	same as above	no	no	no	no	Pumping for 4 days reduces considerably the oxygen in Cu
Cu	VCOFC[5]	-	-	-	no pre-treatment	no	no	little	yes	Oxygen-reduced Cu gives no sticking.

Notes:

1. Earlier results excluded the selenium as the cause of sticking [5]. Therefore, no pre-treatment was given to the high purity selenium used.
2. Pre-etching of the metal pellets was carried out using HNO_3 for Cu and HCl for In.
3. 5N: 99.999% nominal purity as supplied from Metal Specialists Inc., for In and Cerac Inc., for Cu.
4. BN: treatment of the metal with a boron nitride block included separately in the evacuated ampoule. Vac: heated while pumping under vacuum.
5. VCOFC: Vertically cast oxygen-free copper, obtained from Otokumpo Ltd., Finland.
6. Synthesis of CuInSe$_2$ at a temperature of 1100 °C with a soak time of 40-65 hours, without BN in the ampoule. Bridgman growth stage not carried out.

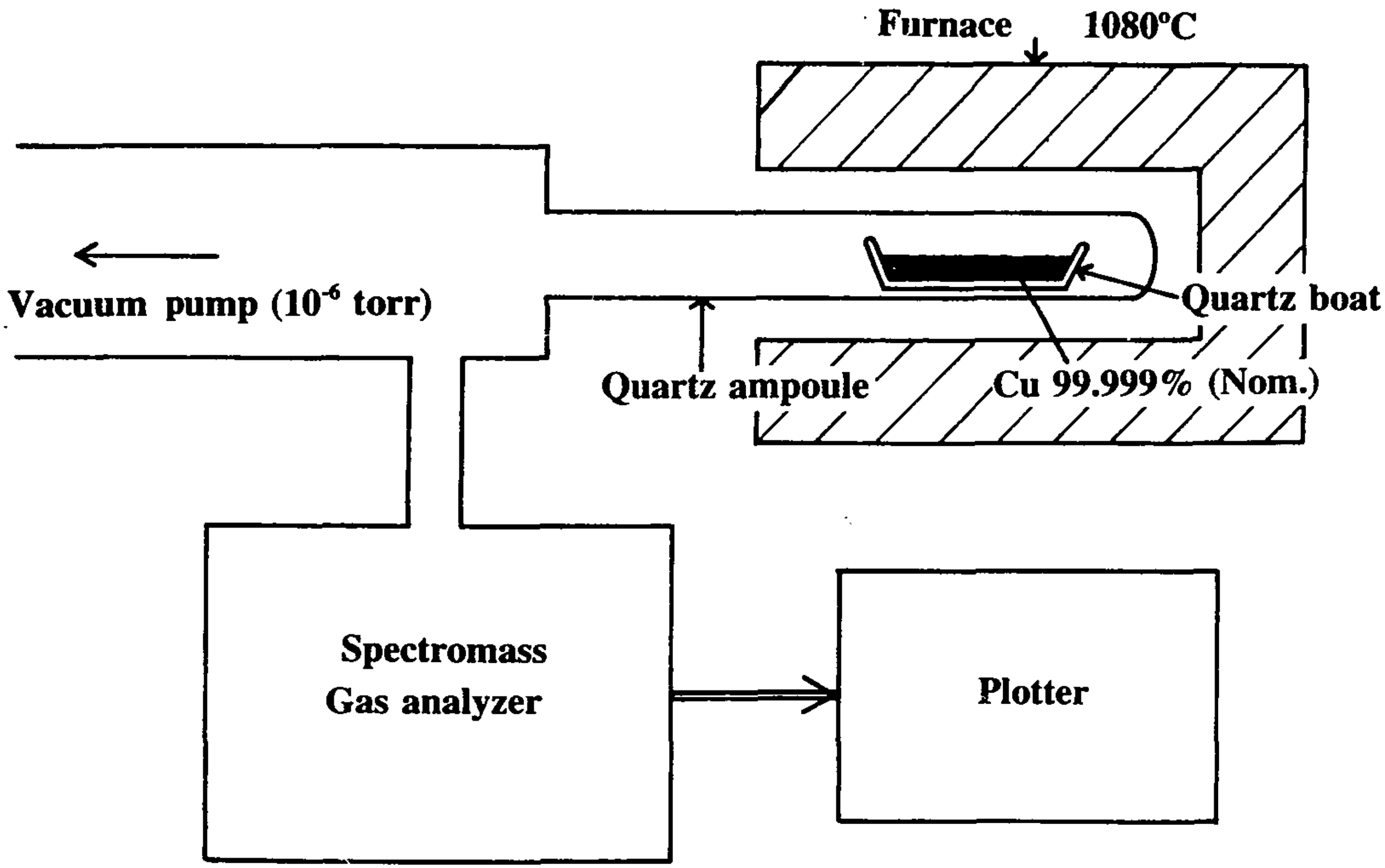

Fig.4.1 Schematic diagram of the arrangement used for the vacuum-melting treatment of the copper.

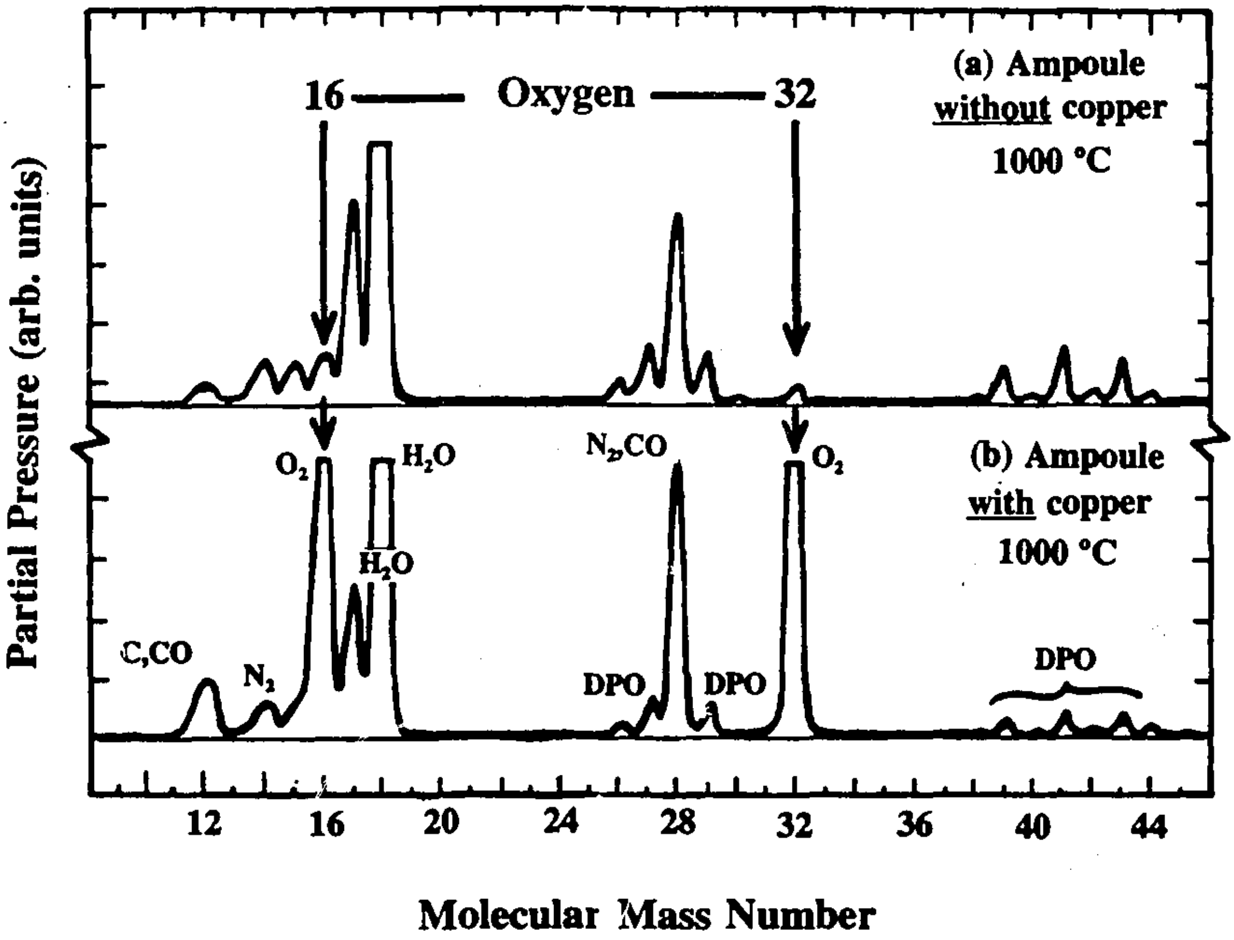

Fig.4.2 Gas analyser partial pressure peaks as a function of molecular mass number recorded during pumping and heating at about 1000 °C of (a) ampoule containing only quartz crucible, (b) ampoule containing quartz crucible plus five nines purity copper. (DPO: Diffusion Pump Oil.)

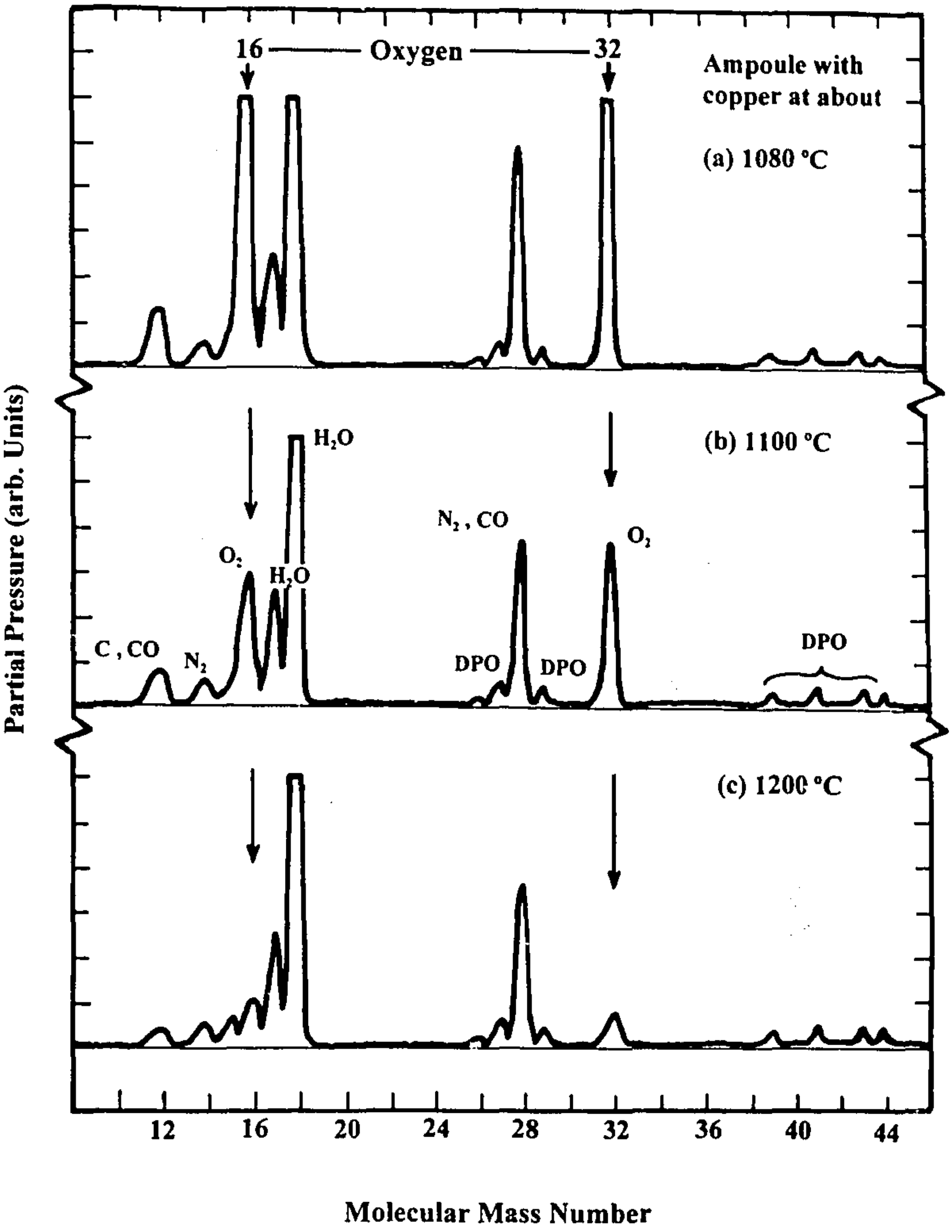

Fig.4.3 Gas analyser partial pressure peaks as a function of molecular mass number recorded during a raise in the copper soaking temperature from about 1080 °C to about 1200 °C, showing (a) oxygen peaks near their maximum at the melting point of Cu, (b) level of the oxygen peaks drops just above the melting point, and (c) oxygen peaks almost disappearing at a temperature of about 1200 °C. (DPO: Diffusion Pump Oil.)

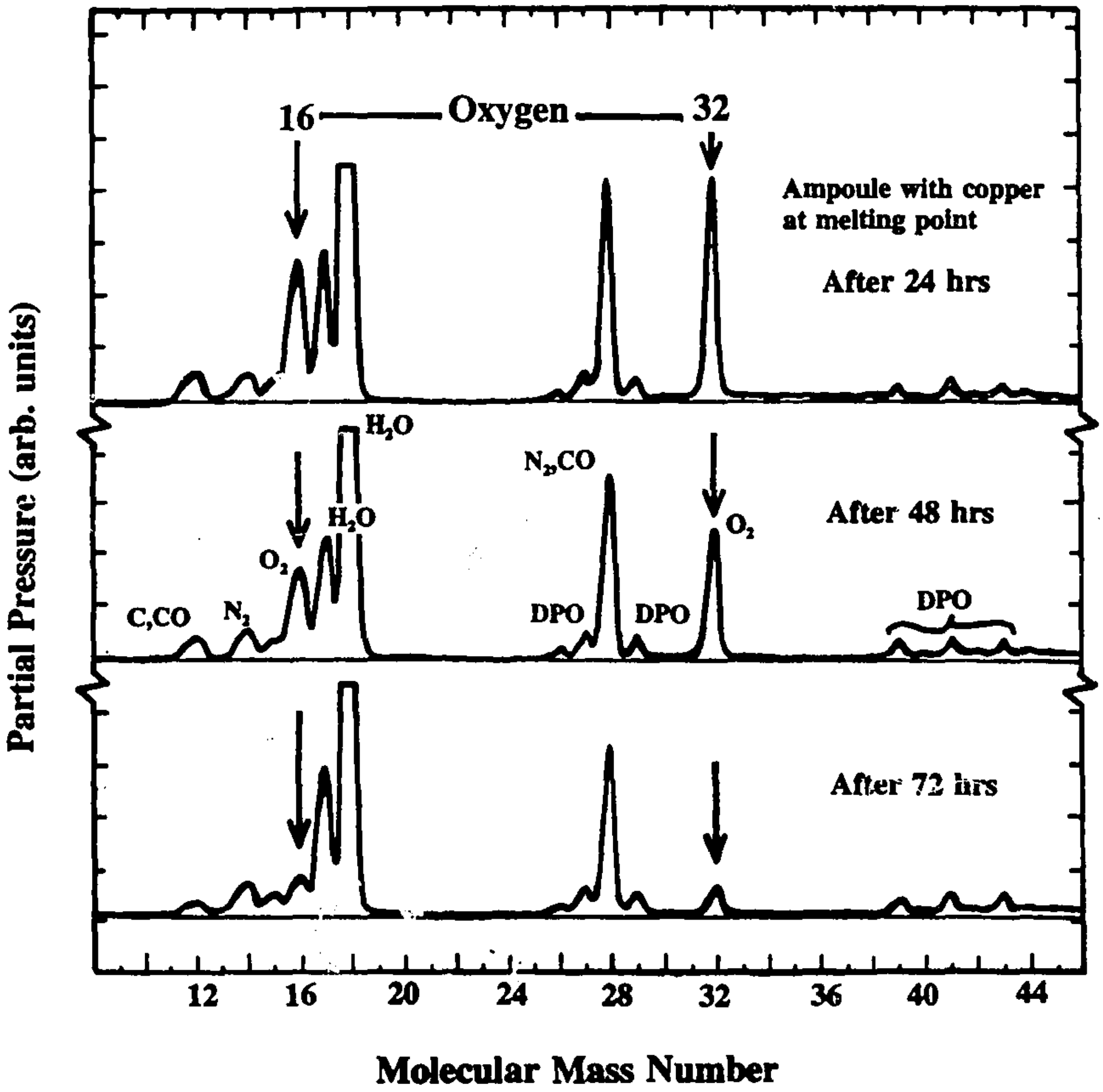

Fig.4.4 Gas analyser partial pressure peaks as a function of molecular mass number for ampoule containing five nines copper pumped-on at about the melting point of copper. Scans were taken after 1, 2 and 3 days of pumping.

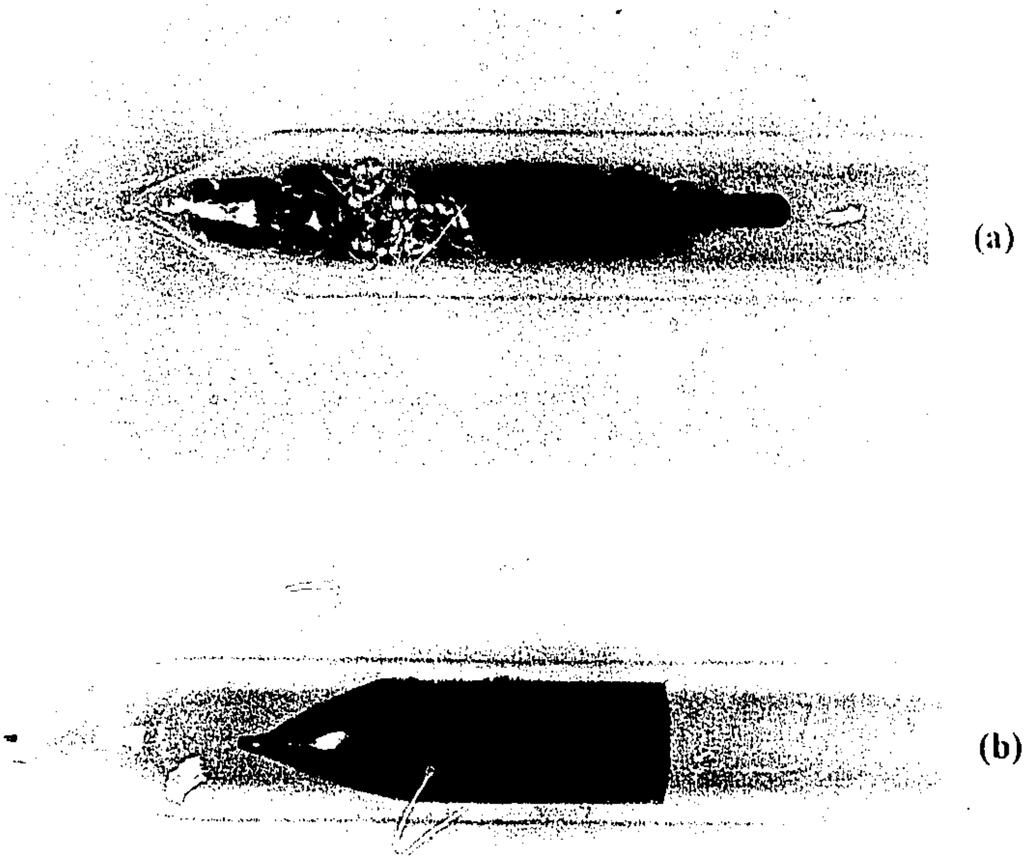

Fig.4.5 Photographs showing (a) the 98 hr-vacuum-treated Cu (row 6, table 4.1) combined with untreated In abd Se in an ampoule, where no BN was used (b) the resulting ingot after a 72 hour soak at 1100°C, showing a clean ingot with no signs of adhesion, no cracking in the quartz and no residue at all.

(a) (b)

Fig.4.6 Photographs of the quartz tube used for the vacuum melting of the Cu, taken on the part of the ampoule oustside the furnace, showing condensation of material (a) region adjacent to the furnace, where a reddish-coloured deposit occured and (b) region away from the furnace, showing only Cu deposit.

CHAPTER 5

COMPOSITIONAL MEASUREMENTS on $CuInSe_2$ INGOTS

5.1 INTRODUCTION

One of the primary objectives of this work was to grow ingots of uniform composition and conductivity type. This is especially important when monocrystals are used as substrates in device work or as filaments in carrying out electrical measurements. It was therefore necessary to carry out compositional measurements on our stoichiometrically-grown material to verify its uniformity. While stoichiometric $CuInSe_2$ was the main subject of study in this thesis, it was also of interest to carry out compositional measurements on non-stoichiometric material and study the effect on conductivity type, especially when the BN coating was used for the crystal growth. This is because the BN was shown to act as a getter during the growth of the compound, where it removes the oxygen from the starting copper, as demonstrated by the work presented in chapter 4. It has been reported in the literature [5.1] that, oxygen acts as an acceptor in $CuInSe_2$ and thus, its presence may affect the study of conductivity type with change in intrinsic composition. Accordingly, work is reported in this chapter, on the compositional studies using electron probe micro-analysis (EPMA) both on stoichiometric and non-stoichiometric runs, where the BN coating was used in the ingot preparation. The objective here, is to determine a relationship between composition and electrical properties for the single phase chalcopyrite $CuInSe_2$ region.

5.2 SAMPLE PREPARATION

In this work, a total of eight runs were prepared for compositional measurements. Of these runs, seven had non-stoichiometric starting compositions and are runs 138, 140, 141, 142, 143, 145 and 146, while one run, No. 144, was a stoichiometric growth run. The starting compositions of these runs are indicated in Table 5.1, which also gives the starting Cu/In and metal/Se ratios for each individual run. Here, the synthesis of the compound and subsequent crystal growth of the ingots was carried out as described earlier in chapter 3. In almost all of the runs, the powder BN, with 99.5 % nominal purity, was used as the source for the BN coating , as indicated in Table 3.1 of chapter 3, which also summarizes the crystal growth conditions. After the crystal growth, the ingot was extracted from the ampoule and cut into two halves along the growth axis, using a diamond saw. One half of the ingot was then used for compositional analysis. Since the length of the ingot was larger than the diameter of the mounting holder on the stage of the electron microprobe unit, the ingot-half was further cut into two pieces which were mounted separately, using Quickmount resin , inside a ring-shaped brass holder used for the EPMA. In the EPMA analysis, it is essential that the surface under examination be extremely flat to minimize error during the measurement. Therefore the cut and mounted pieces were polished using 1 μm followed by 0.05 μm alumina powder until a mirror-like finish was obtained. After the polishing was complete, the ready surfaces were cleaned thoroughly with DI water and dried with nitrogen. The samples were then ready to be coated with a thin layer of carbon which was evaporated onto the exposed polished surface of each sample, serving as a conducting layer which prevents charge build-up on the sample surface during the EPMA examination.

5.3 MEASUREMENT TECHNIQUES

The ingots with variation of stoichiometry were investigated in two ways. First, EPMA measurements were carried out to determine the composition at different locations on the polished ingot surface. Then, hot probe measurements were taken at the same locations, to determine the conductivity type of each region. The measurements were carried out as follows.

5.3 (a) EPMA Compositional Measurements

EPMA measurements were carried out with a JEOL electron superprobe (model JXA-8900L), using wavelength dispersive spectroscopy (WDS). The samples were loaded on a mounting stage and pumped down to a pressure of less than 10^{-6} Torr. The probe electron current was preset at 30 nA, while the accelerating voltage was about 15 kV. Fig.5.1 shows a schematic diagram of the electron probe measurement. In order to measure quantitatively the elemental compositions in the ingots, a standard was needed for each of the three constituent elements Cu, In and Se. Therefore, a polished reference specimen was prepared using the high purity five nines Cu, In and Se . The electron beam was positioned on selected spots on the surface of each element and the intensities of the emitted characteristic X-rays were registered from some six locations. An average of these measurements was taken which determined a reference intensity for each of the elements. Having done this, the unknown composition of the ingots could now be determined. The sample was then moved into position and several points were selected on the main body of the ingot for compositional measurements along the growth axis as well as in a transverse direction. The compositional data was analysed using two different correction schemes employed by the EPMA, a ZAF method [5.2] and a CIT ZAF scheme [5.3], which yielded compositional values which were similar but with a slight difference in value. A representative ingot is shown schematically in Fig.5.2 (ingot 141), where the exact locations of the electron beam were recorded and are indicated in the figure. This was done by photographing the ingot during the measurements, using an *in-situ* thermal image camera, and marking the exact position of the beam on the photograph. By placing all the pictures together, a map was obtained, which indicated the measurement locations precisely, for each of the ingots.

In the runs containing a non-stoichiometric starting charge, an excess of one of the elements, or related compounds, appeared in the last region to freeze. This is indicated by the multi-phase region in the schematic of Fig.5.2. As indicated in this figure, compositional measurements were also taken on these secondary phases besides the main single phase region of the ingot. Unlike the single phase region, which exhibited no special features, the secondary phases were quite apparent, particularly when observed using the backscattered electron image. This is because the backscattered electron image is more sensitive to the atomic weight of the different elements as compared with the secondary electron image.

5.3 (b) Conductivity Type Determination

The conductivity type was determined by hot point probe measurements on all of the locations examined by the electron probe. Fig.5.3 shows a schematic of this method, where the back of the sample was in contact with a brass block and its front surface probed with a heated tip of metal. The thermoelectric voltage was then monitored and its sign was an indication of type: positive indicated n-type while negative indicated p-type. By using the constructed map for each ingot showing the location of the compositional measurements, conductivity type determinations were carried out at the same locations where the probing was done under a microscope set to the same magnification as that used to obtain the ingot photographic map. This allowed the composition and the conductivity type to be measured on essentially the same location on the ingot surface.

5.4 EXPERIMENTAL RESULTS

5.4 (a) Composition versus Conductivity-Type Measurements

As mentioned earlier, a total of eight ingots were measured in terms of composition and conductivity type. Compositional measurements were carried out on each ingot, where some 60 data points (e.g. Fig.5.2) were taken on different regions of the ingot surface. The conductivity type was then determined at the same locations for all of the eight ingots. The results of all of these measurements are plotted in Fig.5.4, on ternary composition diagrams. In Fig.5.4(a), the compositional values obtained using the ZAF correction scheme are shown and in Fig.5.4(b), those for the CIT ZAF scheme are given. The compositions corresponding to n-type regions are represented by solid circles, while p-type compositions are shown in open circles. It is seen, in Fig.5.4(a) and (b) that, using the ZAF method, the measured compositions were not very different from those determined by the CIT ZAF scheme, whereby the compositions corresponded to a narrow region on the diagram. In Fig.5.4(a), n-type conductivity was obtained for atomic compositions in the region where indium was greater than about 26 % and copper less than 24 %. The apex of this region corresponded to a selenium concentration of about 50%. In the region where the copper was more than about 26%, and the indium was less than 25%, the resulting conductivity was p-type. For intermediate Cu and In compositions, both n and p type conductivity was found. In Fig.5.4(b), the n and p regions were not very different from those in Fig.5.4(a) although the selenium concentration, as well as the Cu/In ratio was somewhat higher. The data points shown in Fig.5.4, exhibited scatter corresponding to the error involved in this method estimated to be about ± 0.5 %.

The compositional data points obtained in this study and shown in Fig.5.4(a), are also plotted, on a larger scale, in Fig.5.5 along with the data of Neumann and Tomlinson [2.29], who studied deviations from stoichiometry in $CuInSe_2$ by annealing their samples under minimum and maximum selenium pressure. Here, it is seen that, on the larger compositional range, the present results seem to follow the general trend of those by Neumann and Tomlinson, whereby n-type conductivity is observed in the region corresponding to indium concentrations greater than about 25%, while p-type behaviour is observed for smaller indium concentrations, regardless of the selenium or copper concentration. This was not the case in the results of L.S. Yip *et al* [2.26][2.28], who found p-type conductivity in the n-region of Fig.5.5, where indium was in excess of 25%. In their work, *un-treated* copper of nominal five nines purity was used in the synthesis of the ingots.

Fig.5.6 shows a plot, on a ternary composition diagram, of the starting and final compositions of all the eight runs. The final composition in each case, was obtained by taking an average of the measurements on the single phase region for the ingot. It is seen here that, there was a shift in the final composition away from that at the start in all ingots, in a direction generally towards the stoichiometric area. This tendency for stoichiometric *"correction"* is also indicated in Table 5.1, where the Cu/In ratio of the final composition tended to be closer to 1 than that at the start. It is important to note here that, while some scatter was observed in the compositions at different points on the same ingot, the conductivity type of all regions measured on the same ingot was uniformly either p-type or n-type. This is indicated in Fig.5.6, where n-type ingots are represented by the broken lines and p-type by the solid-lines. Thus, this suggested that, the *deviation from stoichiometry in the starting composition* controlled the final conductivity type of the entire single phase region of the ingot. For example, ingots with excess indium or a large deficiency of selenium in the starting composition always exhibited n-type conductivity, while runs with starting excess copper or excess selenium exhibited p-type conductivity.

5.4 (b) Compositional Uniformity

The compositional measurements given above were taken on the main part of the ingot where the material was single phase. The measurements were taken both along the ingot axis and also in a transverse direction. Fig.5.7(a) shows a plot of elemental concentration verses distance along the ingot for the stoichiometric run 144. Here, it is seen that the concentration of the Cu and In were essentially the same in the main part of the ingot, with no significant excess indium over the copper observed, as was reported by

Tomlinson [2.17] for his ingots . The selenium, while slightly below the 50% mark, was also essentially constant with distance along the ingot. The same may be said about Fig.5.7(b), where the concentration across the ingot is given for the elements in the same ingot, exhibiting little or no variation with distance, which confirmed that the composition was essentially uniform throughout the ingot.

Fig.5.8, shows a plot of atomic concentration versus distance along the ingot for run 141, where excess indium was used in the starting composition of 20 % Cu, 30% In and 50% Se. In this figure, it is clear that, in the main part of the ingot, the concentration of the indium was noticeably higher than that of the copper. Near the top end however, where other phases existed, the concentration of the Cu and In in the single phase $CuInSe_2$ areas within the multi-phase region were not very different. In this multi-phase region, the selenium concentration exhibited a slight decrease below the 50 % level.

Fig.5.9 shows a similar plot for run 142 with 24% Cu, 24% In and 52% Se starting compositions. Here, the selenium concentration, throughout the ingot, in the single phase region, did not appear to be different from that of the stoichiometric run and did not seem to be affected by the addition of the excess selenium. The selenium in this run did precipitate, however, as a second phase in the last region to freeze. The In concentration was slightly above that of the copper in the main part of the ingot, despite their equal starting compositions.

A plot showing the composition, against distance, for an excess copper run 143 (31%Cu, 23% In, 46% Se), is given in Fig.5.10. Here it is apparent that there was excess copper in the bulk of the single phase region of the ingot as well as in the last region to freeze. Here, the observed departure from stoichiometry in the single phase region, for the copper and the selenium, was far more pronounced than in any of the earlier runs.

5.4 (c) Compositional Measurements in Multi-Phase Regions

Compositional measurements were also carried out on phases, other than the main $CuInSe_2$ phase, which precipitated in the last region to freeze. These are summarized in Table 5.2. In Table 5.2(a), all of the observed Cu-In phases are given, while in Table 5.2(b), the selenium and selenide phases are indicated. The table gives the nominal compositions measured, and also the runs in which they were present. Some examples of these phases are shown in the photographs of Fig.5.11. Fig.5.11(a) shows a photograph of the second phase region in run 140 with a deficiency of selenium, where the phases Cu_7In_4 and Cu_9In_4 were identified, and appeared to be in the shape of "fish" in a "sea" of $CuInSe_2$. Fig.5.11(b) shows second phases of Cu and Cu_4In, in the excess Cu run 143, precipitated in the form of globules. In run 145, with a starting deficiency of indium, the secondary phases observed were CuSe and Se, as shown in Fig.5.11(c). In this figure, the $CuInSe_2$ single phase, in the top end of the ingot, developed a dendritic shape, as seen pointing downwards. The excess indium run, 146, exhibited the secondary phase InSe, shown in Fig.5.11(d), and Cu_7In_4 as well as the undocumented phase In_7Se_5, both shown in Figs.5.11(e) and (f). It is noted here, that no other phases such as Cu_2Se and In_2Se_3, which are encountered in thin film work were observed in this study.

5.5 DISCUSSION

The results in this chapter firstly confirm that, with stoichiometric starting proportions, uniformly p-type ingots with uniform composition are obtained by the Bridgman process used. The fact that a significantly higher proportion of indium was not observed along the ingots in the present work disagrees with the early work of Tomlinson [2.17] and of Vahid Shahidi *et al* [1.10] . Thus, the present results are also at variance with the phase diagram of Fearheiley [2.22], which predicts that a gradient freeze should yield a $CuInSe_2$ chalcopyrite phase with more than 10% of dissolved In_2Se_3. For non-stoichiometric proportions, Fig.5.8 indicates that in the main part of the ingot, the chalcopyrite can, as a single phase, contain a few percent of excess indium, in conformity with the phase diagrams of Palatnik and Rogacheva [2.3] and that of Fearheiley [2.22]. However, Fig.5.10 indicates that the chalcopyrite can also tolerate 1 or 2 percent of excess copper without precipitating a second phase in the main part of the ingot, which is not in accord with the phase diagrams of Palatnik and Rogacheva [2.3] and Fearheiley [2.22]. In fact, in all the runs with non-stoichiometric starting proportions, the first 80% or so of the ingots was always single phase chalcopyrite having a composition fairly close to stoichiometry. In other words, the gradient freezing process is "forgiving" in that it automatically results in a movement of composition, towards stoichiometry in the main part of the ingot, no matter how far the original proportions differ away from the stoichiometry.

A multi-phase region was only found, in the last portion to freeze of the ingot, where the deviation from stoichiometry in the starting proportions was large; the rest of the ingot was always single phase chalcopyrite and always uniformly n-type or p-type.

In the multi-phase regions. the following phases. besides the chalcopyrite. were observed: Cu_7In_4. Cu_9In_4. Cu_4In. Cu. Se. CuSe and InSe. Other undocumented apparent compounds found were: Cu_5In_3 . Cu_4In_3 and also In_7Se_5, where the last named was similar to In_3Se_2 reported by Yip. Weng. Shih and Champness [2.27]. It is significant that the well-known compounds Cu_2Se and In_2Se_3. reported in thin film work, were not observed at all. due probably due to the higher temperature used in the synthesis of the $CuInSe_2$.

In respect of the relation between composition and conductivity type for the single phase chalcopyrite material. the present results are somewhat clearer than those reported earlier by Yip. Weng. Shukri. Shih and Champness [2.28]. This is probably because the present data was obtained on material free of oxygen. which is reported to act as an acceptor in $CuInSe_2$ [5.1]. With the ZAF-corrected EPMA results, it was found that n-type conductivity was obtained with an In content greater than about 26.5 % and p-type with it less than about 25%. With the CIT ZAF correction. these two percentages are respectively 26.2 and 25.2 %. Within the 25 to 26.5 % In region (ZAF-corrected results), both n-type and p-type conductivity was obtained. arising possibly from the ± 0.5 % error in the composition determination by the EPMA. It is interesting to note here that, the copper and selenium proportions are apparently not directly involved in determining the conductivity type. Thus the chalcopyrite can have an excess of Se and still be n-type if the indium content is sufficiently high. Comparison of the present results with those of Neumann and Tomlinson [2.29]. indicates a rather better agreement than for the earlier results of Yip *et al* [2.28]. Thus, here it would seem that the demarcation line between n- and p-type material is a line drawn on the composition diagram corresponding approximately to [In] = 25%, whereby, n-type is obtained for [In] > 25 % and p-type for [In] < 25%. As an example, consider a change of composition from $Cu_{20}In_{20}Se_{60}$ to $Cu_{30}In_{30}Se_{40}$ representing a loss of Se but no change in the Cu/In ratio. The initial material would be p-type because [In] < 25 % and the final material n-type since [In] > 25 %. Thus, there is a type change arising apparently from a loss of selenium, although the critical factor is the relative proportion of indium. Note that the Cu_2Se-In_2Se_3 tie line is not relevant to this criterion. This is consistent with the fact that these binary compounds have never been observed in melt-grown $CuInSe_2$ crystals.

The present results also confirm a phenomenon previously reported by Yip *et al* [2.28] , that the conductivity type is decided, not so much by the final composition of the single phase region, but by the composition of the melt. Thus if the original starting proportion was rich in copper or rich in selenium, the final crystal was p-type; if it was rich in In, it was n-type. However, this result actually fits in with the criterion mentioned above, namely that it is the indium concentration that determines the conductivity type. Examination of Fig.5.6 shows that, the original compositions yielding n-type conductivity started out from an area on the diagram where the indium concentration was greater than 26 % and the compositions yielding p-type conductivity started out from areas where it was less than 25 %. It is important to point out that this does not contradict earlier reports involving conductivity-type control by the selenium.

Table 5.1

EPMA Results from Single Phase Region of Runs with Deviation from Stoichiometry

	Starting Composition					**Final Composition[1]**						
Run No.	Cu (Atomic percent)	In (Atomic percent)	Se (Atomic percent)	Cu/In Ratio	Metal/Se Ratio	Cu (Atomic percent)	In (Atomic percent)	Se (Atomic percent)	Cu/In Ratio	Metal/Se Ratio	Conduct. type[2]	Comments[3]
138	28.5	23.8	47.7	1.20	1.09	26.2	25.1	48.7	1.04	1.05	p	Cu excess
140	27.0	27.0	46.0	1.00	1.17	25.1	25.4	49.5	0.99	1.02	n	Se deficiency
141	20.0	30.0	50.0	0.67	1.00	22.6	27.1	50.3	0.83	0.99	n	In excess, Cu deficiency
142	24.0	24.0	52.0	1.00	0.92	25.0	26.0	49.0	0.96	1.04	p	Se excess
143	31.0	23.0	46.0	1.35	1.17	26.5	25.2	48.3	1.05	1.07	p	Cu excess
144	25.0	25.0	50.0	1.00	1.00	24.6	25.9	49.5	0.95	1.02	p	Stoichiometric
145	28.0	21.0	51.0	1.33	0.96	25.5	25.4	49.1	1.01	1.04	p	Cu and Se excess, In deficiency
146	22.0	31.0	47.0	0.71	1.13	24.5	25.8	49.7	0.95	1.01	n	In excess, Cu and Se deficiency

1. Representative average compositions of the data points for each ingot ,as determined by EPMA , for the homogeneous single phase region.
2. Conductivity type as determined from the hot point probe method.
3. Elemental excess or deficiency in the starting composition with reference to proportions 25%, 25% and 50% for Cu, In and Se respectively.

Table 5.2(a) Copper and Copper-Indium Phases

(Atomic Conc. %)[1]		Elemental ratio			
Cu	In	Cu/In	Possible composition[2]	Compound known	Present in run no.
63.7	36.3	1.75	Cu_7In_4	Yes	140, 141, 146
68.9	31.1	2.22	Cu_9In_4	Yes	140
79.7	20.3	3.93	Cu_4In	Yes	143
62.7	37.3	1.68	Cu_5In_3	No	146
56.5	43.5	1.3	Cu_4In_3	No	146
≥90.0	≤10.0	≥9.0	$Cu + Cu_4In$?	Yes	138, 143

1. Atomic concentrations, determined by EPMA, averaged over several data points and rounded-off. The selenium concentration was below the detection limit of the electron micro probe, where the resolution was about ± 0.5%.
2. Chemical formula having the nearest elemental ratio.

Table 5.2(b) Selenium and Selenide Phases

(Atomic Conc. %)[1]			Elemental ratio		Possible composition[2]	Compound known	Present in run no.
Cu	In	Se	In/Se	Cu/Se			
50.8	BD	49.2	-	1.03	CuSe	Yes	142, 145
BD	51.0	49.0	1.04	-	InSe	Yes	140, 141, 146
BD	58.2	41.8	1.39	-	In_7Se_5	No	141, 146
BD	BD	99.9	-	-	Se	Yes	142, 145

1. Atomic concentrations, determined by EPMA, averaged over several data points and rounded-off. BD indicates concentrations below the detection limit of the electron micro probe. The error in the measurements is estimated to be about ± 0.5%.
2. Chemical formula having the nearest elemental ratio.

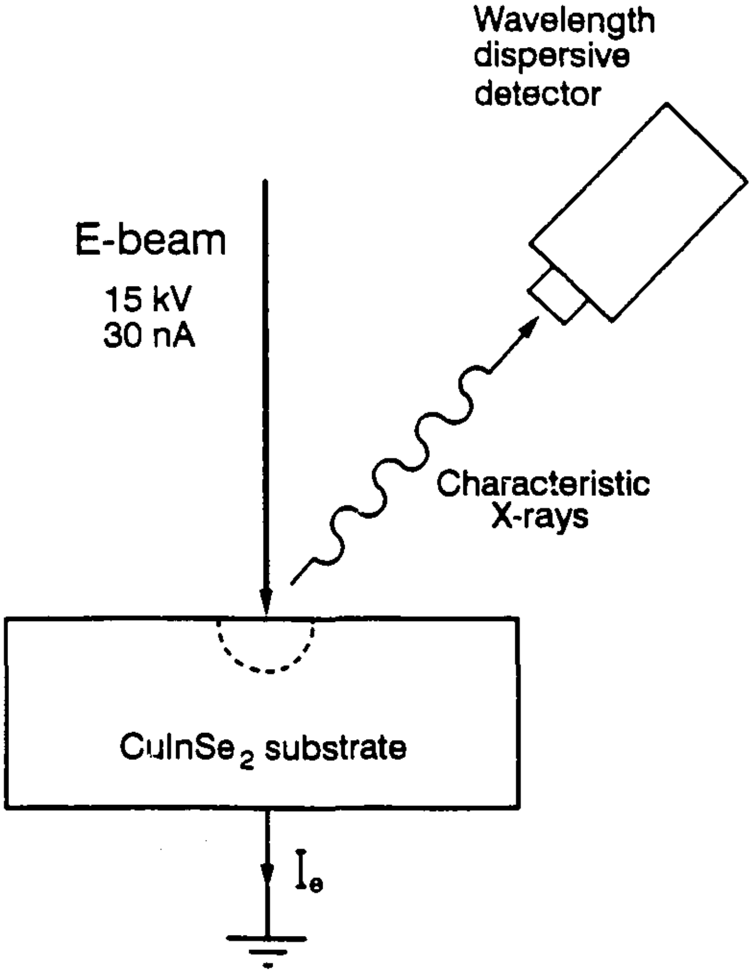

Fig.5.1 Schematic diagram of the electron probe micro-analysis (EPMA) measurement setup.

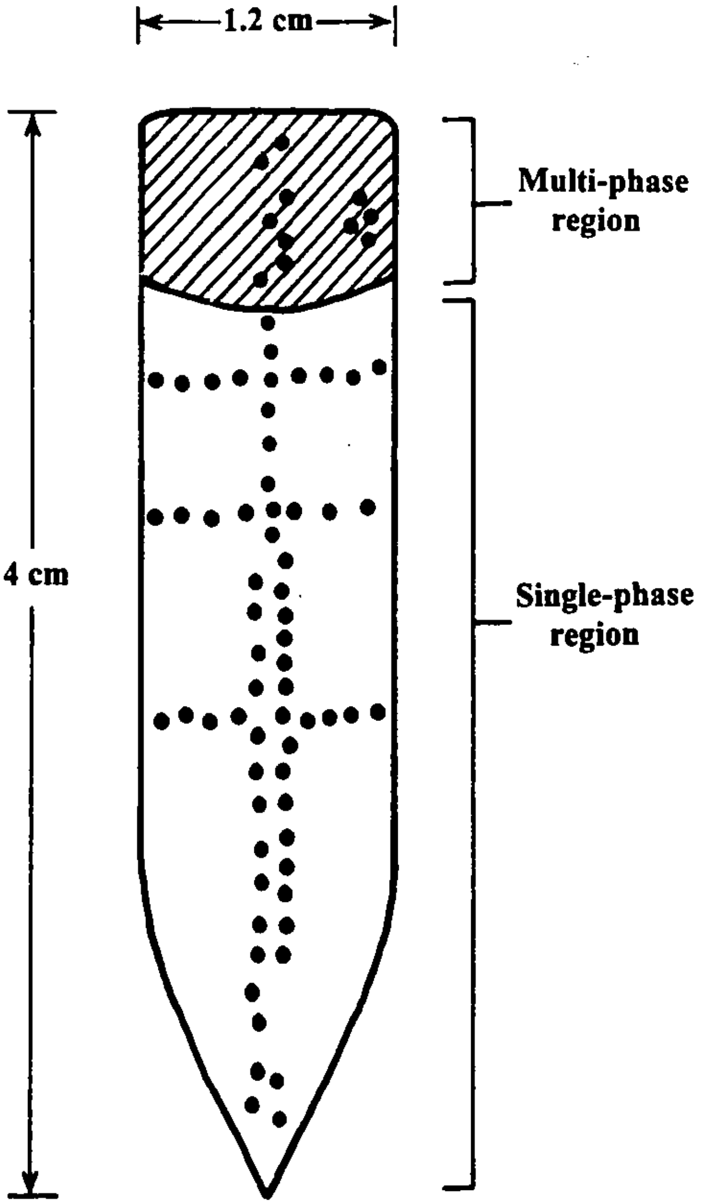

Fig.5.2 Schematic diagram of ingot 141, showing the location of the compositional measurements on the single phase and multi-phase regions of the ingot.

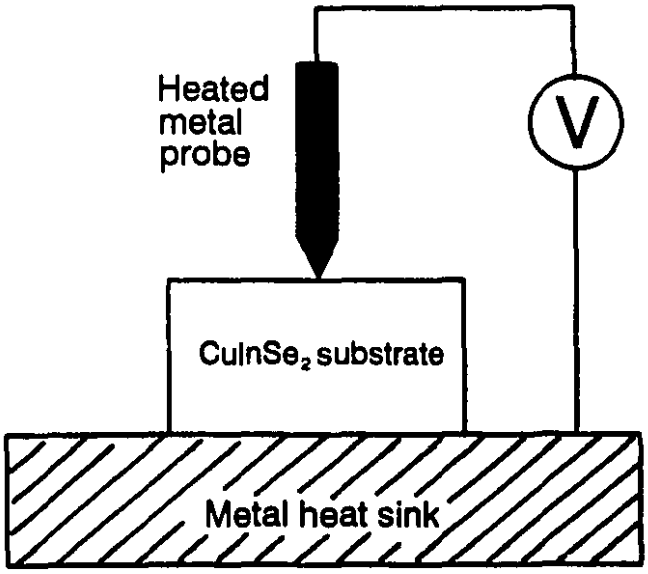

Fig.5.3 Schematic diagram of the hot point probe setup used for conductivity type determination.

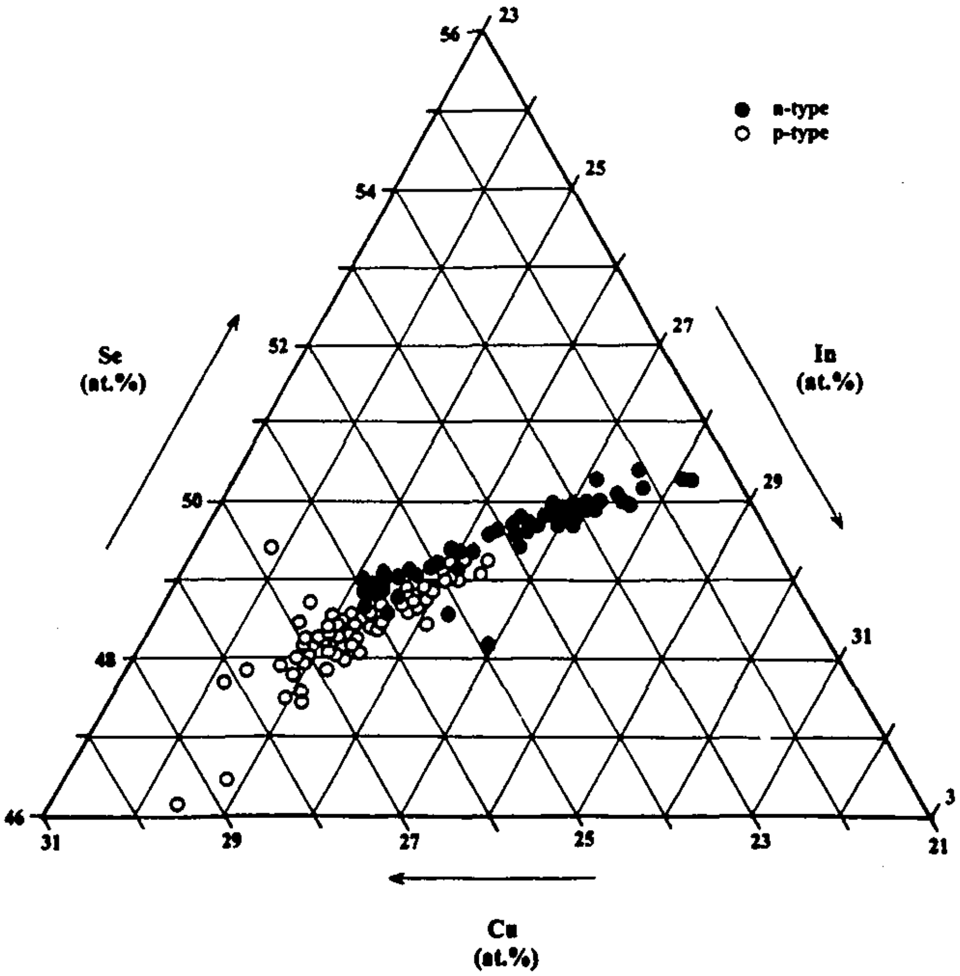

Fig.5.4(a) Ternary composition diagram showing the compositional measurements taken on all eight ingots using the ZAF correction scheme.

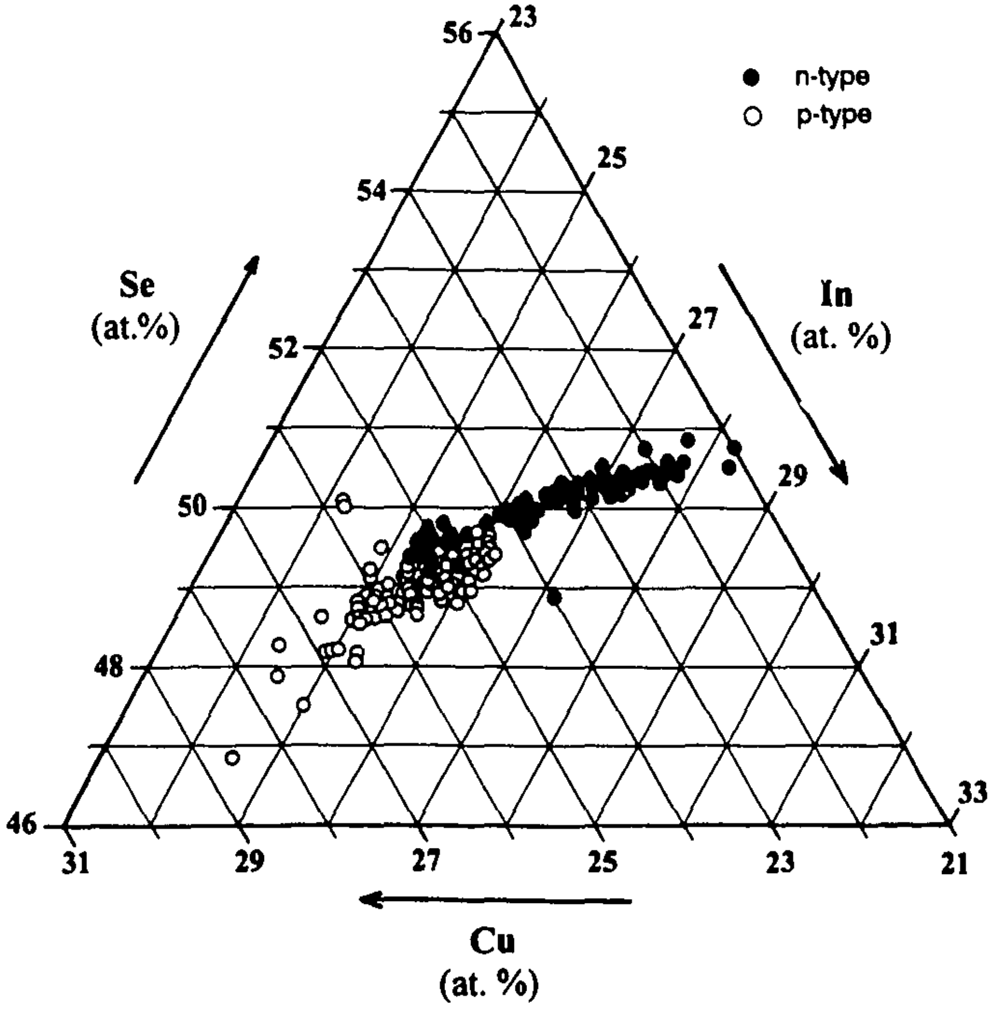

Fig.5.4(b) Ternary composition diagram showing the compositional measurements taken on all eight ingots using the CIT ZAF correction method.

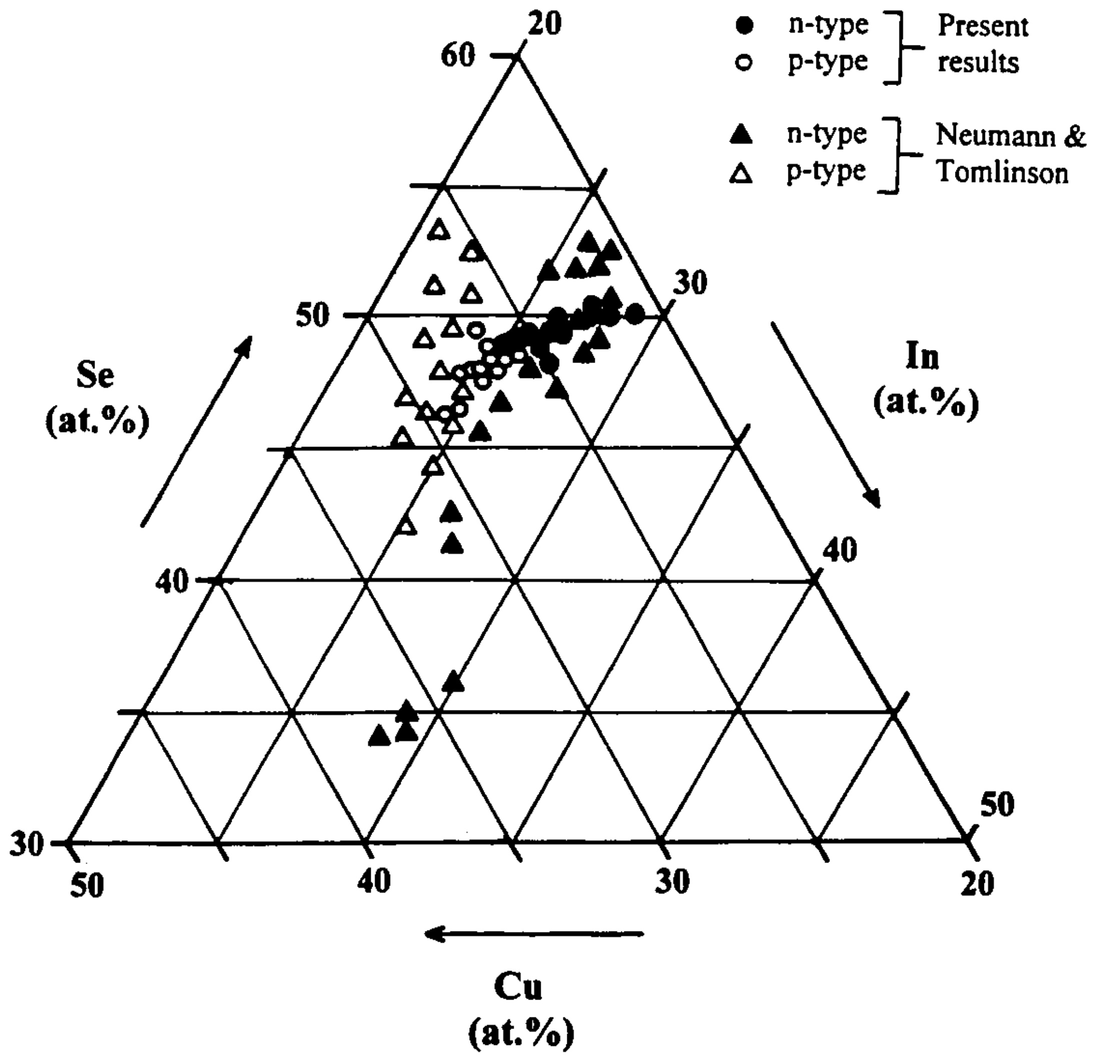

Fig.5.5 Ternary composition diagram shown the present results (circles) plotted along with those of Neumann and Tomlinson (triangles).

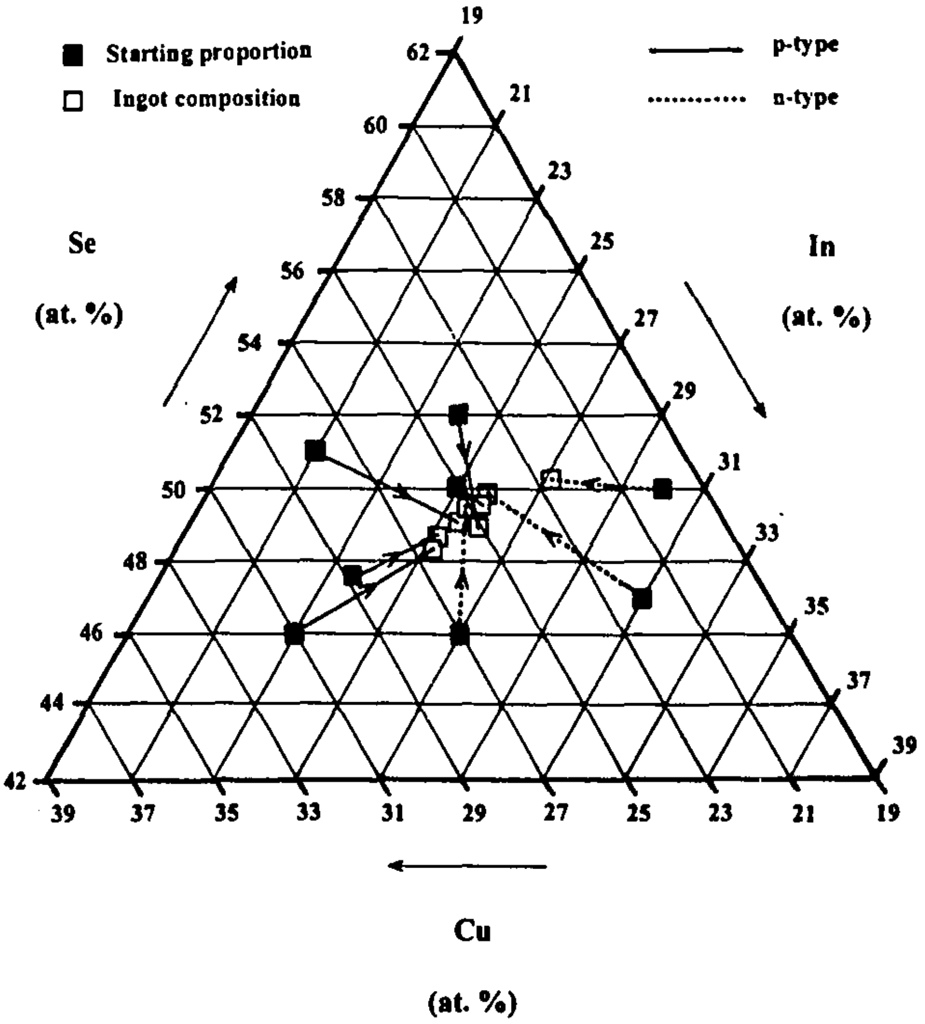

Fig.5.6 Ternary composition diagram showing a plot of the starting compositions of the ingots used in this study along with their final compositions, as measured after growth.

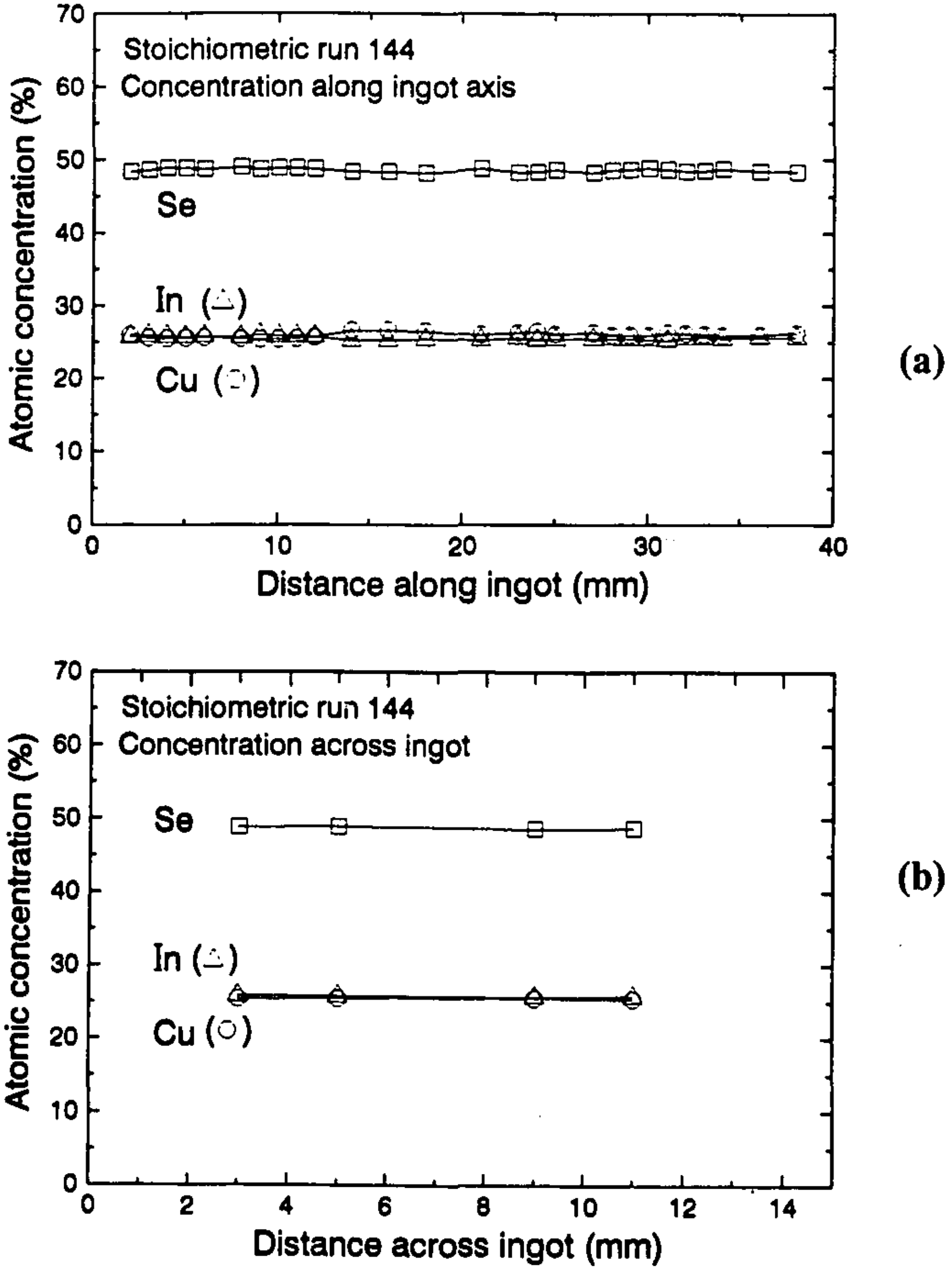

Fig.5.7 Plot of elemental atomic concentration in the stoichiometric ingot 144 (a) against distance along ingot and (b) against distance across ingot.

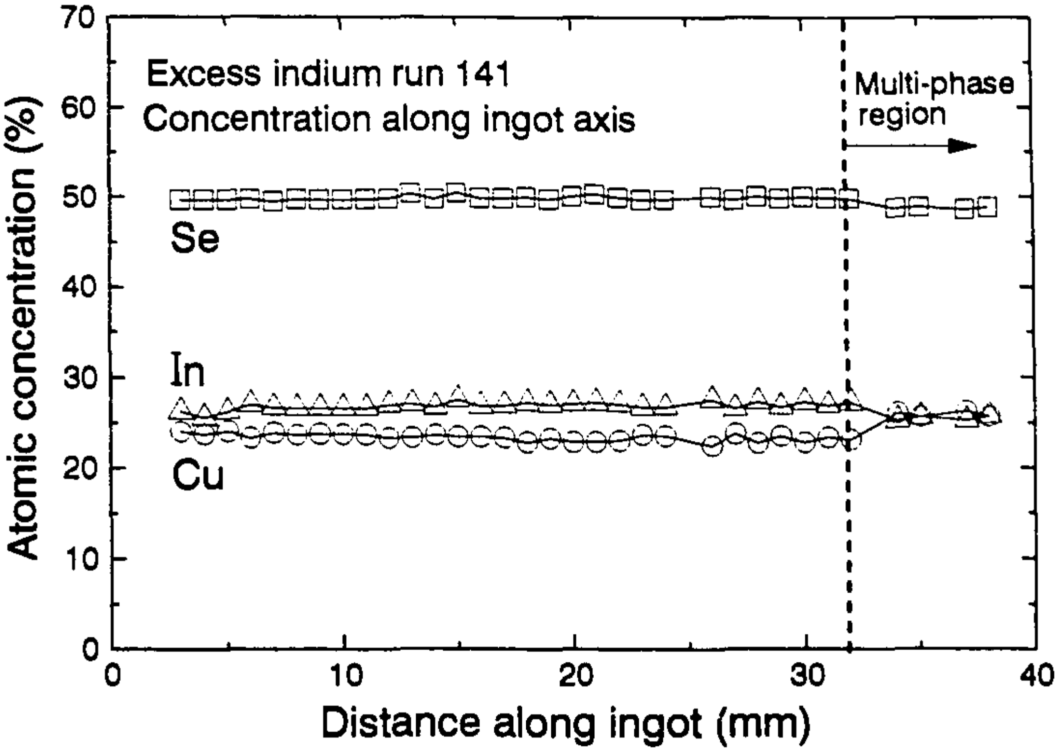

Fig.5.8 Plot of elemental concentration against distance along ingot on the single phase region of ingot 141, with excess indium.

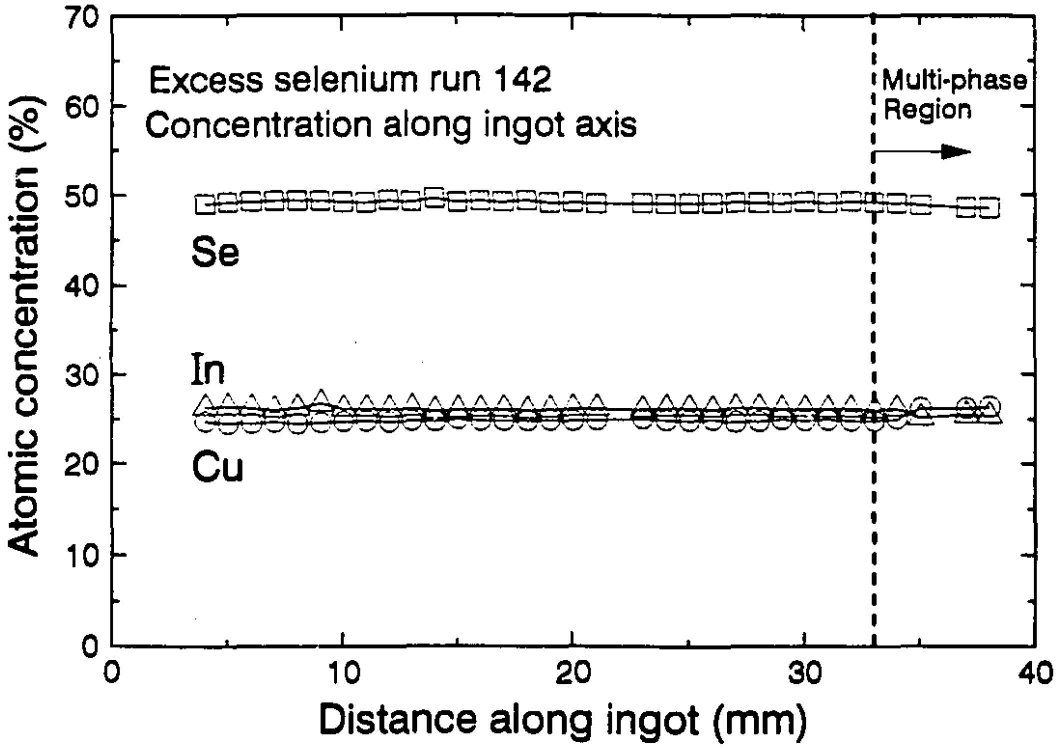

Fig.5.9 Plot of elemental concentration against distance along ingot on the single phase region of ingot 142, with excess selenium.

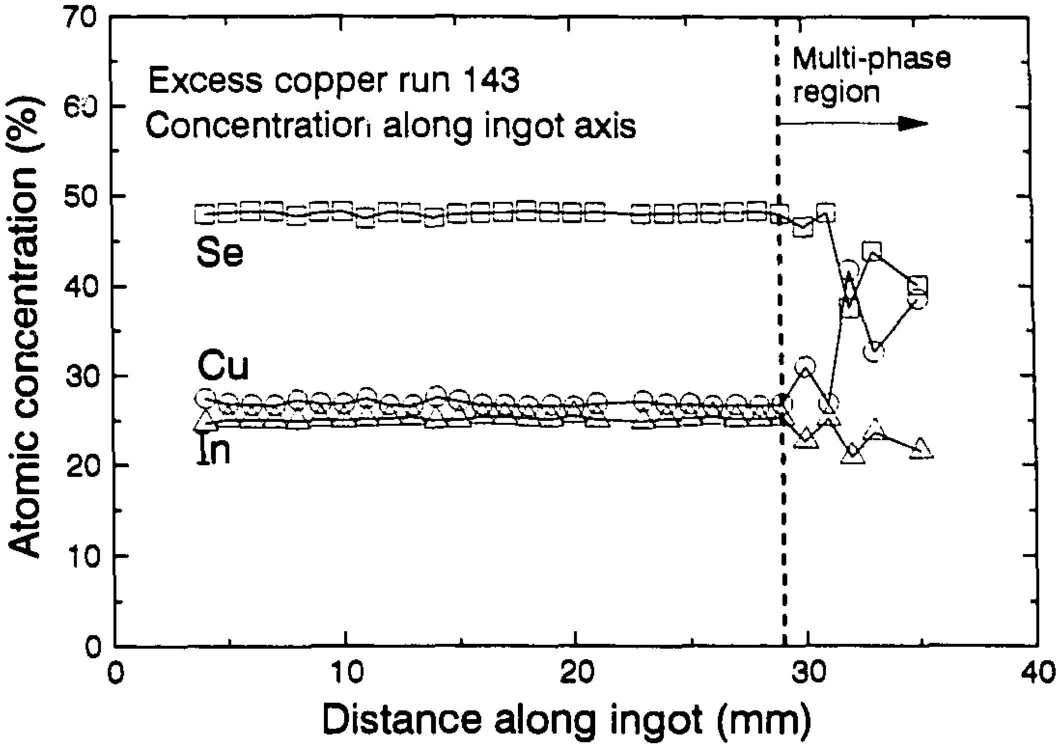

Fig.5.10 Plot of elemental concentration against distance along ingot on the single phase region of ingot 143, with excess copper.

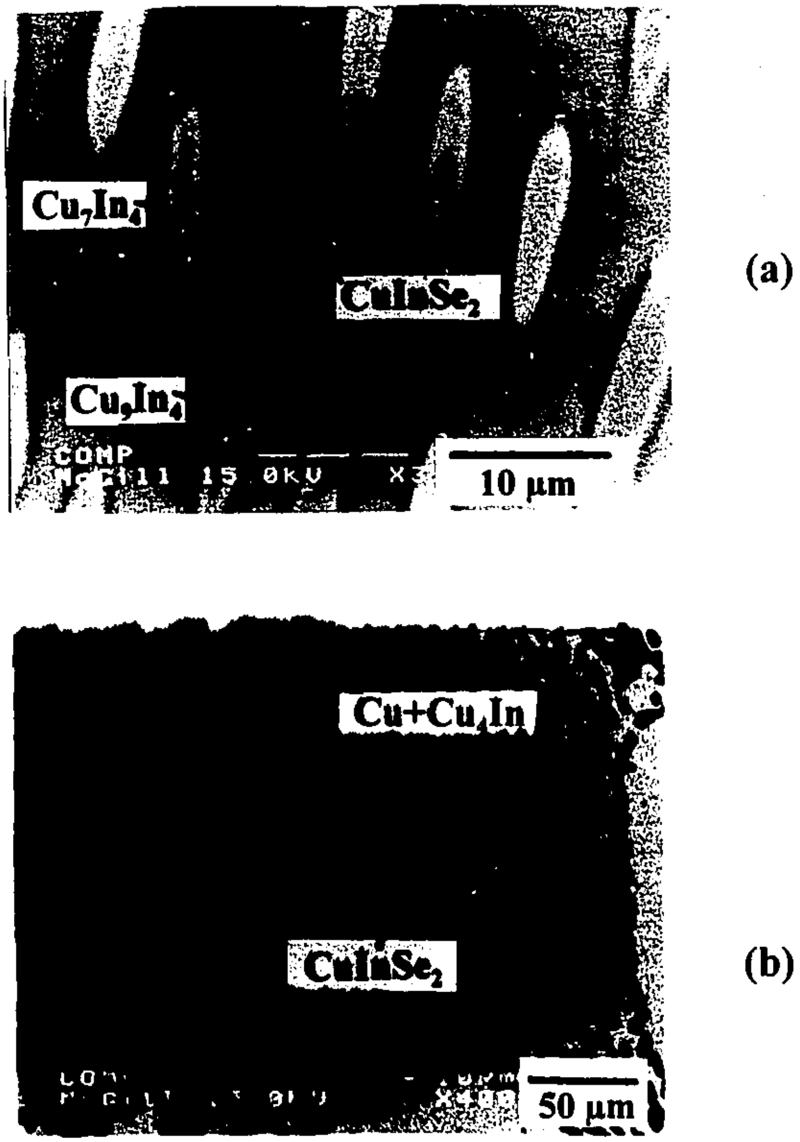

Fig.5.11 Photographs of secondary phases observed in the last region to freeze in (a) ingot 140 with a selenium deficiency, (b) ingot 143 with excess copper.

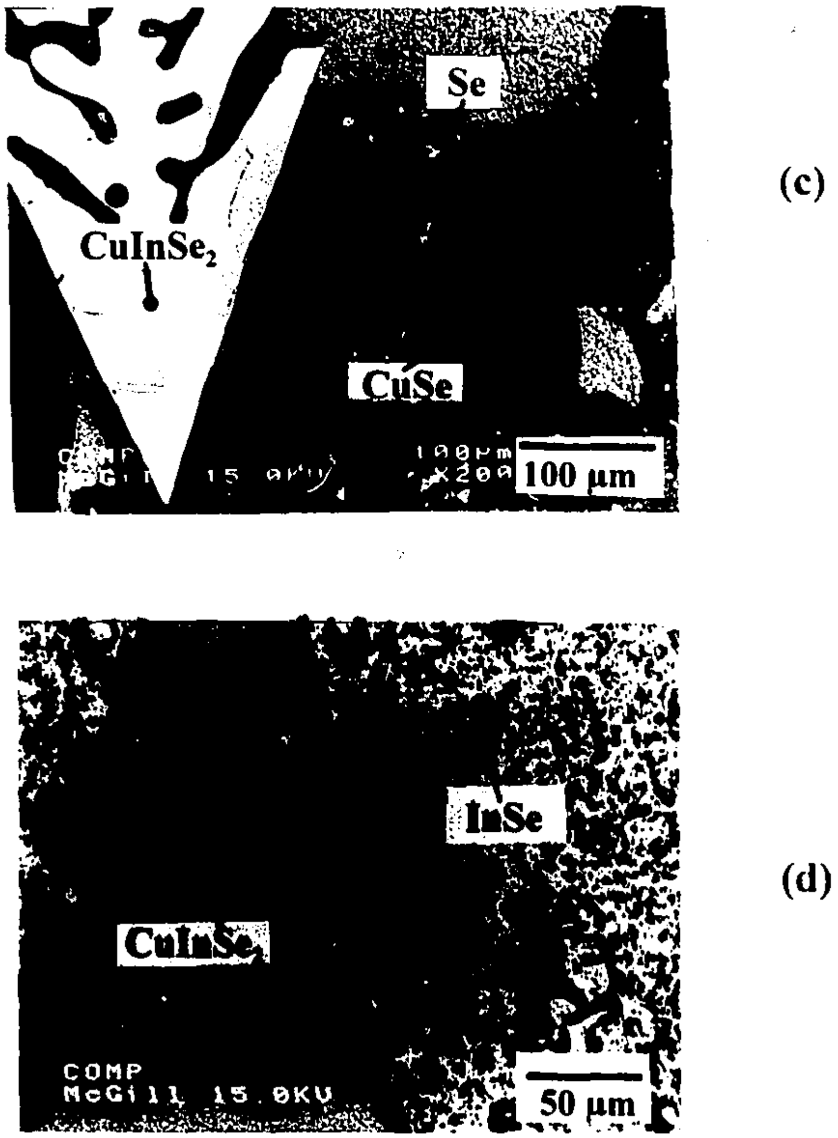

Fig.5.11 (cont'd) Photographs of secondary phases observed in the last region to freeze in (c) ingot 145 with an indium deficiency, (d) ingot 146 with indium excess.

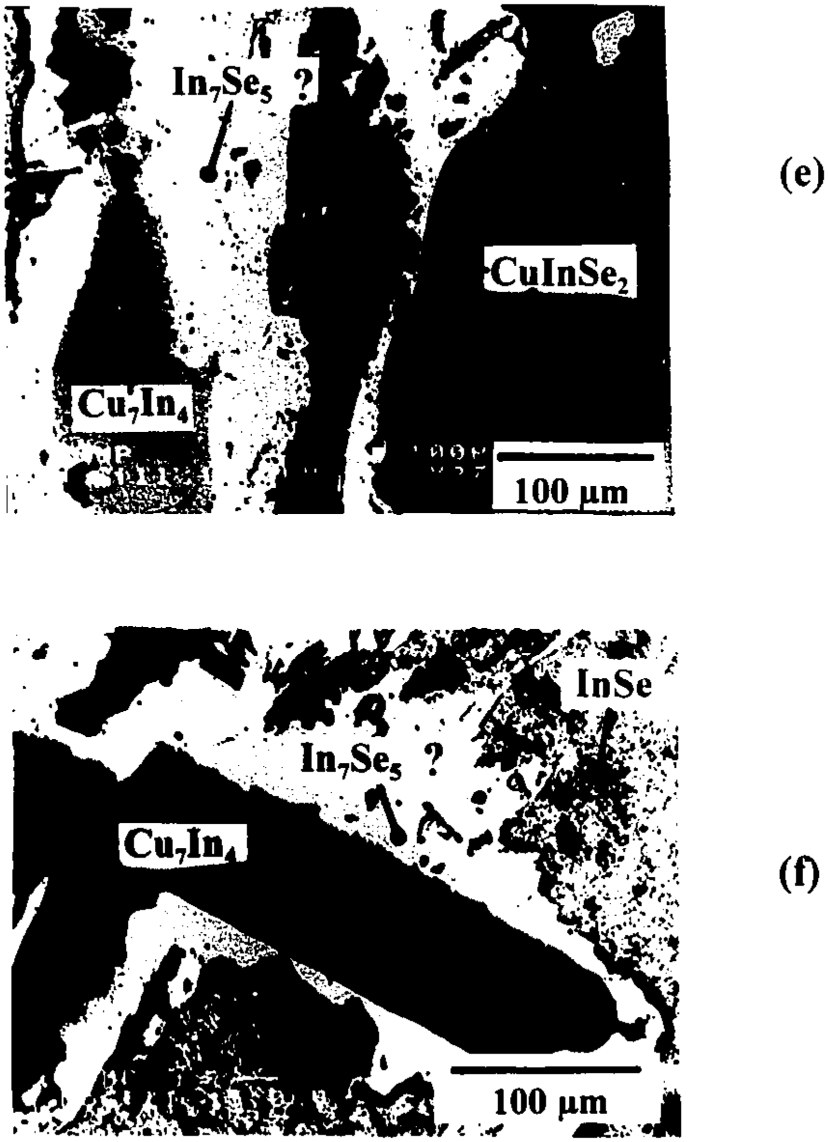

Fig.5.11 (cont'd) Photographs (e) and (f) of secondary phases observed in the last region to freeze in ingot 146 with an excess of indium.

CHAPTER 6

CLEAVAGE AND TWINNING IN $CuInSe_2$ CRYSTALS

6.1 INTRODUCTION

In earlier work, it was reported that $CuInSe_2$ single crystals could be easily cleaved along the {110} plane [6.1], but more recent results have shown that cleavage along the {112} and {101} planes also occurred in $CuInSe_2$ [6.2]. In any case, a detailed study of occurrence and characterization of these planes has not previously been made. Accordingly, a need arose to confirm these results and obtain a more comprehensive specification of all of the common cleavage planes in single crystals of $CuInSe_2$. Work is therefore described, in the first part of this chapter, on the characterization of all of the cleavage planes found in this semiconductor and, in the second part, on the measurement of all of the angles between the cleaved planes. In the final section, work on identification of the twinning plane, commonly occurring in our crystals, is presented.

6.2 CLEAVAGE PLANES

Single crystal samples of $CuInSe_2$ were cleaved by applying gentle pressure at room temperature on opposite ends of a grown ingot, without a particular orientation, using a sharp cutting blade. While this technique was rather primitive, it was possible to obtain cleavage planes ranging from 5 to 100 mm^2 in area. In some of the samples, the applied pressure also resulted in a conchoidal, almost glass- like, fracture which was not helpful for the purpose of this study. Frequently, however, the single crystal ingot cleaved into two pieces, each revealing a macroscopically flat plane.

While many cleaved samples were obtained, only three distinct cleavage planes were identified in the $CuInSe_2$ crystals, namely the {112}, {101} and {110} planes. These planes are shown schematically in the chalcopyrite unit cell, as shaded areas, in Fig.6.1. The chalcopyrite description of the planes assumes a unit cell with a c/a ratio of 2, which is very close to the actual value of 2.006 [1.10]. A photograph showing a top view for each of the three cleavage planes on actual samples is given in Fig.6.2, as observed under an optical microscope. In Fig.6.2(a), it is seen that the cleavage in the {112} plane is essentially flat but exhibits terraces with edges that define angles of 60 or 120° between them. These characteristics are typical of the three-fold symmetry of this plane. The {101} plane, shown in Fig.6.2(b), also exhibits some terracing and is less planar than the {112} surface. The curved nature of the edge of the terraces on the {101} plane distinguishes it from the {112} and {110} planes. The {110} plane, however, has a completely different appearance, as shown in Fig.6.2(c). Here, the clearly visible straight and parallel striations represent parallel V-shaped ridges, as revealed by the SEM photograph in Fig.6.3. It is seen here, that the planes on either side of a ridge are flat and have a constant angle between them, which was measured, as described in the next section, and found to be about 70°. This indicates that the side planes are in fact {112} micro-planes, for which the calculated angle would 70.53°.

Confirmation of the crystallographic orientation of the planes was carried out using X-ray diffractometry, in a Rigaku diffractometer model D/Max-2400 using a copper target. Fig.6.4 shows X-ray diffractograms of the three distinct cleavage planes scanned between 10 and 100° of 2θ, where θ is the Bragg angle. The {112} cleaved sample shows a principal peak (Fig.6.4(a)) at a 2θ value of about 26.51°, corresponding to a lattice d-spacing of 3.359Å, which is in accord with that from powder diffraction data (Appendix A.1). Less intense second and third order reflections from the parallel {224} and {336} planes, with nominal d-spacings of respectively ½ and ⅓ that of the {112} plane, are also observed, where the Bragg condition is also satisfied. It is noted here, that the weak {224} peak, measured on a single crystal surface, is not observed in the diffraction pattern of a powdered sample of this material. Fig.6.4(b) shows similarly the peaks of the cleaved {110} plane. In this trace, the strongest peak corresponds to the {220} plane at a 2θ of 44.18°. The nominal d-spacings of the {220} and {440} planes are respectively ½ and ¼ that of the {110} plane. It is noted that the third order reflection, from the {330} plane, is not apparent in this figure. This is only what would be expected if all the atoms were identical, as in a diamond structure. The diffraction pattern from a cleaved {101} plane is given in Fig.6.4(c). Here, the {101}, {303}, {404} and {505} reflections are observed, with the second order {202} reflection not present. The peaks of this cleavage plane are less intense, by about one order of magnitude, than those of the other two cleavage planes. The splitting of the higher order peaks {336}, {440} and {505} is due to the CuKα_1 and CuKα_2 lines in the incident X-ray beam. Fig.6.5 shows characteristic Laue X-ray reflection photographs of the three cleavage planes, along with schematic diagrams of the corresponding spot patterns. Shown also are the axes of symmetry in each case. Here, it is easy to see that the {112} plane has three such symmetry axes, as indicated by the broken lines in Fig.6.5(a), while the {110} has two (Fig.6.5(b)) and the {101} only one axis of symmetry (Fig.6.5(c)).

6.3 ANGLE MEASUREMENTS

The cleaved $CuInSe_2$ samples exhibited angles where two or three cleavage planes intersected. Since in any known crystal structure, the angles between any two crystallographic planes can be calculated [6.3], a measurement of these angles on actual crystals can be used as a means of identifying the cleavage planes in that crystal system. This assumes, of course, that the angles measured belong to one crystal and also that the method of measurement has sufficient accuracy. Accordingly, on the $CuInSe_2$ crystals grown by the Bridgman method, angles were measured on some 11 separate samples obtained from ingots, having some 22 different angles (edges). In order to measure the angles with sufficient accuracy, a high precision goniometer was used for this purpose, with a He-Ne laser, having a beam width of about 1 mm, as the light source. The arrangement is shown schematically in Fig.6.6. The sample was mounted on the goniometer with the intersection edge of the two cleaved planes in a direction initially perpendicular approximately to the plane of rotation (i.e. in the plane of the page). The sample mounting was then finely-adjusted so that both cleaved planes were aligned perpendicular to the incident laser beam. This was done by continuously adjusting the sample until the light spots of the incident and reflected beams on a glass plate (points A and B respectively) coincided. After this was done on both planes, the angle between them could be properly measured. The measurement was carried out by simply rotating, into position, the first plane so that a reflection was obtained and taking a reading from the goniometer. Then, the goniometer was rotated so that the second plane was brought into position and a second reading was obtained. The difference between the two goniometer readings gave the appropriate angle between the two crystal planes. The distance between the sample and the laser beam was chosen to be some 60 cm, which was large enough so that the reflected beam at B could be accurately adjusted, but at the same time not too large to avoid the spreading out of the reflected spot at B. With this arrangement, an accuracy of about ± 0.1 of a degree in the measured angle was possible. Table 6.1 gives a summary of all the angles measured on all the crystal samples using this method.

In column 1 of the table, the measured angles are shown. As can be seen, only eight unique angles were found from these measurements on the samples (excluding the two 180° between parallel cleavages). The measured angles are compared with their calculated values, given in column 2, where it is evident that there is agreement to within ± 0.1°. The crystal planes that define the individual angles are given in column 3 of the table. In all but one of the cases, the planes defining the angle were identified easily, by comparing the measured angle values with the calculated ones. In the case of the 90.1° angle, it was necessary to identify the crystal planes using a Laue photograph as well as X-ray diffractometry (columns 4 and 5). This is because, a 90° angle also occurs between two {110} planes or between two {101} planes. This can be seen in Table 6.2, where all the possible calculated angles, between the three main cleavage planes, are tabulated. In the case of the 150.3° angle (last row of Table 6.1), no match was found with any calculated crystal angle. A Laue and an X-ray diffraction scan were taken on both planes of this sample and it was revealed that both were {101} planes. While this was puzzling at first, since there is no such angle between two {101} planes in one crystal, it was later found that this angle occurred frequently between {101} planes involving a crystal and its twin. This will be described in more detail in the next section. The frequency of occurrence of all the observed angles is shown in column 6 of Table 6.1. While the total number of samples measured was not large enough to draw any statistical conclusions, it does appear that some 20% of these measured crystal samples contained twinning, as evidenced by the frequency of occurrence of the 150° angle. It is also evident in these results that, occasionally it was necessary to rely on X-ray diffraction to confirm the orientation of the cleavage planes. This, however, should not detract from the usefulness of the measurement of angles for identifying crystal planes, particularly if a large number of samples is involved. Given that there are just the three sets of cleavage planes, the only angle that was not observed in these measurements was the 90° angle between two {110} planes, as indicated in Table 6.2, since only one {110} cleavage plane was obtained.

Fig.6.7 presents a photograph and a schematic of a representative sample exhibiting a well-defined angle of about 90°. This is the same sample listed in row 7 of Table 6.1. The planes defining the angle are the {110} and {112} planes indicated on the schematic in Fig.6.7(a). The {110} plane, on the top side, is seen to be dark, while the {112} plane on the right hand side is shiny. This is due to the effect of lighting on the sample. The angle itself is better seen in Fig.6.7(b), where a view of the same sample from a perspective parallel to both cleavage planes is shown. Here, the reader may use a protractor to verify the 90° value of the angle. In the next section, results specifically on twinning are presented.

6.4 TWINNING

In this section, results are reported specifically on the observation of a twinning plane in crystals of $CuInSe_2$. Three single crystal samples with cleavages along the {112}, {110} and {101} planes were studied and found to reveal twinning. Laue photographs were used to examine the orientation of twinned regions in these crystals. From these measurements, it was determined that the twinning plane observed in these $CuInSe_2$ samples, was in fact a {112} plane. No other twinning plane was found in this study.

Twinning was detected visually, in this study, by properly orienting the cleaved or polished sample under a collimated light source, revealing shiny and dark regions exhibiting straight edges. Fig.6.8, shows two photographs of the sample indicated in the last row of Table 6.1. This sample exhibited a twin, which is seen clearly in Fig.6.8(a), as a dark band in the central part of the crystal. The main crystal appears bright due to light reflecting from the cleaved plane, which happens to be a {101} plane. In fact, the crystal exhibits two cleavages on either of its sides. The darker surface of the twinned region is also cleaved in a {101} plane and makes an angle of 150° with that of the main crystal. A side view of this sample reveals how this 150° angle occurs, as shown in Fig.6.8(b). It is seen that by proper lighting, twins in crystals can be detected easily.

6.4 (a) Twins Observed with a {112} Cleaved Surface

In order to reveal the crystallographic orientation of the twinned crystals, the X-ray back-reflection Laue method was used for this purpose. Fig.6.9 shows a photograph of a crystal with a large {112} cleavage plane. The cleavage plane consists of two regions separated by a ridge, a larger upper region, called crystal A, and a smaller lower region, crystal B. The lower portion of the cleavage plane represents a twinned crystal and is shown as the shaded area in the schematic of Fig.6.9(b), while the upper portion, crystal A, is shown unshaded. In the photograph, while the {112} cleavage planes of crystals A and B appear similar, the exterior surfaces of the crystals show a different reflection of light. Crystal B exhibits a shiny narrow band which stretches along the entire ingot exterior parallel to the cleavage plane, while crystal A has a darker appearance. This is also shown schematically in Fig.6.9(b). The orientation of the {112} cleavages of crystals A and B are different. Two Laue photographs were taken on the {112} cleavage, as shown on the schematic, as Laue A and Laue B. The Laue pictures are shown in Fig.6.10. with a schematics of the spot patterns. A close examination of the two schematics reveals that the spot pattern of Laue B can be generated by a rotation of that of Laue A, about an axis normal to the page, of 180°. This is emphasized by the large arrows on the two schematics. This shows that twinning in this crystal occurs parallel to the {112} plane. This fact was also evident in Fig.6.7(b), shown earlier, where a twin plane indicated on the schematic is also shown to be parallel to a cleaved {112} plane in that sample.

6.4 (b) Twins Observed with a {110} Cleaved Surface

Fig.6.11(a) shows a photograph of a sample with a {110} cleaved plane. This sample also exhibits twinning as shown in the photograph and indicated schematically by the shaded and unshaded areas in Fig.6.11(b). The main part of the crystal, labelled crystal A, appears bright in the photograph. The twinned crystal, labelled crystal B, consists of a horizontal slice seen at the upper part of the sample with a darker appearance. This is the shaded region in the schematic. The twinning {112} plane, in this case, is perpendicular to the plane of the page. In the middle part of the sample, a second twinned region is seen as a narrow line segment, which makes an angle of about 70° with the horizontal edge of the twinned crystal at the top of the sample. This is an angle between the two {112} twinning planes oriented perpendicular to the page. The orientation of the {110} cleavages, in the plane of the page, of crystals A and B is shown by the two Laue photographs given in Fig.6.12. Here, it is seen that, in going from Laue A to Laue B, the twinning has resulted in a rotation of the projection plane of the spots. This rotation is about an axis indicated on the two schematics by the chain lines. The angles between this axis and the axes of symmetry of both crystal A and B (θ_1 and θ_2 respectively) are the same, and have a value of about 55°. This angle occurs between a {112} plane and a <110> direction. A closer look at the actual interface between the two twins (Fig.6.13), shown by the photomicrograph, indicates that the <110> direction of the ridges in each crystal makes the same angle of about 55° with the {112} twinning plane, perpendicular to the plane of the page.

6.4 (c) Twins Observed with a {101} Cleaved Surface

Fig.6.14, shows a sectional view of a twinned sample. The view here shows clearly the two crystal regions. These regions are labelled crystal A and crystal B in the schematic. The boundary of the twinning {112} plane is also quite evident, as the oblique straight line, again perpendicular to the plane of the page. The top edge of the sample represents the location of the cleavage planes. In this case, both crystals were cleaved along the {101} plane, as indicated by the schematic, perpendicular to the page. Resulting from the twinning, the cleaved planes make an obtuse angle of about 150° between them. This is the same anomalous angle mentioned earlier in Table 6.1. However, it is easy to understand here, how this comes about. The twin plane, being a {112} plane makes an angle of 75.04° with each of the {101} cleavage planes. Therefore, the total angle is twice that, giving a value of 150.08°. Laue photographs were taken on the cleaved {101} planes of both crystals A and B, as indicated by the arrows in the schematic of Fig.6.14(b), to reveal their respective orientations. Here, in order to have the X-ray beam normal to the sample surface in each Laue exposure, the sample had to be rotated by some 30° about an axis (not shown) parallel to the line of intersection of the {101} cleavage planes. The resulting spot patterns are shown in Fig.6.15(a) and (b). Again it is seen here that, the pattern of Laue B can be obtained from that of Laue A by a simple rotation about the indicated horizontal axis by 180°, confirming that the two regions are indeed twinned crystals. The angles, θ_1 and θ_2, between the rotation axis and the symmetry axis of each pattern are again equal.

6.5 TWINNING MODEL

Fig.6.15 shows a photograph of a ball and stick crystal model of a twin in a $CuInSe_2$ crystal along with its schematic. Here, the solid line on the schematic indicates where the twinning plane occurs. The dashed arrows in each of the two crystals, are the <110> directions and the angle between either of these directions and the {112} twinning plane is 54.74°. It is seen here that, in going across the twinning plane, from crystal A to crystal B, the order of the apparent "long" and "short" bonds reverses. If the two crystals were separated at the twin plane, and one was rotated by 180° about an axis perpendicular to the twinning plane, the twinning would be eliminated.

6.6 DISCUSSION

The work in this chapter clearly confirms that the principal cleavage planes in $CuInSe_2$ are the {112}, {101} and {110}. While the {112} and {101} cleavage surfaces appeared mirror-like and were essentially flat, the physical surface of the {110} plane, by contrast, consisted of V-shaped ridges or grooves, where the planes on each side of the ridge are {112} planes. The {101} planes showed parallel terracing with edges having no special direction, while the {112} planes, on the other hand, showed less parallel terracing but with edges exhibiting triangular patterns having 60° angles between them. It is important to point out that these planes were the ***only*** cleavage planes found in these Bridgman-grown crystals and that other low index planes, such as for example the {100}, {111} or {221} planes were not observed. The fact that two expected angles were not observed (Table 6.2) must be due to the relative infrequency of the {110} cleavage plane.

In silicon and germanium, having the diamond structure, the {111} plane is the predominant cleavage plane [6.4],[6.5], due most likely to its low density of bonds. By contrast, for III-V compounds such as GaAs [6.4],[6.6],[6.7],[6.8] and CdTe [6.4],[6.9],[6.10], a II-VI compound, all crystallizing in the zincblende structure, the most common cleavage plane is not the {111}, but the {110} plane. In these compounds, the bonds across the {111} plane are not purely covalent but have also an ionic character due, in the case of GaAs for example, to opposite ionic charges on the Ga and the As atoms, thereby giving rise to a coulombic attraction in addition to covalent bonding between consecutive {111} planes. This renders cleavage along this plane less likely than in the diamond structures. In the chalcopyrite $CuInSe_2$, the {112} plane layers consist of alternating Se (group VI) layers and metallic layers of Cu and In (groups I and III respectively), as indicated in Fig.6.17(a). The extent of the ionic nature of the bonds between the metal and Se layers in this plane, averaged over a large area, could be less effective than in the case of the zincblende and thus, the {112} cleavage in the chalcopyrite occurs more readily. The opposite may be true however, for the case of the {110} plane. In this plane for the zincblende materials, there are equal numbers of Ga and As atoms (in GaAs for example), making this plane on the average electrically neutral. In the case of the chalcopyrite lattice however, the Cu and In atomic positions alternate across this plane (Fig.6.17(b)) and hence there would still be some localized coulombic attraction between consecutive {110} planes. The observed ridged structure of the {110} surface in this chalcopyrite material is due to small zig zag {112} micro-cleavages, cutting across the tetrahedral bonds as shown by the lower dashed line in Fig.6.17(b). As a result, in the $CuInSe_2$ crystals, the {110} "cleavage" may not be a true cleavage, but one where the real surface consists of ridged {112} microcleavages.

The {101} plane has been previously reported to be a cleavage plane in natural crystals of the chalcopyrite mineral $CuFeS_2$ [6.4],[6.11] as well as in $CuInSe_2$. However, to the author's knowledge, there are no reports of such a cleavage plane in either the diamond or the zincblende structures, where the corresponding cubic description of this plane would be {201}. Accordingly, the question is raised: why is the {101} plane a predominant cleavage plane in the chalcopyrite structure and, furthermore, why is it even more evident than the {112} plane in the $CuInSe_2$ crystals? Fig.6.18 shows a view of a $CuInSe_2$ lattice, where the {101} planes are perpendicular to the paper. Shown also are the depth layers of the atoms below the {010} plane of the page, where the surface atoms are vertically above those in the 4th layer. Within the unit cell of size **a** x **a** x **2a**, where **a** is the length of the cell smaller side, a {101} plane, perpendicular to the paper has been marked by the broken line between the Se and the In atoms. Counting the number of bonds involved, indicates that a cut along this plane has to break eight of the short tetrahedral bonds to separate the cell into two parts; six of these are Se-In bonds, while two are Se-Cu bonds. Since the Se-In bond is weaker (59 kcal/mole in a diatomic molecule) than the Se-Cu bond (70 kcal/mole) [6.12], such a cut would require less energy per unit area than a parallel cut between the Se and Cu atoms. In comparison with the {112} plane, cleavage along this {101} plane would at first seem more favourable, since this cleavage encounters 75% of the weaker Se-In bonds, while a {112} cleavage encounters only 50% of these bonds. However, the density of bonds per $\mathbf{a}^2$ is greater by 55% than that in the {112} plane, which reverses the total energy ratio in favour of a {112} cleavage. Therefore a more detailed calculation of the energies involved is needed.

In the case of the zincblende lattice, however, a corresponding {201} cut would also require the breaking of 8 bonds per cell but here, the bonds would be of equal strength, so that there would not be a weaker link involved. As a consequence, the easier splitting between the neutral {110} planes would be preferred. It should be pointed out here, that these qualitative considerations are purely speculative and in no way can they substitute for detailed quantitative calculations of least energies between parallel planes of the atoms involved. Such calculations lie outside the scope of this study.

Regarding the X-ray diffractograms, besides confirming the orientation and yielding the correct d-spacing for the different planes, the results also indicated that certain reflections, which are absent in polycrystalline samples, were present in the single crystal samples and these were the {224} reflection from the {112} cleavage plane, the {110} and {440} from the {110} cleavage plane and the {303} and {404} reflections from the {101} plane. In the last two cleavage planes, two reflections were missing and these were the {330} from the {110} cleavage and the {202} from the {101} sample. It is possible that the intensities of these reflections were too weak to detect, particularly since the {202} reflection has been observed on samples, not presented in this study. In the case of silicon, certain reflections are expected to be missing because they are "forbidden", since they have a zero geometrical scattering factor. However, unlike the diamond structure, where all the atoms are identical, the chalcopyrite structure has three different atom types with different atomic scattering factors (due to the different atomic numbers of 29, 49 and 34 for Cu, In and Se respectively), and therefore weak reflections might be expected. As a result, the {110} reflection, forbidden in diamond, was detected as a weak line in these $CuInSe_2$ crystals.

In respect of the observed twinning in the {112} plane in $CuInSe_2$, while it is the first reported study on this material, the result is not different from the case of silicon [6.13], GaAs or CdTe [6.9], where twinning occurs along the equivalent {111} plane in these materials. In the chalcopyrite material $AgGaS_2$, twinning was also reported along the {112} plane [3.9]. This comes back to the face-centred-cubic lattice, on which the diamond, zincblende and the chalcopyrite structures are based, where twinning occurs along the {111} plane. However, it is reported that twinning is also possible along the {112} *cubic* plane, at least in silicon [6.13] but it is thermodynamically less favourable, compared with the {111} plane, for twinning.

Table 6.1

Angle Measurements between Cleavage Planes in $CuInSe_2$ Crystals [1]

Angle (deg.) Measured[2]	Angle (deg.) Calculated[3]	Defining Planes {hkl} - {hkl}	Plane Identification[4] Laue	Plane Identification[4] XRD	Angle frequency[5]	Comments
39.4	39.23	{112}-{101}	on both planes	on both planes	2	
50.8	50.77	{110}-{101}	{110}	{110}	2	
53.3	53.14	{101}-{101}	both	both	2	
70.5	70.53	{112}-{112}	both	both	1	
75.0	75.04	{112}-{101}	{112}	both	3	
78.6	78.46	{101}-{101}	both	both	3	
90.1	90.0	{112}-{110}	both	{110}	2	A 90° angle was not observed between {110} planes.
180.1	180.0	{112}-{112}	both	-	1	Parallel {112} cleavage.
180.2	180.0	{101}-{101}	both	-	1	Parallel {101} cleavage.
150.3	None!	{101}-{101}	both	both	5	Angle between twin crystals.

1. Only those angles between planes having a common edge are included. Total number of angles (edges) measured was 22. Total number of samples was 11.
2. Accuracy of measurement is about ± 0.1 degree.
3. Assuming the chalcopyrite unit cell has a c/a = 2.
4. Measurement was carried out to confirm the crystallographic plane provided the cleavage was large enough.
5. Number of samples measured with this particular angle.

Table 6.2

Calculated Angles between Principal Cleavage Planes in $CuInSe_2$

Cleavage Planes[1] {hkl}-{hkl}	Calculated Angle(s)[2] (degrees)	Observed[3] (Y/N)
{112}-{112}	70.53	Y
{112}-{101}	39.23 75.04	Y Y
{112}-{110}	35.26 90.00	Y[4] Y
{101}-{101}	53.13 78.46	Y Y
{101}-{110}	50.77	Y
{110}-{110}	90.00	N

---

1. Only the {112} {101} and {110} chalcopyrite crystal planes are listed here.
2. Assuming the c/a ratio to be exactly 2 in the chalcopyrite unit cell for $CuInSe_2$.
3. Indicates whether or not the angle was observed in this study. (Y: observed; N: not observed).
4. Observed between the {110} surface and the {112} microcleavage ridges.

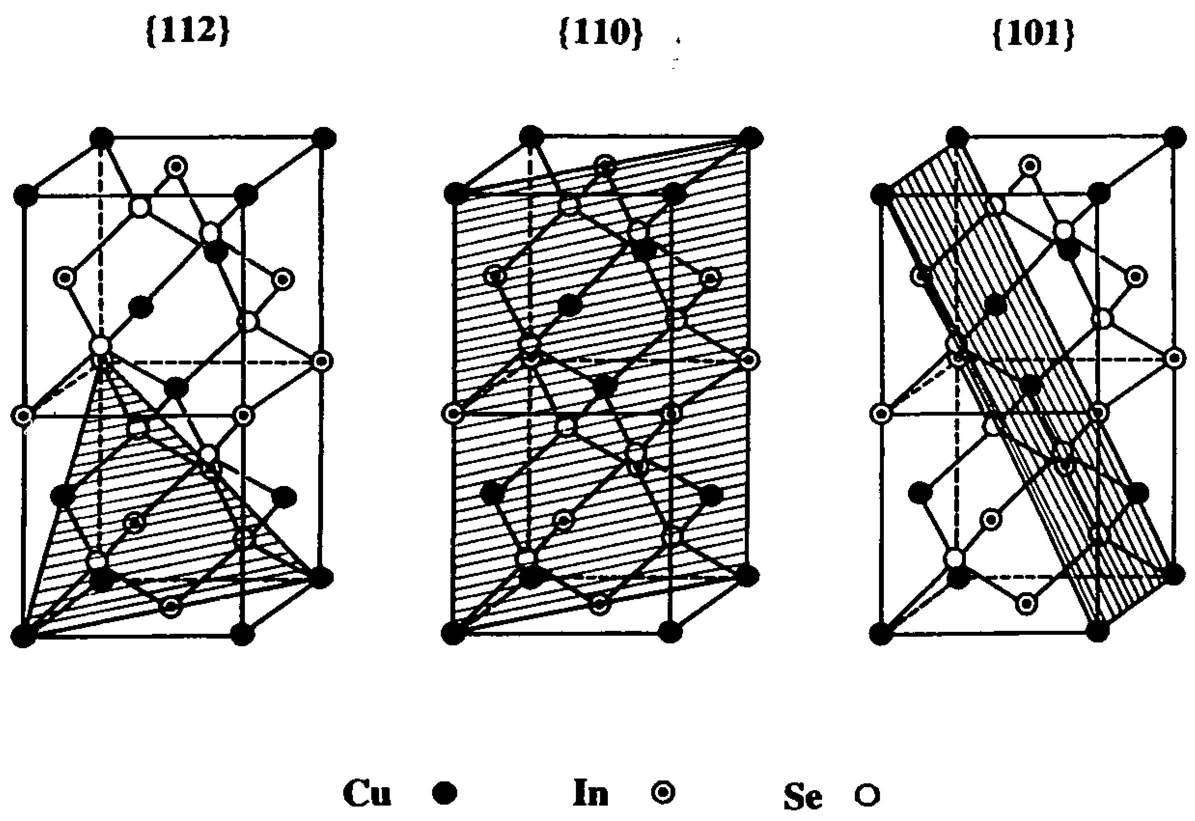

Fig.6.1 Chalcopyrite unit cell schematic diagrams, indicating the three principal cleavage planes: {112}, {110} and {101}.

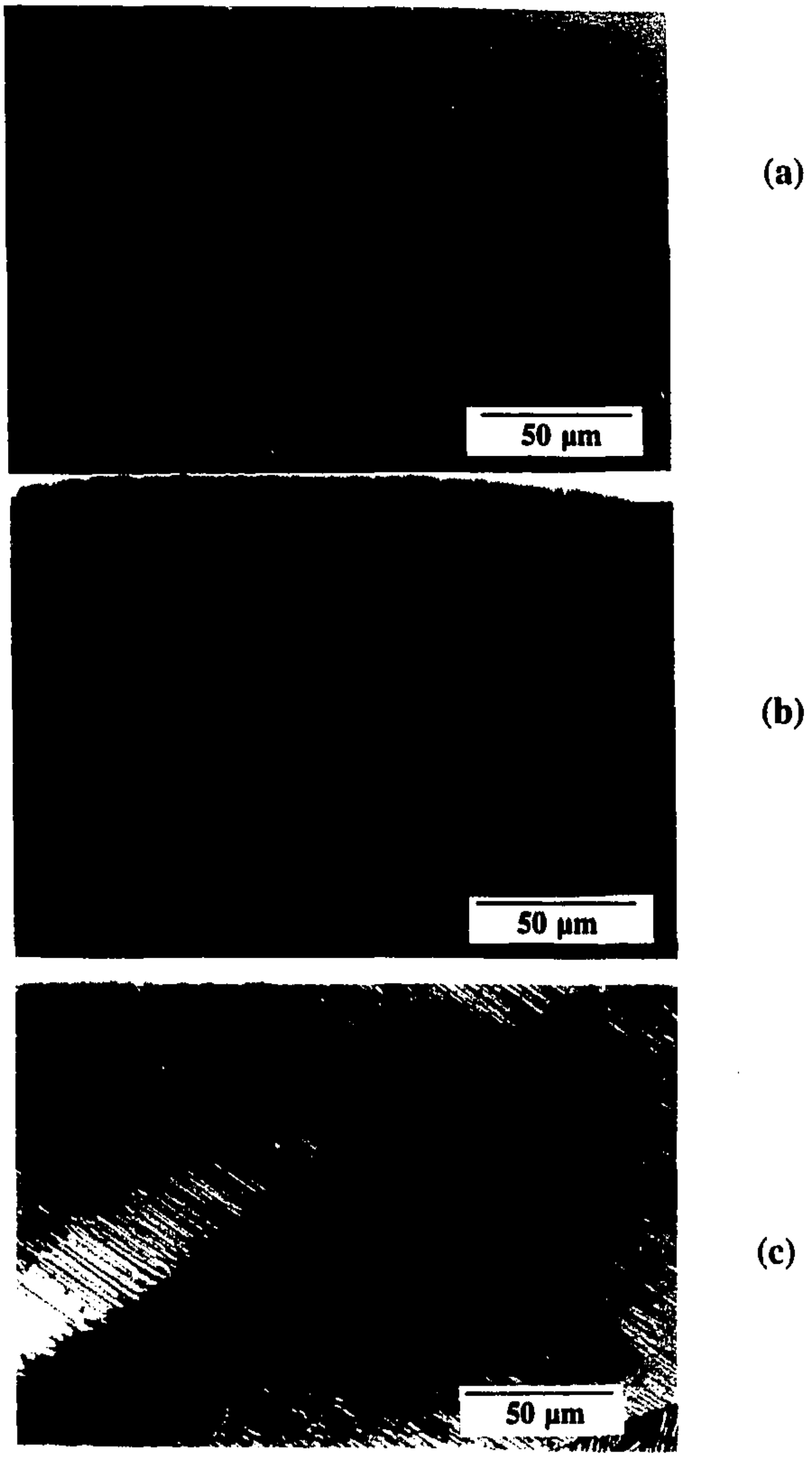

Fig.6.2 Photomicrographs of cleavage planes in $CuInSe_2$ crystals revealing surface features of the planes (a) {112}, (b) {101} and (c) {110}.

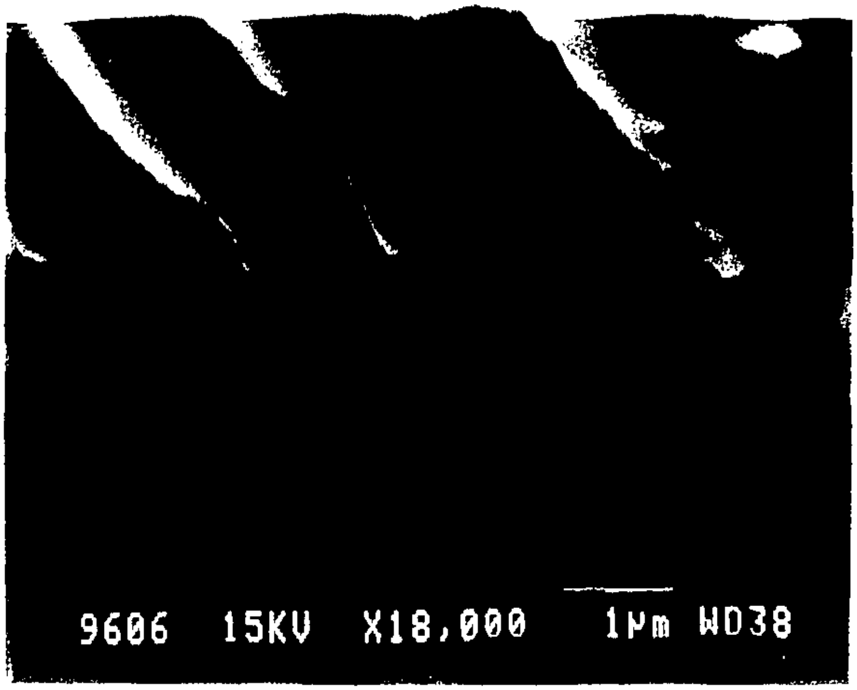

Fig.6.3 SEM photograph of the {110} plane, showing the parallel ridges pointing in a <110> direction.

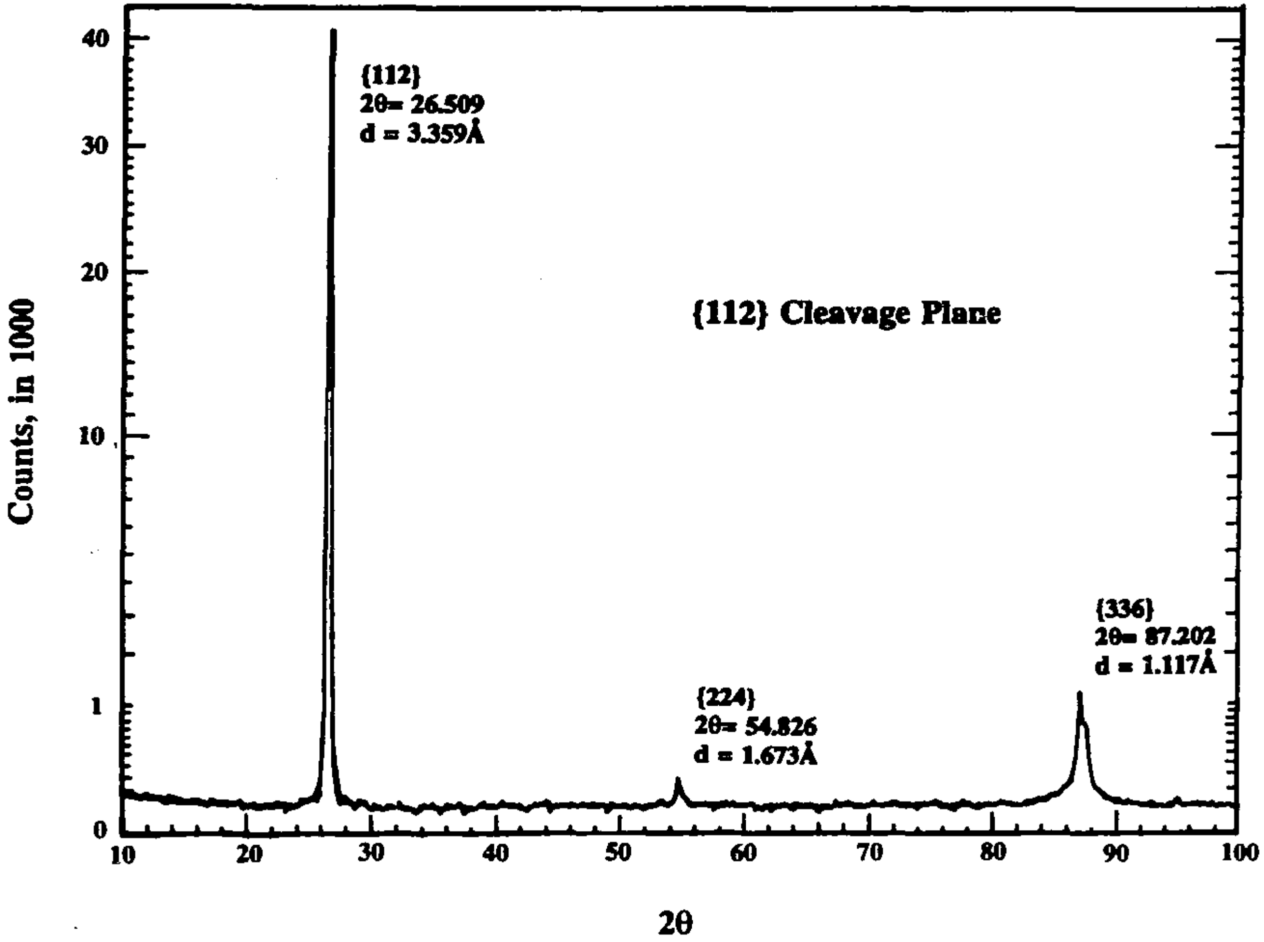

Fig.6.4(a) X-ray diffraction scan of the {112} cleavage surface in $CuInSe_2$, showing an intense peak from the {112} plane and weaker peaks from the {224} and {336} planes. Note that the ordinate is a square root scale.

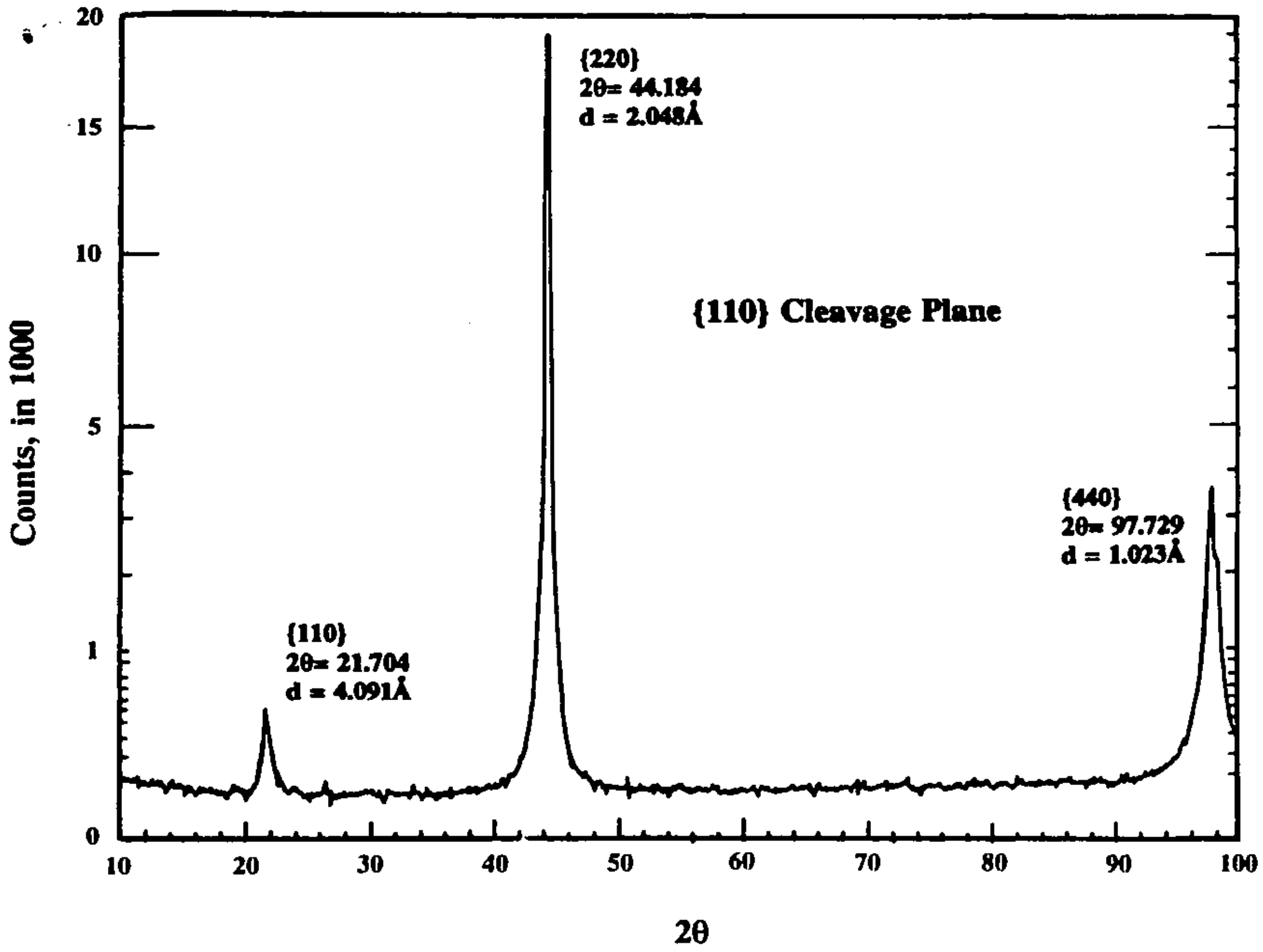

Fig.6.4(b) X-ray diffraction scan of the {110} cleavage surface in CuInSe$_2$, showing a strong {220} peak with weaker {110} and {440} peaks. The ordinate is a square root scale.

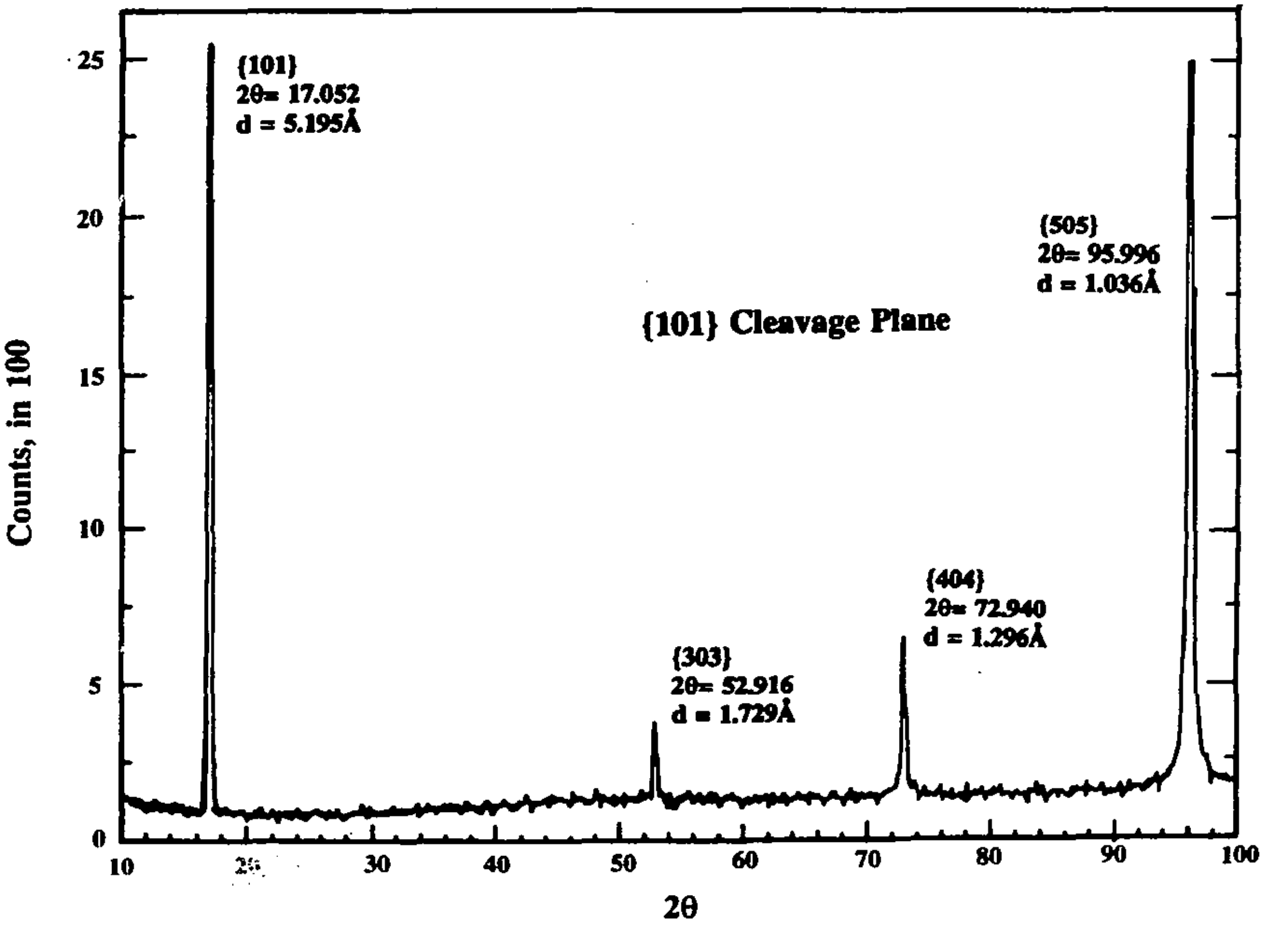

Fig.6.4(c) X-ray diffraction scan of the {101} cleavage surface in $CuInSe_2$, showing {101}, {303}, {404} and {505} reflections. The ordinate is a linear scale.

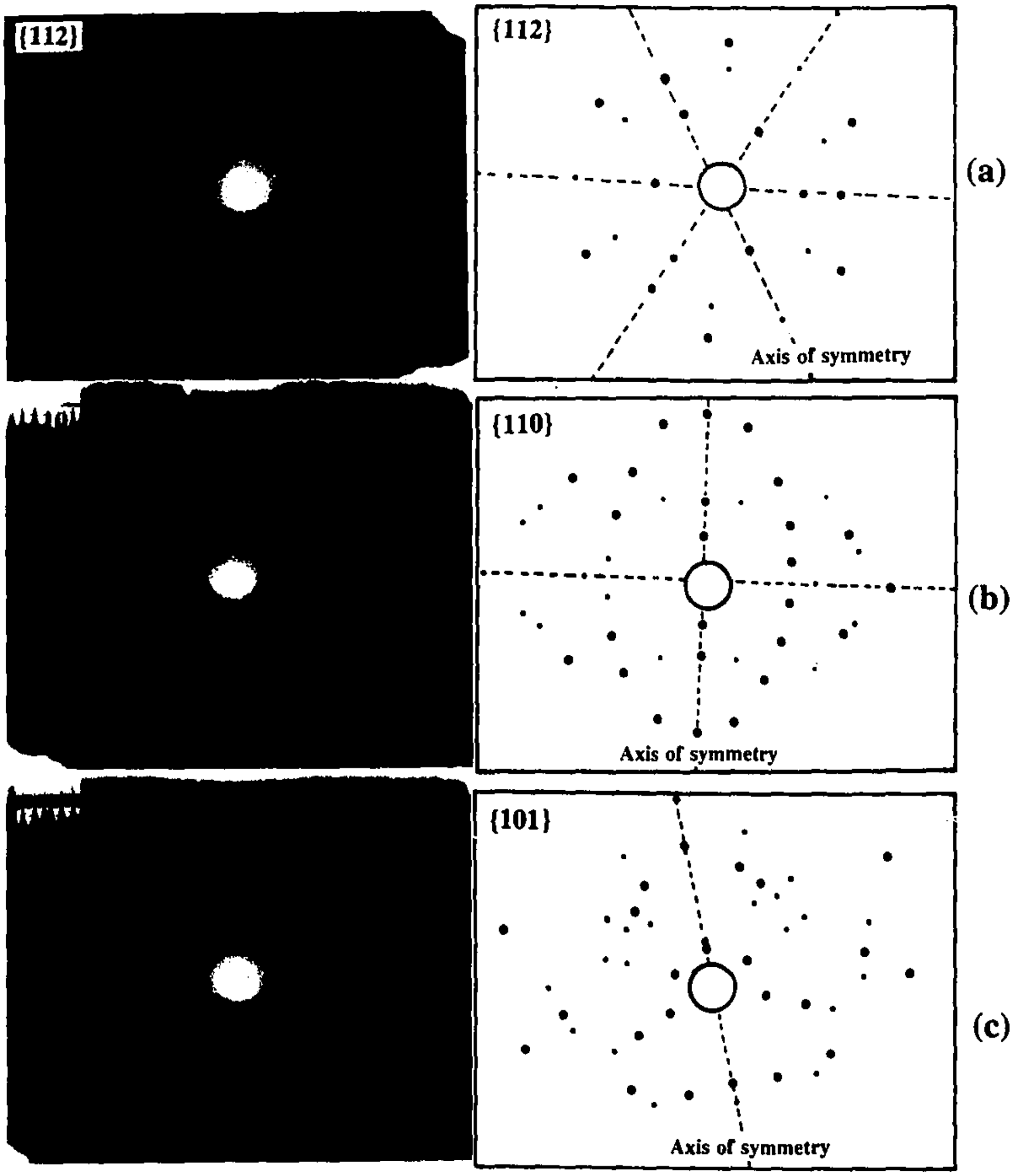

Fig.6.5 Characteristic Laue X-ray reflection photographs of the three cleavage planes in CuInSe$_2$, shown with schematic diagrams of the reflected spot patterns for (a) the {112} plane, (b) {110} plane and (c) the {101} plane. The dashed lines indicate the axes of symmetry in the spot patterns. The smaller spots in the schematics represent faint reflections in the photographs.

Angle Measurement Setup

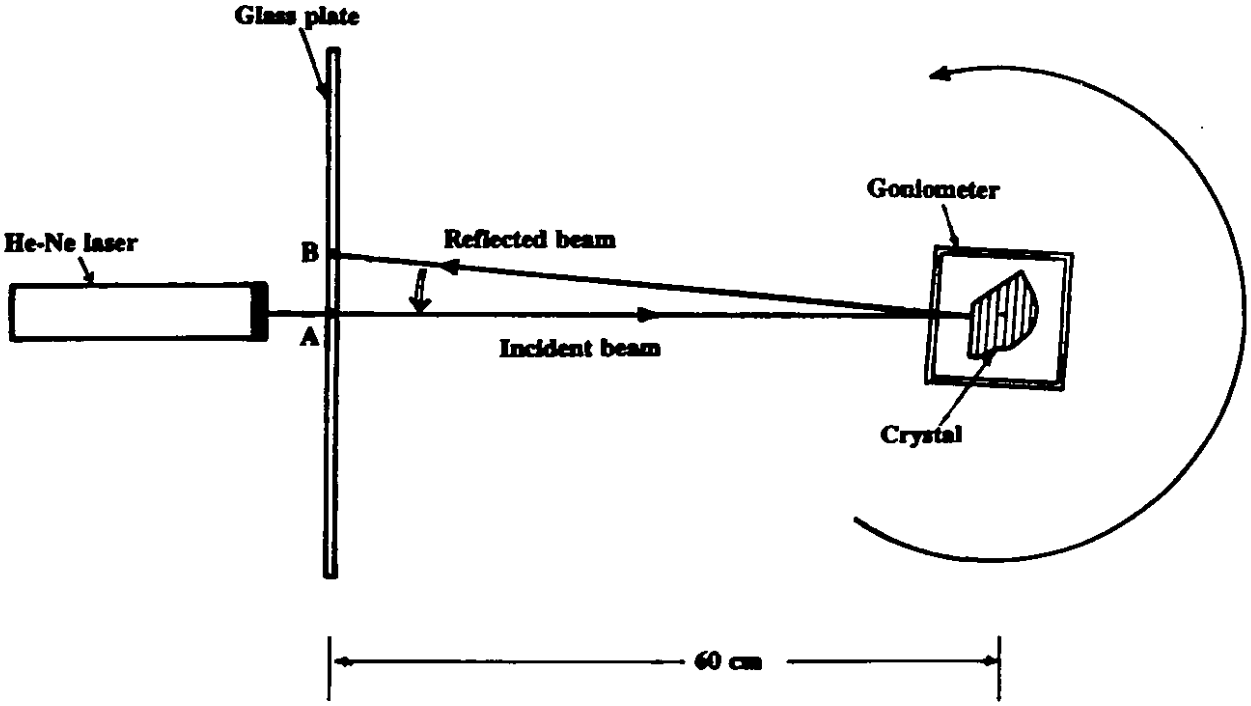

Fig.6.6 Schematic diagram of the arrangement used in the measurement of angles between cleaved planes in $CuInSe_2$ single crystals.

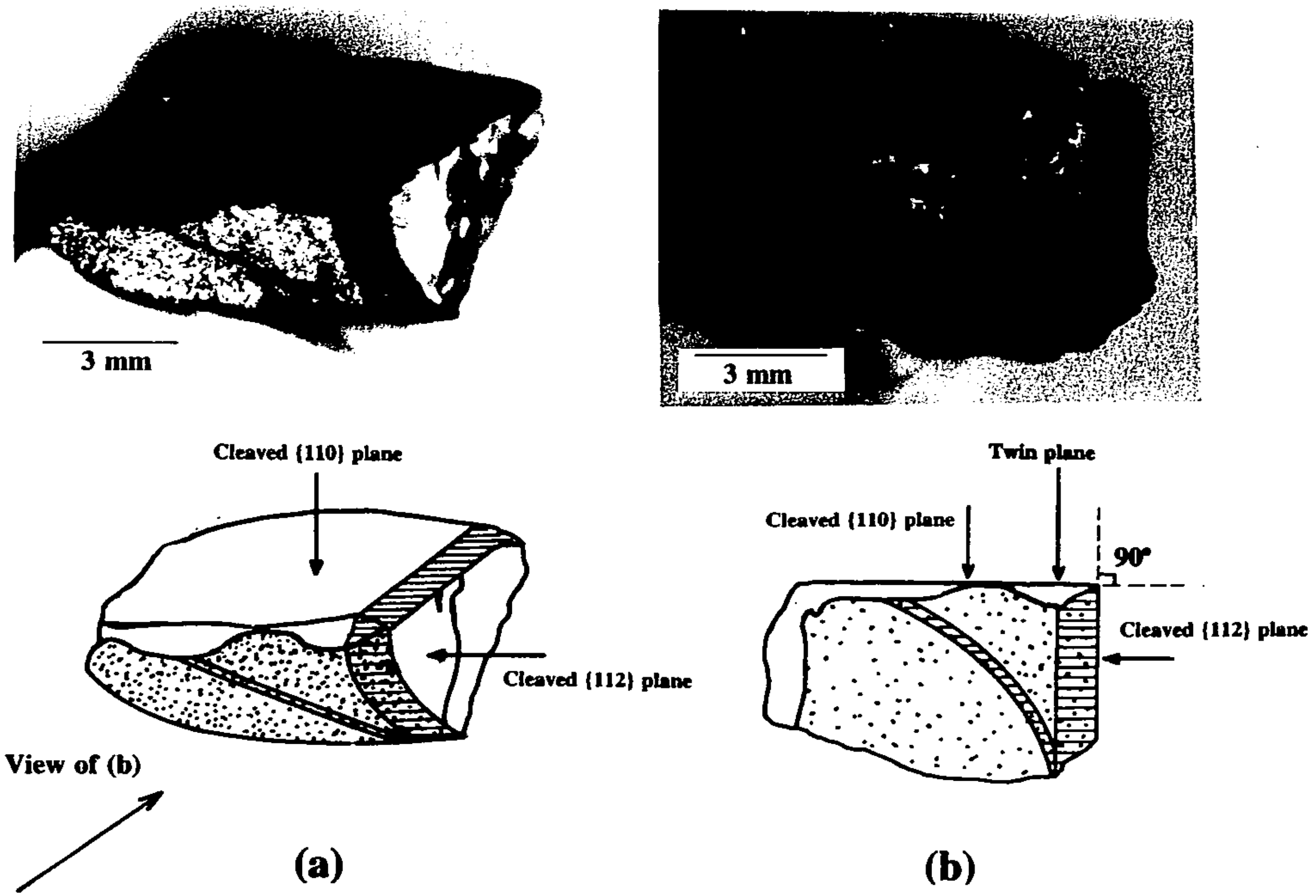

Fig.6.7 Photographs and schematics of a representative sample of CuInSe$_2$, exhibiting {110} and {112} cleavage planes with a 90° between them. (a) A three-dimensional perspective, and (b) a view parallel to both cleavage planes.

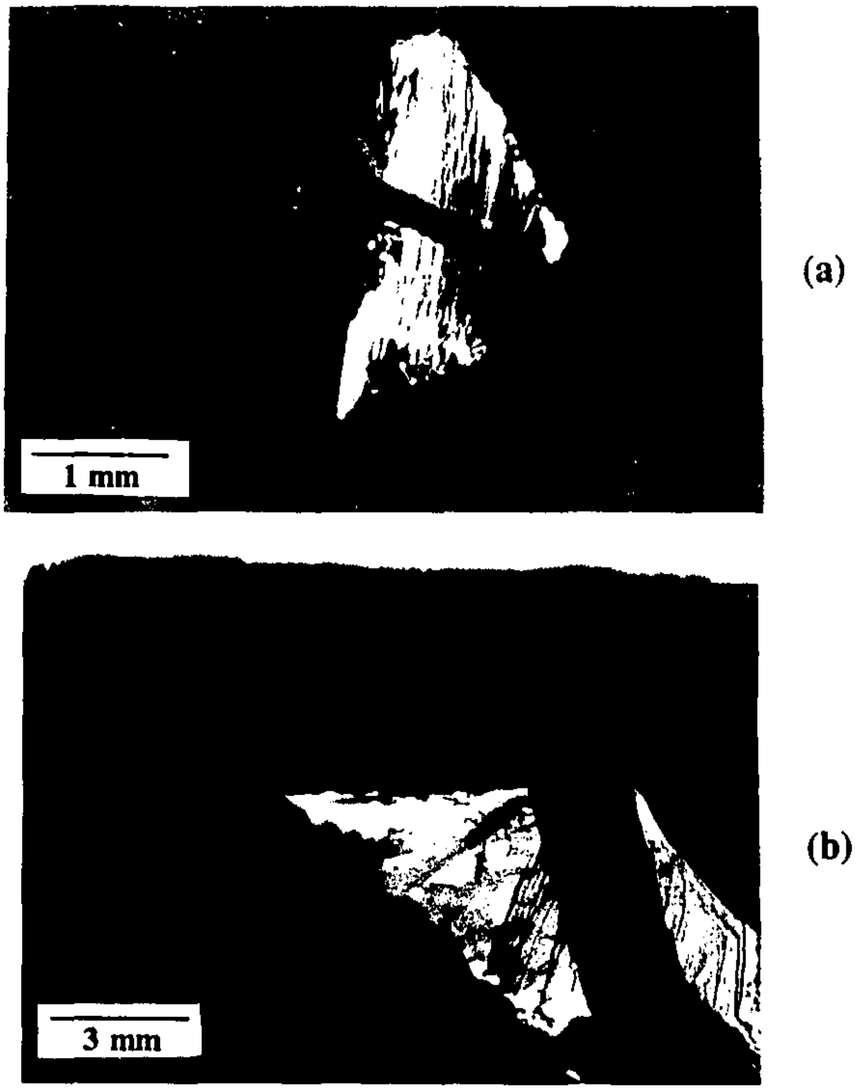

Fig.6.8 Two photographs of a representative CuInSe$_2$ sample, cleaved in the {101} plane, exhibiting a twinned region. (a) A top view and (b) a sectional view showing a twinning band.

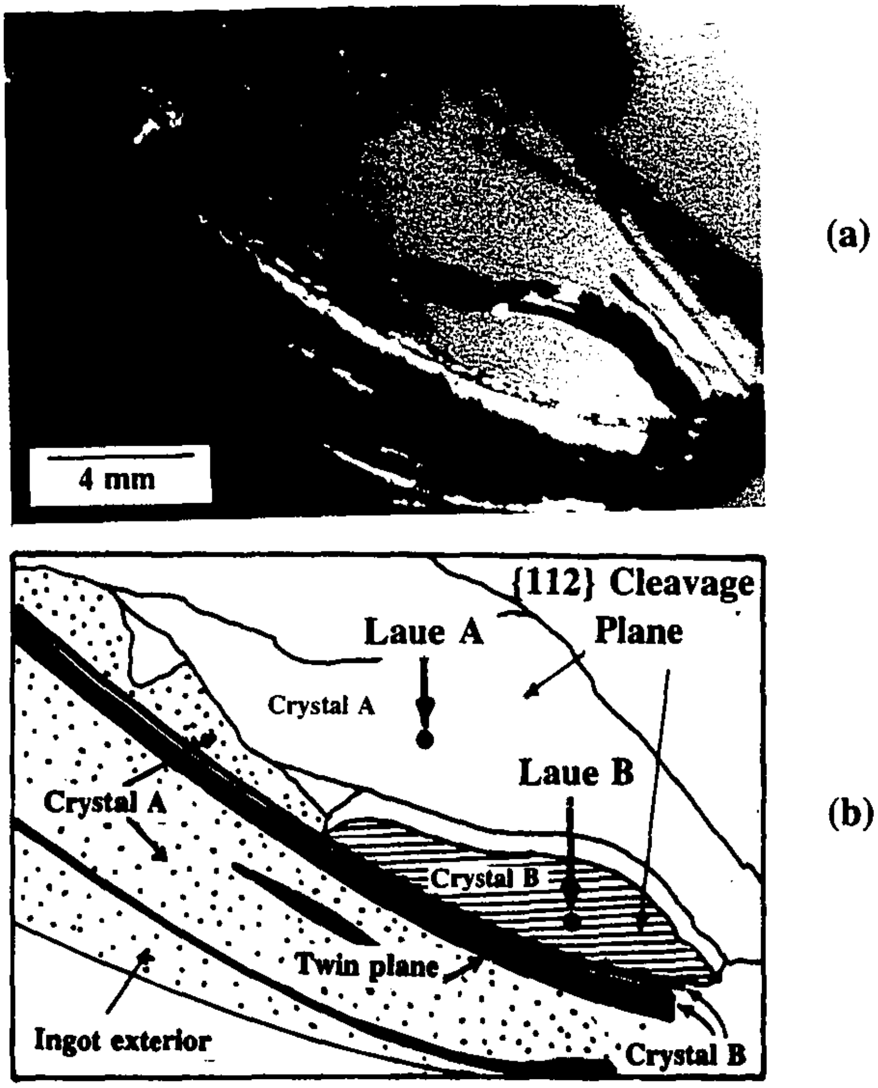

Fig.6.9 (a) Photograph of a twinned CuInSe$_2$ sample cleaved in the {112} plane. (b) Schematic showing the twinned region in this sample and the position of the two Laue pictures of Fig.6.10.

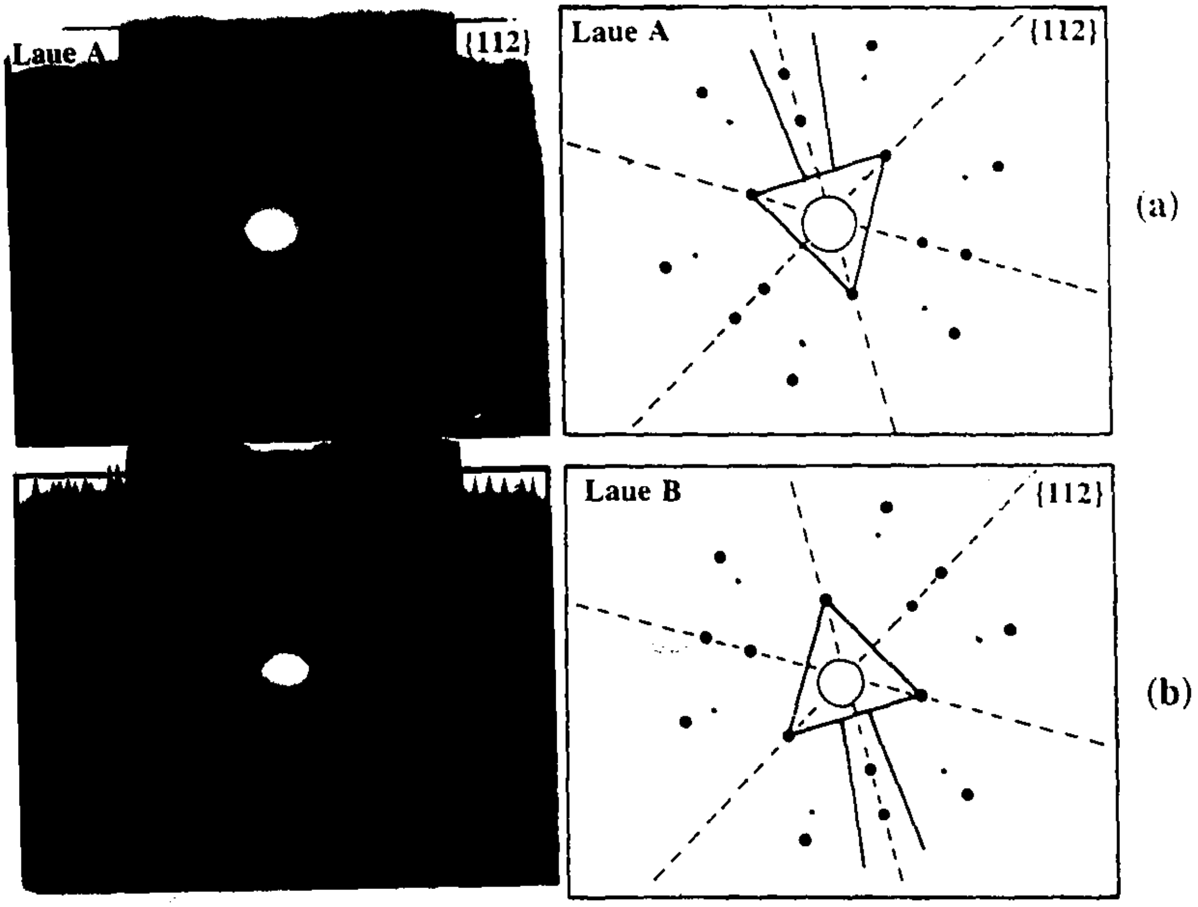

Fig.6.10 X-ray Laue photographs on the twinned {112}-cleaved sample of Fig.6.9. (a) Pattern of crystal A (Laue A), (b) pattern of the twinned crystal B (Laue B). The schematics show coincidence of the spot pattern on rotation by 180°, about an axis perpendicular to the page.

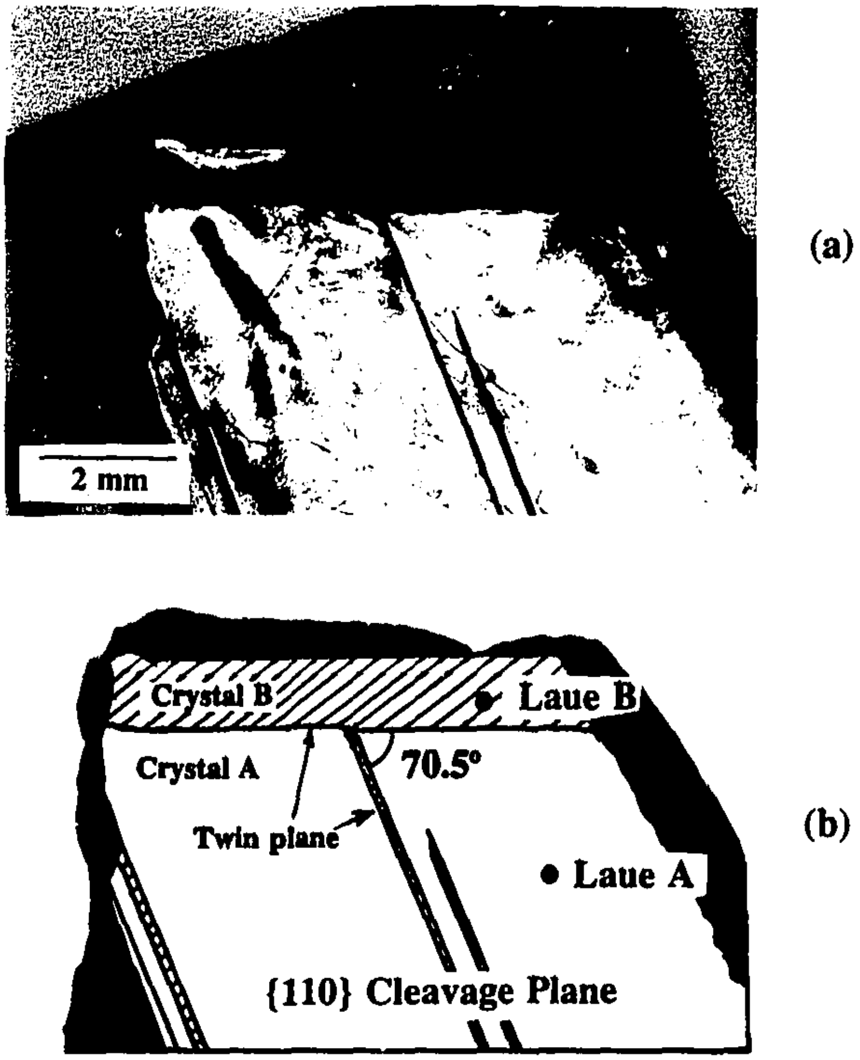

Fig.6.11 (a) Photograph of a twinned CuInSe$_2$ sample cleaved in the {110} plane. (b) Schematic showing the twinned region in this sample and the position of the two Laue pictures of Fig.6.12.

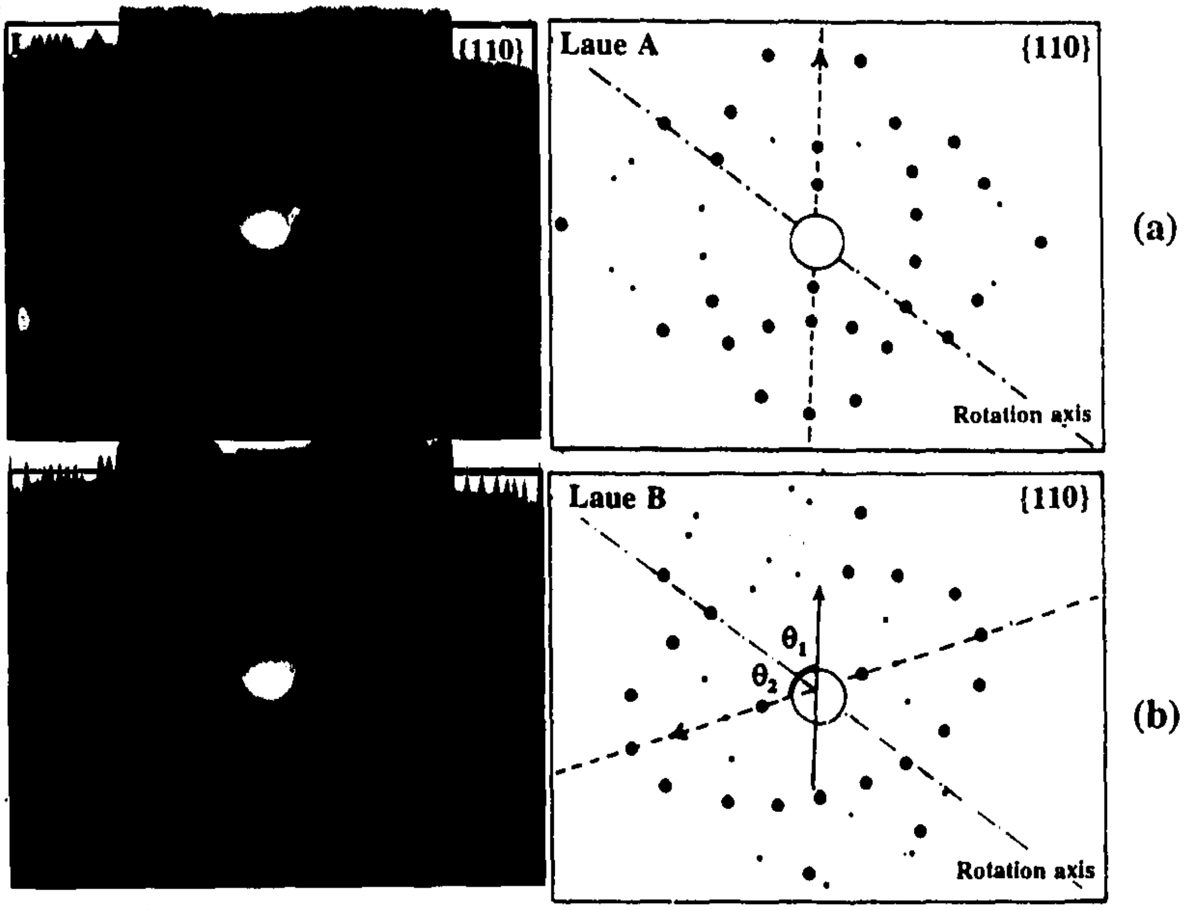

Fig.6.12 X-ray Laue photographs on the twinned {110}-cleaved sample of Fig.6.11. (a) Pattern of crystal A (Laue A), (b) pattern of the twinned crystal B (Laue B). The schematics show coincidence of the spot patterns by a rotation of 180°, about an axis indicated by the chain line. The broken lines in (a) and (b) indicate the <110> direction in each crystal. The angles θ_1 and θ_2 are equal.

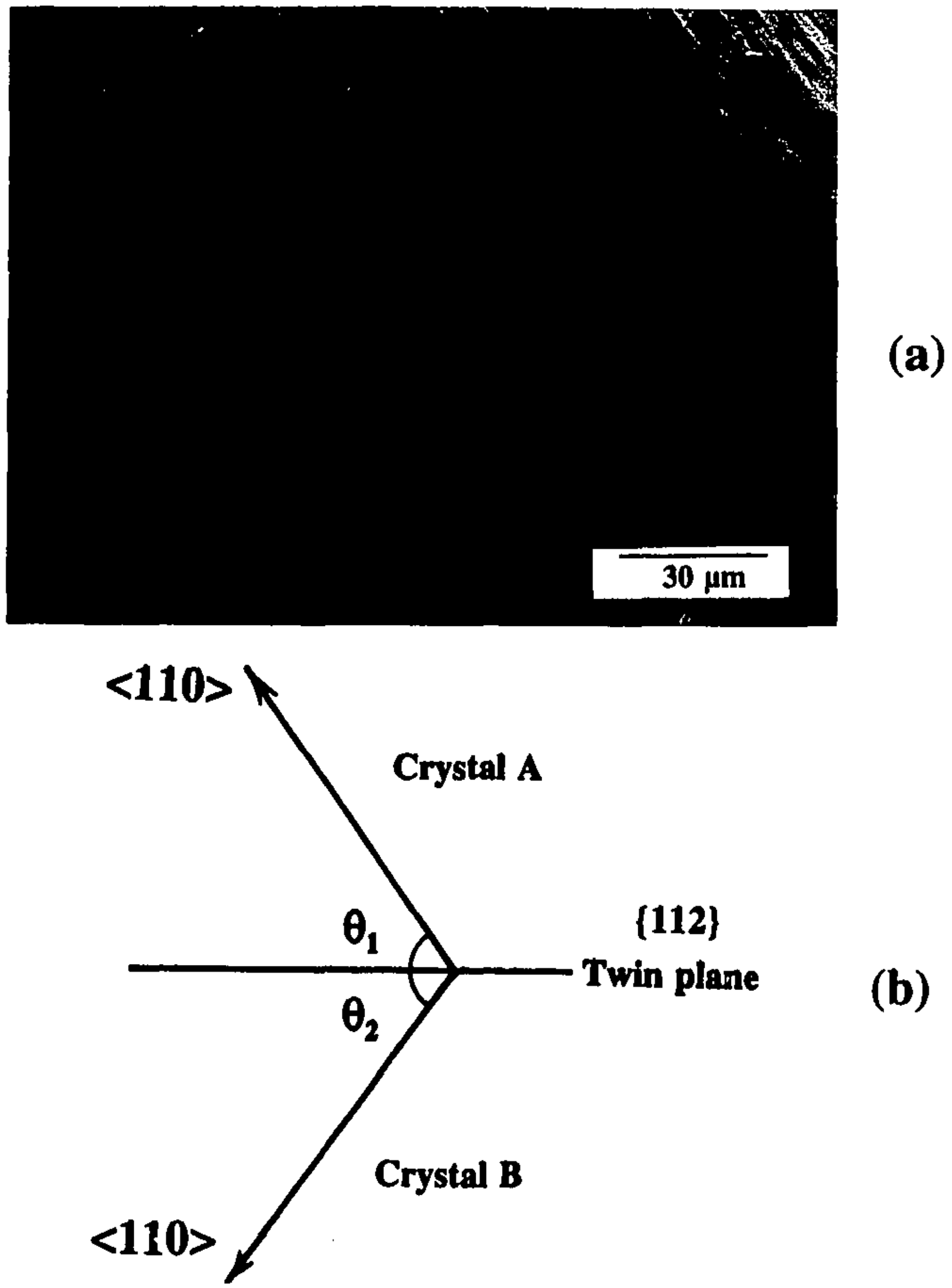

Fig.6.13 Photomicrograph showing the {112} twinning plane boundary between two crystals having a {110} cleavage plane. The ridges, in the photograph point in the <110> direction in both crystals and make an equal angle of about 55° with the {112} twinning plane, as shown in the schematic.

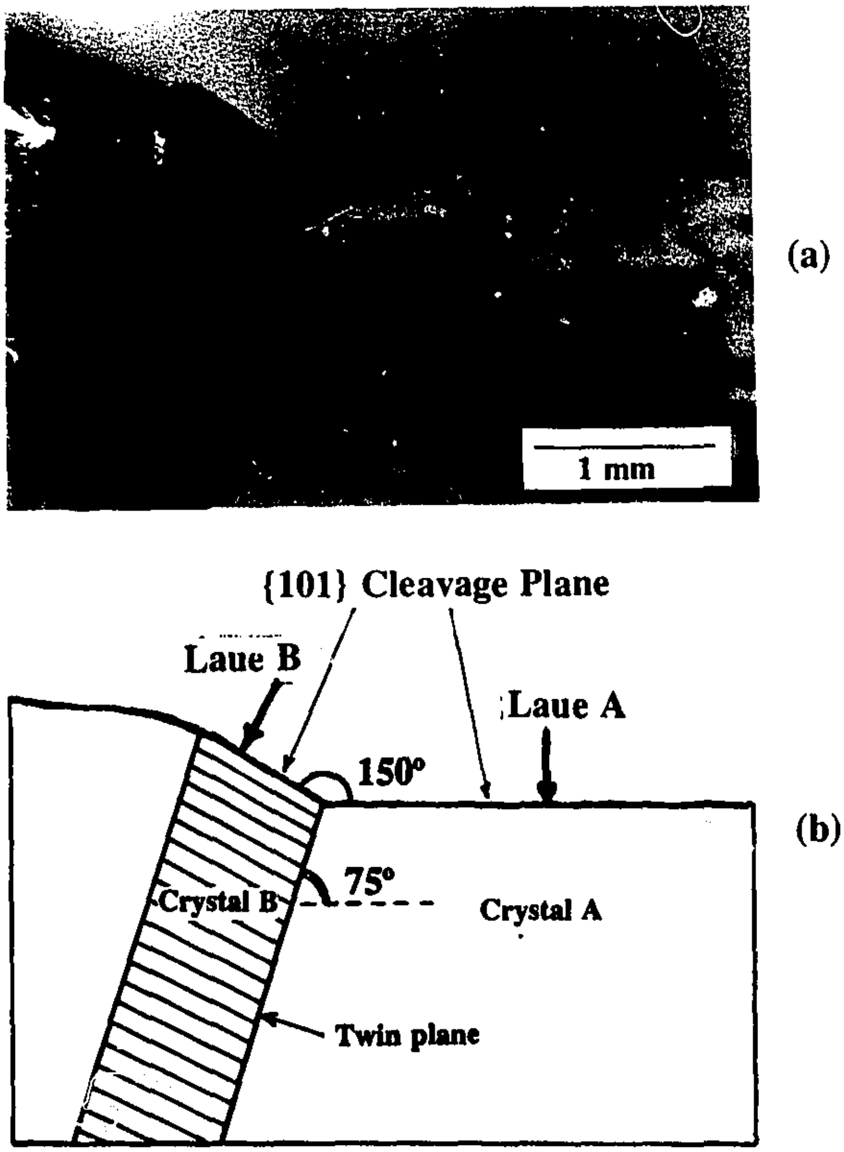

Fig.6.14 (a) Photograph of a twinned CuInSe$_2$ sample cleaved in the {101} plane. (b) Schematic showing the twinned region in this sample and the position of the two Laue pictures of Fig.6.15.

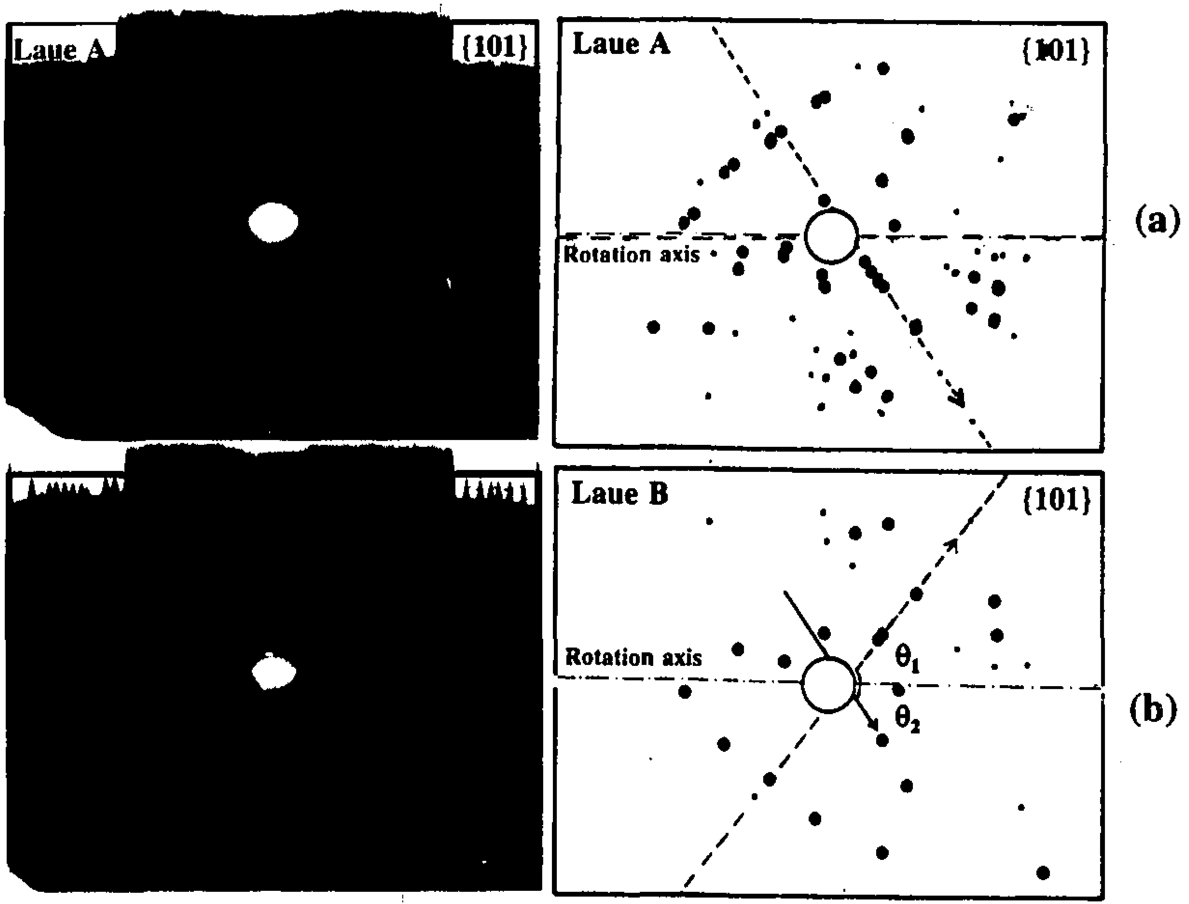

Fig.6.15 X-ray Laue photographs on the twinned {101}-cleaved sample of Fig.6.14. (a) Pattern of crystal A (Laue A), (b) pattern of the twinned crystal B (Laue B). The schematics show coincidence of the spot pattern by a rotation of 180°, about an axis indicated by the horizontal chain line. The broken lines in (a) and (b) indicate the symmetry axis of each crystal. The angles θ_1 and θ_2 are equal.

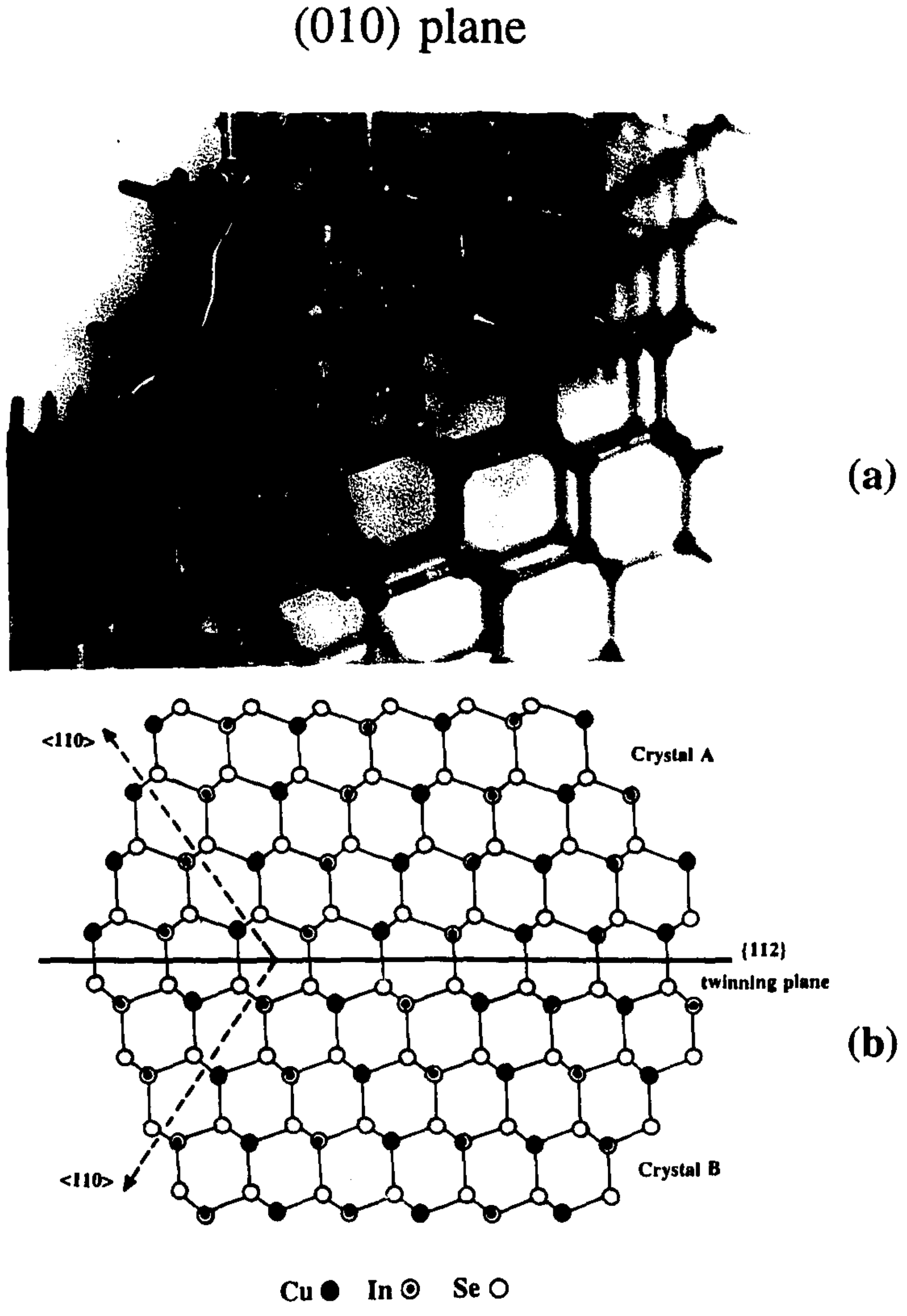

Fig.6.16 (a) Photograph of a "ball" and "stick" crystal model and (b) a schematic diagram showing twinning in the chalcopyrite structure, where the {110} plane is the plane of the page. The schematic shows the {112} twinning plane perpendicular to the page and makes equal angles (54.74°) with the indicated <110> directions (broken arrows) on the two crystals.

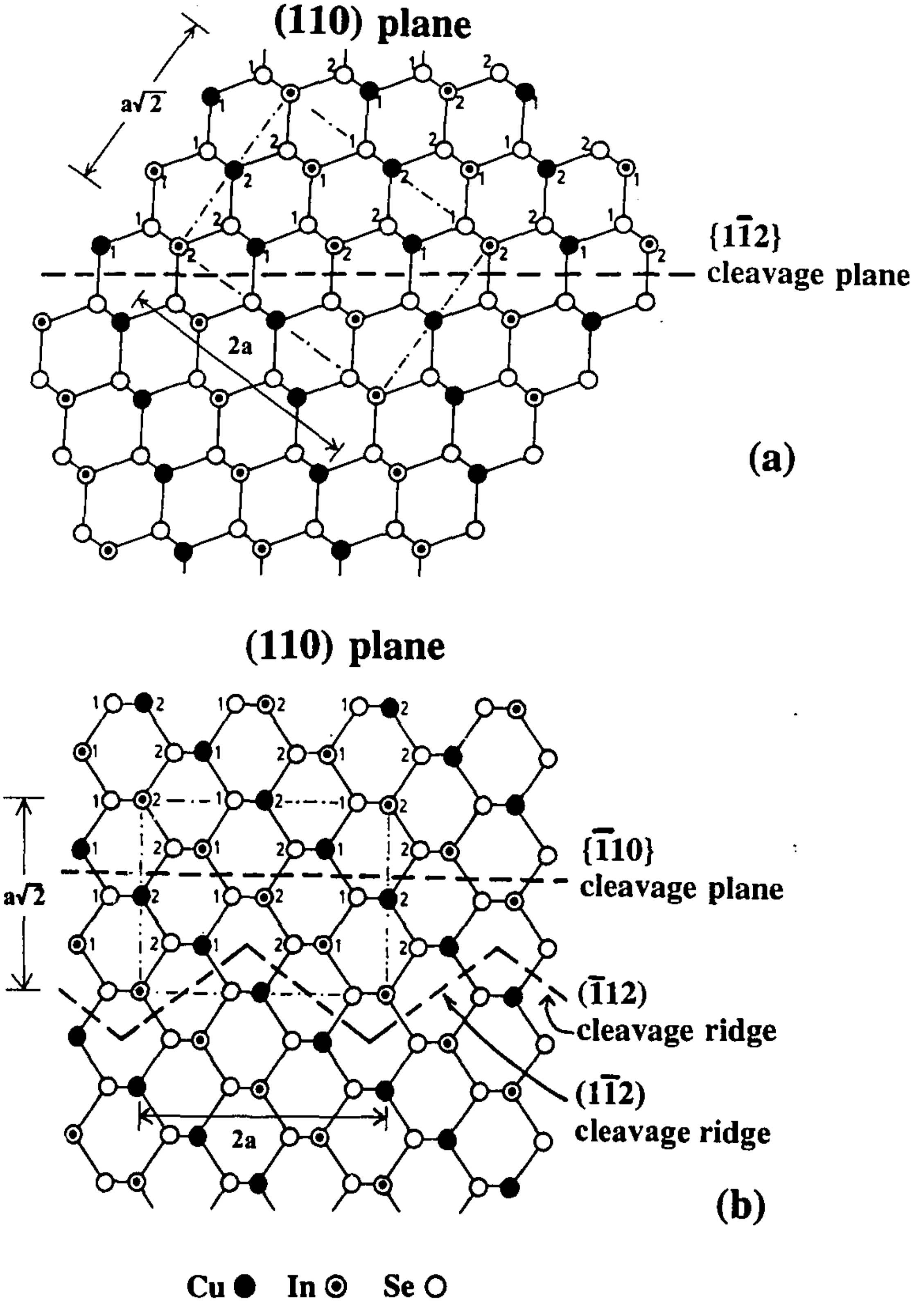

Fig.6.17 Schematic diagram of atomic layers of the (110) plane of the chalcopyrite structure, viewed with the {1$\bar{1}$2} plane (a) horizontal and (b) rotated by about 35°. Possible cleavage planes normal to the page, are indicated by the broken lines for (a) a {1$\bar{1}$2} cleavage and (b) a {$\bar{1}$10} cleavage. The chain line represents the unit cell in each plane. The labels 1 and 2 refer to consecutive depth layers of the atoms.

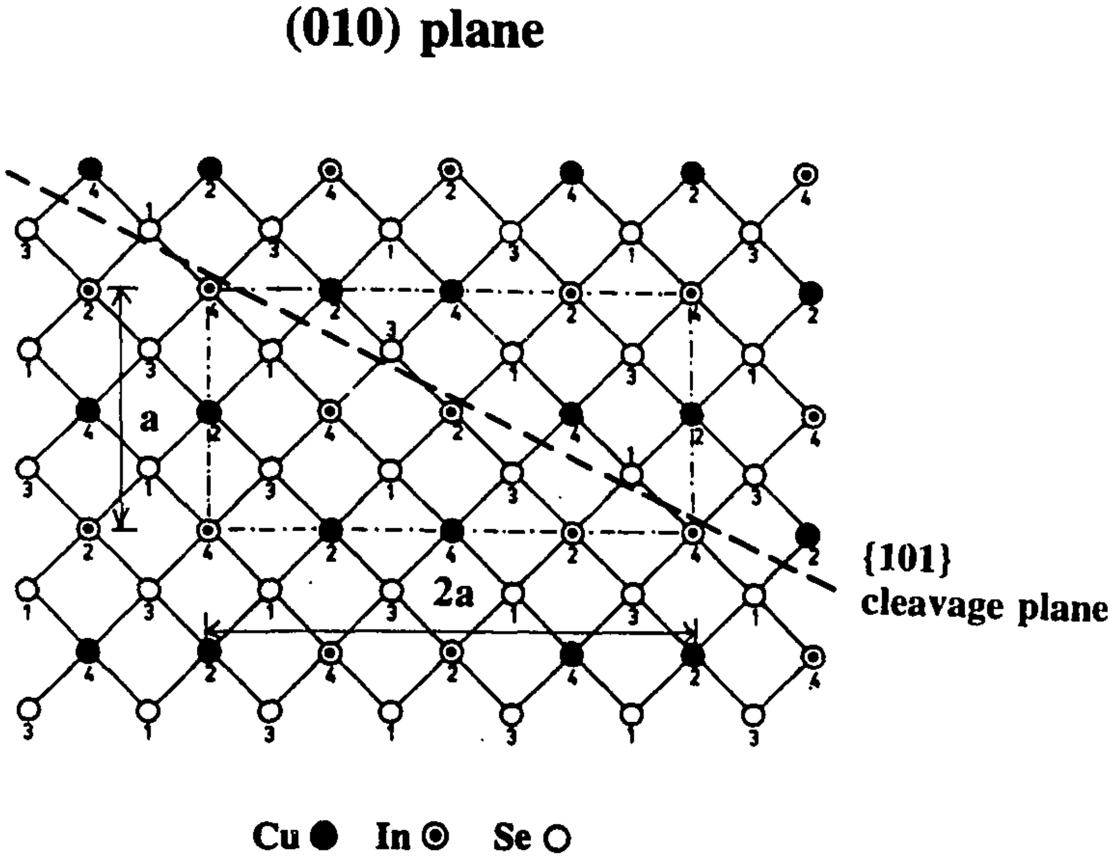

Fig.6.18 Schematic diagram of atomic layers of the (010) plane of the chalcopyrite structure showing a possible {101} cleavage plane, normal to the page, as indicated by the broken line, predominantly between In and Se atoms. The chain line represents the unit cell. The labels 1,2,3 and 4 refer to consecutive depth layers of the atoms.

CHAPTER 7

PHOTOVOLTAIC CELLS ON MONOCRYSTALLINE $CuInSe_2$ SUBSTRATES

7.1 INTRODUCTION

The main objective of the work in this thesis, as stated in chapter 1, is to obtain more information on $CuInSe_2$ in order to improve performance of solar cells made with this material. Hence, it is necessary to determine if the single crystal material prepared in this laboratory is of device quality, so that photovoltaic cells can be fabricated and tested for performance evaluation. Therefore, the subject of this present chapter is to prepare preliminary research cells using single crystal substrates of $CuInSe_2$ taken from the grown ingots. The cells fabricated, consisted of $CuInSe_2$(p)/CdO(n) structures, where the CdO was deposited by d.c. reactive sputtering. While this was not the most efficient structure for a high performance cell, it made use of the extensive experience in our laboratory with deposition of CdO obtained over many years. The semiconductor CdO has a direct energy gap of about 2.3 eV [7.1] and crystallizes in the rocksalt structure with a lattice constant of 4.689Å. This results in a lattice mismatch between the CdO and the $CuInSe_2$ **a**-parameters of about 23%. As will be seen later, despite the large mismatch between the two materials, the above cell structure has given surprisingly good efficiencies. The higher efficiency cells based on the structure $CuInSe_2$(p)/CdS(n)/ZnO(n+), described in the literature [7.2], [7.3], [7.4], [7.5], [7.6], [7.7], would have required extensive optimization of the CdS and ZnO layers and was therefore, not attempted in this thesis work. However, in earlier studies [7.8], [7.9], a preliminary $CuInSe_2$(p)/CdS(n)/CdO(n+) cell structure was made but this work is just touched upon here. In all of the cells reported here, the active surface of the $CuInSe_2$ substrate was cleaved in either the {112} or {101} plane, rather than abrasively polished. The use of cleaved planes in this study was not intended for lattice matching but rather for consistency in substrate orientation. However, despite the large mismatch between the CdO and the substrate, a hint of preferred orientation in the CdO layer was suggested, at least on the {112} $CuInSe_2$ plane, which is reported in Appendix A.2. In the early phase of cell fabrication, the substrates were not annealed prior to the deposition of the CdO layer and the contacts. This yielded acceptable cells at that time. However, arising from the work of L.S. Yip [7.10], [7.11] of this laboratory, on $CuInSe_2$/CdS/ZnO cells, an improvement in cell performance was obtained by annealing the $CuInSe_2$ in argon prior to cell fabrication. Therefore, in this chapter, results are presented for annealed and un-annealed cells with the $CuInSe_2$/CdO structure. It must be emphasized here that, it was not the intent of this work to develop the techniques for the highest efficiency cell, but rather to fabricate working devices with sufficient and reproducible performance to yield information about the $CuInSe_2$ material. The organization of this chapter is as follows. In the first section, the fabrication of the cells is presented .This is followed by a description of the measurement techniques used to evaluate the cells in the second section. The measurements included dark and illuminated current-voltage characteristics, photoresponse, capacitance-voltage characteristics and diffusion length estimation using the photocurrent-capacitance method. In the third section, all the experimental results are presented on the cells and this is followed by a discussion of the results.

7.2 FABRICATION PROCEDURE

7.2 (a) Sample Preparation

The $CuInSe_2$ cells fabricated in this study were prepared as follows. Monocrystalline portions of $CuInSe_2$ were extracted from the cylindrical ingots by cleaving along either the {112} or {101} planes. The cleavage was done by applying pressure along a predetermined direction using a sharp-edged tool. The fracture frequently resulted in a cleavage of at least a few square millimeters. The cleaved sample was then shaped into the form of a platelet by thinning it down on the non-cleaved surface to a thickness of about 2 mm, using abrasive polishing. The polishing was carried out under running water initially with coarse sand paper (Diamond grit #400), followed by polishing with 1 μm grit alumina powder. This provided a flat surface for the back contact . In this step, the cleaved "top" surface was protected with Apiezon wax to prevent the cleaved surface from being damaged. After the polishing, the wax was removed by rinsing the sample with trichloroethylene (TCE) and then with acetone. The sample was then thoroughly rinsed with DI water and dried under a flow of nitrogen.

7.2 (b) Substrate Annealing

The substrate annealing step was only carried out for three cells, which were samples 149-1, 149-2 and 125-3 (Table 7.1). The annealing was carried out, as shown schematically in Fig.7.1, in a resistive furnace containing a quartz tube some 12 mm in diameter and 40 cm in length. The open-ended tube was connected at one end to an argon gas cylinder, so that a steady flow of argon gas was allowed to pass through the tube at atmospheric pressure. The sample was inserted from the open end and a thermometer tip was also placed inside the tube adjacent to the $CuInSe_2$ sample. The quartz tube, with the sample and thermometer tip inside, was placed in a metal block having a cylindrical hole of the same diameter as the quartz tube, so as to provide a thermal mass for temperature stability. The gas flow rate was adjusted to be around 200 ml/min. and the temperature was slowly raised until the desired set point, of around 320 to 360 °C, was reached. The annealing was continued for about 2 to 2½ hours and then the furnace was turned off and the sample allowed to cool down under the flow of argon. The $CuInSe_2$ substrate was then removed and prepared for the back contact deposition.

7.2 (c) Back Contact

In this work, the first step in the cell fabrication process was the deposition of the back contact. While the most popular metal used for the ohmic contact in thin film polycrystalline $CuInSe_2$ cells is molybdenum, in this work on single crystal cells, gold was chosen instead. This is due to its lower melting point, its relatively high work function and the fact that low resistance contacts to filamentary samples were obtained with it in this laboratory [7.12]. The deposition of Au was carried out by evaporation in a high vacuum system (Edwards model E306A) in the following manner. The pre-cleaned $CuInSe_2$ substrate was mounted with its cleaved surface down on a glass slide containing a patch of molten Apiezon wax. The wax held the sample in place, thus protecting the plane of cleavage from damage during mounting and also acted as a mask against any Au deposition onto the front surface. The abrasively polished back surface was kept exposed . The sample was then mounted in the vacuum system some 10 cm above a Mo boat containing the source material in the form of Au wire . The system was pumped down to a pressure of about 4×10^{-7} Torr and the evaporation was then begun. The current through the Mo boat was slowly raised until the Au was molten and then maintained at about 80 amps for 2 to 3 minutes, which allowed most of the Au to evaporate. This gave a deposited film thickness of about 1 μm on the sample. The deposited Au layer was sufficiently adherent to the $CuInSe_2$ back surface, since this surface was prepared with a rough finish by the abrasive polishing. After the evaporation was complete, the sample was allowed to cool down for about one hour before removing it from the vacuum system. After removal, the wax was dissolved away in trichloroethylene and the sample cleaned in acetone followed by DI water. Finally, a copper wire was soldered to the Au layer, forming the electrical back contact, and the $CuInSe_2$ substrate was mounted on an aluminum stud, using Quickmount resin . The Al stud acted only as a mechanical holder for the cell and had no electrical role. With the top cleaved surface exposed, the sample was now ready for the CdO window deposition.

7.2 (d) CdO Window Layer

The $CuInSe_2$ cells fabricated in this study, employed CdO as the transparent window layer in the cell. The CdO layer was deposited directly onto the cleaved surface of the $CuInSe_2$ sample without an interfacial layer in the main work to be described here. The sample, with its cleaved plane exposed, was mounted in a special holder where an Al mask was positioned in front of the cell. Depending on the cleavage area available, an aperture of up to 12 mm^2 in area was defined with this mask for the CdO deposition. The CdO layer was then deposited by d.c. reactive sputtering - a method extensively employed in this laboratory [7.13], [7.14], [7.15], [7.16]. Fig. 7.2 shows a plot of an important cell parameter - short circuit current density against CdO film thickness obtained on cells in earlier work [7.8] . While the data points show some scatter. the trend suggests that the optimum thickness for this layer is between 0.7 and 0.8 μm in these cells. Accordingly, for the CdO deposition in this study, the parameters of sputtering were chosen so as to yield film thicknesses of this order for most of the cells. A glass slide was also included in the sample holder to monitor the CdO film thickness during deposition. The masked sample was loaded into a special vacuum system some 3 cm above a high purity cadmium metal target, which was negatively biased, while the sample itself was connected to ground. The vacuum system was then pumped down to a pressure of about 10^{-6} Torr and then the pressure was then raised up to about 75 mTorr by admitting a gas mixture of argon with 1% oxygen. The total flow rate was kept at about 20 ml/min. After the chamber pressure had stabilized, the sputtering was begun by adjusting the sputtering current to about 15 to 20 mA. The negative potential of the cadmium target was about 700 volts. The deposition was done in a continuous manner for a period of between 2 to 3 hours until the desired thickness was achieved. In order to prevent excessive sample heating during the sputtering, a water-cooled sample holder arrangement was used. Surprisingly, however, it was found that, the deposited CdO layer, at least on the cleaved {112} plane, was preferentially oriented as compared with that deposited on glass. This is shown in Appendix A.2, where X-ray diffraction results indicated a preferential {111} orientation for the CdO layer on the cleaved {112} plane of $CuInSe_2$, despite the large lattice mismatch of some 23 %, between the two layers. Following the CdO deposition, the sample holder was taken out of the vacuum system and, with the sample still in place, the CdO mask was replaced with another mask for the front metal contacts.

7.2 (e) Front Contacts

After the CdO layer was sputtered onto the substrate, two Au contacts were evaporated onto the CdO , to act as the front electrical contacts of the device. Here, the CdO metal mask was replaced by one having two stripe-shaped openings, which defined two Au stripes on the CdO layer. The sample was aligned and loaded into the vacuum system. The Au was then evaporated in the same vacuum system as that used for the Au back contact (Edwards model E306A) in a vacuum of about 4×10^{-7} Torr. The evaporation was carried out for about 3 to 4 minutes and then the sample was allowed to cool down in vacuum for about 1 hour. The sample was then removed from the system and copper wires were soldered to the Au regions for the external electrical contact. Fig. 7.3 shows a schematic diagram of the final structure, indicating the different device layers. The fabrication conditions of all of the devices presented in this study are summarized in Table 7.1, along with some of their photovoltaic properties.

7.3 MEASUREMENT TECHNIQUES

Following the fabrication of each cell, certain measurements were carried out to evaluate its photovoltaic performance. The measurements, as mentioned earlier, were illuminated and dark current density-voltage characteristics, current-voltage under actual sunlight, photoresponse, capacitance-voltage and estimation of the minority carrier diffusion length in the single crystal $CuInSe_2$ cell. These measurements are described next.

7.3 (a) Illuminated and Dark Current-Density-Voltage (j-V) Characteristics

Measurements of illuminated and dark current-density -voltage (j-V) characteristics reveal important photovoltaic parameters about a solar cell. The j-V characteristics were obtained under simulated solar conditions using a xenon arc lamp solar simulator (Kratos model LH 150/1), which was fitted with an AM1 filter and adjusted to give about 100 mW/cm^2. This adjustment was done by first placing a silicon reference cell, calibrated to give 3.1 mV under AM1 conditions for an illuminated area of 0.125 cm^2, on an adjustable platform under the simulator beam. The cell was positioned in the center of the illuminated area and the vertical position of the cell was adjusted until a reading of 3.1 mV was obtained. The separation between the top surface of the reference cell and the beam exit aperture of the simulator was noted and the reference cell was replaced with the actual device to be tested. The electrical circuit is shown in Fig.7.4. Bias was applied to the sample using a stabilized power supply (Farnell model TSV 30/5CL) through a variable potentiometer . The voltage drop across the cell was measured using a Keithley electrometer model 610C, while the current through the cell (up to 2 mA) was recorded with a Keithley model 485 picoammeter. Larger current (above 2 mA), was measured with a multimeter (Fluke model 37). The bias voltage was varied between +1.2 volts in the forward direction to -2.0 volts in the reverse direction and current readings were taken at intervals of 0.05 volt. This gave the illuminated current-voltage curve for the cell. The measurement was repeated in the same manner with the simulator light blocked and the cell covered with a dark cloth to yield the dark characteristics of the cell. The current density , j, was obtained for each reading by dividing the measured current I, by the illuminated "active" CdO area, A_a , of the cell. The value of the CdO area for each cell was determined by measuring it directly under a microscope having a built-in scale. In calculating the active area of the cell, it was verified using a He-Ne laser, that regions outside the boundary of the CdO area did not contribute significantly to the photovoltaic action of the cell.

7.3 (b) Current-Voltage under Actual Sunlight

In order to have confidence in the simulated illumination measurements, performance of some cells was tested under actual sunlight. The electrical circuit used here, shown in Fig.7.5 , was slightly different from that described earlier. Here, no bias was applied to the cell. Instead, the cell output was connected to a variable load resistor R_L . A separate sensing resistor with a value of 10Ω, connected in series with R_L, was used to indicate the output current. This was done by measuring the voltage drop, V_I, across it with a multimeter (Fluke model 37) and dividing the reading by 10Ω . The voltage drop across the cell itself was also registered with a second Fluke multimeter. The j-V measurement was done in a point-by-point manner where the load resistor R_L was varied between about 20Ω (short circuit condition) to about 25kΩ (open circuit condition). The measurement was typically done on a sunny day on a rooftop outdoors, in un-obscured sunlight in Montreal near midday. The exact details of the measurements are noted on the plots shown. This yielded the cell characteristics under the sun. The intensity of the solar radiation was measured using three reference detectors: a pyroelectric detector (Molectron model PR 200), a pyranometer (Eppley model PSP) and a Solarex silicon cell; the average irradiation of these was taken.

7.3 (c) Spectral Response

Measurement of spectral response was carried out on the $CuInSe_2$/CdO cells between a wavelength (λ) of 400 and 1300 nm. The measurement set-up is shown in Fig.7.6. Here, the sample was illuminated with monochromatic light from a Photon Technology International grating monochromator (model L1), where the exit slit was set at 2 mm (corresponding to a $\Delta\lambda$ of about 8 nm) and the sample was positioned at about 6 cm from the exit slit. The incident light beam was chopped at a frequency of about 153 Hz using a Stanford Research Systems light chopper (model SR 540). The photogenerated current signal from the cell was converted into a voltage signal using a 10Ω sensing resistor. The voltage across the resistor was measured with a lock-in amplifier (EG&G model 5302), which was set at the same frequency of 153 Hz using a reference signal from the chopper. A preamplifier (model 5316) was used to increase the signal by a factor of 10. Measurements were taken at wavelengths starting from 400 to 1100 nm in increments of 25 nm and also at 1200 and 1300 nm. In the range between 600 to 1100 nm, a long pass filter ,with a cut-off wavelength of 610 nm was employed to reduce second order and higher harmonics. For the wavelengths of 1200 and 1300 nm, corresponding band pass filters were used (each having a $\Delta\lambda$ of about 50 nm) for the same purpose. After the sample was measured at these wavelengths, it was replaced with a pyroelectric radiometer (Molectron model PR 200) to measure the light intensity, W(λ), at each individual wavelength, in mW/cm^2. The photoresponse of a cell, P(λ), in amps/watt, was then calculated for each wavelength as follows:

$$P(\lambda)=\frac{I(\lambda)}{A_a \times W(\lambda)}$$

where: I(λ) is the current from the cell in mA, A_a is the cell area in cm^2, W(λ) is the detector reading in mW/cm^2. The quantum efficiency Q(λ), was obtained for each wavelength λ as follows:

$$Q(\lambda) = P(\lambda) \times \frac{hc}{\lambda q}$$

where, h is Planck's constant, c is the speed of light and q is the electronic charge. Both the photoresponse and the quantum efficiency curves were obtained by plotting P(λ) and Q(λ) respectively against λ.

7.3 (d) Capacitance-Voltage

Parallel mode differential capacitance, C_p, was measured on the cells with variation of reverse bias from 0 to 5.0 volt in increments of 0.2 volt. In this measurement, a LF Impedance Analyzer (Hewlett Packard model 4192) was used to measure the capacitance at a frequency of 10 kHz with a test signal of 20 mV. The bias source was internal. The voltage across the sample was verified using a Keithley electrometer (model 610C). The circuit diagram for this measurement is shown in Fig.7.7. Capacitance-voltage measurements were used to obtain Mott-Schottky plots of $(A/C_p)^2$ against reverse voltage bias, V_R, where A is the cell junction area (noting that $A > A_a$). It is well known that in a pn+ junction, the concentration profile on the p-side, N_A, is given by:

$$N_A = \frac{2}{q\epsilon_o\epsilon_r} \times \frac{1}{\frac{d[(A/C_p)^2]}{dV_R}}$$

where, ϵ_o is the permittivity of free space, ϵ_r is the relative dielectric constant of the p-side, and q is the electronic charge. Thus, by measureing the slope of the curve of $(A/C_p)^2$ against reverse voltage, an estimate of the carrier concertration can be obtained.

7.3 (e) Estimation of Diffusion Length

The diffusion length of the electrons in the $CuInSe_2$ single crystal substrate of the cells fabricated in this study , was estimated using the photocurrent-capacitance method. The theoretical considerations of this method are discussed in detail by Champness and Chan [7.18], [7.19] and a brief description of this treatment is presented in Appendix A.3. In this section, only the experimental procedure is outlined. The method basically consisted of two steps. First, a measurement of the illuminated-to-dark change in the short circuit current (ΔI) of the cell at different reverse bias voltages and under long wavelength illumination was carried out, and this was followed by the measurement of the junction parallel capacitance, C_p, for the same reverse bias values and illumination. The measurement procedure was as follows. The sample was first placed in the path of the monochromatic beam, 6 cm away from the exit slit of the monochromator (Photon Technology , model L1) such that the whole of the sample area was illuminated. The radiation wavelength was first varied between 0.9 and 1.3 μm with the slit width fixed at 4 mm; then the slit width was changed between 2 and 5 mm, with the wavelength set to 1200 nm. The monochromatic illumination was chopped at a frequency of about 153 Hz , as was done in the spectral response measurement. The cell was connected to a stabilized power supply (Farnell model TSV 30/5CL) which provided the reverse bias, while the voltage drop across the cell was verified with an electrometer (Keithley model 610C). The cell was connected in series with a sensing resistor of 10Ω. The a.c. voltage drop across this resistor was measured with a lock-in amplifier (EG&G model 5302) to yield the cell photocurrent.The illuminated -to-dark change in the output current of the cell ,ΔI, was measured for reverse bias voltages between 0 and 5.0 volts, in increments of 0.2 volt. This arrangement is shown in Fig. 7.8. In the second part of this measurement, the capacitance was measured as a function of reverse bias ,as was described earlier. However here, the cell was illuminated with unchopped light at the same wavelength as that used for the photocurrent measurement. The capacitance was again measured using the Hewlett Packard LF Impedance Analyzer (model 4192A), where the test signal frequency was again set at 10 kHz and the test signal amplitude at 20 mV. The reverse bias voltage across the cell, was again varied between 0 and 5.0 volts, in increments of 0.2 volt. This set-up is shown in Fig.7.9. The values of ΔI and C_p at each reverse bias voltage were paired together and these values were used to plot ΔI against $1/C_p$. One condition of using the photocurrent capacitance method is that αW should be much smaller than unity [7.18], [7.19], which in practice means using monochromatic light of band edge wavelength. In the case of $CuInSe_2$, this would correspond to a wavelength of about 1.2 to 1.3 μm. Thus, if the wavelength is too short, the αW condition is violated, while if it is too long, the photocurrent is too small to measure accurately. Thus, although the ΔI measurements were made from 0.9 to 1.3 μm, only those values at the longer wavelengths, strictly speaking should be accepted, since they comply with the $\alpha W << 1$ condition.

7.4 EXPERIMENTAL RESULTS

In this section, experimental results are now presented on the single crystal $CuInSe_2$/CdO cells fabricated in this study. In the initial part of this work, cells were fabricated where the CdO layer was deposited directly onto cleaved substrates of $CuInSe_2$ with or without a CdS interfacial layer. These cells typically exhibited a poor fill factor. However, upon adopting the pre-annealing step of the $CuInSe_2$, prior to the cell fabrication, as already mentioned in the introduction of this chapter, a significant improvement in the fill factor was attained in these cells. In the results to follow, first a brief presentation of results on early $CuInSe_2$/CdS/CdO cells is given. This is followed by the current-density-voltage results for the initial $CuInSe_2$/CdO cells where no annealing was done. Next, results on the effect of annealing are presented, including results on the estimation of the diffusion length in the these cells. The diffusion length measurements in the $CuInSe_2$/CdO cells in this study were made possible by the use of the annealing process, as will be described in the sections to follow.

7.4 (a) Results on Early Un-annealed $CuInSe_2$/CdS/CdO Cells

In an early phase of this work, some preliminary cells having the structure $CuInSe_2$/CdS/CdO were fabricated, where the CdS layer between the $CuInSe_2$ and the CdO was deposited by a chemical bath method [7.17] and had a thickness of about 1000Å. The illuminated measurements on these cells was made under a rather uncertain irradiation level of about 150 mW/cm^2 or more and for this reason are difficult to compare with more recent results. Never-the-less, Appendix A.4 shows a table of results on these cells, where it is seen that, the illuminated open circuit voltages (V_{oc}) were generally up to about 0.4 volt.

The current-voltage characteristics of some of the cells was determined under actual sunlight and Fig.7.10 shows an example of two of these cells. It is seen that the short circuit-current-density was as much as 30 mA/cm^2, although the fill factors were rather poor.

7.4 (b) Results on j-V Characteristics of Un-annealed CuInSe$_2$/CdO Cells

The performance of cells of CuInSe$_2$/CdO with no pre-annealing of the CuInSe$_2$ was found to vary from device to device. The illuminated characteristics of a representative cell 105-5 is shown in Fig.7.11(a). It is seen here that, this cell exhibited a reasonably high open circuit voltage of around 0.4 volt and a short circuit current density of some 20 mA/cm^2. However, the fill factor, FF, and therefore the efficiency, η, were somewhat low with values of 0.43 and 4% respectively. The dark characteristics of this cell are shown in Fig.7.11(b) in the form of a $\ell n(j)$ - V plot. Here, it is seen that at a bias voltage of 1 volt, the rectification ratio is about 2 orders of magnitude. Evidence of some shunt current can also be seen below a forward voltage of 0.4 volt. The ideality factor (n) of this cell is slightly greater than 2, suggesting that recombination current may be dominant.

The performance of this cell under actual sunlight is shown in Fig.7.12. The measurement was performed outdoors under clear skies in Montreal in October, where it is seen that both j_{sc} and V_{oc} were not very different from their values (Fig.7.11(a)) under the solar simulator. The cell performance was also verified at the National Renewable Energy Laboratory (NREL), of Golden, Colorado under the ASTM spectrum of AM1.5 Global, as shown in Fig.7.13. Here, it is clear that there is reasonable agreement between the measurements taken at both laboratories. The above cell features were rather typical of the un-annealed cells, but, in some cases, significant series resistance was present, which reduced the cell performance. This is shown, for instance, in Fig.7.14(a), where the illuminated characteristic of cell 125-1 is given, exhibiting a slow rise in forward current with voltage, corresponding approximately to a resistance of some 250 Ω. The dark characteristics, shown in Fig.7.14(b) indicate poor rectification and also significant shunt current.

7.4 (c) Results on j-V Characteristics of Annealed $CuInSe_2$/CdO Cells

The effect of annealing the $CuInSe_2$ substrate prior to the fabrication of the cell on the illuminated and dark j-V characteristics is treated here. A total of 3 cells were fabricated with the annealing treatment, as described in section 7.2(b) of this chapter and these are cells 149-1, 149-2 and 125-3. Figs.7.15(a) and (b) show the j-V curves for cell 149-1. This cell was annealed for 2 hours at 320 °C (Table 7.1). It is also the cell with the largest active CdO area of all the devices made in this study, annealed and un-annealed, of 11 mm^2. It is seen here that j_{sc} was about 24 mA/cm^2, while V_{oc} was just over 0.4 volt. However, the fill factor and the efficiency, with values respectively of 0.5 and 5.0%, were slightly higher than those of the un-annealed cell 105-5, despite the slight excess in the shunt current at lower voltages, indicated in Fig.7.15(b) for this cell.

Cell 149-2 was also annealed but at a slightly higher temperature of about 360°C for some 2½ hours. The j-V characteristics, given in Fig.7.16(a), again show improved performance over the unannealed cells, with j_{sc}, V_{oc}, FF and η having values of 28 mA/cm^2, 0.42 volt, 0.5 and 5.7% respectively. While the fill factor of this cell was comparable to that of annealed cell 149-1, the efficiency of cell 149-2 was slightly higher due to its larger j_{sc}

value. The dark j-V characteristics of this cell, shown in Fig.7.16(b), indicate a rectification ratio of just over two orders of magnitude at 1 volt and a reduced shunt current at lower voltage. Evidence of some series resistance, in both figures 7.16(a) and (b), is apparent at a forward voltage greater than 0.6 volt.

The j-V characteristics of annealed cell 125-3 are given in Figs.7.17(a) and (b). This cell yielded the highest conversion efficiency and fill factor of all of the 3 annealed cells. While the short circuit current density and open circuit voltage were not very different from the other annealed cells, the fill factor and efficiency values of this cell were 0.63 and 6.2% respectively, as shown in Fig.7.17(a). These were the highest reported values so far obtained for these $CuInSe_2/CdO$ cells, where no interfacial layer, such as CdS was used. The steep rise in the j-V curves of Fig.7.17(a) in the forward direction, indicates low series resistance. The dark j-V curves of Fig.17(b) indicate a rectification ratio of almost 3 orders of magnitude at a bias voltage of 0.7 volts.

7.4 (d) Results on j-V Characteristics of the Commercial $CuInSe_2$ Cell

In order to establish some basis of comparison between the $CuInSe_2/CdO$ cells and cells fabricated with the present thin film technology of $CuInSe_2$, a commercial cell was obtained from one of the leading photovoltaic companies, Siemens Solar Industries, of Camarillo, California. The original thin film polycrystalline cell was about 4 cm^2 in area which was too large to fit under the circular beam of the solar simulator. It was therefore, scribed into several smaller pieces using a glass cutter. The actual cell tested had a total area of about 0.6 cm^2, where the edges, after scribing, were not treated in any special way. The structure of the cell is one where the substrate is a $CuInSe_2$-based alloy (including Ga and S) with CdS and ZnO deposited as window layers.

The illuminated and dark j-V characteristics of this cell, as measured in our laboratory, are presented in Figs.7.18(a) and (b). While the dark characteristics exhibit some shunt current below 0.4 volt, values for j_{sc}, V_{oc}, FF and η of about 36 mA/cm^2, 0.48 volts, 0.68 and 12% respectively, were obtained. These values are of course substantially higher than those obtained on our cells with a CdO window layer. It is also noted that the ideality factor, n, from Fig.7.18(b), is also slightly smaller for the commercial cell than for the $CuInSe_2$/CdO cells of this study.

7.4 (e) Results on Spectral Response of $CuInSe_2$/CdO Cells

Photoresponse measurements were carried out on 4 $CuInSe_2$/CdO cells, namely one un-annealed cell 125-1 and three annealed cells 125-3, 149-1 and 149-2. The photoresponse curves for all 4 cells are shown in Fig.7.19. It is clearly seen in this figure that, the photoresponse of all of the cells has a peak in the wavelength range between 800 and 1000 nm. It is also seen that the fall-off after the maximum is steeper than the rise below the peak. From this figure, it is also noted that the un-annealed cell 125-1 exhibited the highest photoresponse amongst all the 4 cells. This is rather puzzling, since this cell also exhibited the lowest short circuit current density of all, with a value of about 18 mA/cm^2, compared with the highest j_{sc} value of 28 mA/cm^2 for cell 149-2, which displayed the lowest response. The same trend of course is also shown in the quantum efficiency plot for the 4 cells, given in Fig.7.20. The peaks of the curves are somewhat broader here, extending from about 700 to 1000 nm. It is also noted here that the response of all the cells at the longer wavelength of 1300 nm is fairly small. This is a point relevant to the results of the measurements of the diffusion length in these cells, which are presented next.

7.4 (f) Results on Estimates of Diffusion Length in $CuInSe_2$ Cells

In this study, using the photocurrent-capacitance method, the diffusion length L_n for electrons was estimated on 5 different samples. Of the 5 samples tested, 3 were annealed cells namely 149-1, 149-2, 125-3, while one sample was un-annealed (125-1) and another sample was the commercial $CuInSe_2$-based cell (CIS-4). In this section, first the results of L_n-estimations are presented for the annealed cells; then a comparison between one annealed and one un-annealed cell is given and finally, the L_n-estimate for the commercial cell is given.

Figs.7.21(a) and (b) show two plots of ΔI against $1/C_p$ for annealed cell 149-2, where straight lines through the experimental points have been extrapolated to the $1/C_p$ axis. Fig.7.21(a) indicates $1/C_p$ intercepts for three different slit widths, where the wavelength of the incident monochromatic light beam was maintained at a value of 1.2 μm. Here, it is seen that, while the extrapolated intercepts were not exactly coincident, they agree with each other to within less than about 10%.The inset to this figure shows a plot of the same experimental points, where the $1/C_p$ axis is expanded between 0.2 and 0.7 nF^{-1}, indicating the linearity of the points. Fig.7.21(b) shows results on the same sample with variation in wavelength from 0.9 to 1.3 μm for a fixed slit width of 4 mm. Here, the extrapolated $1/C_p$ intercepts are more spread out than those in Fig.7.21(a). However, the values for the wavelengths of 0.9 and 1.0 μm should really be excluded, since the αW condition is violated in this case. The smaller intercept for the 1.3 μm setting is due to the very low, and thus less accurate, measurement of photocurrent at this wavelength. The L_n value for this sample, obtained by averaging out the intercepts of the measurements taken at a 4 mm slit width (Fig.7.21(a)) and at a 1.2 μm wavelength setting (Fig.7.21(b)), was around 3.4μm, as indicated in Table 7.2, where the L_n estimates on 4 of the cells are given.

Figs.7.22(a) and (b) show similar plots for annealed cell 149-1, where the insets to both figures again show more clearly the experimental points for these measurements. Here, the experimental values for ΔI, as plotted in the these two figures, show less linearity for the same variation of $1/C_p$ (i.e. variation of reverse bias) compared with those of cell 149-2. However, in order to obtain L_n estimates from this sample, straight lines were extrapolated to the $1/C_p$ axis from only the first 6 points in the lower reverse voltage range. It is noted from Fig.7.22(a) that, despite this procedure of using only part of the observed ΔI variation, the spread of intercept values in this sample with variation of slit width is not large. The same may be said of the intercept values obtained through variation of wavelength in Fig.7.22(b), except for the less accurate value corresponding to the 1.3 μm wavelength. The L_n value for this cell, again obtained from the averaged intercepts of the 1.2 μm wavelength and the 4 mm slit width measurement, was about 2.7 μm, which is of the same order as that for cell 149-2 (Table 7.2).

The ΔI-$1/C_p$ variations for the third annealed sample 125-3 are shown in Figs.7.23(a) and (b). Here, again, the experimental point variation exhibited some curvature and the extrapolated straight lines were again drawn from the first 6 points at the lower reverse bias range. Unlike the results for the two previous cells, the intercepts for the slit width measurements were somewhat spread out, as shown in Fig.7.23(a), while those for the wavelength variation measurements given in Fig.7.23(b), were even more so. Furthermore, the intercept of the 1.2 μm measurement of Fig.7.23(b), where the slit width was 4 mm, did not agree with that of the 4 mm slit width measurement (Fig.7.23(a)), corresponding to the same conditions. With a difference of about 20%, the average value of L_n was about 2.6 μm (Table 7.2).

Measurement of photocurrent-capacitance was also attempted on one un-annealed cell, 125-1, with a similar variation of slit width and wavelength. However, the trend of the ΔI experimental points, against $1/C_p$, did not yield a straight line at all under any of these conditions. This is indicated in Fig.7.24(a), where a comparison is made between the results on this un-annealed cell and cell 149-2, which *was* annealed. The comparison is made under similar conditions of wavelength and slit width settings. Here, it is clear that the data points for the un-annealed cell could not be extrapolated in a meaningful way to the abscissa. By contrast, those for annealed cell 149-2 do have a region of sufficient linearity for extrapolation, resulting in a satisfactory negative $1/C_p$ intercept. Fig.7.24(b) shows the same experimental data, where the $1/C_p$ range is plotted on a larger scale between 0.1 and 0.7 nF^{-1}, with those for another wavelength of 1.0 μm. The difference between the characteristics of the two cells is thus further emphasized.

In order to evaluate the performance of the $CuInSe_2$ /CdO cells relative to that of a commercial cell, an L_n-estimate was also carried out on the commercial cell CIS-4, whose j-V characteristics were shown earlier in Fig.7.18. The photocurrent-capacitance measurements on this cell were similarly carried out as done in the $CuInSe_2/CdO$ cells with variation of slit width and incident wavelength and the results are shown in Figs.7.25(a) and (b) respectively. Fig.7.25(a) shows that the extrapolated lines from the experimental points converge, yielding an approximate L_n value of the order of 1.3 μm. This value is of a similar magnitude to that from Fig.7.25(b) for the wavelengths of 1.1 and 1.2 μm.

7.4 (g) Results on Capacitance-Voltage Measurements

Capacitance-voltage characteristics of some of the cells are presented here. Fig.7.26 shows a Mott-Schottky plot of $(A/C_p)^2$ against bias voltage for the three annealed cells 149-1, 149-2 and 125-3. The curve for the commercial cell is also shown for comparison. It is seen here, that in the reverse direction, the slopes of the characteristics of the three annealed cells are not very different from one another, yielding a corresponding slope-determined carrier concentration in the bulk in the range of 5×10^{16} to about 10^{17} cm^{-3}. It is apparent, however, that near zero bias, the trend of the points exhibits a downward curvature for all the cells. This is even more pronounced in the case of the commercial cell, shown by the solid circles, suggesting that the doping profile of the absorber layer in these cells decreases as the metallurgical junction is approached. The slope of the linear region of the characteristics of the three annealed samples in the higher reverse bias region, if extrapolated, would yield an intercept on the positive bias voltage axis of about 4.0 volt, which is rather large for these cells. However, extrapolation from the curved region (not shown), at small reverse bias, would yield a much smaller voltage intercept. Ideally, the intercept on the voltage bias axis in such a plot would yield the value of the built-in potential for the junction.

Fig.7.27 presents another Mott-Schottky plot, showing a comparison between the characteristics of annealed cell 149-2 with that of un-annealed cell 125-1. The slopes of the two curves appear similar at higher reverse bias; however, it is quite evident that the behaviour of the two cells near zero bias is different. While the experimental points of the annealed cell 149-2 exhibit some curvature between 0 and -1.0 volt, the points of the un-annealed cell show a continuation of the same slope from the larger reverse bias region. The intercept of the extrapolated line from the two curves is also different giving a value for the annealed cell of some 4.0 volts, compared with that for the un-annealed cell of about 1.5 volt.

7.4 (h) Results on "Forming" of Un-annealed CuInSe$_2$/CdO Cells

Frequently, the fabricated cells exhibited high reverse current, which it was found could sometimes be reduced . By passing a large current for an extended period of time, not only was the leakage current reduced, but also the illuminated characteristics were slightly improved as well. This treatment, which may be called electrical "forming", is indicated in Figs.7.28(a) and (b), where the illuminated and dark characteristics are shown for cell 110-2. In both figures, the characteristics are plotted before and after the forming treatment. The forming was carried out for a period of about 40 hours in darkness, where the initial reverse bias current density and voltage were set at about 50 mA/cm^2 and 10 volts respectively. After some 40 hours, the reverse current decreased by more than one order of magnitude to about 1 mA/cm^2 for the same applied reverse voltage. This is better seen in Fig.7.28(b), where the improvement in rectification is evident. From Fig.7.28(a), it is seen that the forming also increased slightly the open circuit voltage from about 0.33 to about 0.4 volt, the short circuit current from 25 to roughly 27 mA/cm^2 and also the fill factor from a value of 0.35 to a value of about 0.4.

7.4 (i) Results on Aging in Un-annealed CuInSe$_2$/CdO Cells

Cells fabricated on un-annealed substrates often deteriorated with time, exhibiting a reduction in their photovoltaic performance. This is shown here, in Fig.7.29(a), where the j-V characteristics of CuInSe$_2$/CdS/CdO cell 83-5 are presented, as measured just after the cell was fabricated (open circles) and also following a period of about 2 weeks (solid circles). During this time, the cell was stored in air at room temperature. As indicated in this figure, the largest degradation in this cell was evidenced in its fill factor, where the reduction in this parameter was about 20%. The reduction in V_{oc} of 10% was also significant. In contrast, however, cells fabricated on pre-annealed CuInSe$_2$ substrates did not undergo any detectable degradation at all and their characteristics remained essentially unchanged with time. This is shown in Fig.7.29(b), where the j-V characteristics of CuInSe$_2$/CdO cell 125-3 are given as measured just after cell fabrication (open circles) and following a period of over two months (solid circles). It is clear from this figure that this annealed cell was far more stable with time as compared with cell 83-5, shown in (a), which was not annealed. It is noted here that both cells were fabricated on a {112} cleavage plane, and while cell 83-5 had an intermediate CdS layer, they both had a comparable CdO film thickness.

7.5 DISCUSSION

The intention of the work in this chapter was to test the grown single crystal material of $CuInSe_2$ for device quality and not especially to develop techniques to make the most highly efficient cell possible, since this would have involved changes in device structure and much effort to obtain optimum fabrication processes. The $CuInSe_2$/CdO structure turned out to be sufficient for test purposes and made use of extensive experience in this laboratory with the d.c. reactive sputtering of CdO. The conversion efficiency, reported here, of around 6%, without the use of a lattice matching interlayer is surprising, since the lattice mismatch between the unrestructured {112} plane of $CuInSe_2$ and the {111} plane of cubic CdO is some 23%. It should be pointed out here also that, an anti-reflection coating and an optimized collecting grid were not used on cells fabricated in the present work. Some early cells were indeed made with the structure of $CuInSe_2$/CdS/CdO, that is with the CdS interface layer present but the fabrication techniques were not very well developed at that time and pre-annealing of the substrate was not done.

No claim is made here for high accuracy in the measurement of the illuminated cell parameter values of j_{sc}, V_{oc}, FF, and η, since the solar simulator used has not been directly checked against precise standards. However, the measured values are probably accurate to about 10 %, since agreement was obtained on one cell between our measurement and that at NREL and because our simulator yielded 12% for the efficiency of the commercial cell, for which Siemens Solar reported about 13%.

The present results show that annealing of the $CuInSe_2$ substrate, prior to the deposition of the CdO is beneficial in increasing both the fill factor and the open circuit voltage and hence also the conversion efficiency. The treatment for the single crystal $CuInSe_2$ substrates was first developed by L.S. Yip [7.10], [7.11], for his abrasively polished and etched surfaces. However, while the annealing was beneficial for his structures, which involved a CdS interface layer with the $CuInSe_2$, it was not clear at first, whether it would be equally beneficial for the cleaved $CuInSe_2$ surfaces, used in this study, not subjected to the abrasive polishing and its consequent microscopic damage to the lattice. Furthermore, the present structure involved an interface with CdO, not CdS. Never-the-less, the results in this chapter, indicate that the beneficial consequences of the annealing process may in fact apply generally, whether the substrate surface is cleaved or abrasively polished or interfaced with CdS or CdO. The difference between the Mott-Schottky plots for an annealed and an un-annealed cell, near zero bias, suggests that the acceptor concentration in the substrate near the device junction was reduced from about 5×10^{16} to about 2×10^{16} cm^{-3} . The acceptor concentration in the range of 5×10^{16} to about 10^{17} cm^{3} for the bulk material has been confirmed by independent Hall effect measurements made on similar p-type stoichiometrically prepared $CuInSe_2$ [7.12]. Thus, it is speculated here that the annealing of the substrate may cause a reduction in the carrier concentration near the sample surface, possibly due to the loss of Se from the outer layer of the substrate during the heat-treatment; this improves the junction integrity by increasing the internal shunt resistance. It is of course well established that heating p-type $CuInSe_2$ material *in vacuum* at high enough temperature for a prolonged period of time causes it to change its conductivity from p- to n-type. This has also been demonstrated to occur at atmospheric pressure if sufficient annealing is used.

While very little work on device aging was done in the present study, it appears that the annealing process may help, here too, in stabilizing the cell against performance degradation. While the un-annealed cells degraded with time, it was found that they could also improve with electrical "forming", that is the passage of a high reverse current through the device for some time. This appears to be similar to what has been observed over many decades with the selenium rectifiers, which are no longer used. The action is possibly due to the drift of charged ions out of a layer close to the junction causing a depopulated zone of acceptors near the junction just as has been speculated for the action of the annealing process.

The photocurrent-capacitance method, employed by C.H. Chan for thin film Se/CdO cells in this laboratory [7.18], [7.19], [7.20], [7.21], was used, for the first time, on single crystal $CuInSe_2$/CdO devices as well as on a commercial thin film $CuInSe_2$-based cell. The method, in this work, yielded values of about 3 μm for the diffusion length of electrons for the $CuInSe_2$/CdO cells and, in comparison, about 1.3 μm for the commercial $CuInSe_2$-based thin film cell. This suggests that, cells with single crystal substrates should give higher photovoltaic performance once the cell fabrication techniques have been fully developed. The error of the reported L_n estimates is probably about 20% but the measurements were very preliminary and the method could be developed further to obtain higher accuracy. This is needed for the wavelength of 1.3 μm, where αW is small as required by theory but where the dark-to-illuminated change in photocurrent is weak relative to the background noise of the measurement. The photocurrent-capacitance method did not work for the un-annealed $CuInSe_2$/CdO cells because of the observed high shunt current in these devices. This is because the method depends on a reverse current arising from carriers generated from the depletion and diffusion regions and not from current driven through an undesired parallel shunt path. On the other hand, the method is tolerent to series resistance in cells which is consistent with results obtained by C.H. Chan in his work with Se/CdO thin film structures [7.18], [7.19], [7.20]. Unlike the EBIC technique, however, the photocurrent-capacitance method has the advantage of being a non-destructive technique which could be developed as a diagnostic tool for in-line photovoltaic cell processing.

As a final note in this chapter, from the surprising efficiency of 6%, obtained on the $CuInSe_2$/CdO cells with an apparent lattice mismatch of 23%, it is of interest to speculate that the junction in such a cell may not be at the metallurgical boundary between the CdO and the $CuInSe_2$. The reason for this speculation arises from the result of an experiment not so far reported in this chapter. Fig.7.30 shows the j-V characteristics of annealed cell 125-3 before and after *complete removal* of the active part of the CdO layer. This was done by etching the CdO with a diluted solution of HCl in DI water (1:10 by volume), leaving the Au front stripes intact. Here, it is seen that, despite the CdO removal, evidence of residual photovoltaic action remained, raising the possibility that the active junction may still very well have been present. However, this is only a suggestion and further work is needed to confirm the validity of this hypothesis.

Finally, it may be said that, the work of this chapter has shown that the Bridgman-grown $CuInSe_2$ material of this laboratory has sufficient quality for potentially fabricating photovoltaic cells of great interest to the semiconductor solar cell community.

Table 7.1 Characteristics of $CuInSe_2/CdO$ Cells

		Annealing of $CuInSe_2$ Substrate [1]		CdO Layer Characteristics			Illuminated Characteristics [2]				
Cell No.	Cleavage plane	Time (hr)	Temp. (°C)	Interference colour	Thick [3] (μm)	Area [4] (mm^2)	J_{sc} (mA/cm^2)	V_{oc} (volt)	FF	η (%)	Comments
105-5	{112}	-	-	7th red	0.91	10.0	21	0.43	0.42	4.0	Un-annealed representative cell.
125-1	{112}	-	-	5th green	0.55	8.0	18	0.40	0.27	2.0	Un-annealed cell with a thin CdO layer.
83-5	{112}	-	-	6th green	0.66	7.0	23	0.40	0.46	4.8	Un-annealed cell degraded with time
110-2	{101}	-	-	6th red	0.78	6.0	27	0.40	0.39	3.8	Un-annealed cell improved with forming.
149-1	{101}	2	320	5th red	0.65	11.0	24	0.41	0.50	5.4	Annealed cell having largest active area.
149-2	{101}	2.5	360	6th red	0.78	8.0	28	0.42	0.51	5.7	Annealed cell having highest L_n estimate.
125-3	{112}	2.5	360	6th red	0.78	5.3	24	0.42	0.63	6.3	Annealed cell having highest efficiency.
CIS-4 [5]	-	-	-	-	-	-	36	0.48	0.68	12.0	Active area = 0.54 cm^2. Window layer not CdO.

1. Annealing of cleaved substrate prior to deposition of CdO layer and electrical contacts.
2. Illumination level was about 100 mW/cm^2 under simulated sunlight using a xenon arc lamp. Calibration carried out using a silicon reference cell tested at the National Renewable Energy Laboratory (NREL) of Golden, Colorado.
3. Estimate of CdO layer thickness derived from interference colour using the formula: $2nd = N\lambda$, where n is the refractive index (2.5), d is the film thickness, N is the interference order and λ is the interference colour wavelength.
4. Active area of the CdO layer.
5. Commercial polycrystalline thin film cell believed to have the structure $CuInSe_2/CdS/ZnO$, supplied by Siemens Solar Industries of Camarillo, California.

Table 7.2 Estimates of L_n for Annealed $CuInSe_2/CdO$ Cells[1]

Cell No.	Area[2] (mm^2)	L_n (μm)
149-2	9.0	3.4
149-1	12.0	2.7
125-3	6.3	2.6
CIS-4[3]	60.0	1.3

1. Estimates derived from plots of ΔI vs. $1/C_p$ for a slit width of 4 mm and wavelength of 1.2 μm, according to the formula $L_n = -(1/C_p)_i \epsilon_0 \epsilon_r A_j$ where, $(1/C_p)_i$ is the $1/C_p$ axis intercept, ϵ_0 is the permittivity of free space, ϵ_r is the relative permittivity, taken to be 10 and A_j is the cell junction area.

2. Total junction area of the cell.

3. Commercial polycrystalline thin film cell believed to have the structure $Cu(In,Ga)Se_2/CdS/ZnO$.

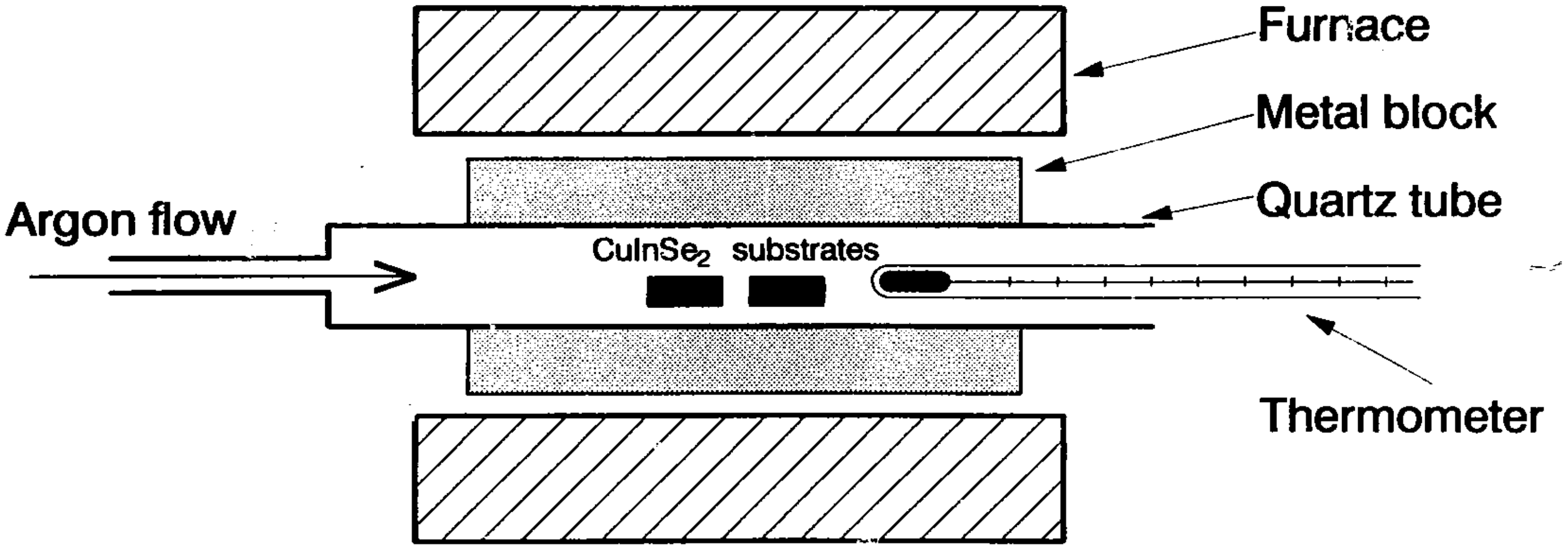

Fig.7.1 Schematic diagram showing the set-up used for the annealing of the CuInSe$_2$ substrates.

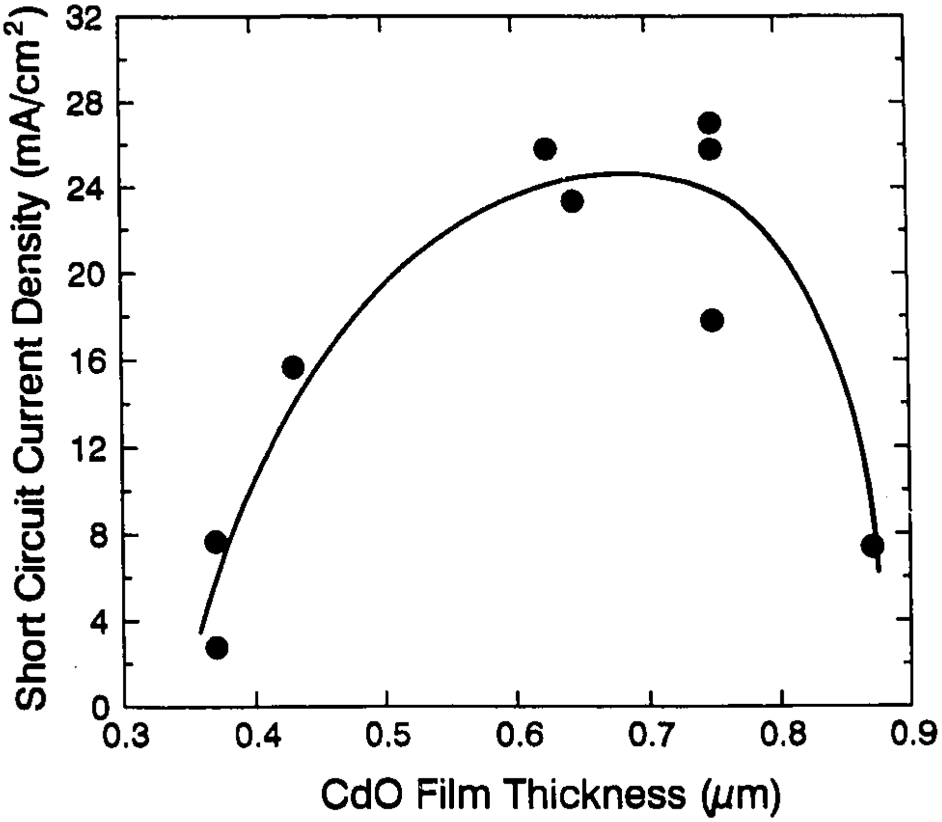

Fig.7.2 Plot of short circuit current-density, j_{sc}, against CdO film thickness for the early $CuInSe_2$/CdS/CdO cells given in Appendix A.4.

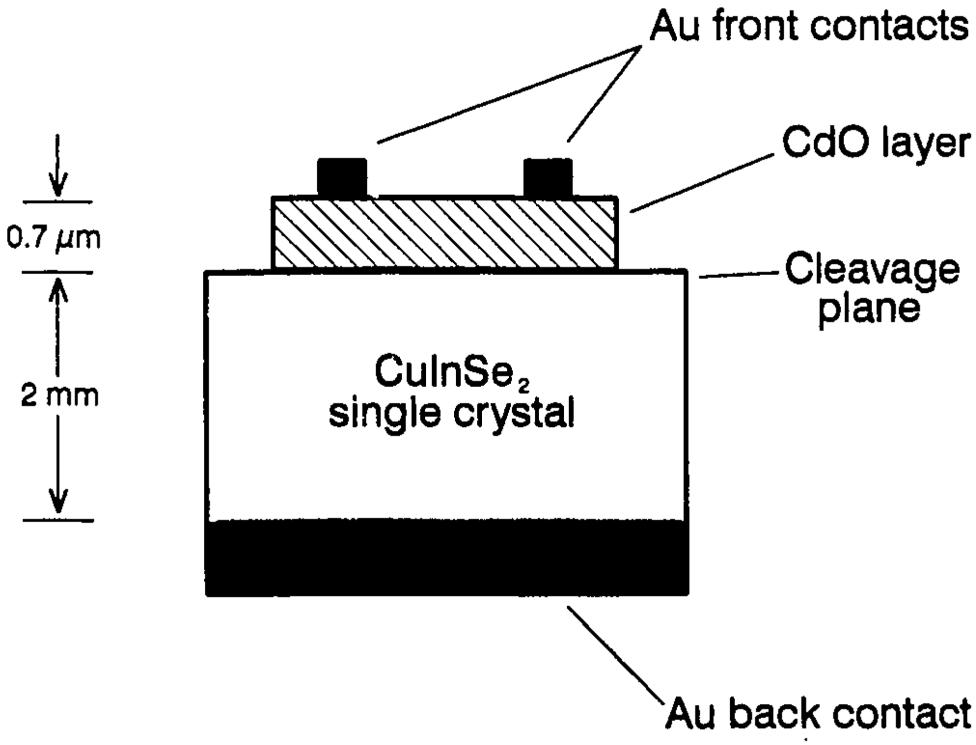

Fig.7.3 Schematic diagram of the $CuInSe_2$/CdO cell structure used in this study, showing the different device layers.

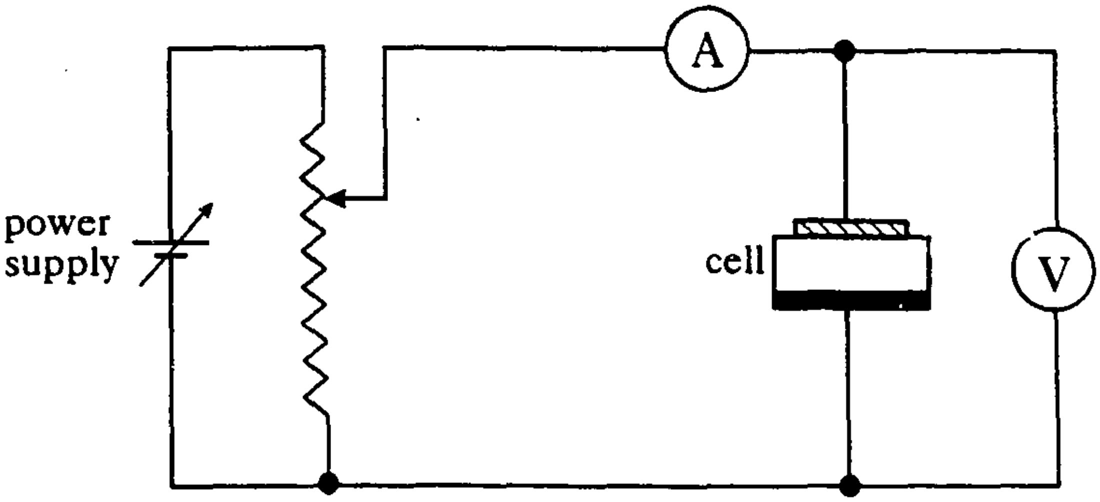

Fig.7.4 Electrical circuit diagram of the arrangement used for the measurement of the illuminated and dark current-density-voltage, j-V, characteristics of the cells.

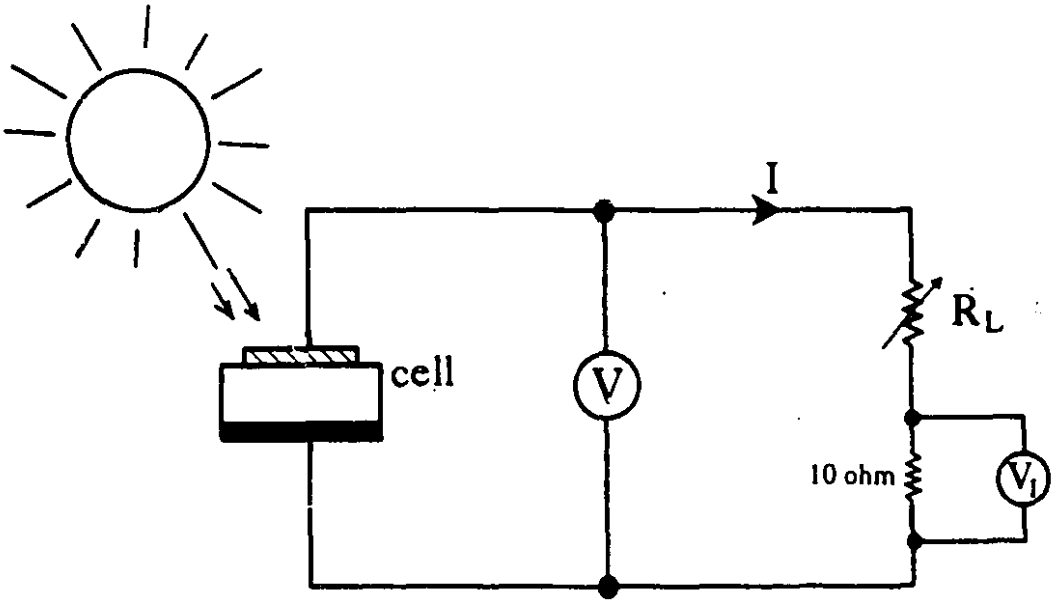

Fig.7.5. Electrical circuit diagram of the arrangement used for the outdoors measurement of the current-density-voltage, j-V, characteristics of the cells, under actual sunlight.

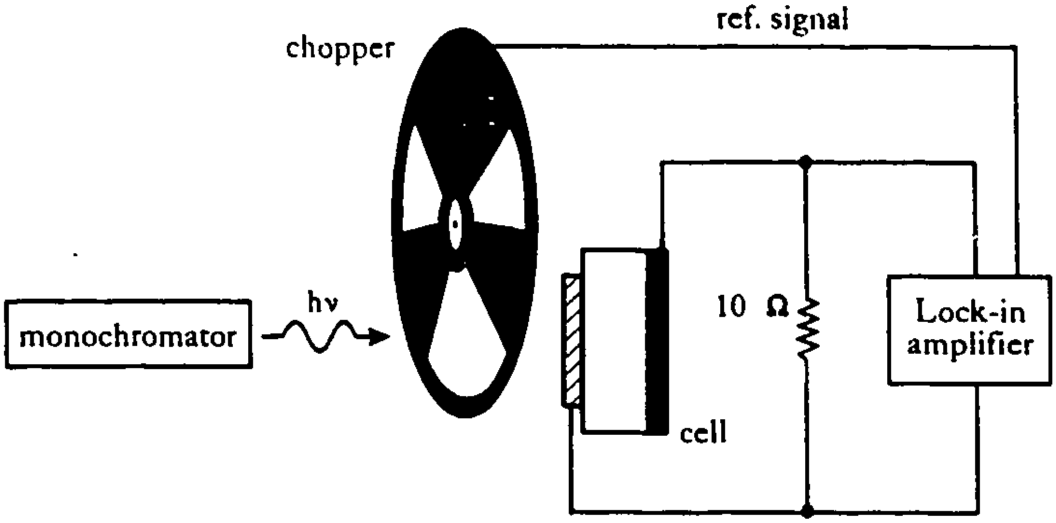

Fig.7.6 Schematic diagram of the experimental set-up used for the photoresponse measurement of the cells.

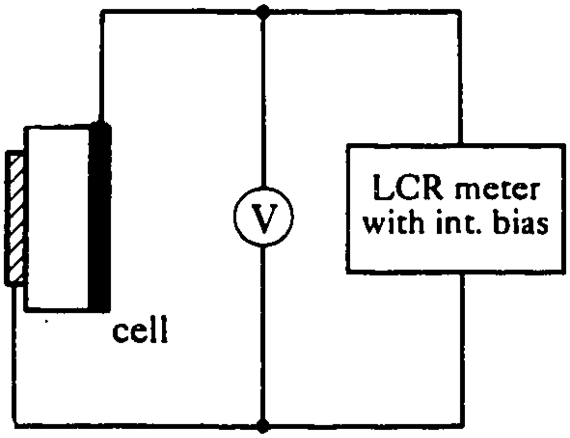

Fig.7.7 Electrical circuit diagram of the arrangement used for the capacitance-voltage measurements of the cells.

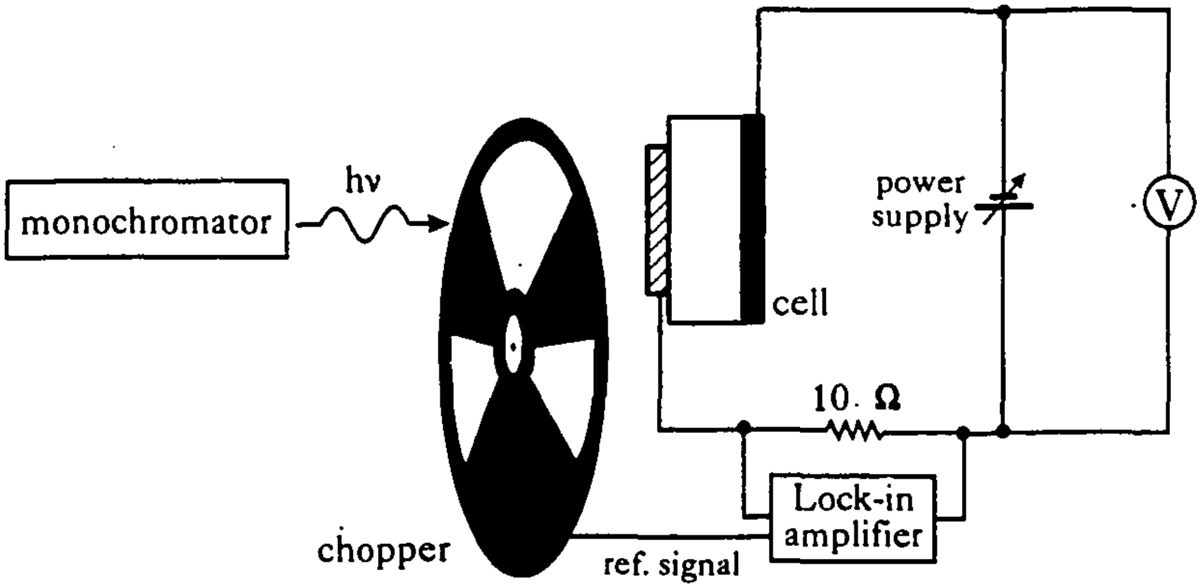

Fig.7.8 Schematic diagram of the experimental set-up used for the measurement of the illuminated-to-dark change in current, ΔI, in the photocurrent-capacitance method.

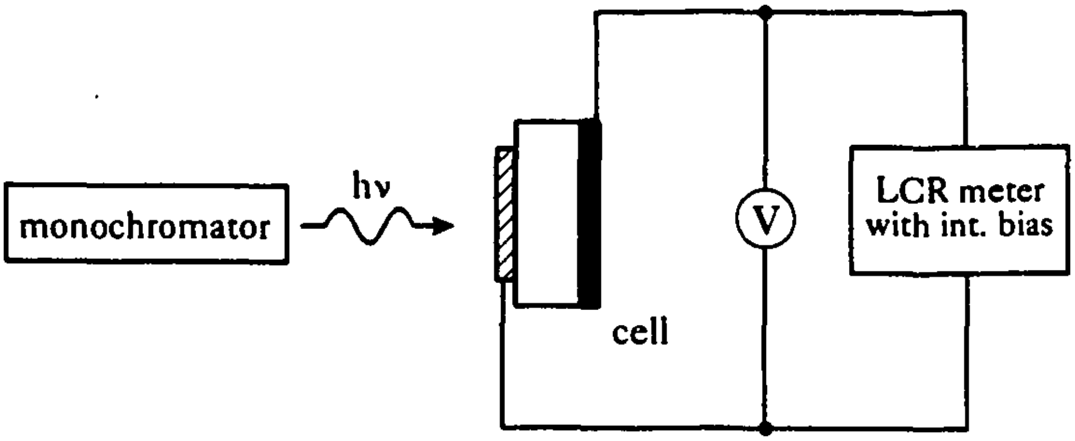

Fig.7.9 Schematic diagram of the experimental set-up used for the measurement of capacitance, C_p, in the photocurrent-capacitance method.

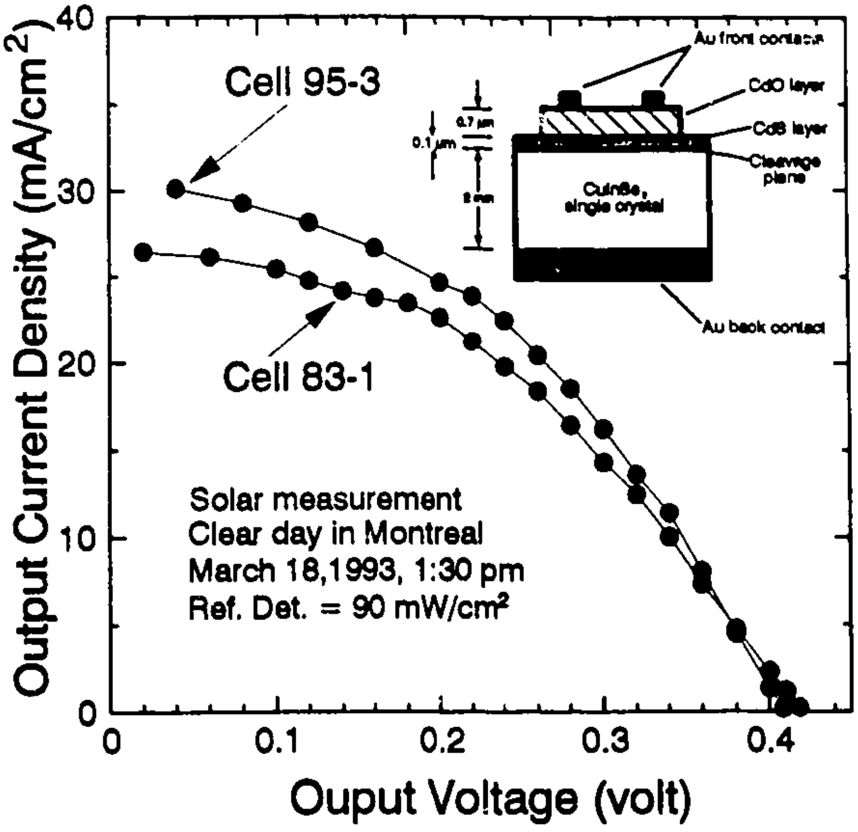

Fig.7.10 Current-density-voltage characteristics of two early CuInSe$_2$/CdS/CdO cells, measured outdoors under actual solar illumination under the conditions stated. The inset shows a schematic diagram of these early cells. (Reference detector : Molectron model PR-200).

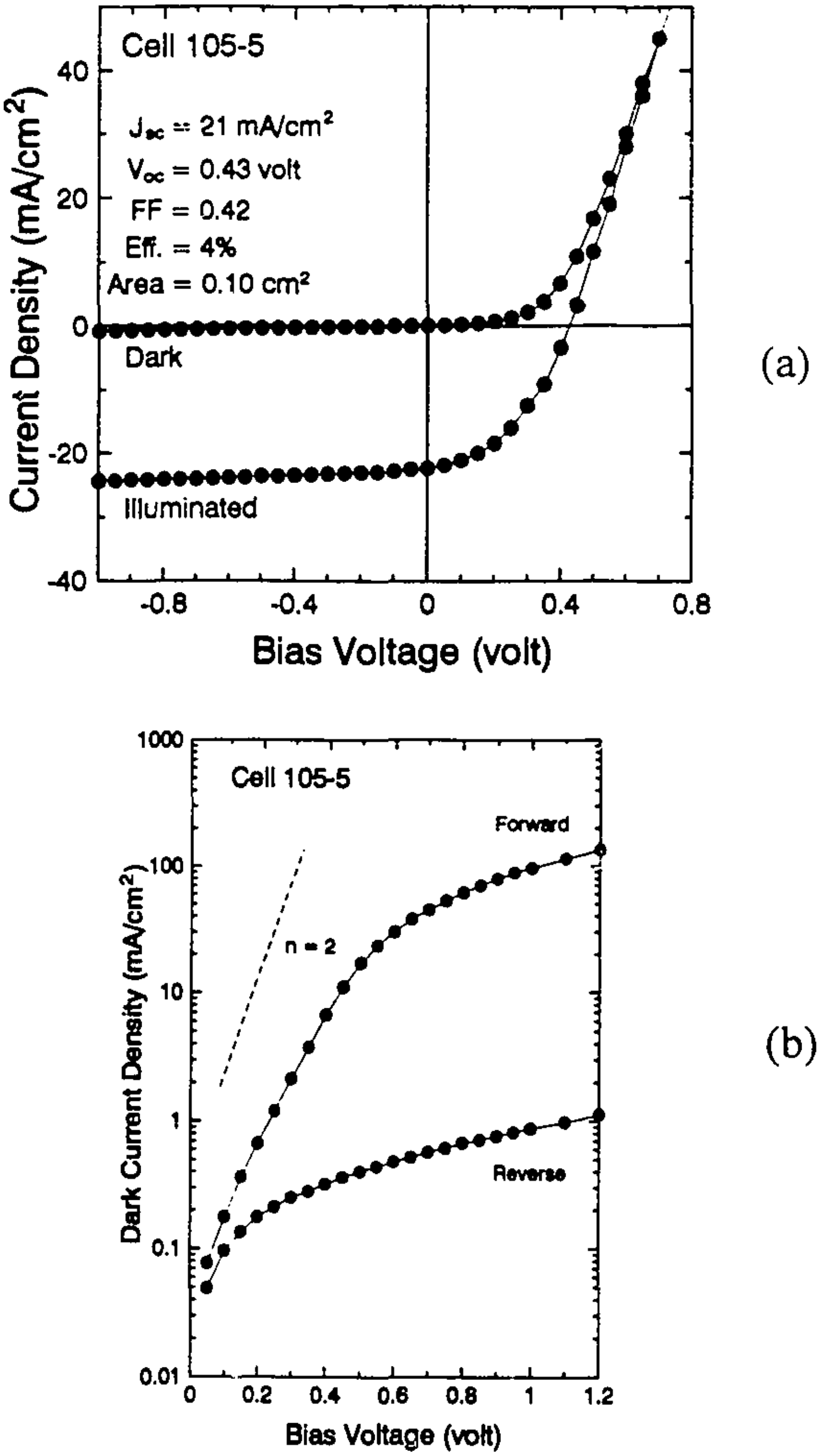

Fig.7.11 Illuminated and dark current-density-voltage characteristics of un-annealed cell 105-5 showing: (a) characteristics under simulated illumination of 100 mW/cm² and (b) dark characteristics exhibiting a rectification ratio of about 2 orders of magnitude. The broken line indicates an ideality factor of 2.

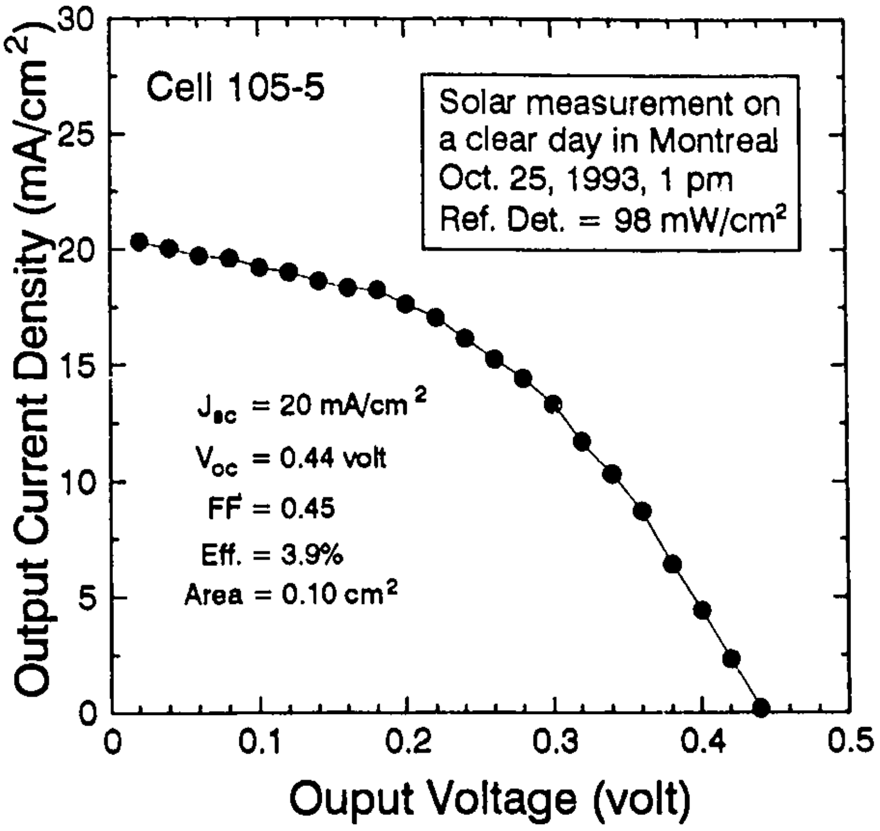

Fig.7.12 Current-density-voltage characteristics of un-annealed cell 105-5 as measured under actual solar illumination under the conditions indicated. The intensity of solar irradiation, as measured with a reference detector, was about 100 mW/cm^2.

McGill Univ. CuInSe$_2$/CdO

Sample: 105-5
Oct 12, 1993 10:37 AM
Spectrum: ASTM E892-87 Global

Temperature = 25.0°C
Area = 0.1010 cm^2
Irradiance: 1000.0 Wm^{-2}

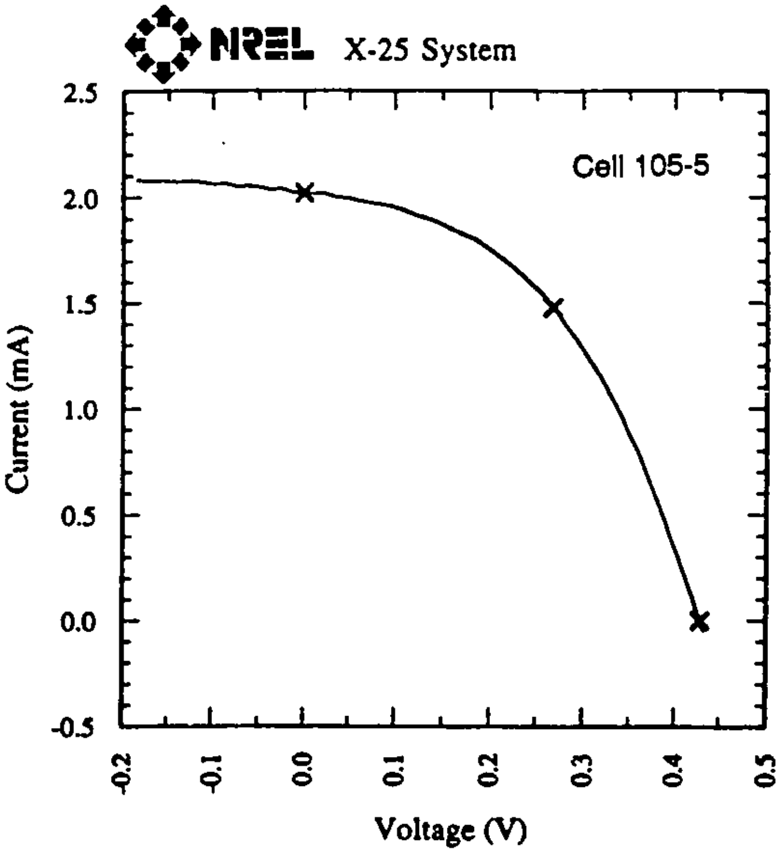

V_{oc} = 0.4290 V
I_{sc} = 2.020 mA
J_{sc} = 19.99 $mAcm^{-2}$
Fill Factor = 45.59 %

V_{max} = 0.2675 V
I_{max} = 1.476 mA
P_{max} = 0.3949 mW
Efficiency = 3.91 %

Fig.7.13 Cuurent-density-voltage characteristics of un-annealed cell 105-5 as measured at the National Renewable Energy Laboratory (NREL) under the ASTM spectrum of AM1.5 Global. The photovoltaic cell parameters are indicated in the figure.

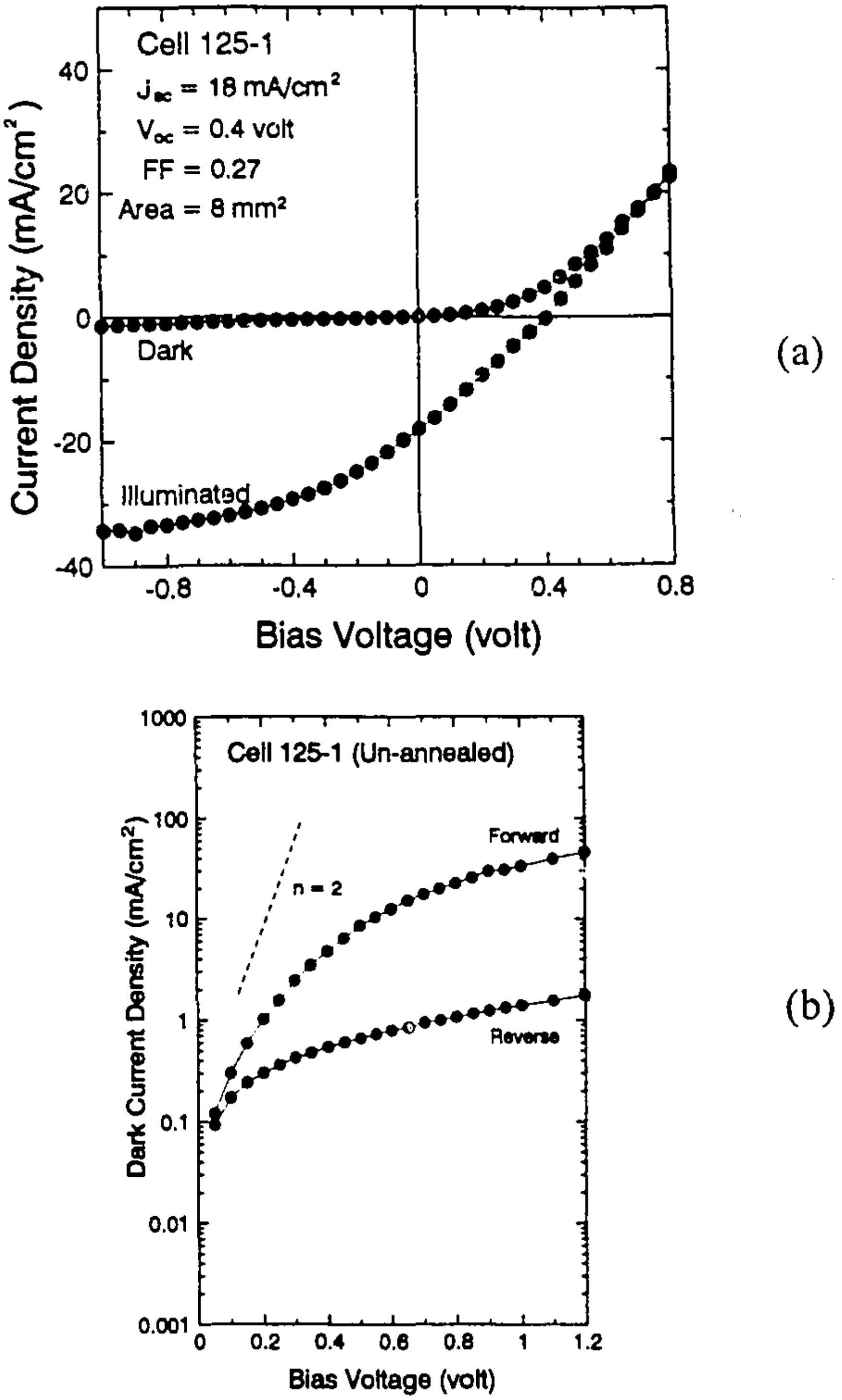

Fig.7.14 Illuminated and dark current-density-voltage characteristics of un-annealed cell 125-1, showing (a) characteristics under simulated illumination of 100 mW/cm², indicating high series resistance in the forward bias region, and (b) dark characteristics, exhibiting poor rectification as well as high shunt current at lower voltage.

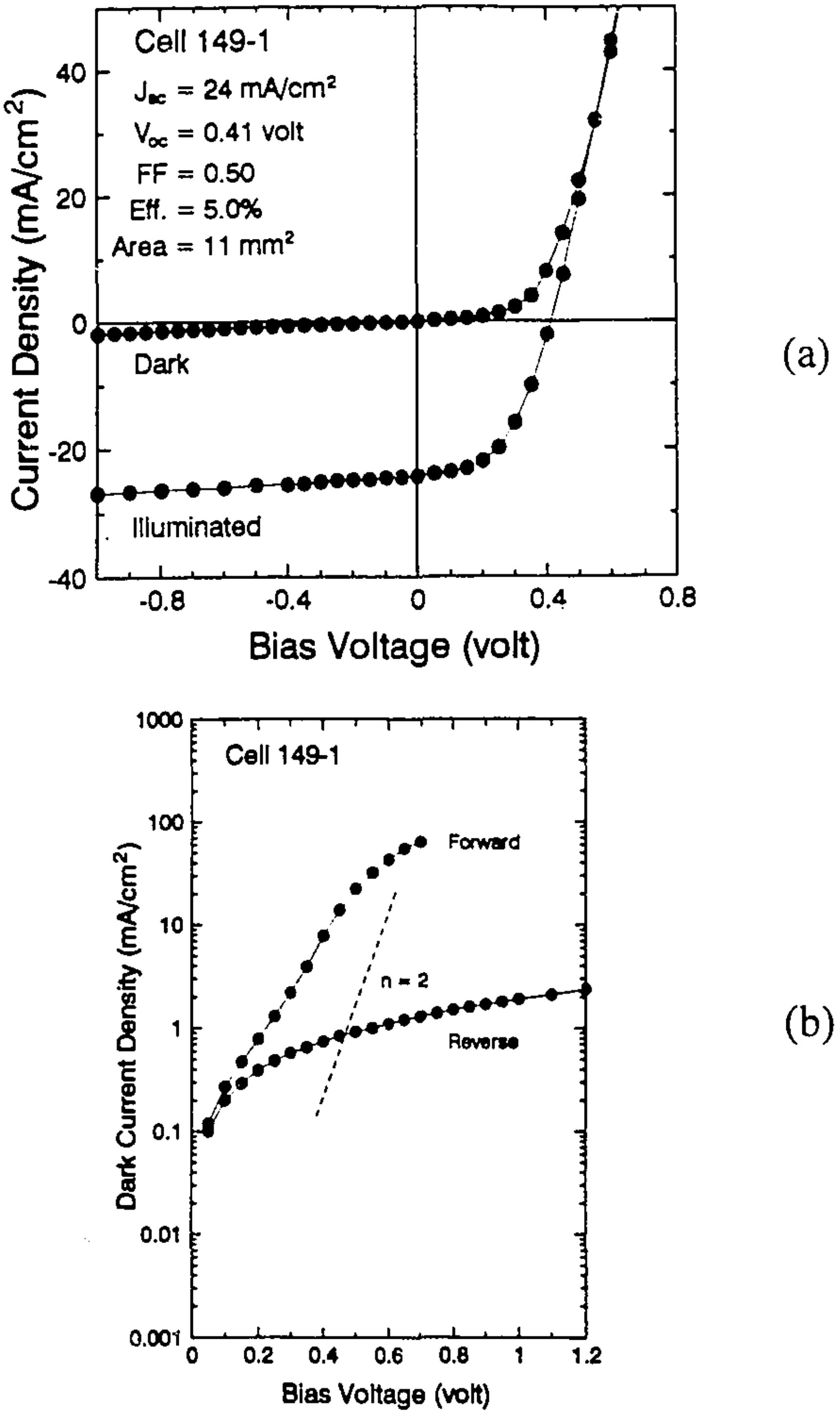

Fig.7.15 Illuminated and dark current-density-voltage characteristics of annealed cell 149-1, showing (a) characteristics under simulated illuminatuion of 100 mW/cm^2, exhibiting an improved fill factor, and (b) dark characteristics exhibiting some shunt current.

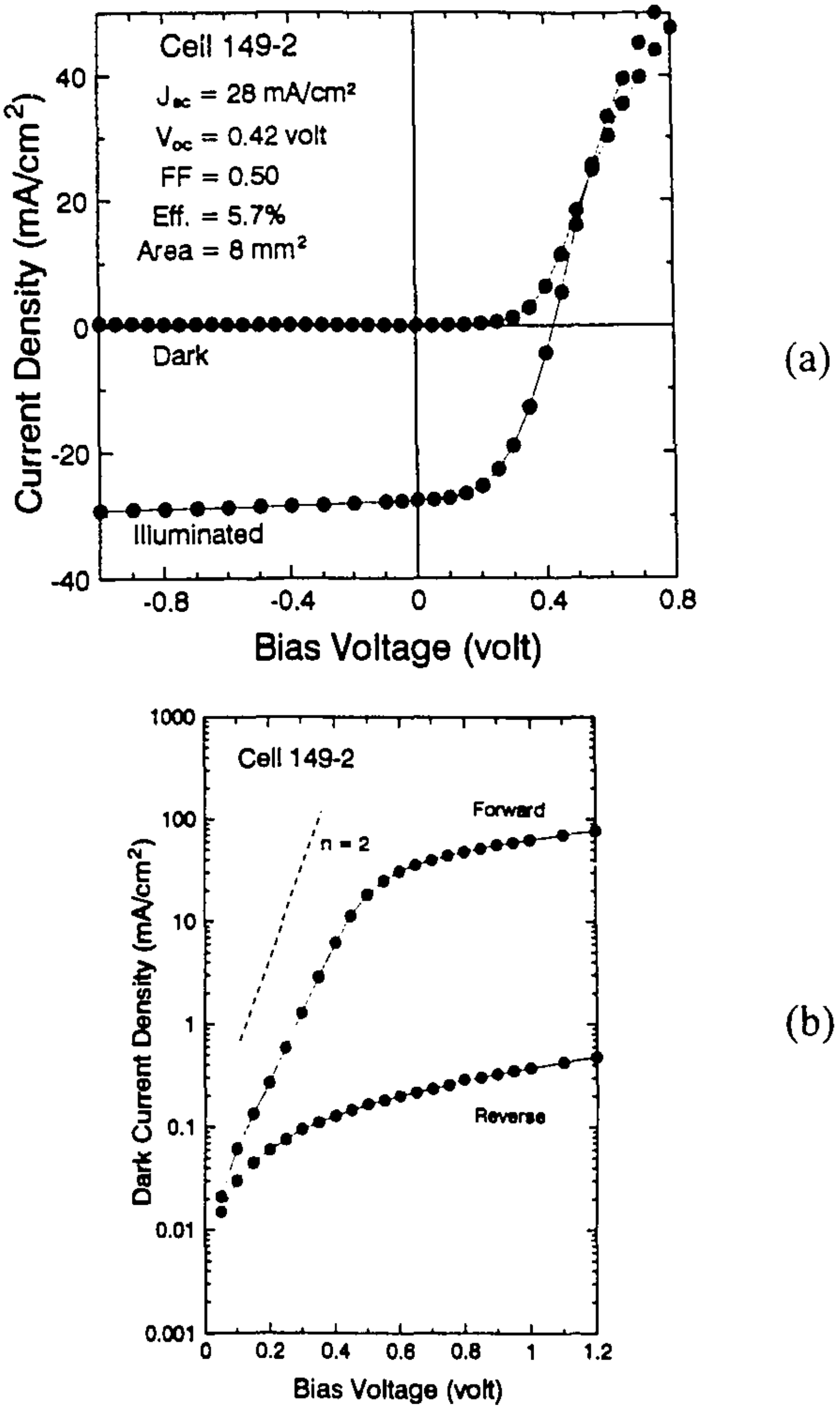

Fig.7.16 Illuminated and dark current-density-voltage characteristics of annealed cell 149-2, showing (a) characteristics under simulated illumination of 100 mW/cm^2, exhibiting a conversion efficiency of about 5.7%, and (b) dark characteristics with an ideality factor slightly greater than 2.

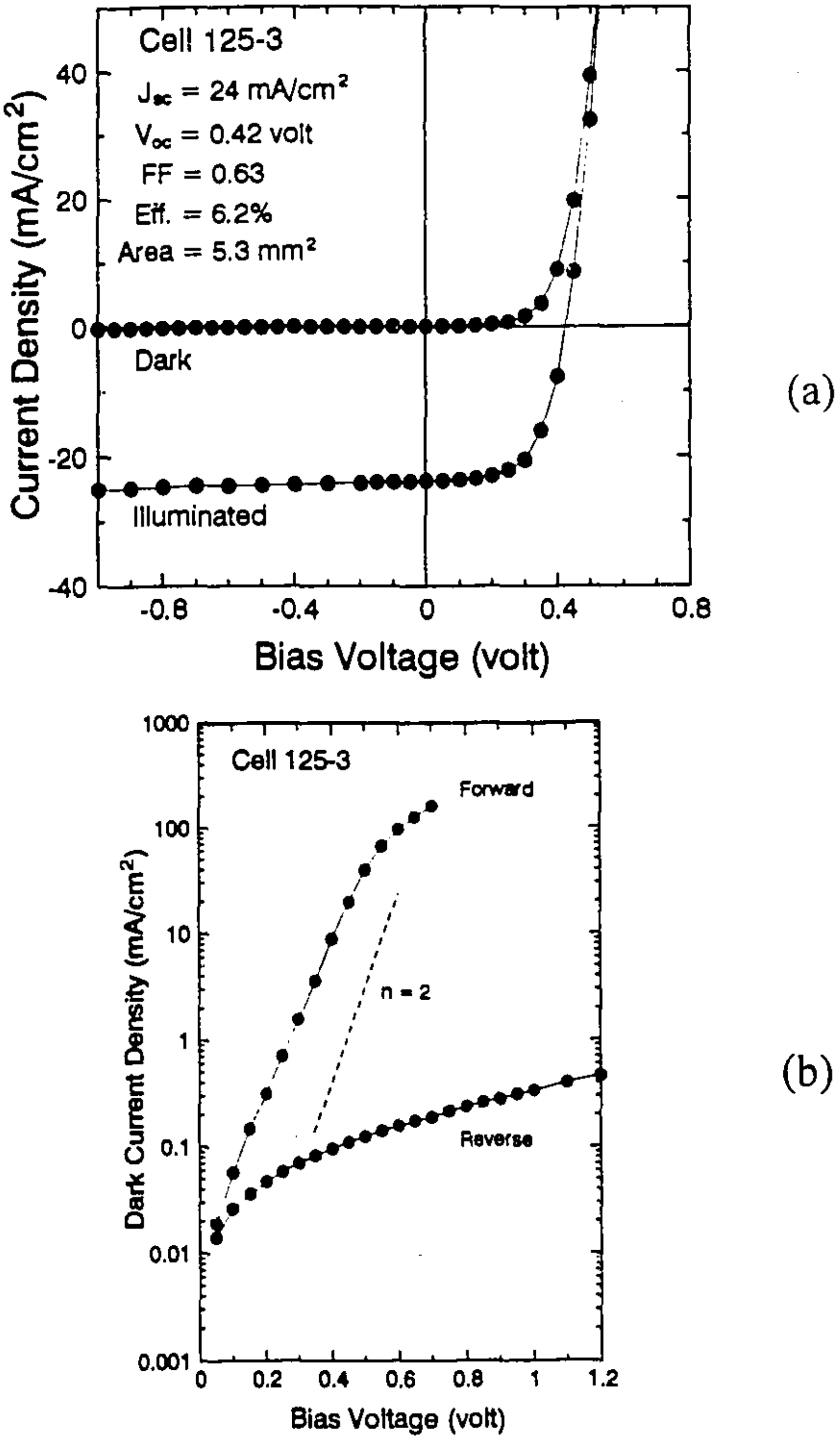

Fig.7.17 Illuminated and dark current-density-voltage characteristics of annealed cell 125-3, showing (a) characteristics under simulated solar illumination of 100 mW/cm^2, exhibiting a conversion efficiency of over 6%, and (b) dark characteristics with a rectification ratio of about 3 orders of magnitude.

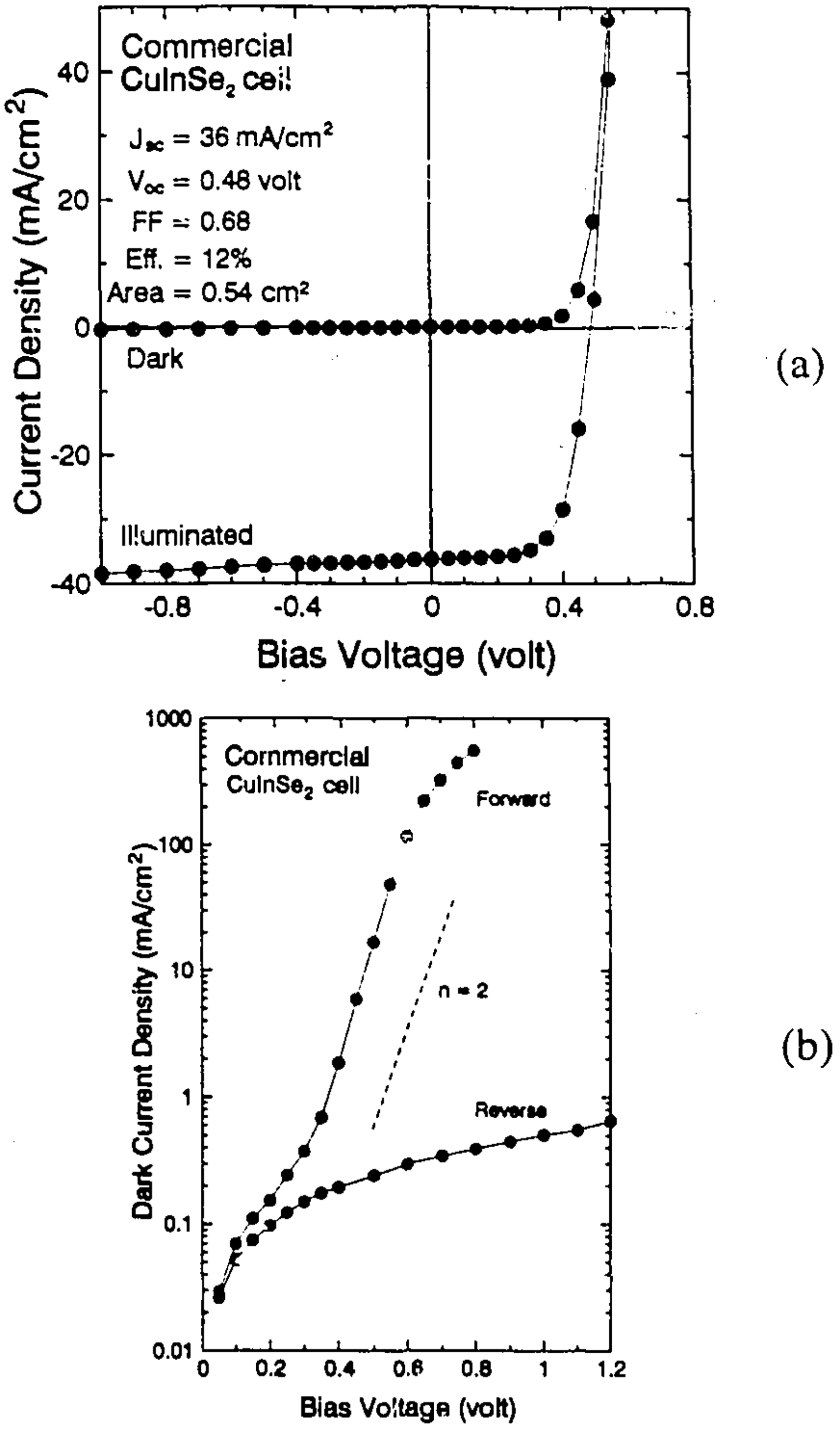

Fig.7.18 Illuminated and dark current-density-voltage characteristics of the CuInSe$_2$-based commercial cell CIS-4 showing (a) characteristics under simulated illumination of 100 mW/cm^2, exhibiting a conversion efficiency of about 12%, and (b) dark characteristics having an ideality factor of less than 2.

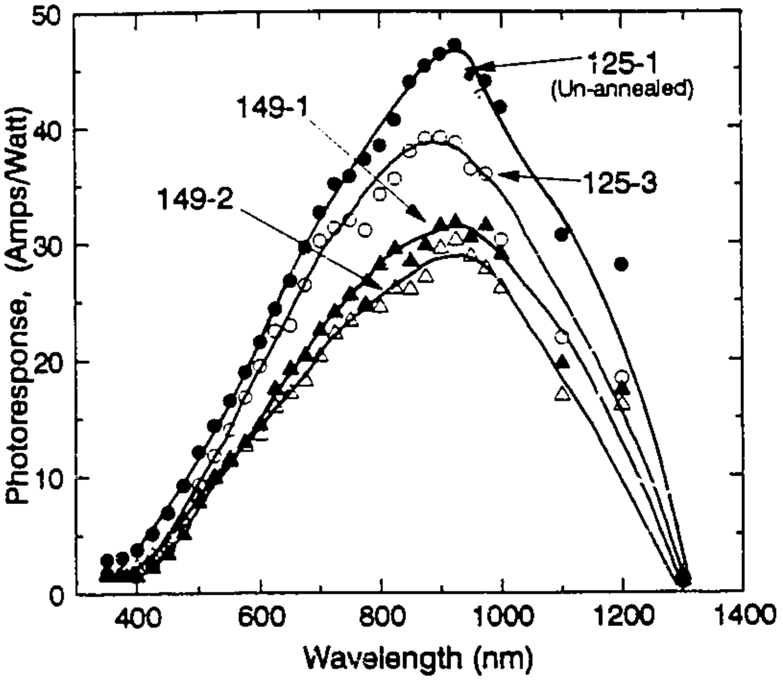

Fig.7.19 Plot of photoresponse against wavelength for the three annealed CuInSe$_2$/CdO cells 149-1,149-2 and 125-3 and one un-annealed cell 125-1.

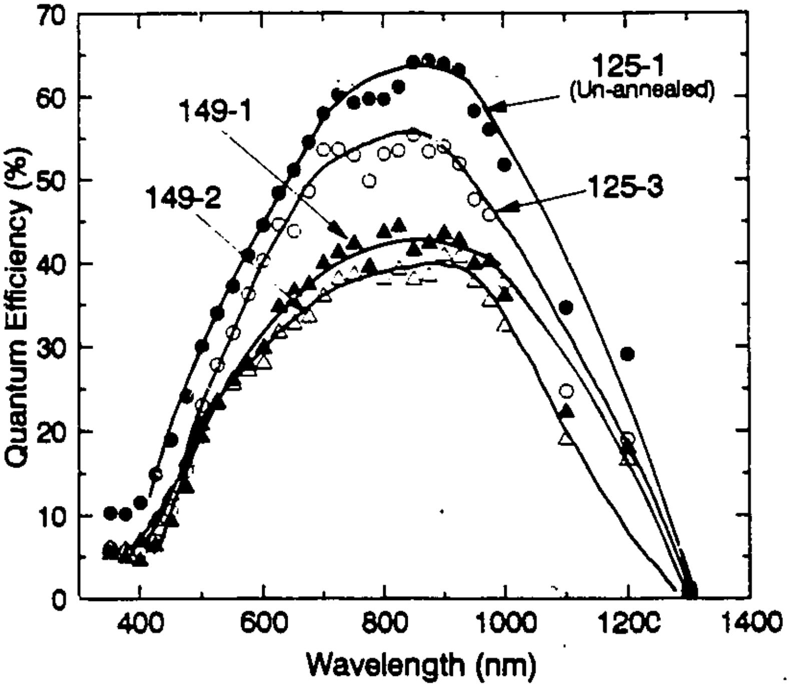

Fig.7.20 Plot of quantum efficiency against wavelength for the three annealed CuInSe$_2$/CdO cells 149-1,149-2 and 125-3 and one un-annealed cell 125-1.

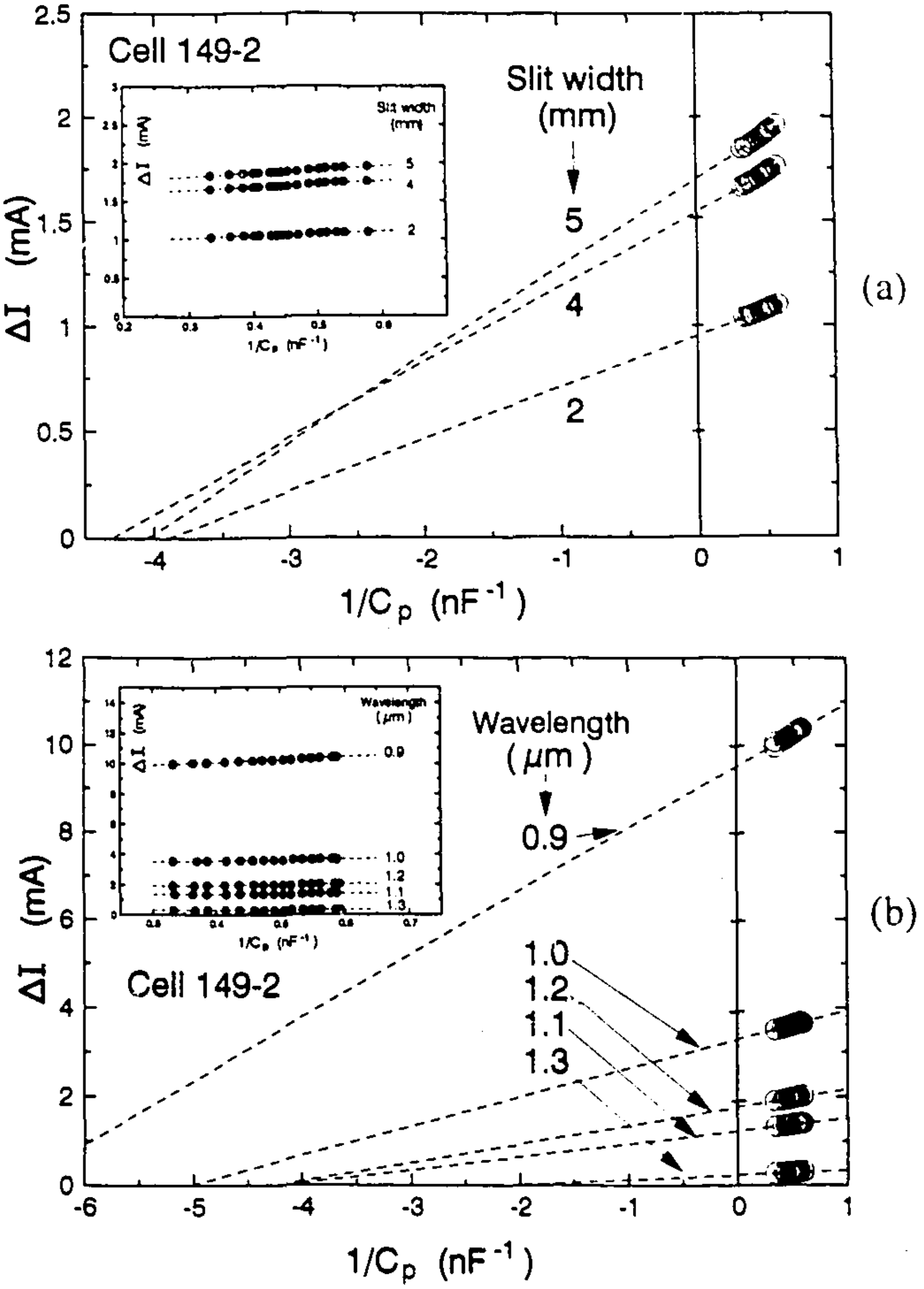

Fig.7.21 Plot of ΔI against $1/C_p$ for annealed sample 149-2 with variation of (a) monochromator slit width and (b) incident wavelength. The $1/C_p$ intercepts of the extrapolated broken lines yield an estimate of the diffusion length. The inset in both figures shows the experimental points on a larger $1/C_p$ scale.

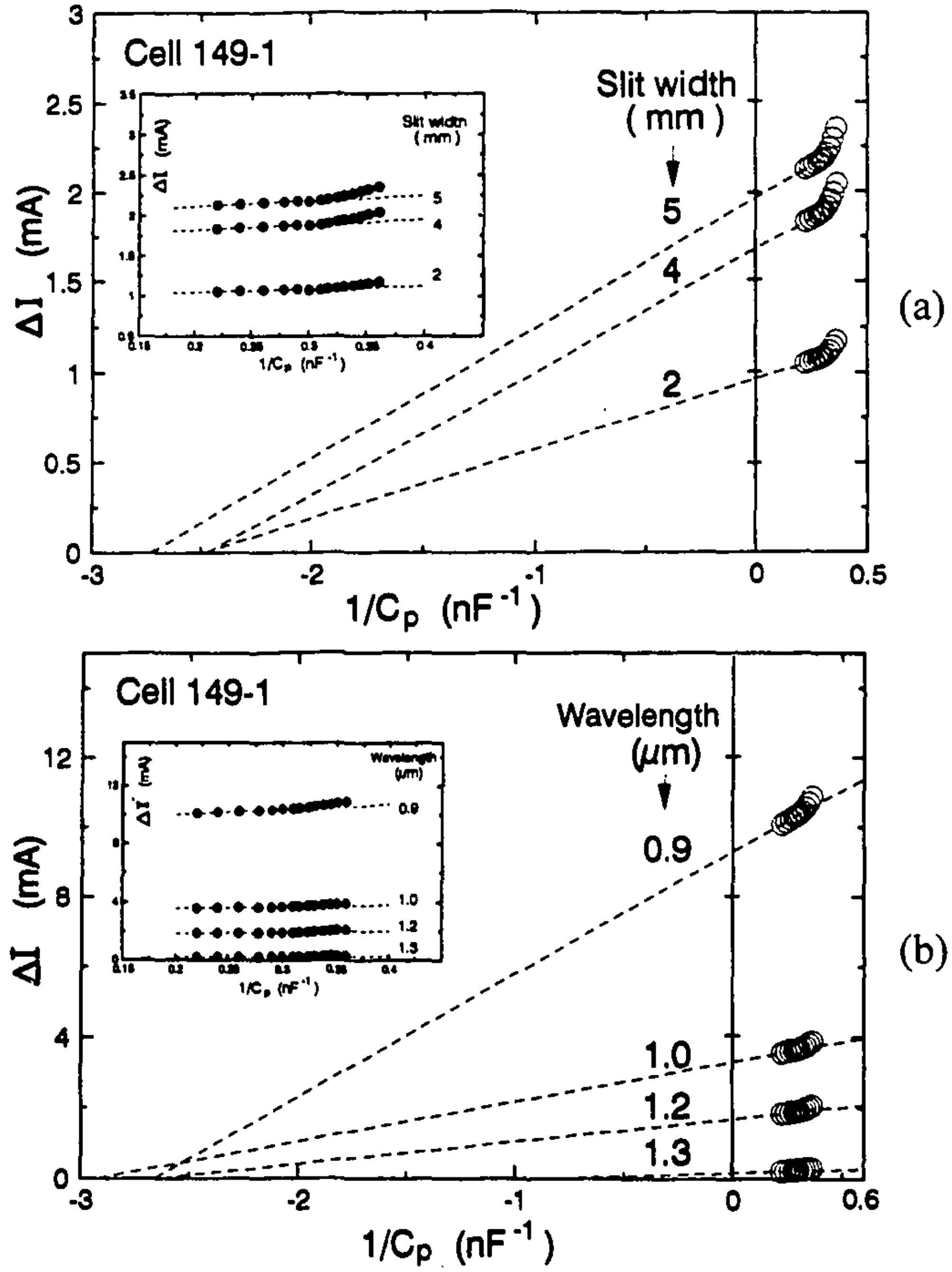

Fig.7.22 Plot of ΔI against $1/C_p$ for annealed sample 149-1 with variation of (a) monochromator slit width and (b) incident wavelength. The broken lines were extrapolated from the first 6 experimental points. The inset in both figures shows the experimental points on a larger $1/C_p$ scale.

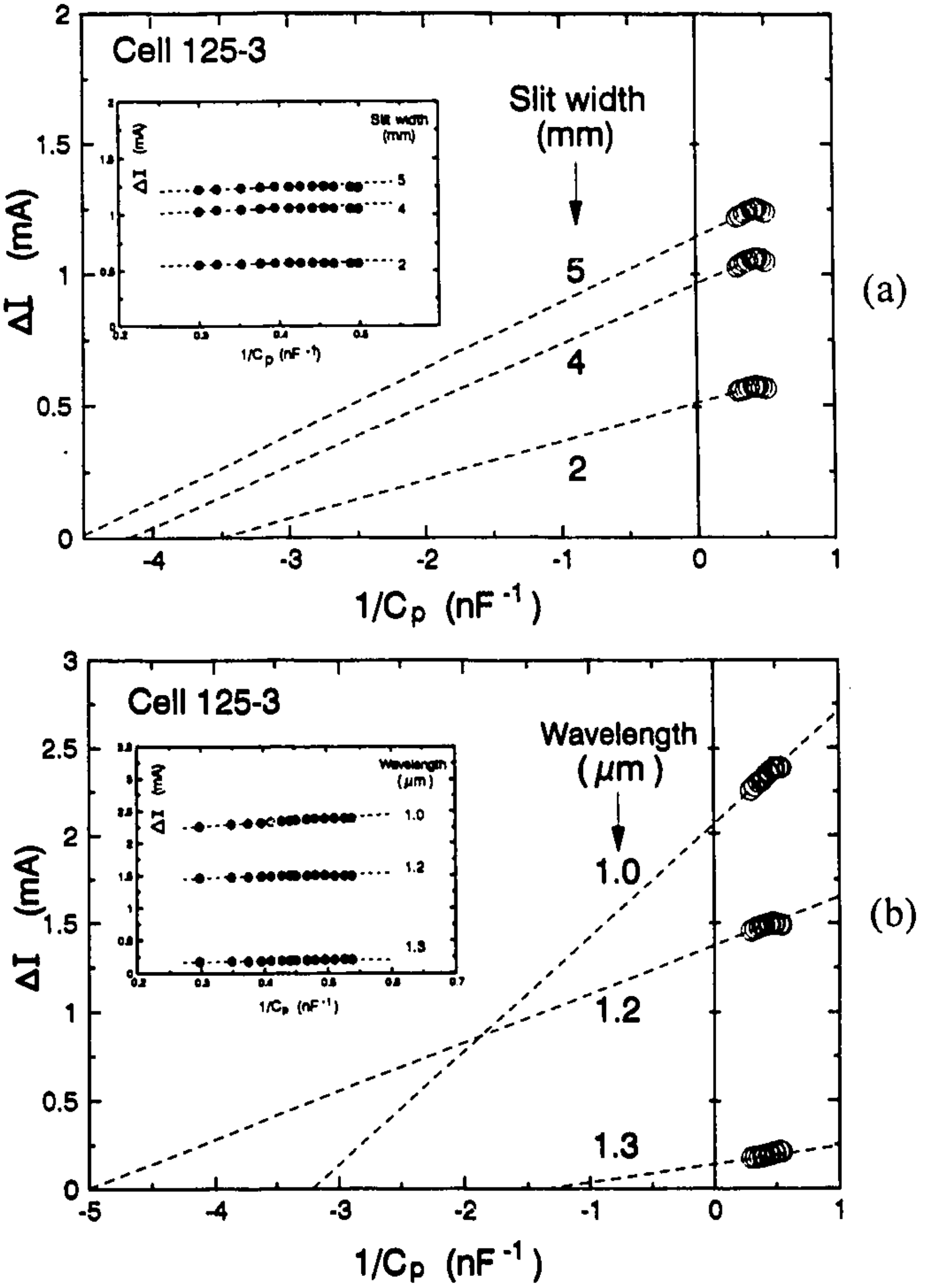

Fig.7.23 Plot of ΔI against $1/C_p$ for annealed sample 125-3 with variation of (a) monochromator slit width and (b) incident wavelength. The broken lines were extrapolated from the first 6 experimental points. The inset in both figures shows the experimental points on a larger $1/C_p$ scale.

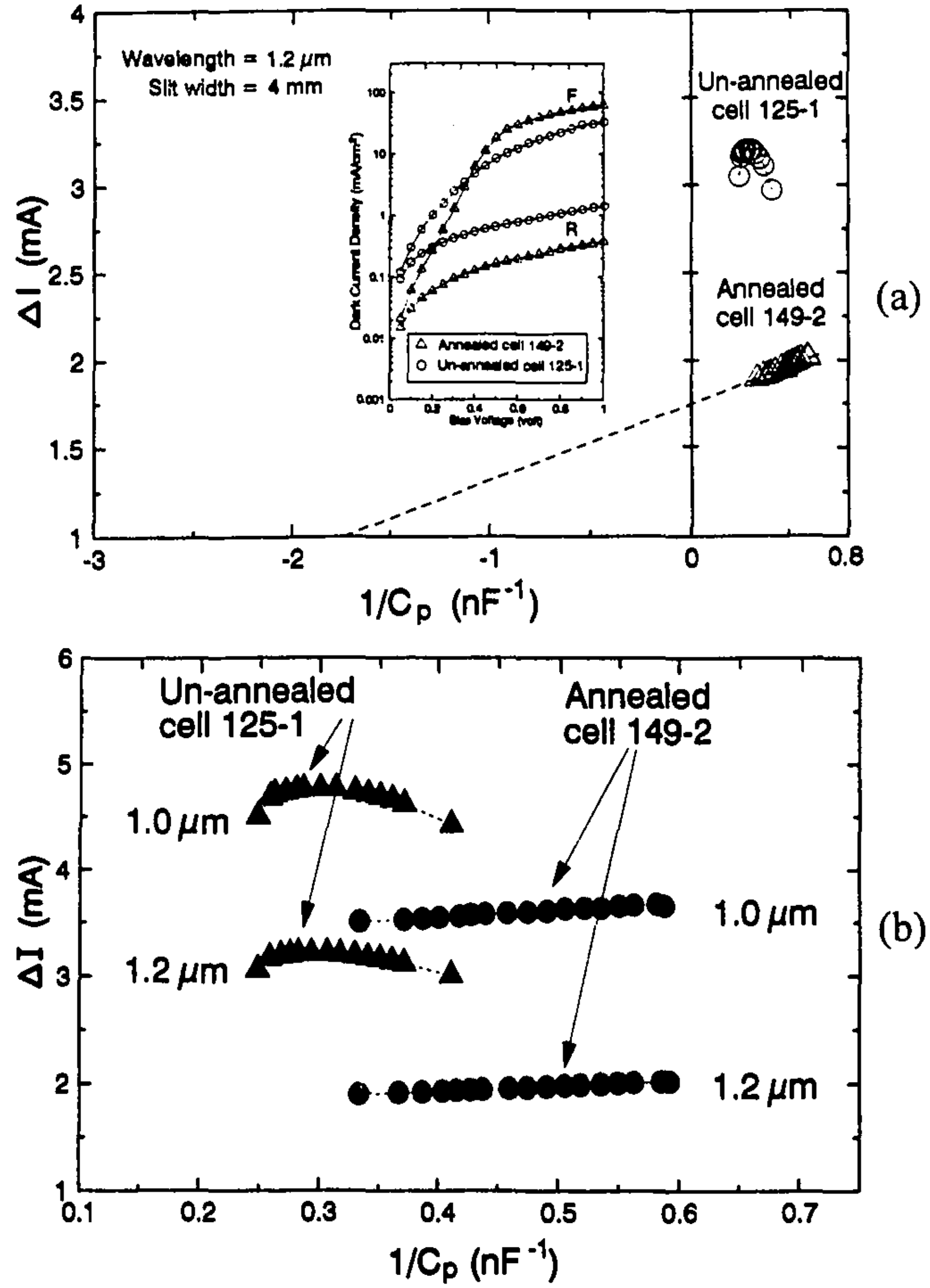

Fig.7.24 Plot of ΔI against 1/C_p showing a comparison between the experimental points of annealed cell 149-2 with un-annealed cell 125-1 at (a) a wavelength of 1.2 μm, together with their dark j-V characteristics, and (b) at wavelengths of 1.0 and 1.2 μm. Note that no meaningful extrapolation is possible for the experimental points of the un-annealed cell.

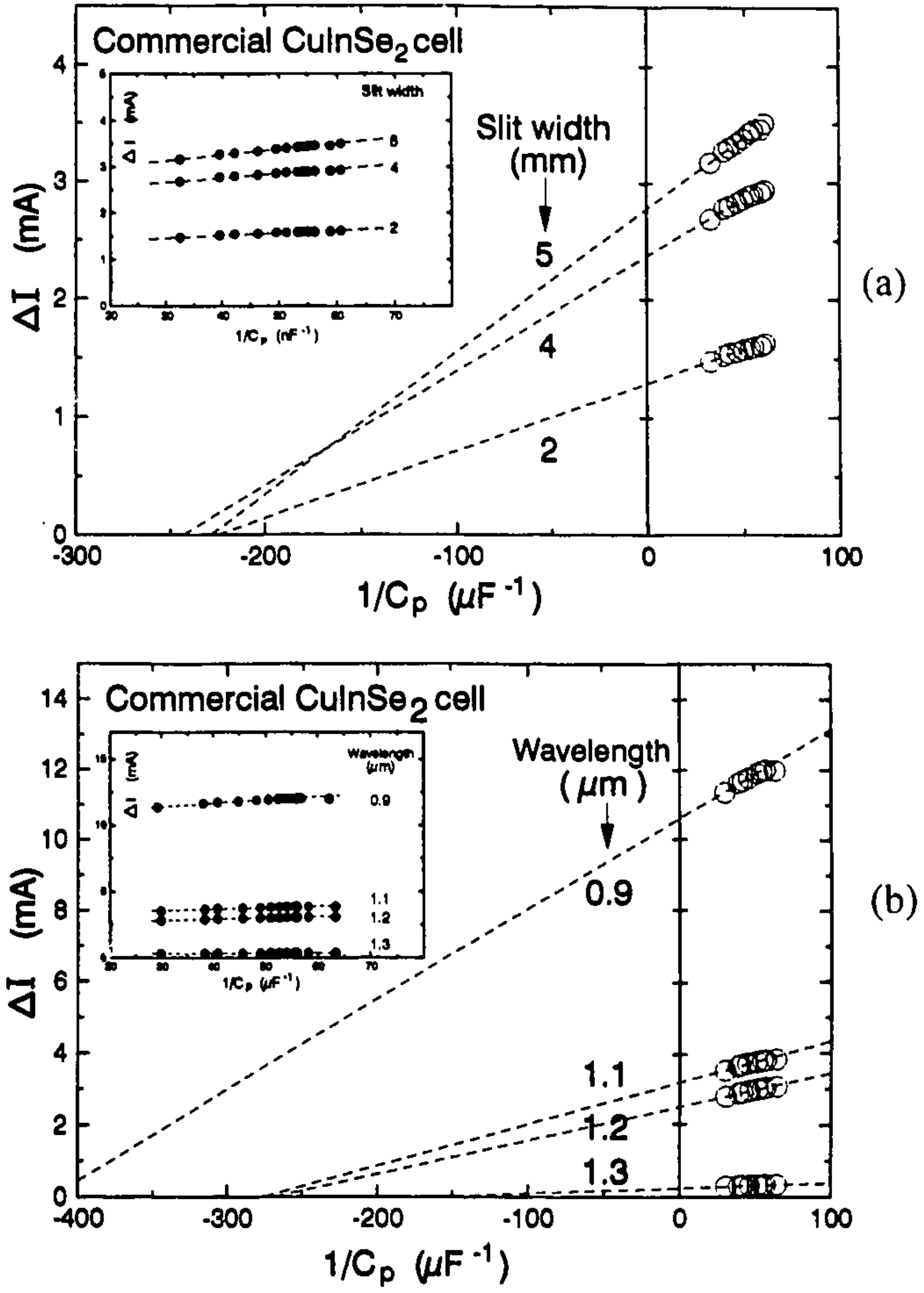

Fig.7.25 Plot of ΔI against $1/C_p$ for the commercial CuInSe$_2$-based sample CIS-4 with variation of (a) monochromator slit width and (b) incident wavelength. Note the $1/C_p$ abscissa scale is in μF^{-1}.

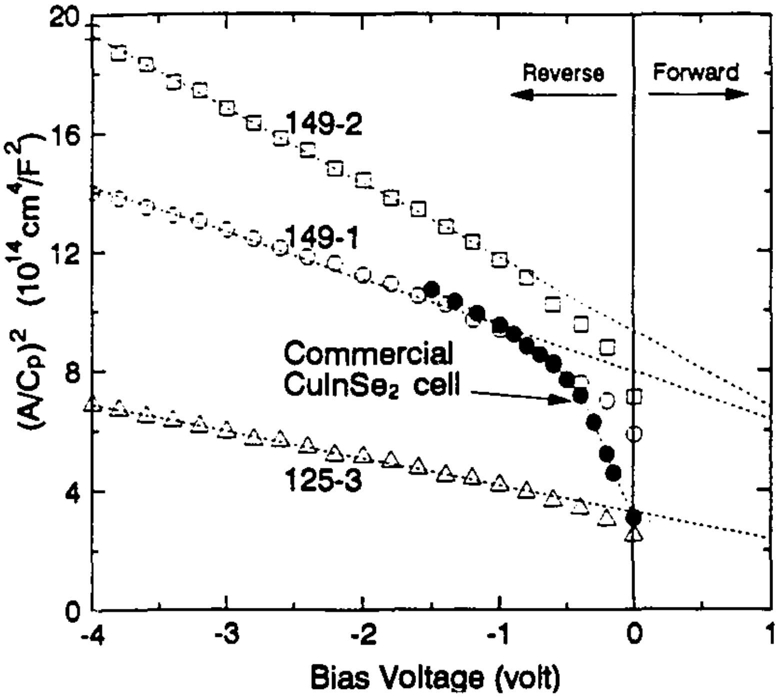

Fig.7.26 Mott-Schottky plot of $(A/C_p)^2$ against bias voltage for the three annealed cells 149-2, 149-1 and 125-3 and the commercial $CuInSe_2$-based cell CIS-4, which shows greater curvature of the line through the experimental points at low reverse voltage.

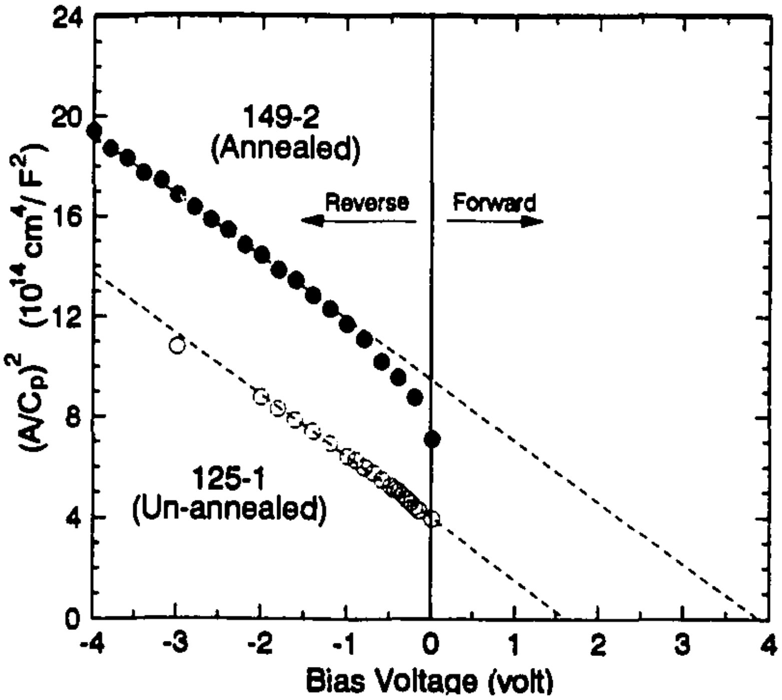

Fig.7.27 Mott-Schottky plot of $(A/C_p)^2$ against bias voltage showing a comparison between annealed cell 149-2 and un-annealed cell 125-1.

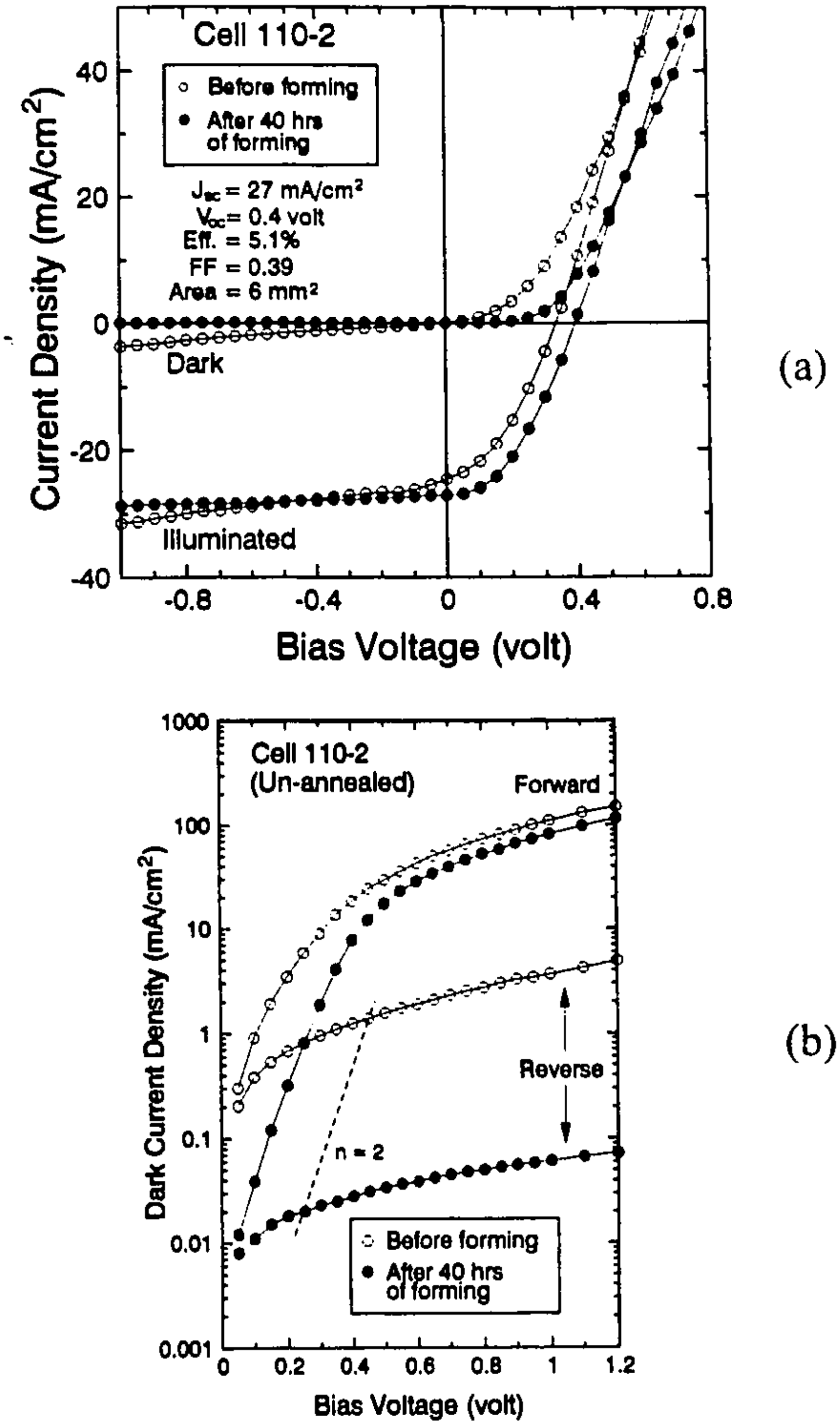

Fig.7.28 Current-density-voltage characteristics of un-annealed cell 110-2, as measured before and after forming. (a) Linear plot of illuminated and dark characteristics and (b) semi-log plot of their dark characteristics. The forming was carried out for a period of 40 hours. The illumintion level of the measurement in (a) was about 100 mW/cm^2.

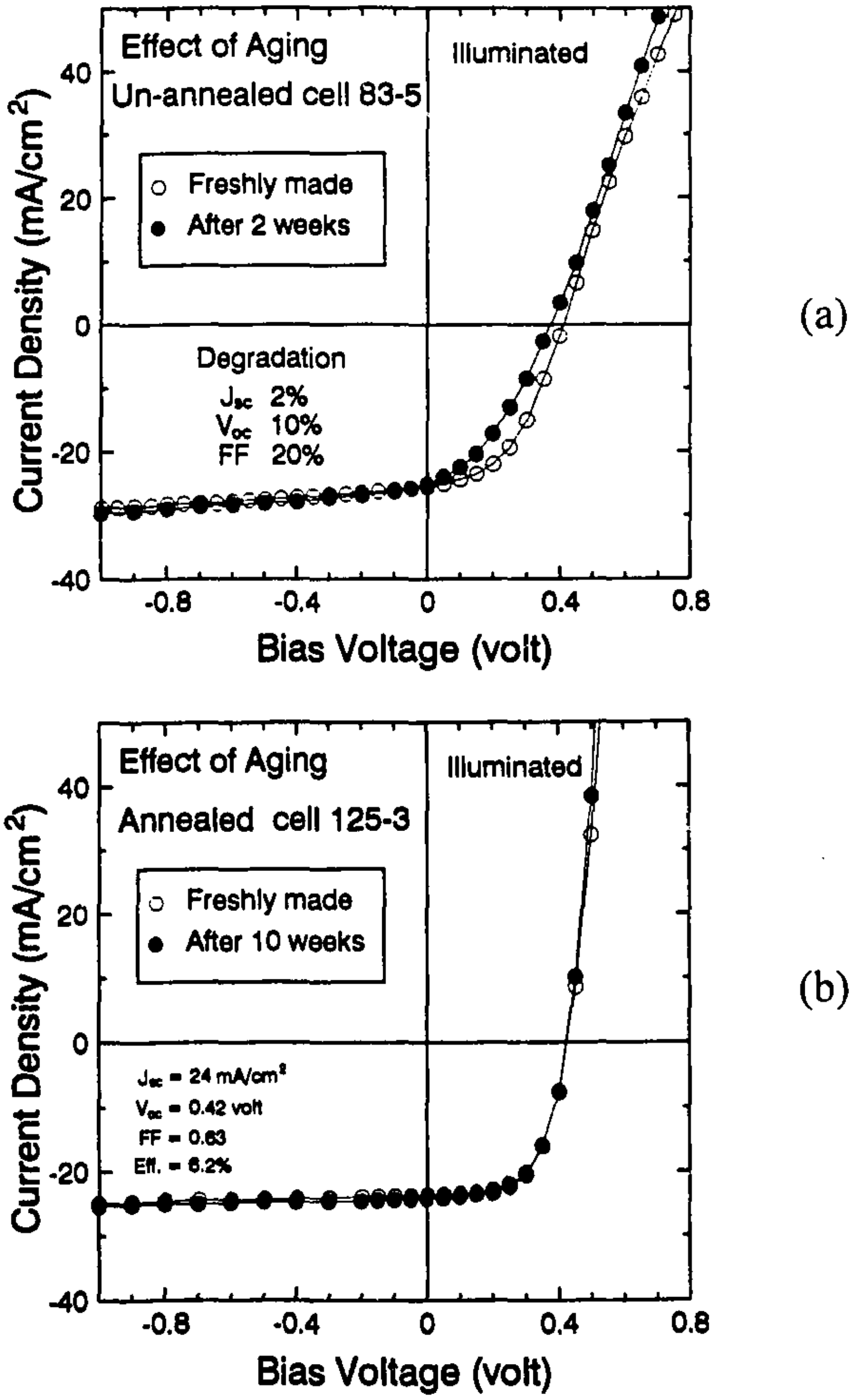

Fig.7.29 Current-density-voltage characteristics of (a) un-annealed cell 83-5 and (b) annealed cell 125-3, showing the effect of aging on the cell characteristics after the indicated period of time. The illumination level was about 100 mW/cm^2.

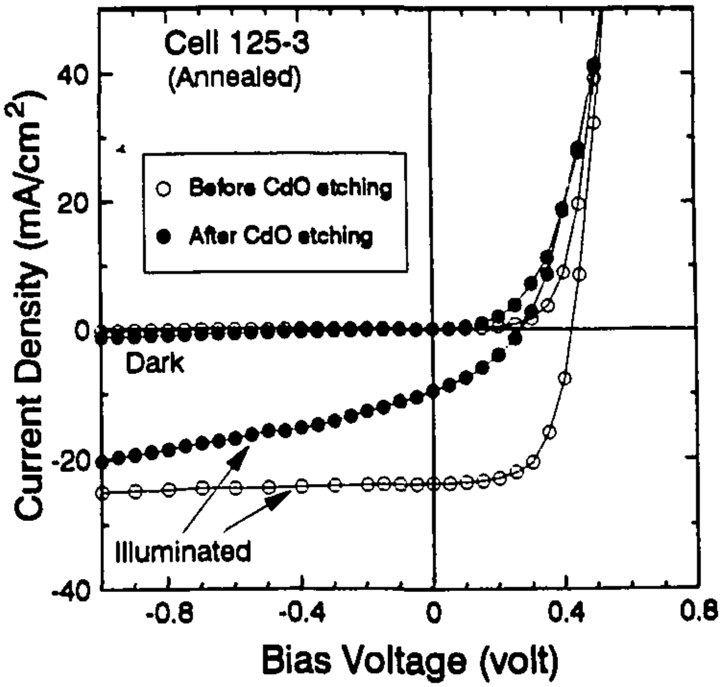

Fig.7.30 Illuminated and dark current-density-voltage characteristics of cell 125-3, measured before and after etching of the active CdO layer, showing evidence of some residual photovoltaic action, even after the CdO removal.

CHAPTER 8

DISCUSSION AND CONCLUSIONS

8.1 INTRODUCTION

The results of the studies in this thesis are now discussed collectively, covering the topics $CuInSe_2$ crystal growth, ingot adhesion, non-stoichiometry, cleavage, twinning and preliminary cell fabrication as reported in chapters 3 to 7. This is followed by a summary of the main conclusions of this work arranged in the form of claims to originality. Finally, some suggestions are made for future studies.

8.2 DISCUSSION OF RESULTS

It is clear from the present work that, the vertical Bridgman process, employing a single sealed ampoule for synthesis and growth of monocrystals of $CuInSe_2$, was very successful. The crystals were limited in size only by the dimensions of the quartz ampoule itself, so that by properly scaling up the dimensions of the crucible and suitably optimizing the growth conditions, larger crystals could be obtained. The present results were obtained in a relatively simple two-zone resistance-heated furnace without ampoule rotation during the growth. It is possible that even better crystals could be obtained, with no twinning for example, with ampoule rotation and improved control of the temperature profile using multiple heaters. However, the existence of twins, which in the present study were found to occur only in the {112} planes, is not a serious crystal defect, as far as device work is concerned. This is because the {112} twin merely involves a 180° (or 60 °) rotation about an axis perpendicular to the {112} plane, so that transport properties should not be affected. However, since twinned crystals can readily be detected by etching or sometimes by simple observation, they can be avoided, if need be, in the substrate preparation.

The success of the crystal growth work is due to the unique use of the boron nitride coating technique, whereby this material is deposited as a film, from BN slurry, inside the ampoule and flamed into the quartz to form a hardened layer, prior to the introduction of the starting elements of copper, indium and selenium. The experiments carried out clearly indicate that the action of the coating was not as a physical barrier preventing the ingot from making contact with the quartz ampoule, but that it performed as a getter absorbing oxygen present in the nominally 99.999% pure copper pellets, thus preventing the undesirable adhesion of the ingot. Oxygen was positively identified to be present in the copper in experiments carried out, using a mass spectrometer gas analyzer, on copper pellets heated under continuous vacuum-pumping. The quartz itself, the selenium and the indium were all exonerated as the sources of the sticking agent - oxygen. Furthermore, no evidence was found in the present work to support the suggestion of Tomlinson [2.24] that residual water vapour was the source of the adhesion. Using either heated-pumped-on or commercial oxygen-reduced copper for the compound synthesis, without the boron nitride, confirmed that oxygen in the copper was the source of the ingot-ampoule sticking problem. It is important to point out here, that the BN acted as a more effective getter in removing the oxygen from the copper pellets as opposed to heating under vacuum-pumping and thus, the latter technique was only used as a means of diagnosing the gas causing sticking rather than as a method to eliminate the adhesion in the ingot. Needless to say that prior to the use of boron nitride, when sticking occurred, the removal of the ingot from the ampoule after growth resulted in its break-up, with the consequent creation of cracks and internal stresses causing defects. Thus, it was not until the development of the boron nitride process had resulted in free non-adherent ingots without microcracks and voids that serious characterization work was done, such as the identification of the cleavage planes in $CuInSe_2$. Prior to this work, a thorough study of cleavage in this material was hampered by the fact that only small monocrystals were available. The getter material graphite, as used by Yip [7.11], also eliminated the sticking but, as a coating, the graphite tended to flake-off and become incorporated into the melt, whereas in using the hardened boron nitride coating, this does not happen. Thus, the BN process was preferred. While the boron nitride does not enter the melt *macroscopically*, it is still conceivable to have microscopically absorbed boron in the ingot. Evidence from work on other materials using BN crucibles suggests that boron is not absorbed to any significant extent. However, if this element is shown to have a doping role in $CuInSe_2$, further testing is needed to determine if traces of it are present in the chalcopyrite. It should be mentioned that, the use of BN crucibles in the past has required the charge to be already pre-reacted, otherwise cracking of the crucible may occur, at least in using sealed quartz ampoules.. The present BN process eliminates this problem by eliminating the need for an extra crucible. Another advantage of the BN method is that it is easier to scale up for use in larger ampoules which would involve less effort and would be cheaper as opposed to using a BN crucible.

The use of a BN coating, as developed by the author, is the first reported attempt to employ such a coating for the Bridgman growth of $CuInSe_2$. This process has attracted interest from other laboratories, including the Center for Advanced Materials Processing (CAMP) at Clarkson University, in Potsdam N.Y., where a similar BN process was adopted for the Bridgman growth of CdTe.

In the Bridgman-grown crystals of Parkes, Tomlinson and Hampshire [2.5], it was reported that the [221] direction was nearly parallel to the growth direction, meaning presumably the direction of the travel. However, in the crystals grown in the present work, the {112} cleavages were often obtained nearly parallel to the ingot axis and thus the [221] direction for such cleavages would be generally perpendicular to the long ingot axis (or travel direction). However, since the angle between two {112} planes in the same crystal is 70.53°, a second {112} plane could be cleaved essentially perpendicular to the long axis of the ingot and thus the growth direction of the present ingots may not be too far of from a [221] direction.

Non-uniformity of conductivity type was never a problem in this work. In runs prepared from stoichiometric starting proportions, the entire ingot was uniformly p-type and single phase chalcopyrite. Even in the case of runs with non-stoichiometric starting proportions, the first 80 % of the ingot was single phase chalcopyrite and uniformly n-type or p-type. In this region, the composition was always near to stoichiometry, despite strong deviation from stoichiometry in the melt. Thus, there was an automatic "*self-correcting*" effect of moving the composition towards stoichiometry, even when the melt was strongly non-stoichiometric. Hence, in the gradient freezing process, the excess elements were contained in the remaining liquid and precipitated as binary compounds or as the elements only in the final zone of liquid to freeze at the end of the ingot. In this multi-phase region. the following materials. besides the chalcopyrite. were identified: Cu_7In_4, Cu_9In_4, Cu_4In. Cu. Se. CuSe and InSe. Present also were some other apparent compounds. which were not documented in the literature; these were Cu_5In_3. Cu_4In_3 and In_7Se_5. The last named compound may not be very different from In_3Se_2 reported earlier [2.27].

It is interesting to note that the well known compounds Cu_2Se and In_2Se_3. which occur in thin film work. where the $CuInSe_2$ chalcopyrite phase formation was incomplete. have never been observed in the multi-phase regions of Bridgman ingots grown from non-stoichiometric melts. However. Matsushita. Jitsukawa and Takizawa [8.1] did observe In_2Se_3 at about 600 °C but not Cu_2Se among other compounds. in heating the elements copper. indium and selenium together to form $CuInSe_2$ at 1050 °C.

In the single phase part of each ingot. the conductivity was p-type if the starting proportions were stoichiometric or had an excess of copper or selenium. while the region was n-type with an excess of indium. It should be pointed out that, the words *single phase chalcopyrite* mean the absence of the extra phases found at the end of nonstoichiometric ingots but they do not rule out the presence of the sphalerite phase, which is reported to be stable above 810 °C. This is because the X-ray diffraction lines of the sphalerite phase differ from those of the chalcopyrite only by the absence of the lines (101), (103) and (105) etc. However, the pattern with these missing lines. characteristic of the sphalerite, has never been observed in this laboratory, even in $CuInSe_2$ quenched from the melt. It is consequently believed that there is a negligible presence of this cubic form in the grown ingots.

In the ternary diagram giving the compositions of crystals obtained from non-stoichiometric melts, the division between n-type and p-type material turned out to be remarkably simple, at least if oxygen was removed from the copper. Material with more than about 26 % indium was n-type and with less than 25 % of this element, p-type, irrespective of the copper or selenium proportions. Between these two values, n- and p-type material was obtained but it should be realized that the error in the EPMA-determined compositions could readily account for this apparent mixed region. This simple demarcation on the composition diagram , based on the present results and those of Neumann and Tomlinson [2.29] , is even consistent with the apparently conflicting result that excess *initial* selenium or copper yields p-type conductivity in the ingot and a deficiency of these elements, n-type. Thus, for example, keeping the Cu/In ratio constant and varying the Se content alone can change the conductivity type, as explained in chapter 5. That such a simply stated criterion prevails, involving the indium concentration alone, is remarkable, and on this account, it needs thorough checking in future work to test its validity.

In the grown crystals, only two *bona fide* cleavage planes were found, namely the {101} set and the {112} set. An apparent {110} cleavage surface was also found but microscopic examination showed it to consist of small {112} planes in the form of triangular parallel ridges. This cleavage character of $CuInSe_2$ is probably the same for all chalcopyrite lattices and differs profoundly from the dominant {110} cleavage in zinc blende crystals.

This is probably due to the difference in bond strengths of the two different Se-metal bonds in the chalcopyrites. Thus, in cutting the Se-Cu and Se-In bonds in $CuInSe_2$ it takes more energy to break these bonds for a {110} cut than for a {112} or {101} cuts. Further more, a particular {101} cut breaks half the number of the stronger Se-Cu bonds than a {112} cut. which may be the reason for the dominant {101} cleavage. In any case , the clear {112} and {101} cleavages enable devices to be made with precise crystallographically-oriented substrates.

To test the device quality of $CuInSe_2$ monocrystals prepared in this work, preliminary photovoltaic cells were fabricated with the basic structure of the form $CuInSe_2$(p)/CdO(n), where the CdO was deposited as a thin film on a cleaved substrate of the chalcopyrite. Such a structure was not that of the most efficient cells reported in the literature but made effective use of the extensive experience in our laboratory with d.c. reactive sputtering of CdO. Initial cells gave a solar conversion efficiency of about 4 %, but if the $CuInSe_2$ substrate was annealed at atmospheric pressure at a temperature of about 350 °C, prior to CdO deposition, an efficiency of more than 6 % was obtained. This substrate annealing step was first developed by L.S. Yip in our laboratory for a cell having the structure $CuInSe_2$(p)/CdS(n)/ZnO(n+), where the $CuInSe_2$ substrate was abrasively polished before the annealing and CdS deposition. The fact that the annealing was also effective in the present $CuInSe_2$/CdO structures, where there was no abrasive polishing and no CdS interfacial layer, indicates that the process does not only involve a decrease in surface defects. In fact, Mott-Schottky plots from the capacitance measurements on the cells suggest that the annealing results in a reduction of the acceptor concentration near the $CuInSe_2$ surface and other evidence (not given here) indicates that this may be due to a loss of selenium from the surface layer of the substrate. The observed slight improvement in cell performance with electrical "forming" - that is the continuous application of reverse bias after fabrication, is possibly due to a movement of charged acceptors by the electric field out of a layer in the $CuInSe_2$ close to the active junction. Thus, like the annealing, this leads to a reduction in the acceptor concentration at this location and could improve the junction integrity by increasing the resistance of any microscopic shunting paths. In the fabricated cells, the 6 % efficiency was obtained without an anti-reflective coating and without an optimized current collecting grid. Thus in a cell where these particular improvements are added, the same device would yield an efficiency of at least 7 %. This is a remarkable result considering the fact that there is a 23 % mismatch between the corresponding lattice parameters of $CuInSe_2$ and CdO, which according to conventional wisdom, should kill the illuminated short circuit current through strong recombination at the metallurgical interface between the two layers. Even more remarkable for the apparently large mismatch, is the fact that X-ray diffraction indicates that some of the CdO grains appear to be partially oriented with their (111) planes parallel to the cleaved (112) surface of the $CuInSe_2$ substrate. Added to this is the result that some photovoltaic behaviour remained, even after the CdO was removed, suggesting that the real photovoltaic action was located not at the $CuInSe_2$/CdO interface but perhaps in a region lying deeper within the substrate it self.

The photocurrent-capacitance method, applied to the $CuInSe_2$/CdO cells with annealed substrates, gave an estimate of about 3 micrometers for the electron diffusion length in the monocrystalline material, assuming a relative dielectric constant of 10. This was more than twice the value estimated for a *Siemens Solar Industries* cell with a reported efficiency of some 13 %. Thus, these results suggest that a photovoltaic device with a monocrystalline absorber, once the fabrication techniques have been fully mastered, could eventually yield a performance superior to that of cells with polycrystalline substrates.

8.3 CLAIMS TO ORIGINALITY

As a summary of the main conclusions arising out of the work in this thesis, the author makes the following claims for originality of ideas in respect of the crystal growth and study of $CuInSe_2$. Thus, the author:

(1) developed the technique of deposition and flaming-in boron nitride to the inner wall of the quartz ampoule, which enabled adhesion-free and void-free ingots to be obtained,

(2) determined that the adherence of the $CuInSe_2$ ingot to the quartz ampoule was due to oxygen arising from the starting high purity copper,

(3) confirmed that, with suitable arrangements, the vertical Bridgman method employing one ampoule for the synthesis and growth of the compound, successfully yields device-quality single crystals with centimeter dimensions,

(4) showed that the *only* principal cleavage planes in $CuInSe_2$ were the {101} and {112}, and that the {110} *macroscopic* cleavage consisted of {112} *micro*cleavages,

(5) showed that twinning in $CuInSe_2$ crystals *only* occurred along {112} planes.

(6) showed that, in single phase material, the conductivity type was determined *only* by whether the indium content was greater or less than about 25 %, thereby explaining also, the type changes with excess of the other two elements over stoichiometry.

(7) demonstrated that effective photovoltaic substrates can be successfully fabricated with *cleaved* monocrystalline substrates.

(8) demonstrated, in a $CuInSe_2$/CdO cell, that a large lattice mismatch between substrate and window layer can be tolerated, without a complete loss of photovoltaic performance.

(9) demonstrated that the nondestructive photocurrent-capacitance method is a useful, technique for estimating the minority carrier diffusion length in a $CuInSe_2$/CdO cell.

Finally, it may be said that, the results of this work will enable single crystals of $CuInSe_2$ to be available free of microcracks and voids and of uniform conductivity type, so that studies can now be carried out, in various laboratories throughout the world, which were difficult to attempt before. This will also help the thin film photovoltaic research community to develop higher performance cells based on this important chalcopyrite material - $CuInSe_2$.

8.4 FUTURE WORK

Without major modification to the present growth furnace , the following are tasks which could be undertaken to improve crystal quality:

(1) the top zone temperature of the furnace should be reduced, *during the crystal growth*, to just above the melting point, so as to minimize excessive heating of the melt.

(2) the temperature of the bottom zone should be kept above 810 °C, and the ingot cooled down slowly, so that sufficient time is given for the sphalerite-to- chalcopyrite transition to take place.

(3) lower cooling rates should be used to minimize defects in the ingot.

(4) higher temperature gradients should employed by narrowing down the thickness of the insulating baffle separating the upper and lower zones of the furnace.

(5) ampoules using a uniformly tapered wall should be used for the crystal growth.

(6) further attempts with seeding should be tried, perhaps using a higher melting point chalcopyrite such as $CuAlSe_2$.

(7) rotation should be incorporated in the crystal growth procedure.

If financial resources permit, a new Bridgman furnace should be acquired which will enable a more suitable temperature profile to be obtained - that is an upper zone with a large flat temperature profile above the melting point, followed by a region having a sharp gradient near the solidification point and then a lower zone also with a flat temperature profile, which can be independently controlled.

The Czochralski technique with liquid encapsulation under high pressure should be examined, since this method has the great advantage of avoiding nucleation from the crucible side wall. However, extensive resources would be needed for such work.

REFERENCES

[1.1] H. Neumann. *Cryst. Res. Technol.*, **18**, 483 (1983).

[1.2] F.A. Abou-Elfotouh, D.J. Dunlavy, A.M. Hermann and L.L. Kazmerski. *Proc. 17th IEEE Photovoltaic Specialists Conf.*, P.1410 (1984).

[1.3] C. Rincon, J. Gonzales and S. Sanchez-Perez. *J. Appl. Phys.*, **54**, 6634 (1983).

[1.4] Y.H. Shing, N.T. Tran and K.J. Bachmann. *Proc. 17th IEEE Photovoltaic Specialists Conf.*, p.774 (1984).

[1.5] L.L. Kazmerski, O. Jamjoum, J.F. Wager, P.J. Irelend and K.J. Bachmann. *J. Vac. Sci. Technol., A*, **1**, 668 (1983).

[1.6] H.J. Möller and E. Rodak. *Proc. of Symp. A3 on Non-stoichiometry in Semiconductors of the Intl. Conf. On Advanced Materials*, p. 281 (1991).

[1.7] B. Schumann, A. Tempel and G. Kühn. *Solar Cells*, **16**, 43 (1986).

[1.8] A.H. Clark and W.N. Unertl. *Jpn. J. Appl. Phys.*, **19**, Suppl. 19-3, 49 (1980).

[1.9] H. Takenoshita, T. Nakan and I. Nakao. *Jpn. J. Appl. Phys.*, **19**, Suppl. 19-3, 33 (1980).

[1.10] A. Vahid Shahidi, I. Shih, T. Araki and C.H. Champness. *J. Electronic Materials*, **14**, No.3, 297 (1985).

[2.1] H. Hahn, G. Frank, W. Klinger, A.D. Meyer and G. Störger. *Zeif. f. Anorg. Allge. Chimie*, **271**, 11 (1953).

[2.2] I.G. Austin, C.H.L. Goodman and A.E. Pengelly. *J. Electrochem. Soc.* **103**, 609 (1956).

[2.3] L.S. Palatnik and E.I. Rogacheva. *Sov. Phys. Doklady.* ,**12**, 503 (1967).

[2.4] J.L. Shay, B. Tell, H.M. Kasper and L.M. Schiavone. *Phys. Rev.* , **B7**, 4485 (1973).

[2.5] J. Parkes, R.D. Tomlinson and M.J. Hampshire. *J. Cryst. Growth*, **20**, 315 (1973).

[2.6] B. Tell, J.L. Shay,H.M. Kasper. *J. Appl. Phys.*, **43**, 2469 (1972).

[2.7] S. Wagner, J.L. Shay, P. Migliorato and H.M. Kasper. *Appl. Phys. Lett.*, **25**, 434 (1974).

[2.8] J.L. Shay, S. Wagner, and H.M. Kasper. *Appl. Phys. Lett.*, **27**, 89 (1975).

[2.9] H. Rau, *J. Chem. Thermodynamics*, **6**, 525 (1974).

[2.10] B. Tell, S. Wagner and P.M. Bridenbaugh. *Appl. Phys. Lett.* , **28**, 454 (1976).

[2.11] B. Tell and P.M. Bridenbaugh. *J. Appl. Phys.*, **48**, 2477 (1977).

[2.12] H. Haupt and K. Hess. *Proc. 3rd Conf. on Ternary Compounds, Inst. Phys. Conf., Series No. 35*, 5 (1977).

[2.13] W. Hörig, H. Neumann, H.J. Höbler and G. Kühn. *Phys. Stat. Solidi*, **680**, K21 (1977).

[2.14] T. Irie, S. Endo and S. Kimura. *Japan. J. Appl. Phys.*, **18**, 1303 (1979).

[2.15] J. Gonzalez, C. Rincon, A. Redondo and P. Negreto. *Japan. J. Appl. Phys.*, **19**, 29 (1980).

[2.16] R.R. Arya, T. Warminski, R. Beaulieu, M. Kwietniak and J.J. Loferski. *Solar Energy Materials*, **8**, 471 (1983).

[2.17] R.D. Tomlinson. *Proc. 7th Intl. Conf. On Ternary and Multinary Compounds*, Materials Res. Soc., p. 177 (1987).

[2.18] I. Shih, A. Vahid Shahidi and C.H. Champness. *J. Cryst. Growth*, **70**, 411 (1984).

[2.19] K.J. Bachmann, M. Fearheiley, Y.H. Shing and N. Tran. *Appl. Phys. Lett.*, **44**, 407 (1984).

[2.20] T.F. Ciszek. *J. Electronic Mat.*, **14**, 451 (1985).

[2.21] R.D. Tomlinson. *Solar Cells*, **16**, 17 (1986).

[2.22] M.L. Fearheiley. *Solar Cells*, **16**, 91 (1986).

[2.23] K.D. Becker and S. Wagner. Phys. Rev., **B27**, 5240 (1983).

[2.24] R.D. Tomlinson. *Proc. Intl. Photovoltaic Science and Engineering Conf.*, p. 467 (1989).

[2.25] W.S. Weng, L.S. Yip, I. Shih and C.H. Champness. *Can. J. Phys.*, **67**, 294 (1989).

[2.26] L.S. Yip, W.S. Weng, I. Shih and C.H. Champness. *Proc. 21st IEEE Photovoltaic Specialists Conf.*, p. 768 (1990).

[2.27] L.S. Yip, W.S. Weng, I. Shih and C.H. Champness. *Tech.Digest of Intl. Photovoltaic Science and Engineering Conf.* , p.401 (1990).

[2.28] L.S. Yip, W.S. Weng, Z.A. Shukri, I. Shih and C.H. Champness. *Proc. of Symp. A3 on Non-stoichiometry in Semiconductors of the Intl. Conf. On Advanced Materials*, p. 119 (1991).

[2.29] H. Neumann and R.D. Tomlinson. *Solar Cells*, **28**, 301 (1990).

[2.30] L.S. Yip, Z.A. Shukri, I. Shih and C.H. Champness. *Proc. 6th Intl. Photovoltaic Science and Engineering Conf.*, p. 1015 (1992).

[2.31] L.S. Yip, Z.A. Shukri, I. Shih and C.H. Champness. *Proc. 11th Photovoltaic Solar Energy Conf.*, p. 846 (1992).

[2.32] L.S. Yip, I. Shih and C.H. Champness. *J. Cryst. Growth*, **129**, 102 (1993).

[2.33] Z.A. Shukri, C.H. Champness and I. Shih. *J. Cryst. Growth*, **129**, 107 (1993).

[3.1] A.N. Tiwari, S. Blunier, H. Zogg, V. Zelezney, D. Schmid and H.W. Schock. *12th Photovoltaic Solar Energy Conf.*, p. 625 (1994).

[3.2] P. Cheuvart, U. El-hanani, D. Schneider and R. Triboulet. *J. Cryst. Growth*, **101**, 270 (1990).

[3.3] M. Kavcar, M.J. Carter and R.Hill. *Solar Energy Materials and Solar Cells*, **27**, 13 (1992).

[3.4] Y.C. Lu, J.J. Shiau, R.S. Feigelson and R.K. Route. *J. Cryst. Growth*, **102**, 807 (1990).

[3.5] J.P. Tower, R. Tobin, P.J. Pearah and R.M. Ware. *J. Cryst. Growth*, **114**, 665 (1991).

[3.6] J. Trauth and B.C. Grabmaier. *J. Cryst. Growth*, **112**, 451 (1991).

[3.7] P.G. Barber, R.K. Crouch, A.L. Fripp, J. Debnam, R.F. Berry and R. Simchick. *J. Cryst. Growth*, **74**, 228 (1986).

[3.8] H. Miyake, M. Tajima and K. Sugiyama. *J. Cryst. Growth*, **125**, 381 (1992).

[3.9] R.S. Feigelson and R.K. Route. *J. Cryst. Growth*, **104**, 789 (1990).

[3.10] K. Grasza and A. Jedrzejczak. *J. Cryst. Growth*, **110**, 867 (1991).

[3.11] L.S. Yip. *Development of High Efficiency Solar Cells on CuInSe$_2$ Single Crystals*. McGill University Ph.D Thesis, p.33-34 (1996).

[3.12] K. Yasuda, Y. Iwakami and M.Saji. *J. Cryst. Growth*, **99**, 727 (1990).

[3.13] A. Omino and T. Suzuki. *J. Cryst. Growth*, **117**, 80 (1992).

[3.14] T.F. Ciszek. *J. Cryst. Growth*, **79**, 689 (1986).

[3.15] H. Yoshida, T. Fujii, A. Kamata and Y. Nakata. *J. Cryst. Growth* , **117**, 75 (1992).

[3.16] A.W. Vere. Crystal Growth, Principles and Progress. *Plenum Press,* p. 76 (1987).

[4.1] Professor Robert Harris, McGill University. Private communication

[5.1] L.L. Kazmerski. *Proc. 23rd IEEE Photovoltaic Specialists Conf.* p.1 (1993).

[5.2] J. Armstrong. *Electron Probe Quantitation* p.261, Plenum Press, N.Y. Editors K. Heinrish and D. Newbury.

[5.3] J. Goldstein *et al. Scanning Electron Microscopy and X-ray Micro-Analysis,* chap. 8, p. 405, Plenum Press, N.Y.

[6.1] T.P. Massopust, P.J. Ireland, L.L. Kazmerski and K.J. Bachman. *J. Vac. Sci. Technol. A*, **2**, 1123 (1984).

[6.2] L.S. Yip, W.S. Weng, L. Li, I. Shih and C.H. Champness. *Proc. 10th Intl. Photovoltaic Solar Energy Conf.*, 921 (1991).

[6.3] B.D. Cullity, *Elements of X-ray Diffraction*, p.502. Addison-Wesley Publishing Co., 1978.

[6.4] G.A. Wolff and J.D. Broder. *Acta Cryst.*, **12**, 313 (1959).

[6.5] K.E. Bean and P.S. Gleim. *Proc. IEEE*, **57**, 1469 (1969).

[6.6] H. Pfister, *Z. Naturforsch.*, **10a**, 79 (1955).

[6.7] M.S. Abrahams, L. Ekstrom. *Acta Met.*, **8**, 654 (1960)

[6.8] S.K. Ghandi. *VLSI Fabrication Principles*, p.13-14. John Wiley and Sons Inc., 1983.

[6.9] M.R. Lorenz. *J. Appl. Phys.*, **33**, 3304 (1962).

[6.10] H. Iwanaga, A. Tomizuka. *J. Mat. Sci. Lett.*, **10**, 975 (1991)

[6.11] L.G. Berry, B.H. Mason and R.V. Dietrich. *Mineralogy*, 2nd edition, p.261. W.H.Freeman and Company, New York, 1983.

[6.12] R.C. Weast and M.J. Astle *CRC Handbook of Chemistry and Physics*, p. F-182, 62nd edition, CRC Press Inc., Boca Raton, 1981.

[6.13] E.I. Salkovitz and F.W. von Batchelder. *J. Metals*, **4** , 165 (1952).

[7.1] J.C. Boettger and A.B. Kunz. *Phys. Rev. B*, **27**, 1359 (1983).

[7.2] A.N. Gabor, J.R. Tuttle, M. Contreras, D.S. Albin A. Franz, D.W. Niles and R. Noufi. *12th Intl. Photovoltaic Solar Energy Conf.*, p. 939 (1994).

[7.3] H.W. Schock. *12th Intl. Photovoltaic Solar Energy Conf.*, p. 944 (1994).

[7.4] W.S. Chen, J.M Stewart, W.E. Devaney, R.A. Mickelsen and B.J. Stanbery. *23rd IEEE Photovoltaic Specialists Conf.*, p. 422 (1993) .

[7.5] L. Stolt, J. Hedström, J. Kessler, M. Ruckh, K.O. Velthaus and H.W. Schock. *Appl. Phys. Lett.*, **62**, 597 (1993).

[7.6] R.W. Birkmire, L.C. Di Netta, P.G. Lasswell, J.D. Meakin and J.E. Philips. Solar *Cells*, **16**,419 (1986).

[7.7] R.E. Hollingsworth and J.R. Sites. *Solar Cells*, **16**, 457 (1986).

[7.8] Z.A. Shukri and C.H. Champness. *Proc, 23rd IEEE Photovoltaic Specialists Conf.*, p. 613 (1993).

[7.9] Z.A. Shukri, L.S. Yip, C.X. Qiu, I. Shih and C.H. Champness. *Solar Energy Materials and Solar Cells*, **37**, 395 (1995).

[7.10] L.S. Yip and I. Shih. *Proc. 24th IEEE Photovoltaic Specialists Conf., (1st World Conf. on Photovoltaic Energy Conversion)*, p.210 (1994).

[7.11] L.S. Yip. *Development of High Efficiency $CuInSe_2$/CdS/ZnO Solar Cells.* McGill University Ph.D. Thesis, chap. 4 (1996).

[7.12] G. Ahmad. *Electrical Studies of $CuInSe_2$ Single Crystal Samples.* McGill University, Course 304-677 Laboratory Report, (1995).

[7.13] C.H. Champness, Y.F. Go and Z.A. Shukri. *Proc. 4th Intl. Symp. Indust. Uses of Selenium and Tellurium.* p. 600 (1989) Banff.

[7.14] Jen-Kon Chen. *Fabrication of a Se/CdO Photovoltaic Cell Using a Mixed Gas Sputtering Technique.* McGill University M.Eng. Thesis (1985).

[7.15] C.H. Champness, J.K. Chen and K. Ghoneim. *Proc. 17th IEEE Photovoltaic Specialists Conf.*, p. 933 (1984).

[7.16] K.M. Ghoneim. *Studies on a Se/CdO Photovoltaic Cell.* McGill University M.Eng. Thesis (1983).

[7.17] N.G. Dhere *et al. Proc. 23rd IEEE Photovoltaic Specialists Conf.*, p. 566 (1993).

[7.18] C.H. Chan. *Reactive Sputtering of CdO for a Se/CdO Photovoltaic Cell.* McGill University M.Eng. Thesis (1992).

[7.19] C.H. Champness and C.H. Chan. *Solar Energy Materials and Solar Cells*, **30**, 65 (1993).

[7.20] C.H. Champness and C.H. Chan. *Proc. 6th Intl. Photovoltaic Science and Engineering Conf.*, p. 827 (1992).

[7.21] C.H. Champness, Z.A. Shukri and C.H. Chan. *Can. J. Phys.*, **69**, 538 (1991).

[8.1] H. Matsushita, H. Jitsukawa and T. Takizawa. *Proc. 11th Intl. Conf. on Crystal Growth*, (1995) to be published.

APPENDIX A.1

POWDER DIFFRACTION DATA OF $CuInSe_2$

Powder diffraction reflections for the chalcopyrite structure of $CuInSe_2$ reproduced from the JCPDS data [1], showing the relative intensities from the different reflecting planes along with their d-spacing and corresponding Bragg angle.

No.	d-spacing (Å)	Intensity(%)	{ h k l }	2θ
1	5.1700	3	1 0 1	17.137
2	3.3510	100	1 1 2	26.579
3	3.2200	4	1 0 3	27.681
4	2.8940	1	2 0 0	30.873
5	2.5280	7	2 1 1	35.481
6	2.1540	2	1 0 5	41.907
7	2.0510	41	2 0 4	44.119
8	2.0460	51	2 2 0	44.233
9	1.9030	3	3 0 1	47.755
10	1.7500	9	1 1 6	52.230
11	1.7450	25	3 1 2	52.391
12	1.4820	3	3 0 5	62.634
13	1.4520	1	0 0 8	64.080
14	1.4460	6	4 0 0	64.378
15	1.3940	1	2 1 7	67.089
16	1.3300	6	3 1 6	70.785
17	1.3270	4	3 3 2	70.969
18	1.3200	2	3 2 5	71.403
19	1.2010	1	4 1 5	79.790
20	1.1840	3	2 2 8	81.172
21	1.1820	10	4 2 4	81.338
22	1.1520	1	5 0 1	83.928
23	1.1180	1	1 1 10	87.102
24	1.1150	2	3 3 6	87.395
25	1.1130	4	5 1 2	87.592
26	1.0690	1	4 1 7	92.205
27	1.0357	1	5 0 5	96.103
28	1.0253	2	4 0 8	97.405
29	1.0228	1	4 4 0	97.724
30	0.9809	1	3 1 10	103.497
31	0.9789	3	5 1 6	103.794
32	0.9770	1	5 3 2	104.079
33	0.9482	1	6 1 1	108.658
34	0.9184	1	2 0 12	114.015
35	0.9145	3	6 0 4	114.771
36	0.8845	1	3 3 10	121.124
37	0.8828	1	5 3 6	121.516
38	0.8815	1	3 2 11	121.818
39	0.8416	1	5 4 5	132.491
40	0.8363	1	4 4 8	134.169
41	0.8255	1	5 2 9	137.856
42	0.8132	1	1 1 14	142.612
43	0.8115	2	5 1 10	143.328
44	0.8093	1	7 1 2	144.280

---

[1] CuKα radiation, λ=1.540598 Å, JCPDS file No. 40-1487.
Ref: D. Suri *et al, J. Appl. Crystallogr.*, **22**, 578 (1989).

APPENDIX A.2

ORIENTATION OF CdO ON {112}-CLEAVED $CuInSe_2$ SUBSTRATES

X-ray diffraction scans taken on the CdO layer as deposited onto (a) $CuInSe_2$ single crystal cleaved along the {112} plane and (b) onto a glass substrate. The scan in (a) shows a strong {112} $CuInSe_2$ reflection as well as a prominent {111} reflection from CdO layer. The absence, in this scan, of {200}, {220} and {311} CdO reflections, present in the scan of the polycrystalline CdO film shown in (b), indicates a preferred orientation of the CdO layer in the <111> (cubic) due to the {112}-cleaved $CuInSe_2$ substrate. This is despite a large lattice mismatch, of some 23 %, between the CdO and the $CuInSe_2$.

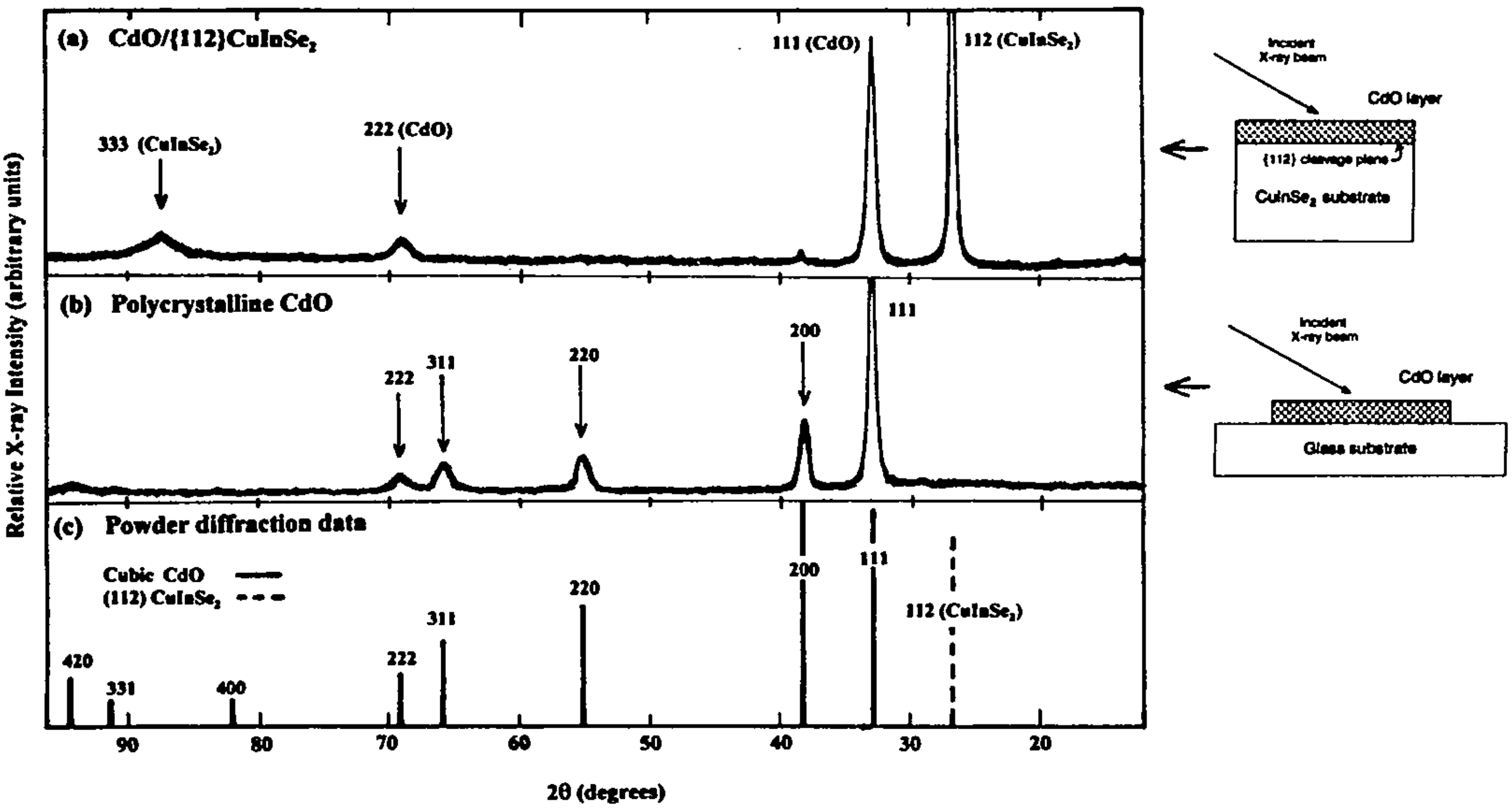

APPENDIX A.3

SUMMARY OF THE PHOTOCURRENT-CAPACITANCE METHOD

A relatively simple way of determining the minority carrier diffusion length in the semiconductor absorber layer of a photovoltaic Schottky junction is from the variation of depletion capacitance and illuminated-to-dark current change with reverse bias. This method has been used by Smith and Abbot [A.1] in GaP cells, by Yong and Rowland [A.2] and by Dorantes-Davila, Lastras-Martinez and Raccah [A.3] in GaAs cells. It has also been used in semiconductor-electrolyte cells by Tyagai for CdS [A.4] and by Lastras-Martinez *et al* for CdTe [A.5].

The basis of the method is as follows. Consider a reverse bias applied to a metal p-type semiconductor junction, where the metal is a film thin enough to transmit light through it. Suppose this cell is illuminated with monochromatic light, such that $\alpha_p W << 1$, where α_p is the optical absorption coefficient of the semiconductor, a condition corresponding to light penetrating well beyond the width of the depletion layer W. In this case, the photocurrent, I_{ph}, can be shown to be given by:

$$I_{ph} = K_l(W+L_n)\,, \qquad \text{(A.1)}$$

where L_n is the diffusion length of the electrons in the p-type semiconductor and K_l is a coefficient independent of applied bias. An ideal cell may be considered to be a current generator, giving the photocurrent I_{ph}, in parallel with a diode, carrying a current I_{Diode}. If an external reverse bias V_R is applied to the device under illumination, the net current I_L is:

$$I_L = I_{ph} - I_{Diode} = I_{ph} - I_o(e^{-\frac{qV_R}{kT}} - 1),$$

which becomes, if $V_R >> kT/q$,

$$I_L = I_{ph} + I_o\ .$$

Here, k is Plank's constant, T is absolute temperature and q is the electronic charge. In darkness, I_{ph} is zero, so that the dark current I_D is just $I_D = I_o$. Hence, the illuminated-to-dark current change ΔI is:

$$\Delta I = I_L - I_D = I_{ph}\ ,$$

so that equation (A.1) can be re-written as:

$$\Delta I = K_l(W+L_n)\,. \qquad \text{(A.2)}$$

Now the capacitance of the Schottky junction is given by $C_j = \epsilon_o \epsilon_r A/W$, where ϵ_r is the relative dielectric constant of the semiconductor, ϵ_o is the permittivity of a vacuum and A is the area of the junction. Substitution for W into equation (A.2) yields:

$$\Delta I = K_2\left(\frac{1}{C_j} + \frac{L_n}{\epsilon_o \epsilon_r A}\right), \qquad \text{(A.3)}$$

where $K_2 = K_1 \epsilon_o \epsilon_r A$.

From equation (A.3), it is seen that a plot of ΔI against $1/C_j$, as the reverse bias is varied, should yield a straight line, with an extrapolated intercept on the $1/C_j$ axis of $-L_n/(\epsilon_o \epsilon_r A)$. From this, the diffusion length L_n can be determined. Linearity would not be expected at low reverse and at forward bias because of violation of the inequality $V_R >> kT/q$ and the deviation from depletion approximation and ideal diode behaviour.

Apart from the application of this method to Schottky junctions, it can also be applied to pn+ homojunctions and heterojunctions. Here, one must consider collection of photogenerated carriers, not only in the depletion region and the p-type semiconductor but also in the n-type region close to the junction. However, if this layer acts as a window layer, it is possible that this contribution could be small and, therefore ,might be neglected with a small error.

[A.1] K.L. Smith and M. Abbot. *Solid State Electronics*, **15**, 361 (1972).

[A.2] M.L. Young and M.C. Rowland. *Phys. Status Solidi A*, **16**, 603 (1973).

[A.3] J. Dorantes-Davila, A. Lastras-Martinez and P.M. Raccah. *Appl. Phys. Lett.*, **38**, 442 (1981).

[A.4] V.A. Tyagai. *Soviet Phys. Solid State*, **6**, 1260 (1964). Translated from *Fizika Tverdogo Tela*, **6**, No. 6, 1602 (1984).

[A.5] A. Lastras-Martinez, P.M. Raccah and R. Triboulet. *Appl. Phys. Lett.*, **36**, 469 (1980).

APPENDIX A.4

RESULTS OF EARLY $CuInSe_2/CdS/CdO$ CELLS

Characteristics of early $CdO/CdS/CuInSe_2$ [7.8] measured under elevated illumination levels above 150 mW/cm^2, where the CdS was deposited by a dip coating method and the CdO by d.c. reactive sputtering. The measurements were taken on freshly made cells, where no annealing was carried out.

	$CuInSe_2$	CdS layer	CdO layer			Illuminated characteristics			
Cell No.	Crystallographic plane	Thick. (μm)	Thick. (μm)	Interference order, colour	Area (mm^2)	j_{sc} (mA/cm^2)	V_{oc} (volt)	FF	Efficiency (%)
86-1	(101)	0.10	0.37	3rd red	12.5	4.5	0.30	-	-
92-1	(112)	0.10	0.37	3rd red	6.3	12.8	0.35	-	-
95-5	(101)	0.10	0.43	4th green	6.7	28.4	0.41	-	-
95-4	(101)	0.10	0.62	5th red	6.9	45.2	0.37	0.3	5.1
83-1	(112)	0.12	0.75	6th red	7.0	44.7	0.41	0.5	8.5
63-1	(112)	0.24	0.87	7th red	12.5	11.8	0.33	-	-
63-2	(112)	0.20	0.64	6th green	7.3	40.2	0.37	0.3	4.8
95-3	(101)	0.10	0.75	6th red	6.7	46.8	0.37	0.4	6.3
96-1	(101)	0.10	0.75	6th red	8.0	30.0	0.35	-	-